

Mass Transfer and Accretion in the Eccentric Neutron-Star Binary Circinus X-1

by

Robert E. Shirey

Submitted to the Department of Physics
in partial fulfillment of the requirements for the degree of

Doctor of Philosophy

at the

MASSACHUSETTS INSTITUTE OF TECHNOLOGY

September 1998

© Robert E. Shirey, MCMXCVIII. All rights reserved.

The author hereby grants to MIT permission to reproduce and distribute publicly
paper and electronic copies of this thesis document in whole or in part, and to grant
others the right to do so.

Author
Department of Physics
June 19, 1998

Certified by
Hale V. D. Bradt
Professor of Physics
Thesis Supervisor

Accepted by
Thomas J. Greytak
Associate Department Head for Education

Mass Transfer and Accretion in the Eccentric Neutron-Star Binary Circinus X-1

by

Robert E. Shirey

Submitted to the Department of Physics
on June 19, 1998, in partial fulfillment of the
requirements for the degree of
Doctor of Philosophy

Abstract

I have carried out a project to study the eccentric neutron-star binary Circinus X-1 through an extensive series of observational studies with the *Rossi X-ray Timing Explorer* satellite and through theoretical computer models I developed to explore mass transfer and evolution in an eccentric binary. We also organized two multi-frequency campaigns to study correlated variability in different frequency bands.

The X-ray observations showed that the intensity of Cir X-1 currently maintains a bright baseline level, with strong flares occurring after phase zero of each 16.55-day cycle of the source. This behavior is thought to be due to enhanced mass transfer occurring near periastron of a highly eccentric binary orbit. Dips below the baseline intensity level also occur near phase zero.

I modeled the evolution of the energy spectrum during dips with a variably absorbed bright component plus a fainter unabsorbed component. I show that variability not attributable to absorption dips is related to the spectral/intensity states of the “Z source” class of low-mass X-ray binaries (LMXBs), namely motion along (or shifts of) the horizontal, normal, and flaring branches of the “Z” track in color-color and hardness-intensity diagrams.

I found rapid X-ray variability properties associated with each spectral/intensity state: On the horizontal branch, quasi-periodic oscillations (QPOs) in the X-ray intensity shift in frequency from 1.3 to 35 Hz. On the normal branch, a different QPO occurs at about 4 Hz. On the flaring branch only strong aperiodic variability occurs. I modeled the evolution of the energy spectra associated with each of these branches.

To study mass transfer in an eccentric binary, I developed computer codes for transfer via Roche-lobe overflow and from a stellar wind. I derive theoretical mass accretion profiles and compare them to the observed profile of the X-ray intensity.

In order to explore the possible evolutionary history of Circinus X-1, I developed a binary-evolution computer code for a neutron-star and low-mass companion in an eccentric orbit. I use this code in a population-synthesis study to show that the number of systems in the Galaxy expected to resemble Cir X-1 is of order unity, consistent with its unique status as an LMXB with high eccentricity.

Thesis Supervisor: Hale V. D. Bradt
Title: Professor of Physics

Acknowledgments

First, I would like to thank Prof. Hale Bradt for giving me the opportunity to work with him and participate in the *Rossi X-ray Timing Explorer* project. He has demonstrated how to think like a scientist and produce clear scientific writings. He has always supported me and encouraged my efforts.

I also want to thank Prof. Saul Rappaport for helping with the several theoretical modeling projects in my thesis. Although I was initially reluctant to delve into theoretical calculations, I eventually found that they were not to be feared and could be quite interesting.

Ed Morgan got me started on Circinus X-1 several years ago by suggesting I work on a proposal to observe Cir X-1 with *RXTE* once it launched. I also learned many analysis techniques from Ed.

Al Levine has provided much-appreciated scientific guidance, especially in writing papers. His participation has certainly improved the quality of my work.

In fact, all the members of the *RXTE* team at M.I.T. have contributed to my education and to this project. Ron Remillard, Wei Cui, and Deepto Chakrabarty have all given helpful advice and shared experiences with analyzing and interpreting *RXTE* data.

The people I've interacted with most at M.I.T. are the other graduate students, and my office mates in particular. Don Smith came to M.I.T. at the same time I did, so we've shared all the ups and downs of the experience. He, Linqing Wen, and Mike Munro have all been great to work with and to discuss ideas with around the office. Our former office mates Charlie Collins and Chris Becker provided a wealth of knowledge and experience about M.I.T., Boston, and astrophysics. In particular my binary evolution code was based on one Chris developed as part of his thesis.

I would like to thank all the members of our multi-frequency campaigns for all their efforts to coordinate observations and willingness to share data: George Nicolson, Ian Glass, Allyn Tennant, Rob Fender, Kinwah Wu, and Helen Johnston.

My parents have supported my interest in astronomy from the beginning. They gave me a 6-inch diameter telescope for Christmas when I was in elementary school (and then let me sell it several years later when an Atari system seemed more important).

Finally, I want to thank my wife, Anne, for supporting me in so many ways throughout the whole process. When we were married, exactly five years ago, I'm sure she didn't know what she was getting into. She has made many sacrifices to help make this happen. Now five years and two children (Ben and Alex) later, we've finally reached this milestone. I thank her for her patience, support, and love. This thesis is for Anne.

Robert Shirey
Cambridge, MA
June 19, 1998

Contents

1	Introduction	23
1.1	X-ray Astronomy	23
1.2	X-ray Binaries	23
1.2.1	Overview	23
1.2.2	HMXBs	24
1.2.3	LMXBs	25
1.3	Circinus X-1	28
1.3.1	Intensity Cycle	28
1.3.2	X-ray Bursts	28
1.3.3	Rapid X-ray Variability	29
1.3.4	Distance	29
1.3.5	Young Runaway Binary	29
1.3.6	Infrared and Optical Counterpart	30
1.3.7	Radio Ephemeris	31
1.4	Objectives and Overview of this Project	31
2	The Rossi X-ray Timing Explorer	33
2.1	Overview	33
2.2	Proportional Counter Array	33
2.3	High-Energy X-ray Timing Experiment	35
2.4	All-Sky Monitor	36
2.5	Experiment Data System	37
3	Overview of RXTE Observations	39
3.1	ASM Observations of Circinus X-1	39
3.1.1	General Features of the ASM Light Curves	39
3.1.2	Cycling Hardness Ratios	41
3.1.3	16.55-day Period	41

3.1.4	Folded Cycle Profile	41
3.2	PCA Observations of Circinus X-1	44
3.2.1	Overview	44
3.2.2	Observation Summaries	46
3.2.2.1	Study A: 1996 March 5–21	46
3.2.2.2	Study B: 1996 April 7	48
3.2.2.3	Study C: 1996 May 7–14	49
3.2.2.4	Study D: 1996 Sept. 20 – Oct. 8	49
3.2.2.5	Study E: 1997 Feb. 18 – Mar. 4	50
3.2.2.6	Study F: 1997 May 16 – May 21	50
3.2.2.7	Study G: 1997 June 4–22	50
3.2.2.8	Study H: 1997 Sept. 18 – Oct. 4	50
4	X-ray Timing and Spectral Evolution vs. Orbital Phase	53
4.1	Overview	53
4.2	Observations and Results	54
4.3	Discussion	59
5	QPOs Associated with Spectral Branches	61
5.1	Overview	61
5.2	Observations	62
5.3	Analysis and Results	64
5.3.1	Color-color and Hardness-intensity Diagrams	64
5.3.2	Power Density Spectra	67
5.3.3	Temporal Behavior versus Position on Spectral Branches	73
5.4	Discussion	73
5.4.1	Horizontal Branch	73
5.4.2	Normal Branch	75
5.4.3	Flaring Branch	76
5.4.4	Relation to Other Sources	76
5.5	Summary	79
6	Correlated Timing and Spectral Behavior	81
6.1	Overview	81
6.2	1997 June PCA Observations	82

6.3	Complete Spectral Track	82
6.4	Evolution of the Power Density Spectrum	89
6.5	Evolution of the Energy Spectrum	91
6.6	Selection of Spectral Models	93
6.7	Fits to Spectra from 20 HID Regions	96
6.8	Summary	101
7	Absorption Dips	103
7.1	Overview	103
7.2	Dips in RXTE Light Curves	103
7.3	Evolution of Hardness Ratios During Dips	104
7.4	Evolution of Energy Spectra During Dips	109
7.4.1	Spectral Model	109
7.4.2	Spectral Fitting Strategy	112
7.4.3	Energy Spectra Inside and Outside Dips	113
7.4.4	Iron Emission Line	117
7.4.5	Spectral Evolution During Dip Transitions	118
7.5	Discussion	122
8	Multi-frequency Observations	125
8.1	Overview	125
8.2	May 1996 Campaign	125
8.2.1	Radio (HartRAO)	127
8.2.2	Infrared Photometry (SAAO)	128
8.2.3	Correlated Multi-frequency Variability	128
8.3	June 1997 Campaign	128
8.3.1	Radio (HartRAO)	130
8.3.2	IR Photometry (SAAO)	130
8.3.3	IR Spectroscopy (ANU)	132
8.3.4	Optical Spectroscopy (AAT)	132
8.3.5	Comparison of the AAT Optical Spectrum to HST Results	132
8.4	Conclusions	135
9	Mass Transfer in an Eccentric Binary	137
9.1	Overview	137

9.2	Mass Transfer via Roche-Lobe Overflow	137
9.2.1	Equipotential Surfaces in an Eccentric Binary Orbit	138
9.2.2	Keplerian Orbits	138
9.2.3	Trajectory of a Particle in the Binary Potential	139
9.2.4	Final Outcome of Particle Trajectories	139
9.2.5	Comparison to the X-ray Intensity Profile	142
9.3	Mass Transfer via a Stellar Wind	142
9.3.1	Bondi-Hoyle Accretion	145
9.3.2	Wind Accretion Profile in an Eccentric Binary	146
9.3.3	Comparison to the X-ray Intensity Profile	147
10	Eccentric Binary Evolution	149
10.1	Overview	149
10.2	Binary Evolution Theory	149
10.2.1	Evolution of Binary Parameters	149
10.2.2	Evolution of the Donor Star Radius	151
10.2.2.1	Nuclear Evolution	151
10.2.2.2	Thermal Readjustment Toward Equilibrium	152
10.2.2.3	Adiabatic Response to Mass Loss	152
10.2.3	Evolution of Orbital Parameters	152
10.2.3.1	Tidal Evolution	153
10.2.3.2	Effect of Mass Transfer on the Orbit	154
10.2.3.3	Magnetic Braking	155
10.2.3.4	Gravitational Radiation	155
10.2.4	Stable Mass Transfer	156
10.3	Binary Evolution Code	158
10.3.1	Code Algorithm	158
10.3.2	Results	159
10.4	Monte-Carlo Population Synthesis	163
10.4.1	Systems Resembling Cir X-1	163
10.4.2	Predicted System Parameters for Cir X-1	165
10.5	Conclusions	170
11	Conclusions	171

A	Fourier Timing Techniques	175
A.1	Introduction	175
A.2	Power Density Spectra	176
A.2.1	Leahy Normalization	176
A.2.2	Estimate of the Poisson Noise Level	176
A.2.3	Fractional RMS Variability	177
A.2.4	Estimates of Power Variance	177
A.2.5	Data Gaps	178
A.2.6	Variable Number of Detectors	178
A.3	Complex Cross Spectra	180
A.3.1	Time Lags	180
A.3.2	Coherence Function	180
B	Standard PCA Light Curves	183

List of Figures

1-1	X-ray color-color diagrams and power density spectra typical of Z sources and atoll sources. The soft color is approximately $I[3-5 \text{ keV}] / I[1-3 \text{ keV}]$ and the hard color $I[6.5-18 \text{ keV}] / I[5-6.5 \text{ keV}]$. Power spectra are shown for the horizontal, normal, and flaring branches (HB/NB/FB) of Z sources, and the island state, lower banana, and upper banana (IS/LB/UB) of atoll sources. (Figure from van der Klis 1995 [78].)	27
2-1	<i>Rossi X-ray Timing Explorer</i> spacecraft.	34
3-1	ASM light curve (1.5–12 keV; 90-s exposures) covering 1996 January – 1998 May. Phase zero is indicated by vertical dotted lines. Bars along the top axis mark the times of PCA observations (labeled A–H; see section 3.2).	40
3-2	Light curve and two hardness ratios for the first ten full 16.55-day cycles of Cir X-1 observed with the ASM. Each light-curve point is the average count rate ($I[1.5-12 \text{ keV}]$) from a single 90-s ASM exposure. The hardness ratios were obtained from 1-day averages of the 90-s intensities and are defined as $HR1=I[3-5 \text{ keV}] / I[1.5-3 \text{ keV}]$ and $HR2=I[5-12 \text{ keV}] / I[3-5 \text{ keV}]$. The vertical dotted lines indicate phase zero.	42
3-3	Folded light curve of Cir X-1 from the three ASM energy bands. The data are repeated in order to show two complete cycles. Each point is from a 90-s exposure, with a typical error bar of 1–2 c/s. The folded data spans the entire time period covered by Figure 3-1.	43

3-4	Left: Folded Cir X-1 light curve from the full ASM energy band (1.5–12 keV) and two hardness ratios. Right: Folded light curves from the three ASM energy bands. The data are binned into 100 phase bins per cycle, averaged in each phase bin, and duplicated to show two complete cycles. Error bars on the light curves indicate the standard deviation of the mean value derived for each phase bin, and these error estimates were propagated when computing the hardness ratios. The folded data spans the entire time period covered by Figure 3-1.	45
3-5	Light curves for each 16.55-d cycle of Cir X-1 observed with the PCA. For each cycle, the phase-zero date and letter of the study (see Table 3.1) are listed. The intensity is for the full PCA energy range, and a conversion factor of $1 \text{ Crab} \approx 2600 \text{ counts s}^{-1} \text{ PCU}^{-1}$ has been used.	47
3-6	PCA light curves in two energy bands (16-s bins), and the ratio of intensity in the hard band to that in the soft band, for the observation on 1996 April 7 (study B), spanning 15 ks. The lowest intensity in both bands during dips is well above the background level ($\sim 30 \text{ c/s}$ and $\sim 45 \text{ c/s}$ for 2–7.4 keV and 7.4–28 keV respectively, not subtracted).	48
3-7	PCA light curves in two energy bands (16-s bins), and the ratio of intensity in the hard band to that in the soft band, for the observations on 1996 September 24 – October 8 (study D). Due to some observations with a PCU not operating, all points in this plot were derived from PCUs 0, 1, & 2 and adjusted by 5/3 for comparison with other figures in this section. Phase zeros occurred at days 346.782 and 363.328.	49
3-8	PCA light curves in two energy bands (16-s bins; 13 kilocounts/s=1.0 Crab for the combined 2–33 keV band), and the ratio of intensity in the hard band to that in the soft band, for the observation on 1997 September 20 (part of study H), spanning 7000 s.	51
4-1	PCA light curves in two energy bands (16-s bins), and the ratio of intensity in the hard band to that in the soft band, for observations 1–11 of 1996 March. Phase zero corresponds to day 148.227. The intensity is well above the background level in both bands ($\sim 25 \text{ c/s}$ and $\sim 40 \text{ c/s}$ for 2–6.3 keV and 6.3–24 keV respectively, not subtracted) even during the dips. Observation 12 is omitted since it was carried out with only three PCUs and a different gain setting.	55

- 4-2 Sample PCA light curves (2–60 keV) comparing 2000-s segments showing (a) strong variability and dips near phase zero (phase 0.98; Obs. 1), (b) a brighter portion of the bright flaring state three days later (phase 0.15; Obs. 2), and (c) a typical observation away from phase zero (phase 0.50; Obs. 6). Background (~ 100 c/s) is not subtracted and no deadtime corrections have been made. 56
- 4-3 Power density spectra from seven *RXTE* orbits away from phase zero, offset downward at decade intervals. (The ordinate scale applies to the top curve.) The curves are ordered by the frequency of the 1.3–12 Hz QPO peak and are labeled with orbital phase. 58
- 4-4 Flat-top power level (a) and QPO frequency (b) as a function of orbital phase over a single orbital cycle. (c) Frequency of the narrow low-frequency QPO and the broad high-frequency QPO vs. the flat-top power level. (d) Cut-off frequency of the flat-topped power vs. flat-top power level. 59
- 5-1 *RXTE* ASM light curves (1.5–12 keV) for three 16.55 d cycles of Cir X-1 showing different flaring profiles. Each intensity point corresponds to a 90-s exposure by one of the three ASM cameras, and the hardness ratio (HR), defined as the ratio of counting rates for 5–12 keV to 3–5 keV, is shown in one-day averages. The 3–5 keV to 1.5–3 keV hardness ratio exhibits very similar behavior and is not shown here. The intensities are for Cir X-1 after background and other sources in the field of view have been subtracted. The Crab nebula yields ~ 75 c/s. Vertical dashed lines indicate phase zero based on the radio ephemeris of Stewart et al. 1991. Day zero corresponds to (a) 1997 April 23.87 (b) 1996 August 2.14 and (c) 1997 February 16.69. For cycle (c), the intensity ranges ($I[2.0\text{--}18\text{ keV}]$) seen in the eight *RXTE* PCA observations (I–VIII in time order) are also shown. 63
- 5-2 PCA light curves (2–18 keV, 5 PCUs) and hardness ratios ($HR = I[6.3\text{--}13\text{ keV}] / I[2.0\text{--}6.3\text{ keV}]$) in 16 s time bins for the eight observations made during 1997 February 18 – March 4. A count rate of 13 kcts/s ≈ 1.0 Crab. The data gaps in Obs. VI were longer than as shown here; the second segment of the observation has been shifted left by 4000 s and the third segment by 5000 s. These data were used to construct the hardness-intensity diagram in Figure 5-3. The association with specific regions of that diagram is indicated below each light curve. 65

- 5-3 Color-color diagram (a) and hardness-intensity diagram (b) for all eight observations (I–VIII). In the CD, soft color is defined as $I[4.8\text{--}6.3\text{ keV}] / I[2.0\text{--}4.8\text{ keV}]$ and hard color as $I[13\text{--}18\text{ keV}] / I[8.5\text{--}13\text{ keV}]$. In the HID, the intensity, $I[2.0\text{--}18\text{ keV}]$, is from all five PCUs and the hardness ratio is a “broad” color: $I[6.3\text{--}13\text{ keV}] / I[2.0\text{--}6.3\text{ keV}]$. Each point corresponds to 16 s of data. Background has been subtracted, but it does not affect the intensity or soft color and only slightly affects the hard color. The three insets in the CD separate overlapping points from observations I–V. The HID track for each observation has been divided into three regions (1–3) for timing analysis. 66
- 5-4 Averaged and rebinned power density spectra (2–32 keV) for each of the three HID regions for each observation. Poisson noise has been subtracted from each PDS (see text). 67
- 5-5 Averaged and rebinned power density spectra for HID region VIII-3 in three energy bands. A harmonic peak of the 7.6 Hz QPO is clearly visible in the high-energy channel (c). The broad high-frequency peak, most clear in (b), occurs near ~ 100 Hz in this observation. The low-frequency noise cuts off less sharply as energy increases. 69
- 5-6 Centroid frequency of the QPOs versus intensity ($I[2.0\text{--}18\text{ keV}]$). A filled circle represents the narrow QPO and a filled square represents the broad ~ 4 Hz QPO (all points below 5 Hz are the broad QPO). Unfilled circles and squares indicate the approximate frequency of a knee or very weak peak that may be associated with the narrow and broad QPO respectively. Error bars on frequency measurements (filled points only) represent 90% confidence intervals for a single parameter ($\Delta\chi^2=2.7$). In many cases, the error bar for the QPO frequency is smaller than the plot symbol. . . 71
- 5-7 Rms amplitude of QPOs versus photon energy. Panel (a) shows the rms for the narrow QPO at 7.2 Hz (solid dot) and (b) for an example of the broad 4 Hz QPO (solid box). In panel (c), unfilled circles and boxes indicate the rms amplitude of a component forming a knee or very weak peak that may be associated with the narrow and broad QPOs respectively. The broad QPO points have been offset slightly to the right in energy for clarity. Errors on QPO amplitudes represent 90% confidence intervals. . . 72
- 5-8 Hardness-intensity diagram showing QPO properties for the regions from Figure 5-3b. The frequency of the 6.8 to 32 Hz QPO is labeled (in Hz) beside each region where it is present. Parenthesized frequencies indicate that this component was unpeaked, i.e., a knee. Letters indicate the strength of the broad 4 Hz QPO: S—strong, M—medium, and W—weak or unpeaked. 74

- 5-9 Broad-color and hard-color CDs and HIDs for observations V and VI. In all four diagrams, Obs. V is in the lower left and Obs. VI in the upper right. The CD and HID tracks for Obs. V both turn upward at the left end in the broad-color diagrams (a,b) but turn downward in the hard-color diagrams (c,d). In the HIDs, presence of the 32 Hz HBO, 4 Hz NBO, and VLFN is indicated along the branches. An apparent shift of the normal branch between observations V and VI is labeled in (b). The intensity, $I[2.0-18 \text{ keV}]$, is from all five PCUs. The soft color is defined as $I[4.8-6.3 \text{ keV}] / I[2.0-4.8 \text{ keV}]$, the broad color as $I[6.3-13 \text{ keV}] / I[2.0-6.3 \text{ keV}]$, and the hard color as $I[13-18 \text{ keV}] / I[8.5-13 \text{ keV}]$. Each point corresponds to 16 s of background-subtracted data. 77
- 6-1 Light curves in four energy bands and two hardness ratios for PCA observations of Cir X-1 from 1997 June 10–20, covering a 10-day period around phase zero ($\phi = 0$). The intensities at the beginning of these observations (day 610) are typical “quiescent” levels. Each point represents 16 s of background-subtracted data from PCUs 0, 1, and 2. Ratios of the intensities in the four bands produce soft ($I[4.8-6.3 \text{ keV}] / I[2.0-4.8 \text{ keV}]$) and hard ($I[13-18 \text{ keV}] / I[6.3-13 \text{ keV}]$) hardness ratios. Segments labeled A, B, C & D were used for spectral studies. 83
- 6-2 Color-color and hardness-intensity diagrams from PCA observations during 1997 June 10–21 (the entire period covered by Figure 6-1). Each point represents 16 s of background-subtracted data from PCUs 0, 1, and 2. 84
- 6-3 Color-color and hardness-intensity diagrams from time segments “C” (left panels) and “D” (right panels) of Figure 6-1 (1997 June 13.625–14.125 and 1997 June 17.075–17.600 respectively). Each point represents 16 s of background-subtracted data from PCUs 0, 1, and 2. 85
- 6-4 Hardness-intensity diagram from time segment C (1997 June 13.625–14.125; day 12.625–13.125). The HID track has been divided into 20 regions from which power density spectra and energy spectra were constructed. 87
- 6-5 Top: light curves in 3 energy channels and bottom: total 2–18 keV light curve, broad color, and HID regions for time segment C (1997 June 13.625–14.125; see Figure 6-1). Based on HID region numbers, the predominant spectral branch is identified for each portion of the data. Absorption dips (omitted from HID regions) are clearly identified by decreased intensity coupled with upward broad-color spikes. 88

6-6	Averaged and rebinned power density spectra (2–32 keV) for each of the 20 regions along the HID track in Figure 6-4. The estimated Poisson noise level has been subtracted from each PDS.	90
6-7	Cir X-1 energy spectra (2.5–25 keV; PCU 0 only) for several regions on each segment of the HID track in Figure 6-4. The region numbers within the figures are ordered vertically to match the relative intensities at the low and/or high-energy ends of the spectra.	92
6-8	Spectrum A and model (histogram) consisting of a disk blackbody and blackbody (see Table 6.1). The residuals show a peak at 6–7 keV that may be due to an iron emission line.	95
6-9	Fitted energy spectra (2.5–25 keV; PCU 0 only) and model components (disk blackbody and blackbody) for HID regions 1, 7, and 11 of Figure 6-4. The disk blackbody dominates at low energy and the blackbody dominates at high energy. Fit parameters are listed in Table 6.2.	98
6-10	Fitted energy spectra (2.5–25 keV; PCU 0 only) and model components (disk blackbody and blackbody) for HID regions 13, 15, and 20 of Figure 6-4. The blackbody only contributes to the high-energy end of the spectrum in region 13, and has faded away entirely in regions 15 and 20. Fit parameters are listed in Table 6.2.	99
6-11	Spectra from HID regions 17 and 20 (crosses) and fitted models (histograms) consisting of a disk blackbody and blackbody. The ratio of residuals to error bars shows a narrow edge or line-like feature above 10 keV.	100
7-1	Light curves in four energy channels and two hardness ratios for PCA observations of Cir X-1 from 1996 September 20–22, covering a two-day period around phase zero ($\phi = 0$). Three dips have been identified for further study. Each point represents 16 s of background-subtracted data from PCUs 0, 1, and 2. Ratios of the intensities produce soft ($I [4.8\text{--}6.3 \text{ keV}] / I [2.0\text{--}4.8 \text{ keV}]$) and hard ($I [13\text{--}18 \text{ keV}] / I [6.3\text{--}13 \text{ keV}]$) hardness ratios. The intensity levels of the segment at day ~ 347.2 (after Dip 1) are close to the level in each band during the quiescent phases of the orbit.	105
7-2	Light curves in four energy channels and two hardness ratios spanning 4000 s including Dip 1. Time zero corresponds to day 347.041 in Figure 7-1. The intensity and hardness ratio points are the same as in Figure 7-1. Energy spectra were extracted from two 96-s time segments (A and B), indicated by dotted vertical lines, and four 16-s segments (a–d) indicated by diamonds.	106

7-3	Light curves in four energy channels and two hardness ratios spanning 4000 s including Dip 2. Time zero corresponds to day 347.254 in Figure 7-1. The intensity and hardness ratio points are the same as in Figure 7-1. Energy spectra were extracted from two 304-s time segments (A and B), indicated by dotted vertical lines, and four 16-s segments (a–d), indicated by diamonds.	107
7-4	Light curves in four energy channels and two hardness ratios spanning 4000 s including Dip 3. Time zero corresponds to day 347.325 in Figure 7-1. The intensity and hardness ratio points are the same as in Figure 7-1. Energy spectra were extracted from six 16-s time segments (a–f), indicated by diamonds.	108
7-5	Color-color and hardness-intensity diagrams for the last 1716 s of data in Figure 7-4, during which the intensity gradually transitioned from the non-dip baseline to the bottom of a dip. Intensity is $I[2.0\text{--}18\text{ keV}]$, and the hardness ratios are defined as soft color: $I[4.8\text{--}6.3\text{ keV}] / I[2.0\text{--}4.8\text{ keV}]$, hard color: $I[13\text{--}18\text{ keV}] / I[6.3\text{--}13\text{ keV}]$, and broad color: $I[6.3\text{--}18\text{ keV}] / I[2.0\text{--}6.3\text{ keV}]$. Each point represents 16 s of background-subtracted data from PCUs 0, 1, and 2.	110
7-6	Color-color and hardness-intensity diagrams for the first three segments in Figure 7-1 (day 346.31–346.52), during which Cir X-1 was in an extended low/dip state. Intensity is $I[2.0\text{--}18\text{ keV}]$, and the hardness ratios are defined as soft color: $I[4.8\text{--}6.3\text{ keV}] / I[2.0\text{--}4.8\text{ keV}]$, hard color: $I[13\text{--}18\text{ keV}] / I[6.3\text{--}13\text{ keV}]$, and broad color: $I[6.3\text{--}18\text{ keV}] / I[2.0\text{--}6.3\text{ keV}]$. Each point represents 16 s of background-subtracted data from PCUs 0, 1, and 2.	111
7-7	Top: Spectral fits for 96-s segments prior to Dip 1 (spectrum A) and during Dip 1 (spectrum B). Bottom: same spectra and model (see text), but with a Gaussian emission-line component included to fit the peaked residuals near 6.5 keV. The data shown are from PCU 0 only.	114
7-8	Top: Spectral fits for 304-s segments prior to Dip 2 (spectrum A) and during Dip 2 (spectrum B). Bottom: same spectra and model (see text), but with a Gaussian emission-line component included to fit the peaked residuals near 6.5 keV. The data shown are from PCU 0 only.	115
7-9	Spectral fits for four 16-s segments (a–d) during the decline into Dip 1. Only the column density of the bright component varies between the four jointly-fit curves. The data shown are from PCU 0 only.	119

7-10	Spectral fits for four 16-s segments (a–d) during the decline into Dip 2. Only the column density of the bright component varies between the four jointly-fit curves. The data shown are from PCU 0 only.	120
7-11	Spectral fits for six 16-s segments (a–d) during the decline into Dip 3. Only the column density of the bright component varies between the six jointly-fit curves. The data shown are from PCU 0 only.	121
8-1	X-ray, IR, and radio light curves of Cir X-1 from 1996 May 7–17. Phase zero is indicated by the vertical dotted line at day 214.413 (1997 May 11.413). PCA intensity is from the 2–32 keV band (16-s bins) and ASM intensity is from 2–12 keV (90-s exposures). Errors on the PCA data are negligible. Typical error bars are shown for the ASM, IR, and radio data: errors on the ASM data are typically 2–5 c/s, on the IR data are typically about 0.03 magnitudes (worse on days 214 & 215), and on the radio data are about 30 mJy. The average quiescent level of 29 mJy has been subtracted from the radio data. (Data provided by I. Glass (IR), G. Nicolson (radio), and the <i>RXTE</i> /ASM team.)	126
8-2	X-ray and IR light curves of Cir X-1 from day 212.93–213.19. X-ray intensity is from the 2–32 keV PCA band (16-s bins). A typical IR error bar of ± 0.03 magnitudes is shown. (IR data courtesy of I. Glass.)	129
8-3	X-ray (PCA and ASM) and radio (5.0 GHz) light curves of Cir X-1 from 1997 May 7 – August 25. Phase zero is indicated by the vertical dotted lines. PCA intensity is from the 2–32 keV band (16-s bins) and ASM intensity is from 2–12 keV (90-s exposures). Errors on the PCA data are negligible and errors on the ASM data are typically 2–5 c/s. For each 16.55-d cycle, the average radio flux for the phase interval 0.3 to 0.9 of that cycle was subtracted from the data; the bias removed was typically 50–60 mJy and a typical error bar is shown. (The radio data was provided by G. Nicolson, and ASM data by the <i>RXTE</i> /ASM team. The PCA data are from studies F and G; see Table 3.1.)	131
8-4	Infrared spectrum of Cir X-1 from ANU on 1997 June 20 (about phase 0.5), showing He I (2.06 μm) and H Brackett γ (2.165 μm) emission lines. This spectrum was compiled from the sum of 16 120-s exposures. (Figure courtesy of H. Johnston.) . .	133
8-5	Optical spectrum of Cir X-1 from AAT on 1997 June 4 (about phase 0.5), showing a prominent H α emission line, as well as weaker He I(6678 Å) and He I(7065 Å) lines. (Figure courtesy of H. Johnston.)	134

- 9-1 Panels (a) and (c): stop time of particles in a system with $e=0.5$ (and $P=16.55$ d) versus time of release from donor ($1 M_{\odot}$), with the final outcome (recapture or entry into disk) indicated. Panels (b) and (d): normalized rate of particles entering the accretion disk versus their arrival time relative to periastron. The top panels, (a) and (b), are for an initial radial velocity from the surface of 30 km/s, and the bottom panels, (c) and (d), are for 60 km/s. In (a) and (c), the solid diagonal line has a slope of unity and indicates zero elapsed time between release and the final outcome; the horizontal dashed line indicates a final outcome occurring at periastron. 141
- 9-2 Panels (a) and (c): stop time of particles in a system with $e=0.8$ (and $P=16.55$ d) versus time of release from donor ($1 M_{\odot}$), with the final outcome (recapture or entry into disk) indicated. Panels (b) and (d): normalized rate of particles entering the accretion disk versus their arrival time relative to periastron. The top panels, (a) and (b), are for an initial radial velocity from the surface of 50 km/s, and the bottom panels, (c) and (d), are for 100 km/s. In (a) and (c), the solid diagonal line has a slope of unity and indicates zero elapsed time between release and the final outcome; the horizontal dashed line indicates a final outcome occurring at periastron. 143
- 9-3 Trajectory of a particle moving in an eccentric binary system ($M_{don}=1 M_{\odot}$, $e=0.5$), where the particle starts with an initial radial velocity of 60 km/s off the surface of the donor at a time t_0 relative to periastron. The plot is in a non-rotating frame with the CM at the origin (+). The location of the particle, donor star, and neutron star at t_0 are indicated by the diamond, asterisk, and solid dot respectively. The subsequent motion of the particle until enters the accretion disk or is recaptured is shown as a solid curve, and the motion of the donor and neutron star in their orbits during that time is indicated by a dashed or dotted ellipse segment respectively. 144
- 9-4 Wind accretion rate versus orbital phase for three eccentricities and wind speeds for a $5 M_{\odot}$ donor. Each curve is normalized by its peak value; the actual wind capture fraction (relative to the mass-loss rate of the donor) decreases significantly with higher velocity. 148
- 10-1 Results of a binary evolution calculation for a system started with the donor star just filling its critical potential lobe, with initial values: $M_{don} = 2 M_{\odot}$, $a = 9.34 R_{\odot}$, and $e = 0.6$. The donor remains in contact with its critical potential lobe throughout the evolution; thus, the curve for R_{lobe} coincides with the curve for R_{don} . A solid dot on some of the curves marks the time corresponding to an orbital period of 16.55 days. 161

10-2	Results of binary evolution calculation for a system started with the donor underfilling its critical potential lobe, with initial values: $M_{don} = 1 M_{\odot}$, $a = 27 R_{\odot}$, and $e = 0.9$.	162
10-3	Eccentricity and mass transfer rate versus time for binaries with initial values $M_{don} = 2 R_{\odot}$, $e = 0.9$, and semimajor axes (a) between 37 and 128 R_{\odot} .	164
10-4	Histograms of number of binaries versus <i>initial</i> M_{don} and e which eventually reach $P = 16.55$ d and $1 \times 10^{-9} M_{\odot}/\text{yr} < \dot{M} < 1 \times 10^{-7} M_{\odot}/\text{yr}$. The y-axis normalization is arbitrary.	166
10-5	Histograms of the number of binaries versus various system parameters at the time when systems resemble Cir X-1, i.e., $P = 16.55$ d and $1 \times 10^{-9} M_{\odot}/\text{yr} < \dot{M} < 1 \times 10^{-7} M_{\odot}/\text{yr}$. The y-axis normalization is arbitrary.	167
10-6	Optical and infrared absolute magnitudes (V,R,I,J,K) of the donor star in systems that resemble Cir X-1, i.e., those from Figure 10-5. The y-axis normalization of the histograms is arbitrary.	169

List of Tables

2.1	Approximate energy ranges for eight PCA bands (A–H) defined in terms of absolute (0–255) and Standard2 (0–128) channels. Gain epoch 1 includes all observations before before 1996 March 21, epoch 2 1996 March 21 – April 15, and epoch 3 after 1996 April 15. Energy values shown are derived from the full PCA with all detectors and layers added.	37
3.1	PCA observations of Cir X-1 (1996–1997).	46
4.1	March 1996 PCA observations of Cir X-1	54
5.1	PCA observations of Cir X-1 during 1997 February 18 – March 4.	62
6.1	Fit parameters for spectra A & B for four models.	94
6.2	Fit parameters for HID regions 1–20 using a model consisting of a disk blackbody and a blackbody.	97
7.1	Top group: joint fit parameters of the bright and faint components of spectra from outside (A) and inside (B) dips 1 and 2. Middle group: the same, but with an added Gaussian line. Third group: joint fit parameters for the four to six 16-s spectra for dips 1, 2, and 3. The absorption parameters ($N_H^{(1)}$) for the bright component are given in Tables 7.2 (A–B) & 7.4 (a–f) and the iron line parameters are given in Table 7.3.	116
7.2	Effective hydrogen column density of the bright component outside (A) and inside (B) Dips 1 and 2 (from fits with and without a ~ 6.5 keV Gaussian emission line).	116
7.3	Gaussian emission-line parameters for the joint fits of spectra outside and inside dips (A–B) and during entry into a dip (a–d, a–f). In each case, the same Gaussian line parameters were used for each spectrum in a joint fit.	118

7.4	Effective hydrogen column density responsible for the variable absorption in the bright component, due to photo-electric absorption and Thompson scattering, during 16-s spectra from Dips 1, 2, and 3.	122
8.1	Multi-frequency Observations of Cir X-1 from 1996 May. Dates in parentheses were cancelled due to poor weather conditions.	127
8.2	Multi-frequency Observations of Cir X-1 from 1997 June. Dates in parentheses were cancelled due to poor weather conditions.	130
8.3	Infrared JHKL photometry measurements from 1997 June 14 & 15. Errors are ± 0.03 , except on the L magnitude the error is ± 0.05	132

Chapter 1

Introduction

1.1 X-ray Astronomy

X-rays are strongly absorbed by the Earth's atmosphere, making ground-based observations of astronomical X-ray sources impossible. Thus, X-ray astronomy did not begin until rockets and high-altitude balloons became available to carry instruments above a significant fraction of the atmosphere. The first celestial X-ray source (other than the Sun), Scorpius X-1, was discovered in 1962 using a rocket-borne detector [22]. Additional X-ray sources were first detected by balloon and rocket experiments during the 1960's.

Many more sources were discovered with the launch of the first astronomical X-ray satellite, *Uhuru*, in 1970. This was followed by a series of satellites in the 1970's, including *Vela 5*, *Copernicus*, *Ariel V*, *SAS-3*, *OSO-7*, *OSO-8*, *COS-B*, *HEAO-1*, *Einstein*, and *Hakucho*. In the 1980's *Tenma*, *EXOSAT*, *Ginga*, and *Mir-Kvant* were launched. Missions in the 1990's include *Granat*, *ROSAT* and *ASCA*, and most recently, *RXTE* and *BeppoSAX*. In the next few years, several major X-ray spectroscopy and imaging missions will be launched, including *AXAF*, *XMM*, and *Spectrum-X-Gamma*.

1.2 X-ray Binaries

1.2.1 Overview

Most of the bright celestial X-ray sources are thought to consist of a neutron star or black hole accreting matter from a binary companion star (see the book *X-ray Binaries* [43] for a thorough review of the subject). The gravitational potential energy released when matter falls onto these

highly compact objects produces high-luminosity radiation (of order 10^{37} – 10^{38} erg/s) from a small area (~ 10 km radius), resulting in an effective temperature of 10^6 – 10^7 K, i.e., primarily X-ray wavelengths ($\lambda \sim 0.1$ – 100 Å, $E \sim 0.1$ – 100 keV).

The binary orbital period can be well established through Doppler studies of X-ray pulsars (see section 1.2.2 below). The period is sometimes detected through modulation of the intensity in X-ray, optical, or other frequency bands. X-ray binaries have periods as short as minutes to as long as months. When the radial component of the orbital velocity of the companion is also measured, from Doppler-shifted lines in the optical spectrum, a lower limit to the mass of the compact object (the mass function) can be derived. A more exact estimate requires knowledge of the mass of the companion (e.g. measured from Doppler shifts of pulsed X-ray emission) and the inclination angle of the orbit relative to the line of sight. Even a lower limit can be very informative, since degeneracy pressure in a neutron star is not expected to be able to support more than about 3 times the mass of the sun (M_\odot). Systems with a mass function in excess of $3 M_\odot$ are considered strong candidate black-holes.

X-ray binaries are generally classified into two groups, based on the spectral type (observed or inferred) of the companion star. High mass X-ray binaries (HMXBs) have O or B-star companions with masses from several to about $40 M_\odot$, while low mass X-ray binaries (LMXBs) have companions later than type A (or even a white dwarf), with masses usually about $1 M_\odot$ or less. The two classes are believed to be produced via different evolutionary pathways.

1.2.2 HMXBs

In HMXBs, the OB star can have a substantial radiative-driven stellar wind, which removes 10^{-10} – $10^{-6} M_\odot/\text{yr}$ ($1 M_\odot/\text{yr} = 6.30 \times 10^{25}$ gm/s) with a terminal velocity up to 2000 km/s. The orbit of the neutron star or black hole can bring it close enough to the OB star so that it can capture a significant fraction of the material in the wind and thus power the X-ray source. Because the compact object is immersed in the wind material, photo-electric absorption often attenuates the X-ray intensity. In some HMXBs, Roche-lobe overflow also contributes to (or dominates) the total mass transfer (see section 1.2.3 on LMXBs). Since OB stars are quite bright in optical/UV light, the optical counterparts of HMXBs are often easily identified.

The spindown rate of radio (rotation-powered) pulsars indicates a high surface magnetic field of ($B \gtrsim 10^{12}$ G). Many HMXBs are X-ray pulsars and are also thought to contain a neutron star with a high magnetic field. Such objects channel accreting material along the magnetic field lines to the magnetic poles. If the spin and magnetic axes are misaligned, the X-ray beam will rotate (like a lighthouse beam). If the beam crosses our line of sight, the system will be observed as an accretion-

powered X-ray pulsar (in contrast to rotation-powered radio pulsars). The accreted matter produces a torque that can slow or increase the spin rate (and pulse frequency) of the compact object. In many systems an accreting white dwarf can be ruled out because the rate of change of the pulse period is too high for an object with a relatively high moment of inertia (compared to a much smaller neutron star) such as a white dwarf [31]. Pulsations are also assumed to require a surface, allowing black holes to be ruled out in systems that pulse. Thus, X-ray pulsars are well established as highly-magnetized accreting neutron stars.

1.2.3 LMXBs

When the companion star in an X-ray binary lacks a significant stellar wind, as is the case for most LMXBs and some HMXBs, mass transfer generally occurs through overflow of the critical equipotential surface (Roche lobe) of the star. Matter transferred in this manner is driven through the inner Lagrange point between the stars and has a high specific angular momentum. The material forms an accretion disk around the compact object and loses angular momentum through viscosity until falling onto the surface (or being expelled). X-ray heating of the disk and companion dominates the optical light from the donor star, often making it difficult to determine the spectral type of the companion.

Some LMXBs exhibit flares known as type I X-ray bursts. These bursts typically have rise times from less than a second to ~ 10 s and slower decay times, in the range of ~ 10 s to minutes. Spectral evolution during bursts suggests a sharp rise in temperature at the onset of a burst and gradual cooling during the decay. This behavior is consistent with thermonuclear ignition of accreted matter that has accumulated on the surface of a neutron star. Because a black hole has no surface, type I X-ray bursts provide strong evidence that a system contains a neutron star.

Most persistently bright LMXBs are believed to contain low magnetic field neutron stars ($B \lesssim 10^9$ G) since they generally show X-ray bursts and do not show pulsations (a higher magnetic field would funnel matter along the field lines onto the poles, where the material would be burned continuously rather than in bursts, and might produce pulsations due to the non-uniform emission from the surface [30].)

Neutron-star LMXBs can be classified as either “Z” or “atoll” sources. These categories are based on the correlated X-ray timing and spectral properties of these sources [27, 78] (see Figure 1-1). The fast timing properties (on time scales of seconds or less) of LMXBs and black-hole candidates are typically studied by computing Fourier power density spectra (PDSs), which often show several broad-band noise components and sometimes peaks due to quasi-periodic intensity oscillations (QPOs). The spectral properties can be examined by forming ratios of count rates in

different energy bands (X-ray hardness ratios or “colors”).

The six LMXBs known as Z sources are: Sco X-1, GX 349+2, GX 17+2, Cyg X-2, GX 5-1, and GX 340+0. These sources typically trace a “Z” pattern in color-color and hardness-intensity diagrams (CDs/HIDs), where X-ray “color” or “hardness” refers to the ratio of intensity in one energy band to that in a lower-energy band, while atoll sources trace a single arc (see Figure 1-1). Z sources show two types of quasi-periodic oscillations: along the top “horizontal branch” (HB) of the Z pattern are 13–60 Hz horizontal-branch oscillations (HBOs) which increase in frequency moving to the right on the diagram, and on the diagonal “normal branch” (NB) are ~ 6 Hz normal-branch oscillations (NBOs). In some Z sources, the normal-branch oscillations are observed to evolve into 6–20 Hz QPOs (FBOs) on the lower “flaring branch” (FB). The broad-band noise components of atoll sources also show correlations with position in the spectral diagrams.

The most widely held model for these two classes of LMXBs proposes two physical differences between them: Z sources have stronger magnetic fields ($1\text{--}5 \times 10^9$ G) and higher mass accretion rates (near the Eddington limit of $\dot{M}_{Edd} \sim 3 \times 10^{-8} M_{\odot}/\text{yr}$, or luminosity $L_{Edd} \sim 1.8 \times 10^{38}$ erg/s) than atoll sources (with magnetic fields $\lesssim 10^8$ G and luminosities between $10^{-3} L_{Edd}$ and a few $10^{-1} L_{Edd}$) [77]. The suggestion that Z sources have stronger magnetic fields than atoll sources was based largely on the existence of QPOs in Z sources and their general absence in atoll sources. In the magnetospheric beat-frequency model for Z-source horizontal-branch oscillations, the QPOs are the result of clumps of matter at the inner edge of the accretion disk (at the magnetospheric radius) which fall in along magnetic field lines to the surface with a frequency that is the difference between the Keplerian frequency at the magnetospheric radius and the neutron-star spin frequency [1, 37]. In this picture, the absence of such QPOs in atoll sources suggests lower fields so that the disk might extend almost to the neutron star surface. Near-Eddington accretion rates in Z sources are thought to be responsible for the QPOs on the normal and flaring branches, where a radial accretion inflow occurs with oscillations in the optical depth [20].

Recently kilohertz QPOs ($\sim 300\text{--}1200$ Hz) have been discovered in a number of Z and atoll sources with the *Rossi X-ray Timing Explorer* (RXTE). These QPOs possess many interesting properties (see van der Klis [79] for a recent review). They often appear in pairs that shift together in frequency. In some sources, nearly coherent oscillations have been observed during type I bursts at a frequency equal to or double the separation between peaks in kHz QPO pairs. This suggests that a beat-frequency mechanism is responsible, e.g., if the higher-frequency QPO peak is related to the Keplerian frequency at the inner edge of the accretion disk and the oscillations during bursts reflect the spin frequency (or twice the spin frequency) of the neutron star, then the lower frequency QPO would occur at the beat-frequency between the former two frequencies. One such beat-frequency is

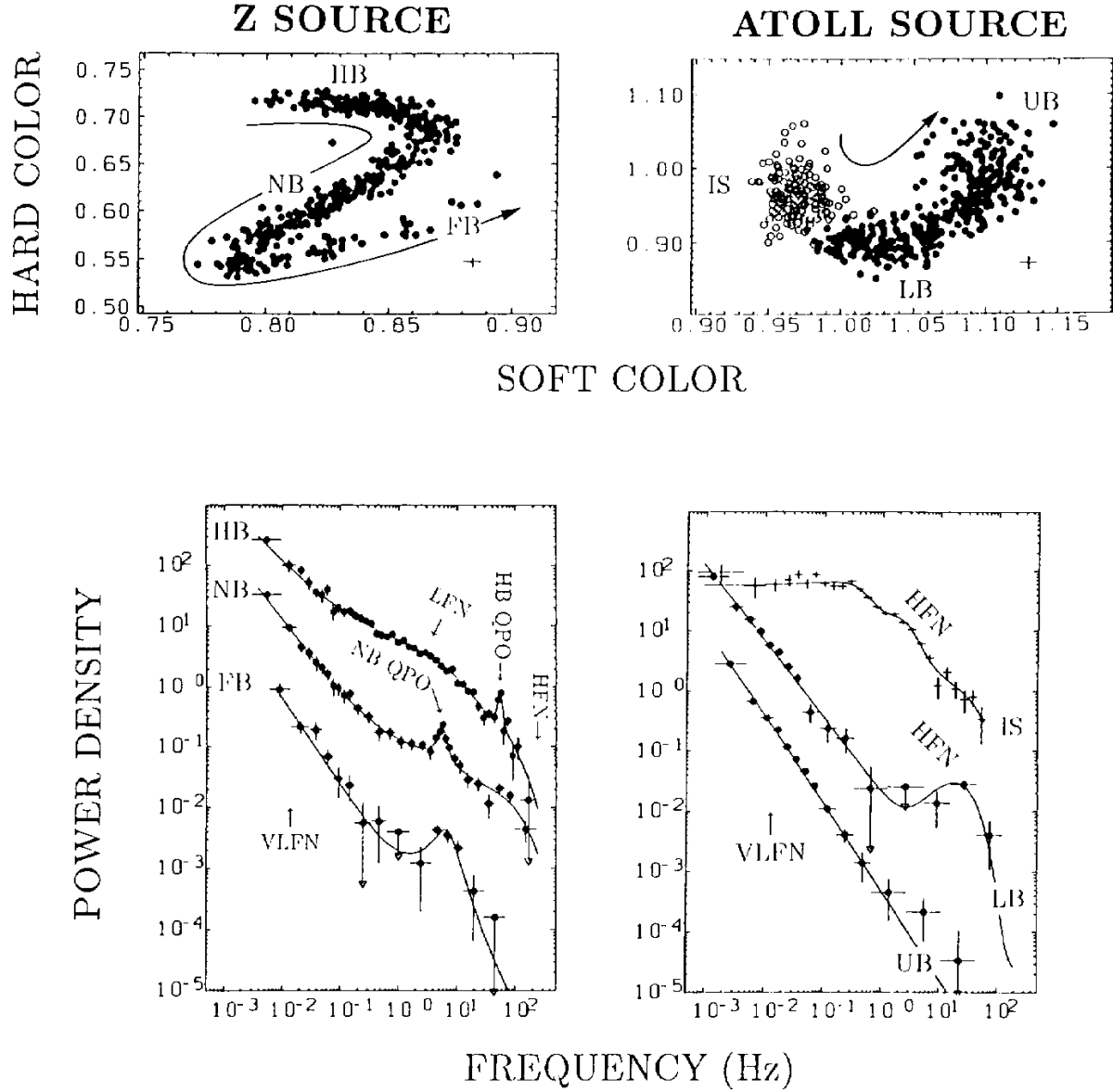


Figure 1-1: X-ray color-color diagrams and power density spectra typical of Z sources and atoll sources. The soft color is approximately $I[3-5 \text{ keV}] / I[1-3 \text{ keV}]$ and the hard color $I[6.5-18 \text{ keV}] / I[5-6.5 \text{ keV}]$. Power spectra are shown for the horizontal, normal, and flaring branches (HB/NB/FB) of Z sources, and the island state, lower banana, and upper banana (IS/LB/UB) of atoll sources. (Figure from van der Klis 1995 [78].)

the magnetospheric beat-frequency model, previously applied to Z-source horizontal branch oscillations (see above). This model cannot be correct for both types of QPOs since sometimes HBOs and kHz QPOs are observed simultaneously; other beat-frequency models propose a different radius associated with the kHz QPOs, e.g., the sonic-point model [48]. Important constraints on neutron star masses, radii, and equations of state can be derived from these oscillations, since they may reflect neutron-star spin frequencies and frequencies of orbits very close to the neutron-star surface.

The recent discovery of coherent 2.49-ms pulsations in *RXTE* observations of the source SAX J1808.4-3658 demonstrates the existence of millisecond X-ray pulsars [85, 13]. Millisecond X-ray pulsars are widely held to be the progenitors of millisecond radio pulsars. Angular momentum transferred to the neutron star by accreting matter is thought to be the mechanism that has spun-up millisecond radio pulsars, and such sources are expected to appear as X-ray pulsars during the mass accretion phase.

1.3 Circinus X-1

1.3.1 Intensity Cycle

The X-ray binary Circinus X-1 is unique in its complex temporal and spectral variability. A 16.55 day cycle of flaring is observed in the X-ray [32] as well as optical [50], IR [23], and radio bands [83]. The high degree of stability of the period of this cycle is evidence that it is the orbital period. The periodic behavior is believed to be the result of a highly eccentric binary orbit, in which mass transfer occurs only near periastron, leading to intermittent obscuration and flaring near phase zero [52, 54, 12].

The X-ray profile and average intensity of the 16.55 day cycle has varied considerably over time scales of years. The phase zero behavior has been described as a high-to-low transition, a low-to-high transition, or complex dips and flares (see e.g., [16, 68, 54, 62]). This has lead some authors to suggest that disk precession or apsidal motion with a time scale of several years plays an important role in the observed profile [52, 54].

1.3.2 X-ray Bursts

Eight X-ray bursts detected during an *EXOSAT* observation of Cir X-1 somewhat resembled type I bursts, but had profiles which left their identification inconclusive [71]. Three additional X-ray bursts seen during a later *EXOSAT* observation provided more convincing evidence for type-I behavior, and thus demonstrated that Cir X-1 is a neutron star with a weak magnetic field [72]. This in turn

suggests that Cir X-1 is an LMXB. Further type I bursts have not been observed from Cir X-1 since the *EXOSAT* discovery, possibly because the source intensity has been higher during subsequent observations. (At higher accretion rates, the material is expected to burn continuously on the surface rather than accumulate, as is necessary for type I bursts [30].)

1.3.3 Rapid X-ray Variability

The rapid X-ray variability of Cir X-1 at times resembles that of both “atoll” and “Z” low-mass X-ray binaries (LMXBs) as well as black-hole candidates [54]. Quasi-periodic oscillations (QPOs) were reported at 1.4 Hz, 5–20 Hz, and 100–200 Hz in *EXOSAT* observations of Cir X-1 in a bright state [69, 70], but other observations at lower intensity showed no such QPOs [54]. Based on these data, it has been suggested that Cir X-1 is an atoll source that can uniquely reach the Eddington accretion rate and exhibit normal/flaring branch QPOs at 5–20 Hz [54, 77]. Similar QPOs were observed in *Ginga* observations of Cir X-1 [45]. A significant portion of this current project is devoted to studying the rapid X-ray variability of Cir X-1. The current results demonstrate behavior associated with all three branches of Z-sources (horizontal, normal, and flaring), including horizontal and normal branch QPOs. No evidence for atoll-source behavior is found in the current observations; this might be related to the currently bright state of the source.

1.3.4 Distance

Neutral hydrogen clouds orbiting in the Galaxy produce 21-cm absorption features in the radio spectrum of sources observed through such clouds. The absorption lines are Doppler shifted by an amount equal to the radial velocity of clouds in their orbits around the Galaxy. The maximum velocity observed in these features indicates the radius of the Galactic orbit tangential to the line of sight, thus putting a lower limit on the distance to the absorbed source. HI absorption features in the spectrum of Cir X-1 extend to as much as -90 km/s, which puts a lower limit on the distance of Cir X-1 at about 80% of the distance from the Sun to the center of the Galaxy (~ 8 – 10 kpc, where $1 \text{ kpc} \equiv 3.086 \times 10^{21} \text{ cm}$), or 6.4 – 8 kpc [25, 24].

1.3.5 Young Runaway Binary

Radio images show that Cir X-1 is embedded in a synchrotron nebula which trails back toward the nearby ($\sim 1/2^\circ$, or 70 pc at 8 kpc) supernova remnant (SNR) G 321.9-0.3. Inside the nebula, there is a compact source at the position of Cir X-1, located at (J2000) RA $15 \text{ h } 20 \text{ m } 40.99 \text{ s}$, Dec. $-57^\circ 09' 59.91''$. Jet-like radio structures emanate outward from the compact source for about 30 arcsec

before curving back several arcmin toward the SNR. This suggests that the system is a runaway from the explosion that created the neutron star $\sim 30,000$ – $100,000$ years ago [67]. The velocity required for Cir X-1 to travel ~ 70 pc in this time is 700 – 2200 km/s. Although this velocity is quite high for a binary system, it is not unprecedented. Furthermore, there is spectral evidence that may also support a high velocity for the system; this is discussed in Chapter 8 in conjunction with our multi-frequency observations, as are the prospects for a measurement of the angular velocity (proper motion) of Cir X-1.

The possibility of a young age makes the object highly interesting from the standpoint of binary-system evolution. For example, mass transfer in a long-period LMXB ($P \gtrsim \text{days}$) is usually initiated when the donor star evolves to become a Roche-lobe filling giant star. If the primary star has only recently collapsed into a neutron star, this scenario implies that the secondary (probably less massive) star would be close behind in its evolution; this may be an unlikely scenario. Based on binary evolution calculations (Chapter 10), I show in this thesis that the system need not be unusually young to have a high eccentricity and substantial accretion rate, and in fact would probably have to be much older than the supernova remnant if the donor star has low mass.

1.3.6 Infrared and Optical Counterpart

An optical counterpart of Cir X-1 was resolved from a group of three stars using images and photometry in the V[$0.55\mu\text{m}$], R[$0.70\mu\text{m}$], and I[$0.90\mu\text{m}$] optical bands and J[$1.25\mu\text{m}$], H[$1.65\mu\text{m}$], and K[$2.2\mu\text{m}$] infrared bands. This counterpart is highly reddened and shows variability with the 16.55-d period [50].

Each cycle shows an infrared flare beginning shortly after phase zero. IR magnitudes at peak can reach $K=7.2$, $H=8.5$, and $J=9.7$, while the non-flaring component has magnitudes $K\sim 11.5$, $H\sim 12.1$, $J\sim 13.3$ [23, 24]. The magnitude of the non-flaring component in optical bands is $I\sim 18.4$, $R\sim 19.6$, and $V\sim 21.5$ [50].

The non-flaring V–K color is ~ 10 mag which would suggest a late type (low-mass) companion. However, the optical spectrum shows no atmospheric features that would identify the spectral type of the companion star, suggesting that disk emission dominates over the light of the companion [17]. An early type (high-mass) star would have to be reddened by $A_V \sim 11$ mag. Based on the minimum X-ray absorption column observed ($N_H \sim 10^{22}$), the interstellar extinction can be estimated to be $A_V \sim 4$ mag, favoring a low-mass star. However, other methods result in $A_V \sim 5 - 11$ mag, so that an O or B-type dwarf or giant (but not supergiant) cannot be ruled out [24]. Past X-ray behavior has suggested that Cir X-1 is a low mass X-ray binary, and the results in this thesis strengthen this X-ray evidence by demonstrating Z-source behavior (Chapters 5 and 6).

1.3.7 Radio Ephemeris

Based on the onset times of radio flares (defined to be phase zero) observed at Hartebeeshoek Radio Astronomical Observatory (HartRAO) between 1978 and 1988, G. Nicolson calculated the following ephemeris equation, reported by Stewart et al. [68]:

$$JD_0 = 2443076.87 + (16.5768 - 0.0000353N)N. \quad (1.1)$$

Although radio flares have been too weak during the past decade to determine an updated radio ephemeris, equation 1.1 has proven to be an excellent predictor of the current X-ray behavior (see Chapter 3). It should be noted, however, that phase zero no longer necessarily corresponds to the onset of radio flares. Furthermore, if the cycle is indeed orbital, the exact time of periastron relative to phase zero is not known. In this thesis, all references to the phase of Cir X-1 cycles are based on equation 1.1, unless otherwise noted.

The quadratic term in equation 1.1 implies that the period is currently decreasing by about two minutes per year ($\dot{P} = 4.26 \times 10^{-6} = 134 \text{ s/yr}$). This would imply a characteristic time scale ($P/2\dot{P}$) of only $\sim 5000 \text{ y}$ for the period to change by an amount equal to the current period, assuming the period changed at a constant rate. If the period truly is changing at such a rapid rate, it would further support the notion that Cir X-1 is very young. However, the radio and X-ray data are not yet able to confirm that a quadratic term is required. The change of period in equation 1.1 amounts to a shift of phase zero of about 25 minutes per year or about 4 hours over a decade.

For convenience, the zero point of equation 1.1 can be shifted by 423 cycles to 1995 December 31.04, immediately after the December 30 launch of *RXTE*, by making the substitution $N' = N - 423$:

$$JD_0 = 2450082.54 + (16.54694 - 0.0000353N')N'. \quad (1.2)$$

Thus, the current period will be quoted as 16.55 d throughout this thesis.

1.4 Objectives and Overview of this Project

The M.I.T. Center for Space Research was heavily involved in the pre-launch planning and instrumentation for the *Rossi X-ray Timing Explorer* satellite (*RXTE*), and continues to participate in the operations and scientific endeavors of that observatory now that it is in orbit. The capabilities and scientific instruments of *RXTE* are described in Chapter 2. Briefly, the main strengths of *RXTE* are: excellent time resolution, large collecting area, broad spectral coverage, flexible scheduling, and ability to monitor the X-ray sky to track the intensity of known sources and detect transient

phenomena.

A main objective of this project was to apply the unique capabilities of *RXTE* toward some of the outstanding problems of Circinus X-1 and to relate the results to X-ray binaries in general. Since the overall intensity of Cir X-1 is known to evolve over a period of years, we first sought to establish the current state of the source and to study the nature of its cycle profile. Chapter 3 gives a summary of the long-term behavior of Cir X-1 observed with *RXTE* as well as an overview of specific studies we carried out through observations of specific cycles.

A major outstanding issue for Cir X-1 is its unique status among LMXBs as a possible high- \dot{M} atoll source that can at times show some types of Z-source behavior. Thus, several studies were carried out to explore the characteristics of the rapid variability in Cir X-1, as well as how those timing properties relate to other properties such as orbital phase (Chapter 4) or spectral/intensity state (Chapters 5 and 6). Chapters 5 and 6 also demonstrate how the energy spectrum evolves during various stages of the flaring state.

The variability of Cir X-1 has been described as both flares and dips. Dips are important to understand for several reasons: (1) they might be caused by some part of the mass transfer process, (2) they help probe the local environment of the system, and (3) they can be confused with other variability if not properly identified. Detailed spectral analysis of dips in the intensity of Cir X-1 is presented in Chapter 7.

Since the periodic flaring activity is also observed at other wavelengths, we organized two multi-frequency campaigns to study correlated variability. These observations are presented in Chapter 8.

An additional objective of this project was to explore how the eccentric orbit of Cir X-1 affects mass transfer and the evolution of the system. In Chapter 9, I show the results of simple computer simulations of mass transfer due to a stellar wind or Roche-lobe overflow, for systems with an eccentric orbit. An eccentric binary evolution code was also developed (Chapter 10) to explore possible evolutionary paths for systems similar to Cir X-1.

The conclusions based on these studies are discussed in Chapter 11, as are several promising future studies of Cir X-1.

Chapter 2

The Rossi X-ray Timing Explorer

2.1 Overview

The *Rossi X-ray Timing Explorer* (*RXTE*, see Figure 2-1) is a NASA orbiting astrophysical observatory designed to provide temporal and spectral information about celestial X-ray sources [10]. The satellite was launched on a Delta II rocket on 1995 December 30. Its primary targets are compact objects in our galaxy, such as white dwarfs, neutron stars, and stellar-mass black holes, as well as active galactic nuclei, which may contain super-massive black holes. The strengths of *RXTE* are its high time resolution, large collecting area, broad spectral coverage, and ability to detect and respond quickly to transient phenomena. These capabilities are achieved through three instruments: the Proportional Counter Array (PCA), the High-Energy X-ray Timing Experiment (HEXTE), and the All-Sky Monitor (ASM). In addition, a specialized on-board computer, the Experiment Data System (EDS), serves to pre-analyze and compress data from the ASM and PCA to maximize use of telemetry. Each instrument is briefly described below. For more details see *The RXTE Technical Appendix* [61].

2.2 Proportional Counter Array

The PCA (built by the Goddard Space Flight Center of NASA) consists of five Proportional Counter Units (PCUs) with a total open area of $\sim 6250 \text{ cm}^2$. This large collecting area allows photons to be detected at a rate high enough to study variability as short as milliseconds. The detector electronics record the arrival time of each photon to an accuracy of $1 \mu\text{s}$, and the EDS is also capable of processing data with $1 \mu\text{s}$ resolution (see section 2.5). The PCUs are sensitive to X-ray photons

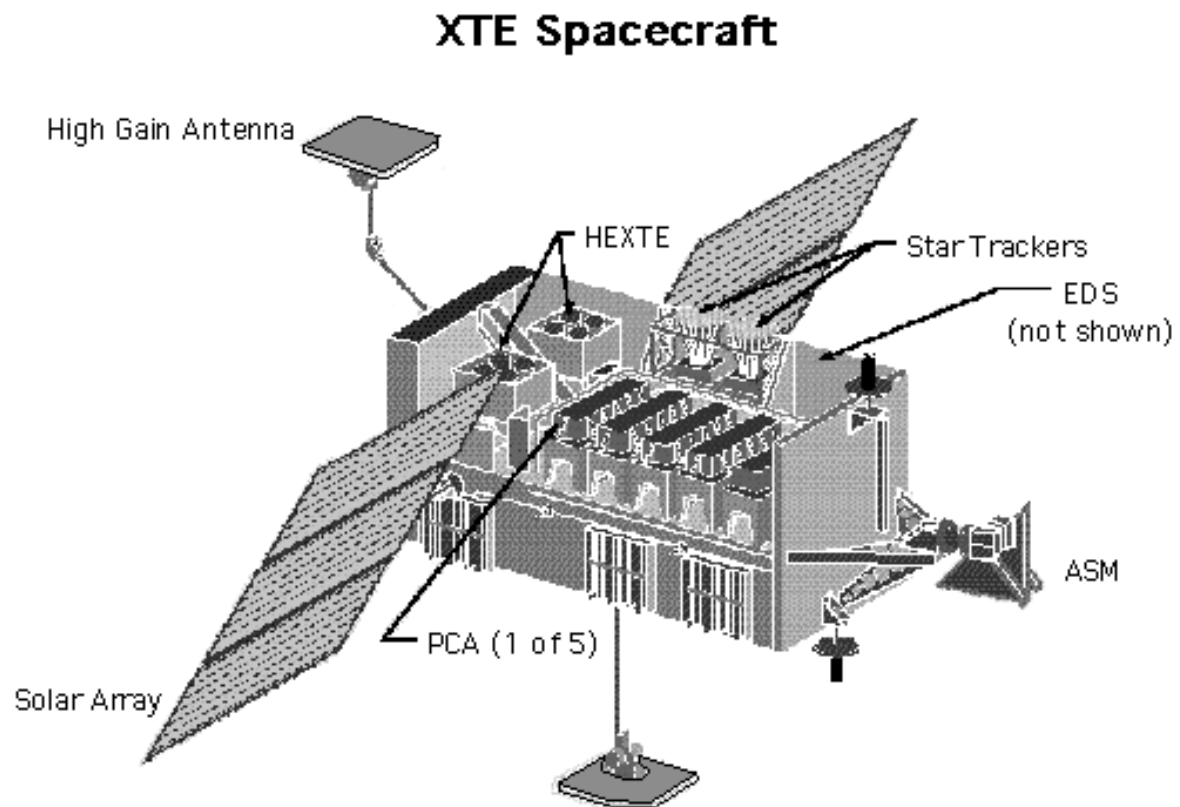


Figure 2-1: *Rossi X-ray Timing Explorer* spacecraft.

with energies between 2 keV and 90 keV, and can detect sources down to a flux level of a few mCrab, where $1.0 \text{ Crab} \approx 1060 \mu\text{Jy}$ at 5.2 keV. The intrinsic energy resolution ($\Delta E/E$, FWHM) of the PCA is about 18% at 6 keV and 10% at 20 keV. The PCUs have no imaging capability, but collimators restrict the field of view to $\sim 1^\circ$. Since the number of bright X-ray sources in the sky numbers less than 100, the 1° field of view is small enough to exclude other bright sources in all but the most crowded fields (i.e., towards the Galactic center).

Each PCU detector consists of a chamber of xenon gas (and a small quantity of methane) with three layers of high-voltage anode wires. The anodes closest to the detector walls, and a fourth layer on the bottom form an anti-coincidence detector used to reject events due to particles which enter through the walls of the detector. X-ray photons enter through the front window of the chamber and eject a photo-electron from an atom in the gas. The electron is accelerated toward an anode wire, creating ion pairs along its path. The multiplied electron signal is read out by the anode electronics. A propane chamber between the main chamber and the detector window is only sensitive to low-energy photons ($\lesssim 3 \text{ keV}$). Anode wires in the propane layer are also used in the anti-coincidence logic to screen out electron-induced events. All data from the PCA is sent to the EDS for processing before being telemetered to the ground (see section 2.5).

The capabilities of the PCA are particularly well-suited for studies of the rapid variability in X-ray binaries, and we have made use of these capabilities in our study of Cir X-1. Data can be obtained at high time resolution (fractions of a millisecond) simultaneously in multiple energy bands to study the variability components (such as the quasi-periodic oscillations) and their energy-dependence (Chapters 4, 5, and 6). All PCA data are also telemetered as 16-s spectra with 129 channels, allowing more detailed spectral studies to be made on time scales shorter than or comparable to most changes in the state of the source (Chapters 6 and 7).

2.3 High-Energy X-ray Timing Experiment

The HEXTE detectors (built by the University of California, San Diego) are sensitive to X-ray photons in the 20–200 keV band, extending the full capability of *RXTE* to cover two orders of magnitude in photon energy (2–200 keV). They are co-aligned with the PCA detectors and are also collimated to produce a $\sim 1^\circ$ field-of-view. The HEXTE consists of two independent clusters of four NaI(Tl)/CsI(Na) phoswich scintillation detectors. Photons entering such a detector undergo multiple interactions in the NaI scintillation crystal, and the resulting signal is transferred through the CsI crystal to a photo-multiplier tube. The CsI crystal also serves to reject photons that only partially deposit their energy and events that are induced by particles. The two detector clusters are

alternately rocked on and off-source to provide continued background monitoring. Each phoswich detector has a net collecting area of 200 cm^2 and an energy resolution of about 13% at 60 keV.

HEXTE data is obtained in parallel with all PCA observations. For Cir X-1, the HEXTE count rates are relatively low since the X-ray spectrum of Cir X-1 is soft, resulting far more counts in the PCA than HEXTE. Furthermore, the analysis of HEXTE data is complicated by the rocking detectors and complex calibration issues. Thus, the data we obtained for Cir X-1 from HEXTE is not incorporated into this thesis.

2.4 All-Sky Monitor

The ASM (built by the Center for Space Research at M.I.T.) consists of three scanning shadow cameras (SSCs) which regularly monitor all bright ($\gtrsim 10 \text{ mCrab}$) celestial X-ray sources (about 10 times per day), providing long-term light curves of their intensity in three energy bands between 2 keV and 12 keV [42]. Each SSC contains a position-sensitive proportional counter mounted below a wide-field collimator ($\sim 6^\circ \times \sim 90^\circ$ FWHM). The PSPCs each contain eight carbon-coated quartz fibers which are used as anode wires in a chamber filled with Xe and CO_2 . The anode electronics read out signals from both ends of each anode and can determine the position along the wire by comparing the relative strength of the signals due to the resistance of the anodes. A mask covering the outer window of the collimator is coded with rectangular slit openings which cast X-ray shadows on the detector and allow positions to be determined (typical error boxes of $3' \times 12'$). The three cameras are mounted on a tripod at one end of the satellite (see Figure 2-1) and are rotated together, stopping for 90-s dwells every 6° . A sensitivity of about 30 mCrab (3σ) is achieved for each such 90-s exposure. The fields-of-view of two of the cameras point in the same direction perpendicular to the rotation axis and cross at a $\sim 24^\circ$ angle (resulting in positional error boxes that cross and can be used for further refinement of positions). The third camera points along the rotation axis. Several of the anodes lost functionality shortly after launch, but this has not significantly affected the overall performance.

For Cir X-1 the ASM has proved invaluable in understanding the general spectral and intensity profile of the 16.55-d cycle. The ASM also plays an important role by placing other observations (e.g., our PCA observations) in context with the rest of the cycle and by aiding plans for future observations. With continued successful performance, the detailed long-term light curve will allow us to track how the source behavior evolves between its various states (see section 1.3). So far, the ASM light curve of Cir X-1 has shown the source to maintain the same high baseline intensity level for the entire duration of the *RXTE* mission (see Chapter 3), with no evidence for evolution on a

Band	Channel		Energy (keV)		
	Abs	Std2	Epoch 1	Epoch 2	Epoch 3
A	0–9	0–5	0–2.6	0–3.0	0–3.5
B	10–13	6–9	2.6–3.6	3.0–4.2	3.5–5.0
C	14–17	10–13	3.6–4.7	4.2–5.5	5.0–6.5
D	18–23	14–19	4.7–6.3	5.5–7.4	6.5–8.7
E	24–35	20–31	6.3–9.5	7.4–11.1	8.7–13.1
F	36–49	32–45	9.5–13.2	11.1–15.6	13.1–18.3
G	50–87	46–66	13.2–24	15.6–28	18.3–33
H	88–249	67–127	24–71	28–84	33–99

Table 2.1: Approximate energy ranges for eight PCA bands (A–H) defined in terms of absolute (0–255) and Standard2 (0–128) channels. Gain epoch 1 includes all observations before before 1996 March 21, epoch 2 1996 March 21 – April 15, and epoch 3 after 1996 April 15. Energy values shown are derived from the full PCA with all detectors and layers added.

few-year time scale as has been suggested based on previous observations (see section 1.3).

2.5 Experiment Data System

The EDS (also built by the CSR at M.I.T.) is a computer containing eight microprocessor Event Analyzers (EAs), of which six are dedicated to handling PCA data while the other two are dedicated to the ASM. For each 90-s dwell, one of the ASM EAs produces position histograms of the X-ray shadow patterns on each wire of each detector in the three energy channels mentioned above. The second ASM EA produces time-series histograms of “good” and background count rates, as well as pulse height histograms useful in monitoring the gain of the detectors based on an on-board calibration source.

Two of the PCA EAs process data using standard modes: one that provides count rates for each layer of the five PCU detectors and other rates every 1/8 s (Standard1) and another which provides 129-channel spectra every 16 s (Standard2). The other four PCA EAs can be set to process data in parallel using a wide variety of modes in order to fit desired information into the telemetry constraints. Most data modes fall into two categories: event modes which send down the time and energy of every event and binned modes which send down the number of photons detected in selectable energy and time bins. Many data modes process data from within standard sub-bands of the entire PCA energy range. These sub-bands are defined in terms of the 256 “absolute” channels of the PCA. Table 2.1 shows the channel and energy ranges for eight standard bands. The gain of the PCA detectors was changed twice early in the mission, resulting in a different channel-to-energy relationship for each of three epochs. Although the relationship is not strictly linear, a single

channel-to-energy conversion factor is a good approximation for each epoch: through 1996 March 21, 0.27 keV/chan; 1996 March 21 – 1996 April 15, 0.32 keV/chan; after 1996 April 15, 0.38 keV/chan. All light curves, hardness ratios, and Fourier power spectra in this thesis have been binned into one or several of these standard bands.

The four PCA Event Analyzers not devoted to standard modes are typically configured, through modes selected by the observer based on science goals, to provide optimal time resolution and energy resolution within the available telemetry. For Cir X-1, we generally chose two or three “single-bit” modes (single-channel binned modes) which covered absolute channels 0–35 of Table 2.1 (up to 13 keV in epoch 3) using various combinations of energy bands A–E. These configurations provided a time resolution of 61 μ s or 122 μ s. Due to lower count rates in the higher channels, the energy and time of every photon with energy above channel 35 (bands F–H in Table 2.1) could be recorded with an event mode having 32 or 64 channels covering absolute energy channels 36–249 and time resolution of 16 μ s or 64 μ s. Sometimes a binned mode was used to provide 32 low-energy channels at 0.5 s resolution to allow the possibility of creating spectra on time scales shorter than the 16 s provided by the Standard2 mode. Thus, all Cir X-1 data were obtained with high time resolution in multiple energy bands for rapid variability studies (Chapters 4, 5, and 6) and good energy resolution every 16-s or less for spectral studies (Chapters 6 and 7).

Chapter 3

Overview of RXTE Observations

3.1 ASM Observations of Circinus X-1

3.1.1 General Features of the ASM Light Curves

The *RXTE* All-Sky Monitor (see section 2.4) has provided 90-s intensity measurements of most bright X-ray sources in three energy channels (1.5–3 keV, 3–5 keV, and 5–12 keV) about 12 times daily since early 1996 [42]. The intensity for each source in the ASM field of view, and the diffuse X-ray background, is obtained from fits to the ASM mask patterns of each 90-s exposure. Thus background has, in effect, been subtracted from the source light curves.

The ASM light curve of Cir X-1 for the entire *RXTE* mission to date (through 1998 May) is shown in Figure 3-1. (A gap of ~ 40 days occurred early in the mission due to instrumental problems, and a gap of 2–3 weeks has occurred annually, near days 420 and 780, due to sun-angle constraints.) These observations show Cir X-1 in a sustained bright state with a baseline intensity level very similar to that of the Crab nebula ($1.0 \text{ Crab} \approx 75 \text{ ASM counts/s}$; $1060 \mu\text{Jy}$ at 5.2 keV). Each cycle shows strong flaring wherein the intensity increases by a factor of three or more. Phase zero of each cycle (based on equation 1.1) is indicated in Figure 3-1. The consistent alignment of brief dips with phase zero and subsequent flaring shortly after phase zero demonstrate that the decade-old radio ephemeris is very successful in predicting the current X-ray behavior.

The flaring state typically begins during the day following phase zero, reaching as high as 3.7 Crab (corresponding to a luminosity at 8 kpc that is several times the Eddington limit) and typically lasting 2–5 days. The profile of the flaring state is actually quite variable, sometimes showing a secondary flare or an extended main flare lasting most of the cycle (see Chapter 5).

Many cycles observed with the ASM show brief dips below the 1 Crab level, usually immediately

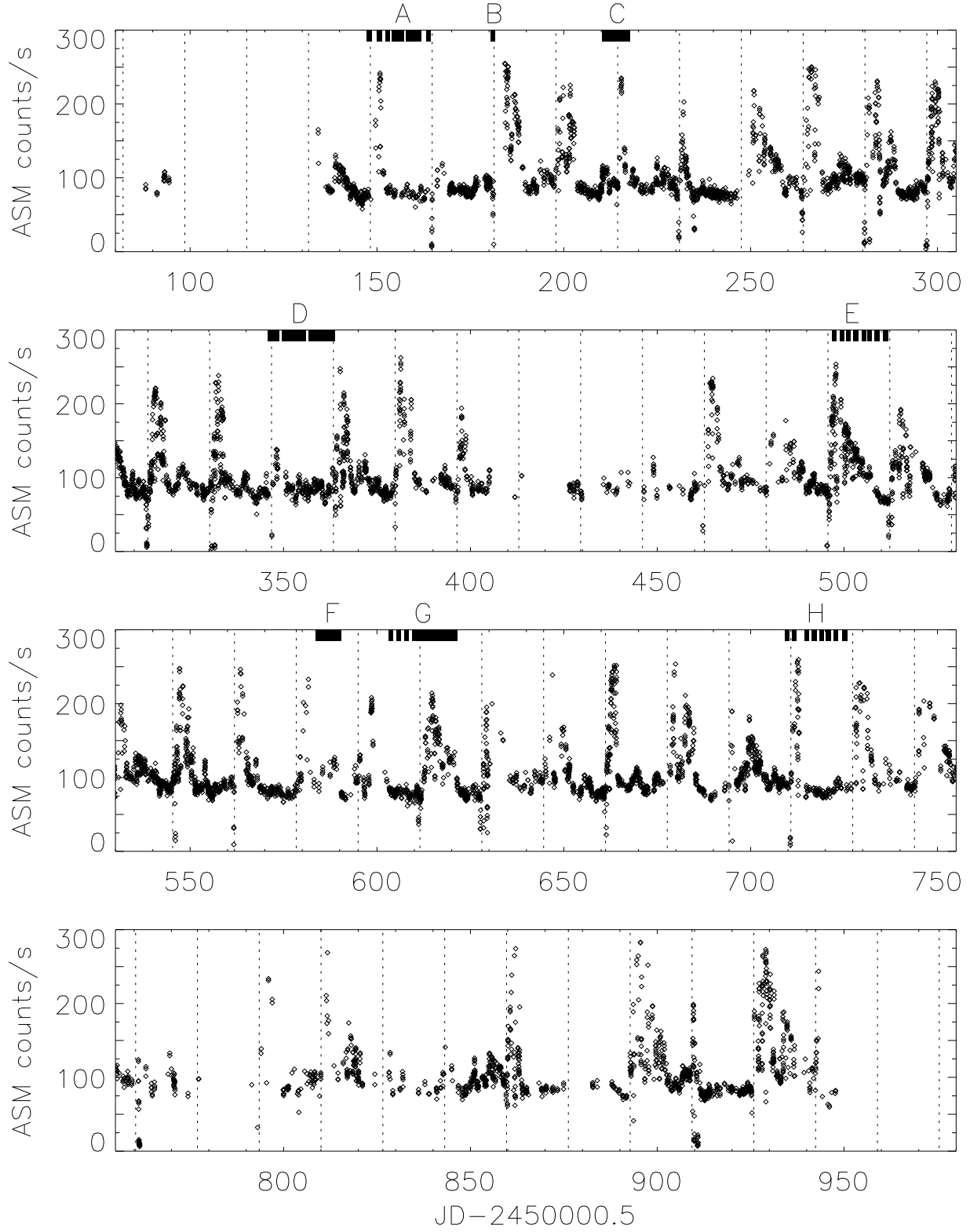


Figure 3-1: ASM light curve (1.5–12 keV; 90-s exposures) covering 1996 January – 1998 May. Phase zero is indicated by vertical dotted lines. Bars along the top axis mark the times of PCA observations (labeled A–H; see section 3.2).

before or shortly after phase zero, but occasionally occurring later in the cycle as well. Previous satellites have also observed intensity dips from Cir X-1 near phase zero. For example, Brandt et al. [12] recently presented evidence for strong absorption during a phase-zero intensity transition in *ASCA* observations of Cir X-1. More extensive *RXTE* PCA observations of dips will be discussed in Chapter 7.

3.1.2 Cycling Hardness Ratios

The light curve and hardness ratios of counts in adjacent energy channels for the first ten 16.55-d cycles of Cir X-1 observed with the ASM are shown in Figure 3-2. These data show significant spectral evolution during the non-flare phases. The hardness ratios were found to generally increase (harden) from about phase 0.2 until phase 0.6-0.85. Beyond this point the hardness ratios usually flatten, decrease, or dip and rise again before phase zero. Near phase zero, the ratios vary dramatically (not apparent in the one-day averages shown) but generally become quite low during the flaring phases ($0 \lesssim \phi \lesssim 0.2$). The hardening in the two colors ($0.2 \lesssim \phi \lesssim 0.7$) is usually due to both an increase in the 5–12 keV count rate and a decrease in the 1.5–3 keV count rate.

3.1.3 16.55-day Period

The onset of flaring relative to phase zero can vary by of order one day. Over the ~ 50 cycles observed by the ASM, this allows the period to be determined to within about $1/50 d = 0.02 d$. Since this uncertainty is similar to the change in period of 0.03 d over 20 yr implied by equation 1.1, it is not yet possible with the ASM to confirm or reject a period change of that magnitude. However, to obtain the best-fitting period I used a 64-times oversampled Fourier power density spectrum from the ASM data in Figure 3-1 (and fitting the peak corresponding to the ~ 16.55 -d period with a Gaussian). This method gave a best-fitting constant period of 16.555 d. Within the 0.02 d uncertainty, this is consistent with equation 1.1, with or without the quadratic term. The possibility of using the phase-zero dips as “markers” for the period is explored in the next section (using the average folded light curve). Hopefully the ASM will continue to operate for several more years, potentially allowing the period to be determined with the accuracy necessary to test the constancy of the period.

3.1.4 Folded Cycle Profile

ASM light curves of Cir X-1 folded at the 16.55-d period (using equation 1.1; Figure 3-3) show the rapid rise and more gradual decline of the profile. The scatter of points during the “flaring” state demonstrates the high degree of variability at those phases. The 5–12 keV band exhibits flaring

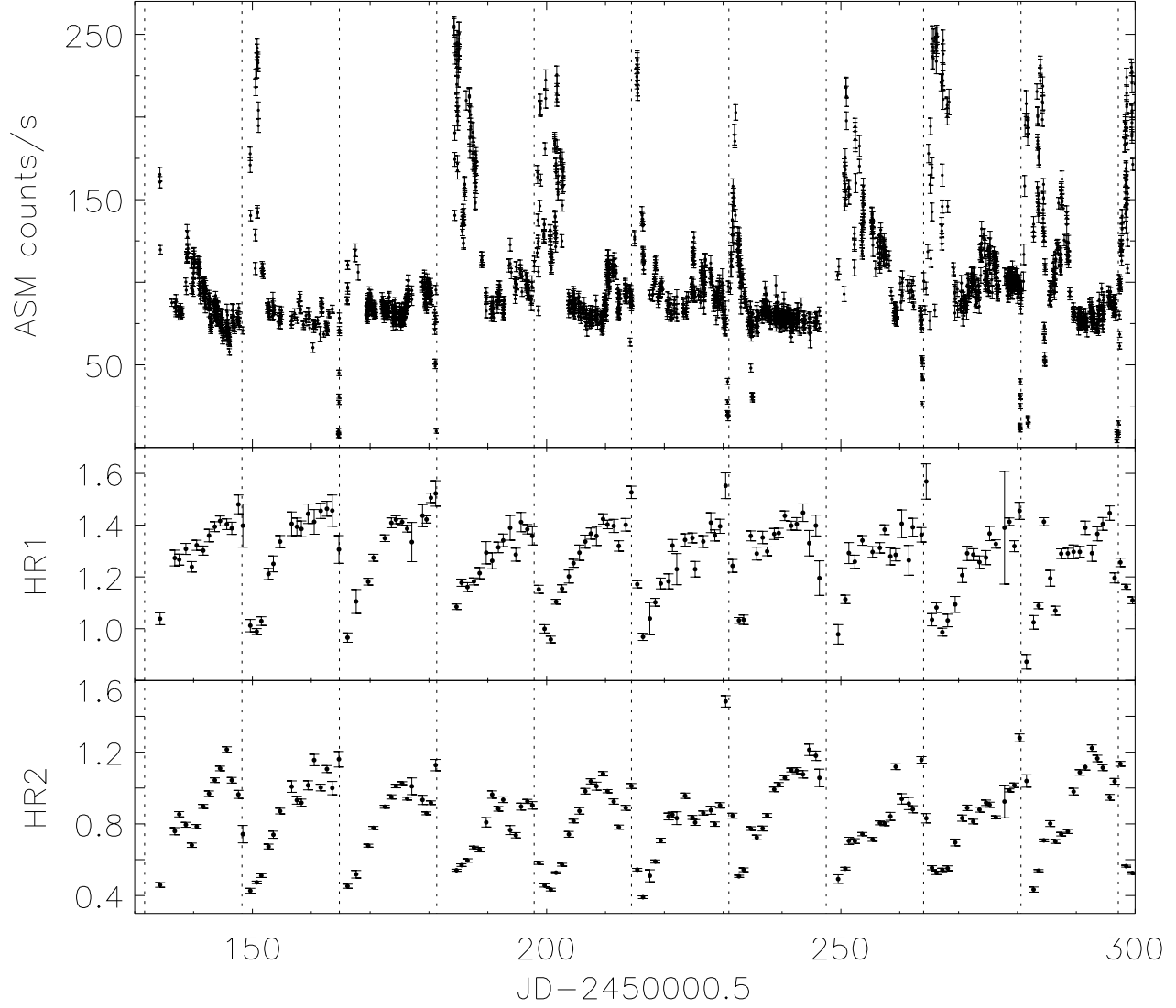


Figure 3-2: Light curve and two hardness ratios for the first ten full 16.55-day cycles of Cir X-1 observed with the ASM. Each light-curve point is the average count rate ($I[1.5-12 \text{ keV}]$) from a single 90-s ASM exposure. The hardness ratios were obtained from 1-day averages of the 90-s intensities and are defined as $HR1 = I[3-5 \text{ keV}] / I[1.5-3 \text{ keV}]$ and $HR2 = I[5-12 \text{ keV}] / I[3-5 \text{ keV}]$. The vertical dotted lines indicate phase zero.

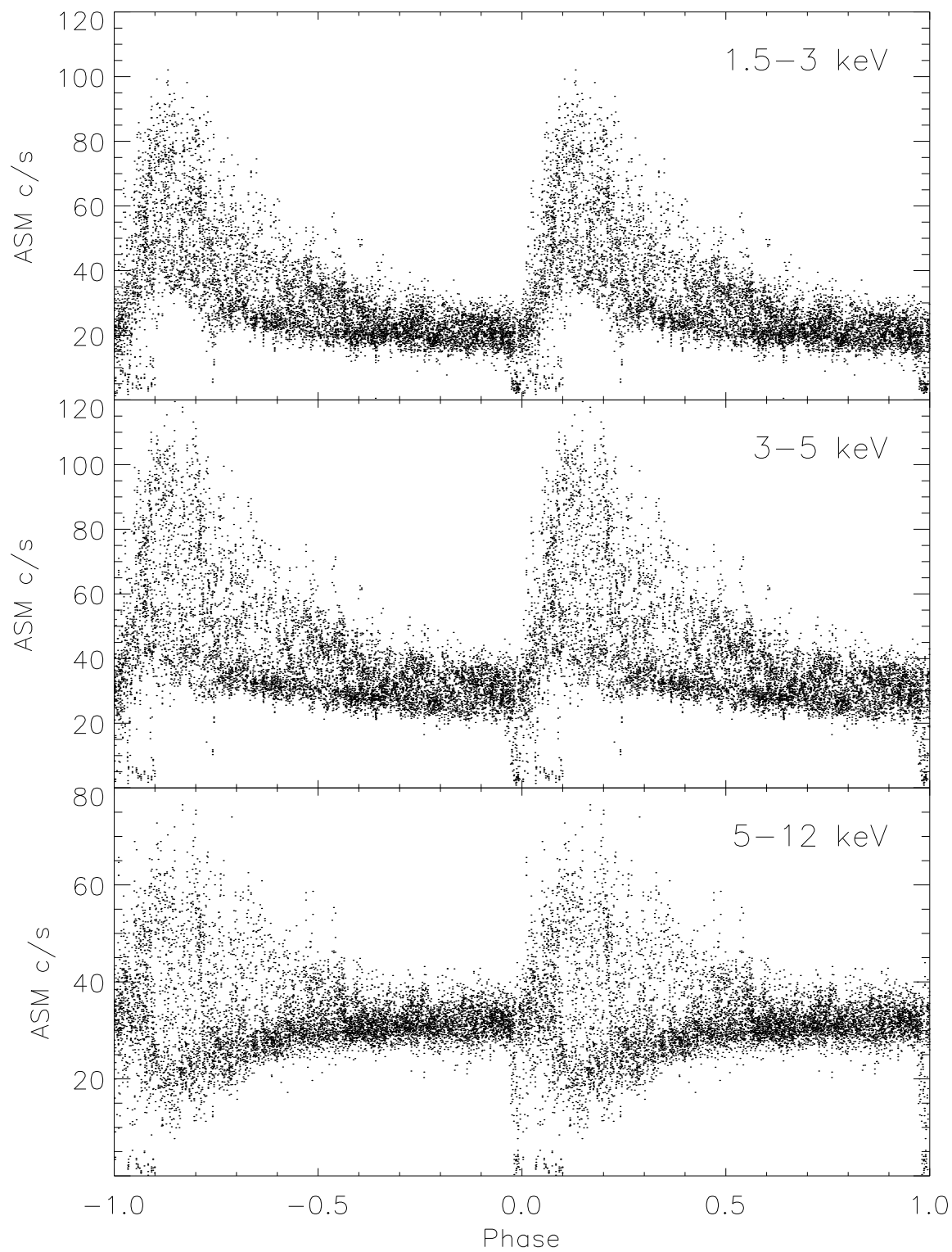


Figure 3-3: Folded light curve of Cir X-1 from the three ASM energy bands. The data are repeated in order to show two complete cycles. Each point is from a 90-s exposure, with a typical error bar of 1-2 c/s. The folded data spans the entire time period covered by Figure 3-1.

above a baseline that dips below the quiescent level. This is related to the spectral softening seen during flaring in Figure 3-2. Although dips typically occur anywhere between phases -0.03 and $+0.10$, they occur most consistently in a narrow range immediately before phase zero. There is a clear absence of points at the baseline level in the narrow phase range 0.985 – 0.989 ; however, the total number of points in a phase range of that width is typically only about 30, so sparse coverage may play a role in the width of this gap.

The data shown in Figure 3-3 for the three ASM bands were also binned into 100 phase bins and averaged within each bin. These average folded profiles, as well as those for the total ASM energy band and the two hardness ratios, are shown in Figure 3-4. The average profile has a very narrow dip at phase -0.012 (± 0.004), followed by a sharp rise over the first 1.5 d of the cycle and a much more gradual decline. The hardness ratios are anti-correlated with the total intensity. Similar intensity and hardness profiles were seen in folded *Ginga* ASM data from 1987 [75]. The folded profile from the highest energy ASM band (5–12 keV) does not exhibit the large increase in flux characteristic of the other two bands and shows only increased variability during the flaring state, due to the scatter of points above and below the baseline (see Figure 3-3).

We attempted to use the narrow dip at phase -0.012 in the average folded curves to constrain the best period. Constant periods of 16.535–16.555 d all showed similar dips, and the dips were deepest (and most similar to Figure 3-4) using a period of 16.540–16.545. Although the range of periods showing the narrow dip is lower than the earlier radio periods by about 0.02–0.04 d, we have no *a priori* knowledge of what shape (if any) this feature should have, and thus must use caution when interpreting periods determined by maximizing its depth (or other property).

3.2 PCA Observations of Circinus X-1

3.2.1 Overview

We have proposed and carried out an extensive observation campaign for Cir X-1 with the *RXTE* PCA, collecting over 800 kiloseconds of data, as shown in Table 3.1. The project consisted of eight separate “studies” which used a variety of strategies for different 16.55-d cycles: We sampled several cycles with brief observations (typically about 6000 s), distributed at different phases, to study how the detailed timing and spectral characteristics evolve with orbital phase and relate to the spectral evolution indicated by the cycling hardness ratios of the ASM (see above). High-efficiency observations (i.e., $\sim 60\%$ coverage) during two long time segments (2 and 7 days) including phase-zero were used to study the highly complex dipping and flaring behavior associated with that portion of the cycle. In order to study correlated behavior at different wavelengths, we coordinated two

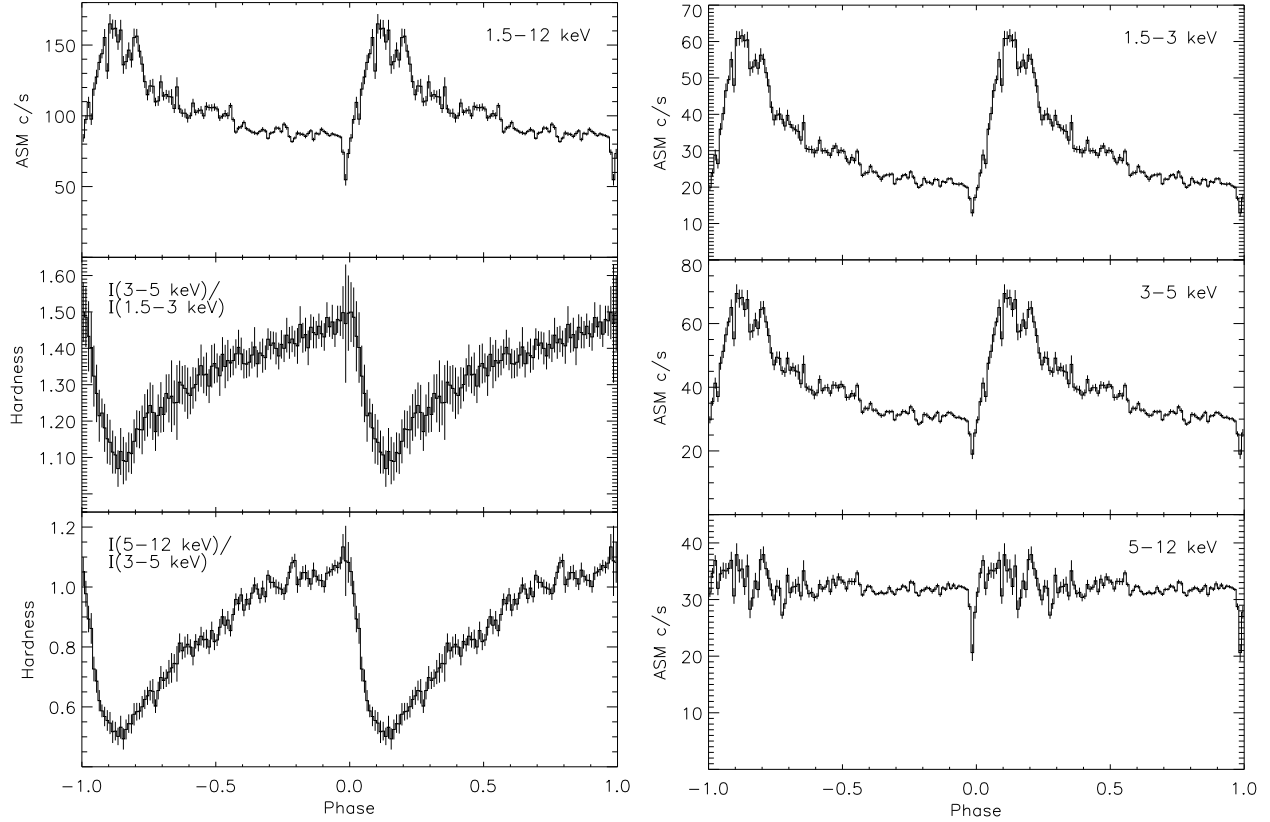


Figure 3-4: Left: Folded Cir X-1 light curve from the full ASM energy band (1.5–12 keV) and two hardness ratios. Right: Folded light curves from the three ASM energy bands. The data are binned into 100 phase bins per cycle, averaged in each phase bin, and duplicated to show two complete cycles. Error bars on the light curves indicate the standard deviation of the mean value derived for each phase bin, and these error estimates were propagated when computing the hardness ratios. The folded data spans the entire time period covered by Figure 3-1.

Study	Dates	Observing Time	Description
A	1996 Mar. 5 - 21	76 ksec	12 observations over one 16.6-d cycle
B	1996 Apr. 7	10 ksec	1 observation during phase-zero dips
C	1996 May 7 - 14	54 ksec	7 observations between phase 0.78-0.16, coord. with HartRAO (radio) & SAAO (IR)
D	1996 Sept. 20 - Oct. 8	190 ksec	60% coverage for 2 days (phase 0.97-0.09), 13 observations over remainder of 16.6-d cycle
E	1997 Feb. 18 - Mar 4	48 ksec	8 samples over one 16.6-d cycle
F	1997 May 16 - 21	13 ksec	13 1-ksec observations, twice daily
G	1997 June 4 - 22	396 ksec	56% coverage for 7 days (phase 0.93-0.33), sampling observations before and after; portions coordinated with AAT (optical), ANU (IR), HartRAO (radio), & SAAO (IR)
H	1997 Sept. 18 - Oct. 4	50 ksec	8 samples over one 16.6-d cycle
		837 ksec	

Table 3.1: PCA observations of Cir X-1 (1996–1997).

multi-frequency campaigns to provide optical, infrared, and radio observations simultaneous with our X-ray coverage. The light curves, from the full PCA energy range, for each of the studies are shown in Figure 3-5 as a function of phase for comparison between cycles. Standard 20-kilosecond light curves of all these observations are collected in Appendix B. The time of each PCA observation is also indicated on the 2.3-year ASM light curve in Figure 3-1.

3.2.2 Observation Summaries

The intensity and activity level of Cir X-1 had been observed to change over a period of years (see section 1.3). We thus did not know what to expect from Cir X-1 once *RXTE* launched. By the end of 1996 February, it was already clear from the very early ASM data that Cir X-1 was currently bright and active. Thus, we requested that our proposed PCA/HEXTE observations of Cir X-1 be activated, and began observations in early 1996 March. The eight studies (A–H) of our project are described briefly here.

3.2.2.1 Study A: 1996 March 5–21

The first study consisted of twelve observations, each ~ 6000 s in duration. They were separated by ~ 2 -day intervals to sample one complete 16-d cycle (see Figure 3-5A). The first observation of study A occurred during the half day before phase zero and showed significant dipping behavior. The second observation occurred shortly after phase zero, and the source was very bright (up to

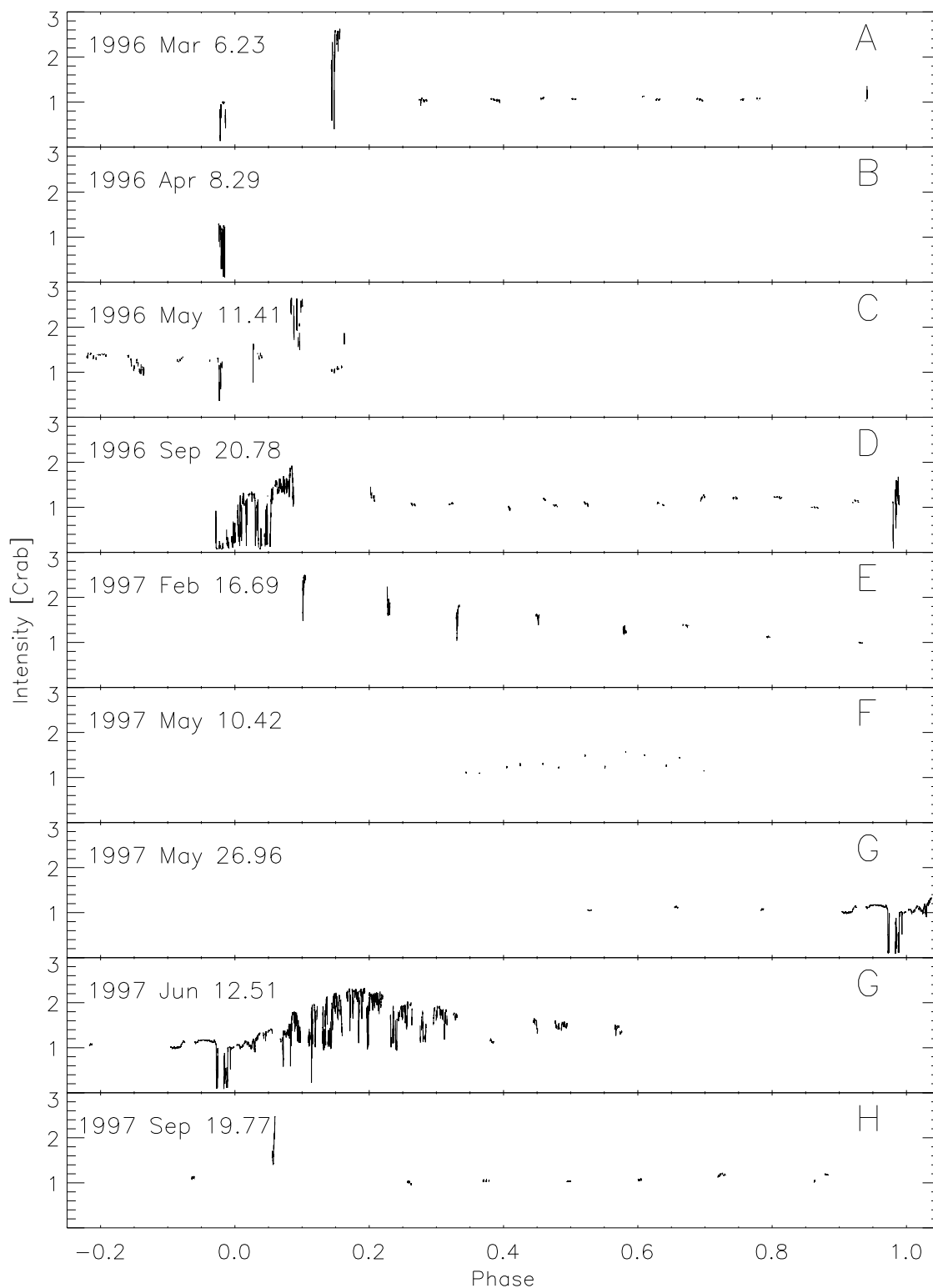


Figure 3-5: Light curves for each 16.55-d cycle of Cir X-1 observed with the PCA. For each cycle, the phase-zero date and letter of the study (see Table 3.1) are listed. The intensity is for the full PCA energy range, and a conversion factor of $1 \text{ Crab} \approx 2600 \text{ counts s}^{-1} \text{ PCU}^{-1}$ has been used.

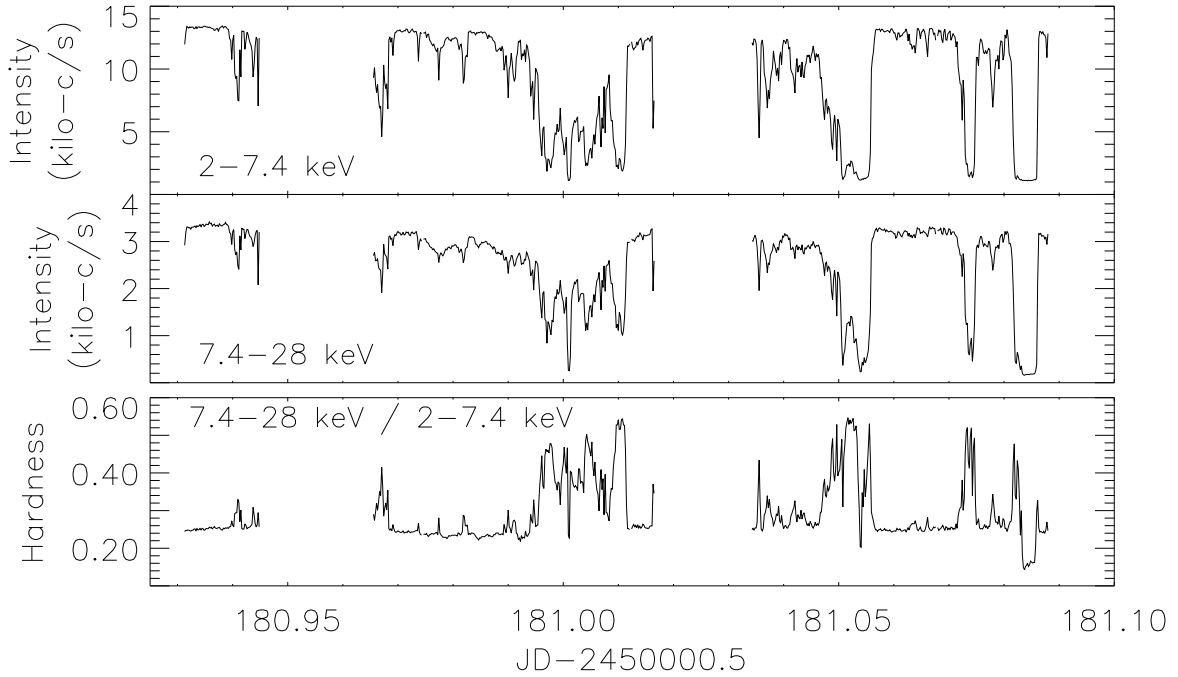


Figure 3-6: PCA light curves in two energy bands (16-s bins), and the ratio of intensity in the hard band to that in the soft band, for the observation on 1996 April 7 (study B), spanning 15 ks. The lowest intensity in both bands during dips is well above the background level (~ 30 c/s and ~ 45 c/s for 2–7.4 keV and 7.4–28 keV respectively, not subtracted).

~ 2.6 Crab) and highly variable. Nine observations carried out between phases 0.2 and 0.8 showed a quite steady flux, and a final observation shortly before the next phase zero showed increased activity again. These data are presented in Chapter 4, with a focus on the evolution of the timing and spectral properties during the non-flaring phases.

3.2.2.2 Study B: 1996 April 7

This study consisted of a single 10-ks observation carried out on 1996 April 7, approximately one full cycle after the end of the initial monitoring campaign (see Figure 3-6). This observation also showed significant dipping below the ~ 1.0 Crab baseline (~ 13 kilocounts/s) during the half day before phase zero. The dips are chaotic and accompanied by dramatic spectral evolution (as indicated by the hardness ratio). Similar dipping behavior from study D (see below) was studied in detail and is presented in Chapter 7. This observation occurred during PCA gain epoch 2 (which defines the channel-to-energy conversion factor, see Table 2.1). All following observations of Cir X-1 occurred during gain epoch 3.

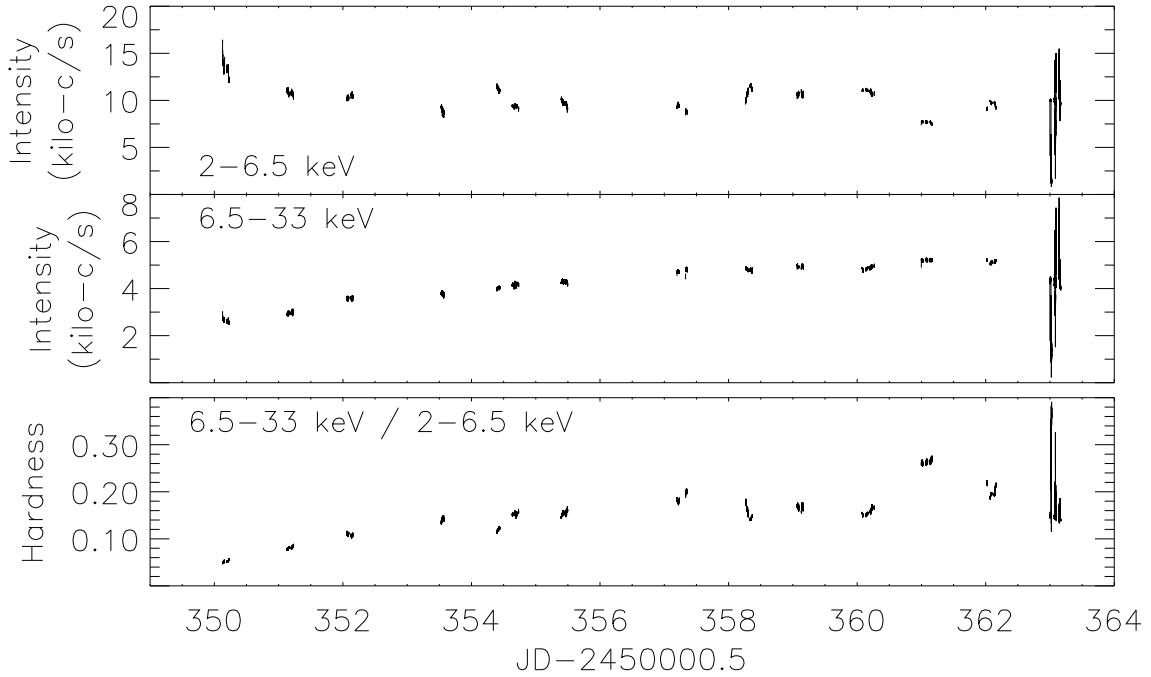


Figure 3-7: PCA light curves in two energy bands (16-s bins), and the ratio of intensity in the hard band to that in the soft band, for the observations on 1996 September 24 – October 8 (study D). Due to some observations with a PCU not operating, all points in this plot were derived from PCUs 0, 1, & 2 and adjusted by 5/3 for comparison with other figures in this section. Phase zeros occurred at days 346.782 and 363.328.

3.2.2.3 Study C: 1996 May 7–14

In 1996 May, the first of two multi-frequency campaigns was carried out, with coordinated infrared, radio, and *RXTE* observations. These observations spanned several days on either side of phase zero, and showed an increase in intensity in all three frequency regimes during the day following phase zero. These multi-frequency observations are discussed in more detail in Chapter 8.

3.2.2.4 Study D: 1996 Sept. 20 – Oct. 8

In 1996 September, a high efficiency observation was carried out, providing 60% coverage of the 48-hour period beginning 0.5 days before phase zero. These data showed extensive dipping both before and after phase zero and are the focus of Chapter 7, in which the spectral evolution of dips is studied in detail. Following this extensive phase zero observation, 13 sampling observations were made over the remainder of the 16.55-d cycle. These are shown in Figure 3-7 and demonstrate a gradual hardening of the spectrum with orbital phase, as well as more dramatic spectral evolution during dips in the last observation.

3.2.2.5 Study E: 1997 Feb. 18 – Mar. 4

Eight 6-kilosecond observations were carried out during 1997 February 18 – March 4, sampling a complete cycle at approximately 2-day intervals (see Figure 3-5E). The intensity of this cycle declined from its peak value gradually over ~ 10 days. These observations are used in Chapter 5 to study the evolution of timing properties as a function of intensity and spectral state.

3.2.2.6 Study F: 1997 May 16 – May 21

In 1997 May, a series of short (1 ks) public observations of Cir X-1 were carried out between phases 0.35 and 0.7 (the data were originally part of another observer’s program, but were made publicly available due to a scheduling conflict). Although these data were not part of our proposed observations, they fit well with our other sampling studies and were thus incorporated into the project. The intensity level during each observation was relatively steady, but the average level varied between 1.0 and 1.6 Crab.

3.2.2.7 Study G: 1997 June 4–22

Our most extensive set of observations were carried out during 1997 June. These included a 7-day period of 56% coverage that included dips before phase zero and most of a very active flaring state. This excellent coverage allowed us to observe continuous transitions between the various spectral/intensity states we found in the earlier 1997 February–March data. These results are presented in Chapter 6.

Some of our June PCA observations were coordinated with with radio, optical, and infrared observations made by collaborators in South Africa and Australia. The results from this second multi-frequency campaign are presented in Chapter 8 along with the previous campaign (study C).

3.2.2.8 Study H: 1997 Sept. 18 – Oct. 4

A final set of eight 6-kilosecond observations were carried out during 1997 September–October to again sample a complete 16-d cycle. These observations all showed the intensity to be near the 1.0 Crab baseline, except for the sample at phase 0.06, where the intensity reached 2.5 Crab. The soft and hard light curves and hardness ratio for the flaring observation are shown in Figure 3-8. There is strong variability on time scales of hundreds of seconds during the climb to 2.5 Crab. The hardness ratio is generally anti-correlated with intensity during the first segment and then correlated with intensity during the remainder of the observation. This bi-modal behavior can be understood as relating to different branches in a hardness-intensity diagram. Both types of behavior are associated

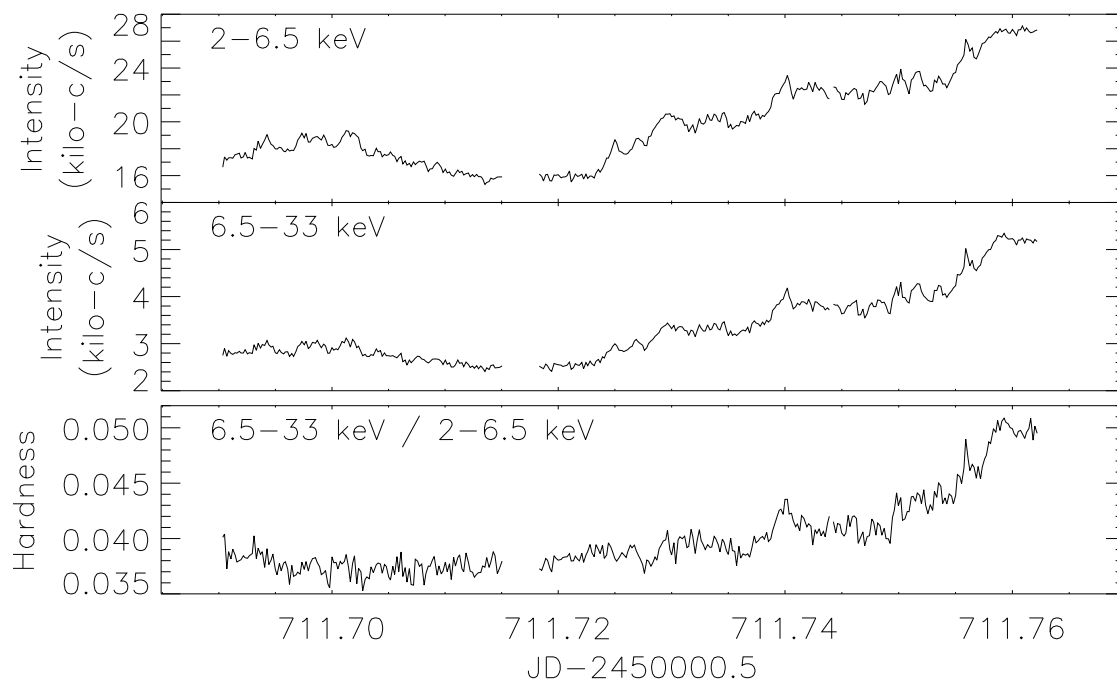


Figure 3-8: PCA light curves in two energy bands (16-s bins; 13 kilocounts/s=1.0 Crab for the combined 2-33 keV band), and the ratio of intensity in the hard band to that in the soft band, for the observation on 1997 September 20 (part of study H), spanning 7000 s.

with the spectral/intensity states that are discussed in Chapters 5 and 6 in the context of studies E and G.

Chapter 4

X-ray Timing and Spectral Evolution vs. Orbital Phase

*This chapter has been published (in a slightly modified form) in the September 20, 1996 issue of
The Astrophysical Journal (Vol. 469) [62].*

4.1 Overview

We have carried out a study of Cir X-1 (study A, see Figure 3-5) through detailed sampling over a single 16.55-d intensity cycle with the *Rossi X-ray Timing Explorer (RXTE)* Proportional Counter Array (PCA). We report here the current state of the source and focus primarily upon the evolution of the emission characteristics away from the flaring activity, i.e., at phases $0.2 \lesssim \phi \lesssim 0.9$ (based on the 1991 radio ephemeris of Stewart et al. [68]). Heretofore, these phases have not been systematically sampled with an instrument of large aperture. In the eccentric binary scenario, the source would be relatively remote from the secondary during these phases.

During the non-flaring phases, Cir X-1 remained unusually bright (~ 1.0 Crab) and relatively steady. The Fourier power density spectrum of the source was observed to vary with strong correlations among low-frequency flat-topped power ($\lesssim 1\text{--}10$ Hz), a QPO peak centered at 1.3–12 Hz, and a broad QPO peak centered at ~ 20 Hz up to ~ 100 Hz. As orbital phase increased within the cycle, the rms amplitude of the flat-topped power generally (but not monotonically) decreased, while the QPO features generally evolved toward higher frequency. The PCA spectrum was observed to generally harden during the non-flaring phases, consistent with results from the *RXTE* All-Sky Monitor (see section 3.1).

Obs. ¹	Julian Date −2450000.5 ²	Orbital Phase ³	Obs.	Julian Date −2450000.5	Orbital Phase
1	147.9	0.98	7	158.3	0.61
2	150.7	0.15	8	158.7	0.63
3	152.8	0.28	9	159.7	0.69
4	154.6	0.39	10	160.7	0.75
5	155.8	0.46	11	161.1	0.78
6	156.6	0.50	12	163.8	0.94

Table 4.1: March 1996 PCA observations of Cir X-1

4.2 Observations and Results

In 1996 March, Cir X-1 was sampled with the PCA (effective area $\sim 7000 \text{ cm}^2$, see section 2.2) twelve times during one 16.55-day orbital period. The observation times and orbital phases are summarized in Table 4.1. The low and high-energy light curves for observations 1–11 are shown in Figure 4-1, along with the hardness ratio derived from those intensities. Observation 12 used a different PCA gain setting (gain epoch 2, see Table 2.1 on page 37) and only 3 PCUs, so it is not included in Figure 4-1. The hardness ratio generally increases during the non-flaring phases as phase increases up to ~ 0.7 , beyond which the ratios are more steady. This confirms the evolution observed in the ASM data (see section 3.1).

Three detailed sample light-curve segments are shown in Figure 4-2. In the full PCA energy band (2–60 keV), Cir X-1 was found to be extremely active, remaining bright ($\gtrsim 1.0$ Crab) throughout the 16.55-d cycle (1 Crab $\approx 13,000 \text{ c/s}$). In the vicinity of phase zero (Obs. 1, 2, & 12), dramatic flares and dips occurred (Figure 4-2a,b). In Obs. 2 (phase 0.15), the count rate climbed to more than 2.5 Crab (Figure 4-2b). Away from phase zero ($0.2 \lesssim \phi \lesssim 0.8$; Obs. 3–11), the count rate remained fairly steady (within 15%) at about 1.0 Crab. Figure 2c shows a sample light curve for phase 0.5, which is typical of these observations. The source is relatively steady but exhibits flickering greatly in excess of Poisson statistics.

Power density spectra (PDS) were produced from PCA data covering 2–8.6 keV in 61- μs time bins. For each 96-min *RXTE* orbit, a continuous observation of 1 to 4 ks was divided into 64-s segments, and the PDS was calculated for each segment. All PDS from the segments of a single continuous observation were averaged together, weighted by the total counts. The resulting average

¹Each observation lasted 1–5 hr and produced 1.4–10 ks of data. Dates and phases listed are the centroids of the observations.

²JD-2450000.5=147 corresponds to 1996 March 5.

³Orbital phase based on the radio ephemeris of Stewart et al. 1991 [68]. Due to faint radio flares in recent years, this ephemeris is still currently in use as the best available (G. Nicolson 1996, private communication).

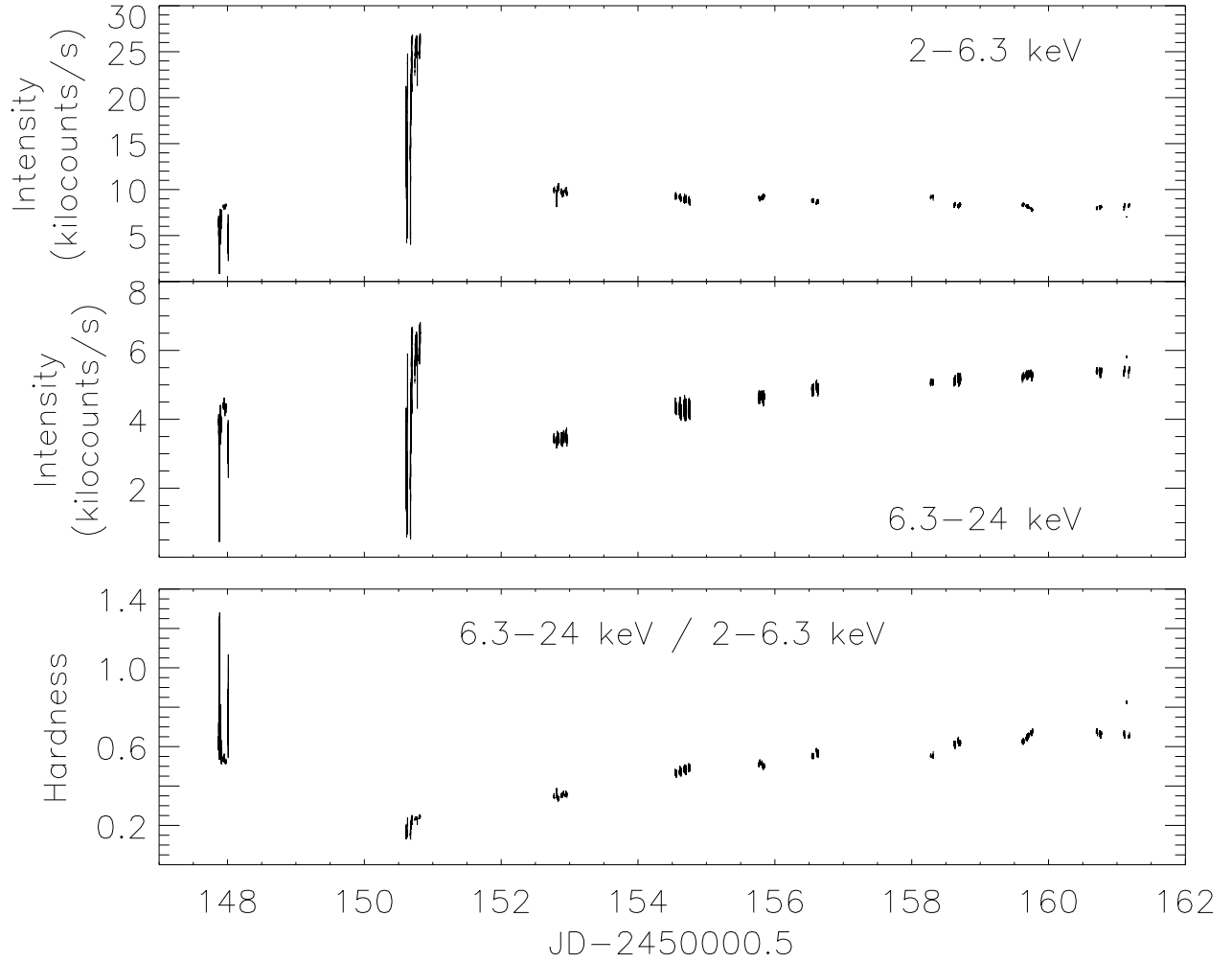


Figure 4-1: PCA light curves in two energy bands (16-s bins), and the ratio of intensity in the hard band to that in the soft band, for observations 1–11 of 1996 March. Phase zero corresponds to day 148.227. The intensity is well above the background level in both bands (~ 25 c/s and ~ 40 c/s for 2–6.3 keV and 6.3–24 keV respectively, not subtracted) even during the dips. Observation 12 is omitted since it was carried out with only three PCUs and a different gain setting.

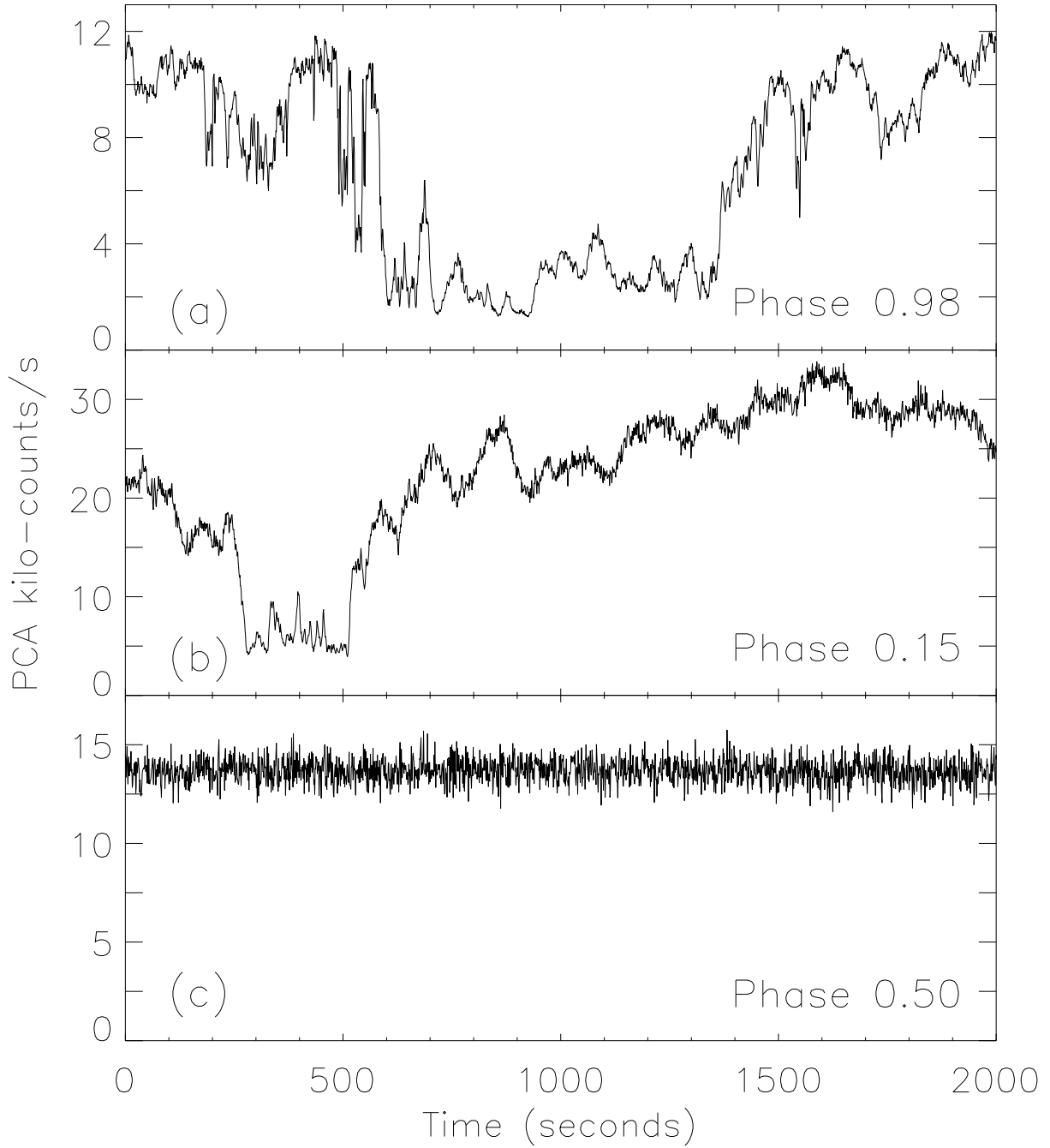


Figure 4-2: Sample PCA light curves (2–60 keV) comparing 2000-s segments showing (a) strong variability and dips near phase zero (phase 0.98; Obs. 1), (b) a brighter portion of the bright flaring state three days later (phase 0.15; Obs. 2), and (c) a typical observation away from phase zero (phase 0.50; Obs. 6). Background (~ 100 c/s) is not subtracted and no deadtime corrections have been made.

power spectrum from each *RXTE* orbit was then logarithmically rebinned, with dead-time-corrected Poisson noise subtracted [88] and normalized to give the fractional rms amplitude squared per Hz (after Belloni & Hasinger [5]).

The PDS from seven orbits are shown in Figure 4-3, offset downward by one-decade intervals. These samples show significant low-frequency flat-topped power which cuts off above 1-10 Hz and also a QPO peak which sits on the high-frequency edge of the flat-topped power at 1.3–12 Hz (compared to 1.4 Hz and 5-17 Hz QPO reported near phase zero by [69, 70]. The PDS in Figure 4-3 are ordered by the frequency of the QPO peak. All the PDS during the non-flaring phases exhibit these features. The flat-topped power level systematically decreases as the cutoff and QPO frequencies increase (note that each flat-top level is more than one decade below the previous level in Figure 4-3). Above the cut-off frequencies, the curves all track together with roughly the same power. A few PDS not illustrated here have a steep low-frequency component below 0.1-0.4 Hz.

A broad high-frequency QPO is also apparent in Figure 4-3 centered at ~ 20 Hz to ~ 100 Hz or more. For observations in which the 1.3–12 Hz QPO frequency is below ~ 8 Hz, the high-frequency broad peak is always clearly present; otherwise, it is sometimes marginally detectable above 100 Hz. Note that this high-frequency QPO peak moves to higher frequencies with the low-frequency QPO peak.

All the PDS in the non-flaring phases were analyzed to further study these trends. The flat-topped component was fit with a zero-centered Lorentzian profile, the two peaked features were also each fit with a Lorentzian, and the high-frequency tail was fit with a power law. Although the results of the fits indicate that this model is crude (via large values of the associated chi-squared statistic), the fits were adequate to determine approximate centroid frequencies and power levels. Errors (rms) for QPO centroid frequencies were estimated from 90% confidence intervals of the fits or 20% of the FWHM of the peak, whichever was greater. Errors for the flat-top power level were estimated to be $\sim 5\%$. As the orbital phase increased, the power level of the flat-topped noise generally decreased (Figure 4-4a) while the narrow QPO frequency increased (Figure 4-4b), in accord with the trends noted above. The trends are not monotonic though; a large excursion occurs at $\phi = 0.4$ in both curves. Remarkably, the correlation between these two quantities (flat-topped level and narrow QPO frequency) in Figure 4-4c is very strong (and negative). Moreover, the frequency of the 20–100 Hz peak scales as ~ 13 times the frequency of the 1.3–12 Hz peak (Figure 4-4c) with a weak tendency for the frequency ratio to decrease (from ~ 16 to ~ 11) with increasing frequency. The frequency difference between the two peaks changes by more than a factor of four over this range, from less than 20 Hz to more than 80 Hz. The cutoff frequency of the flat-topped component (as measured by the width of the best fitting zero-centered Lorentzian) also moved to higher frequency with the

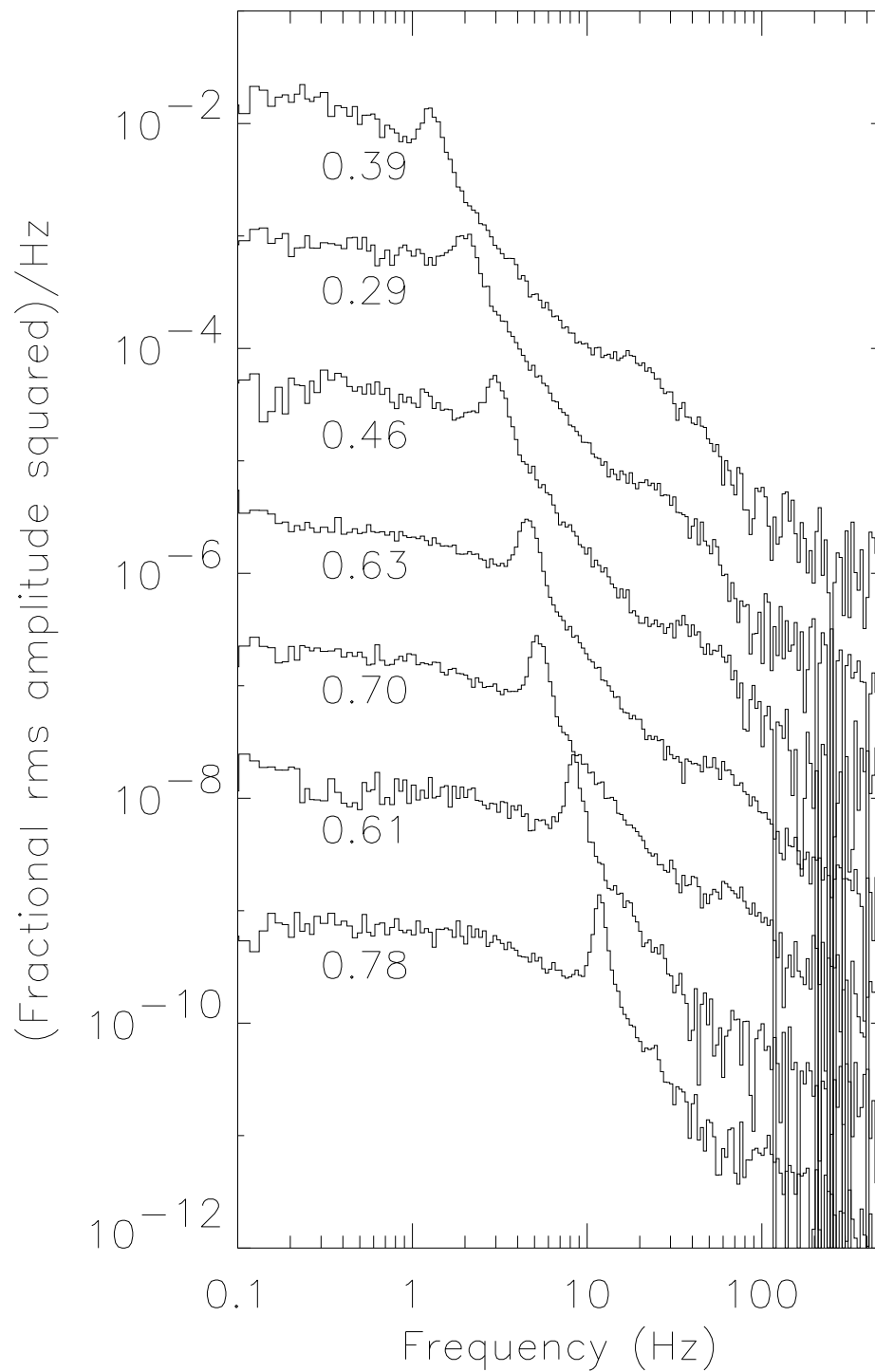


Figure 4-3: Power density spectra from seven *RXTE* orbits away from phase zero, offset downward at decade intervals. (The ordinate scale applies to the top curve.) The curves are ordered by the frequency of the 1.3–12 Hz QPO peak and are labeled with orbital phase.

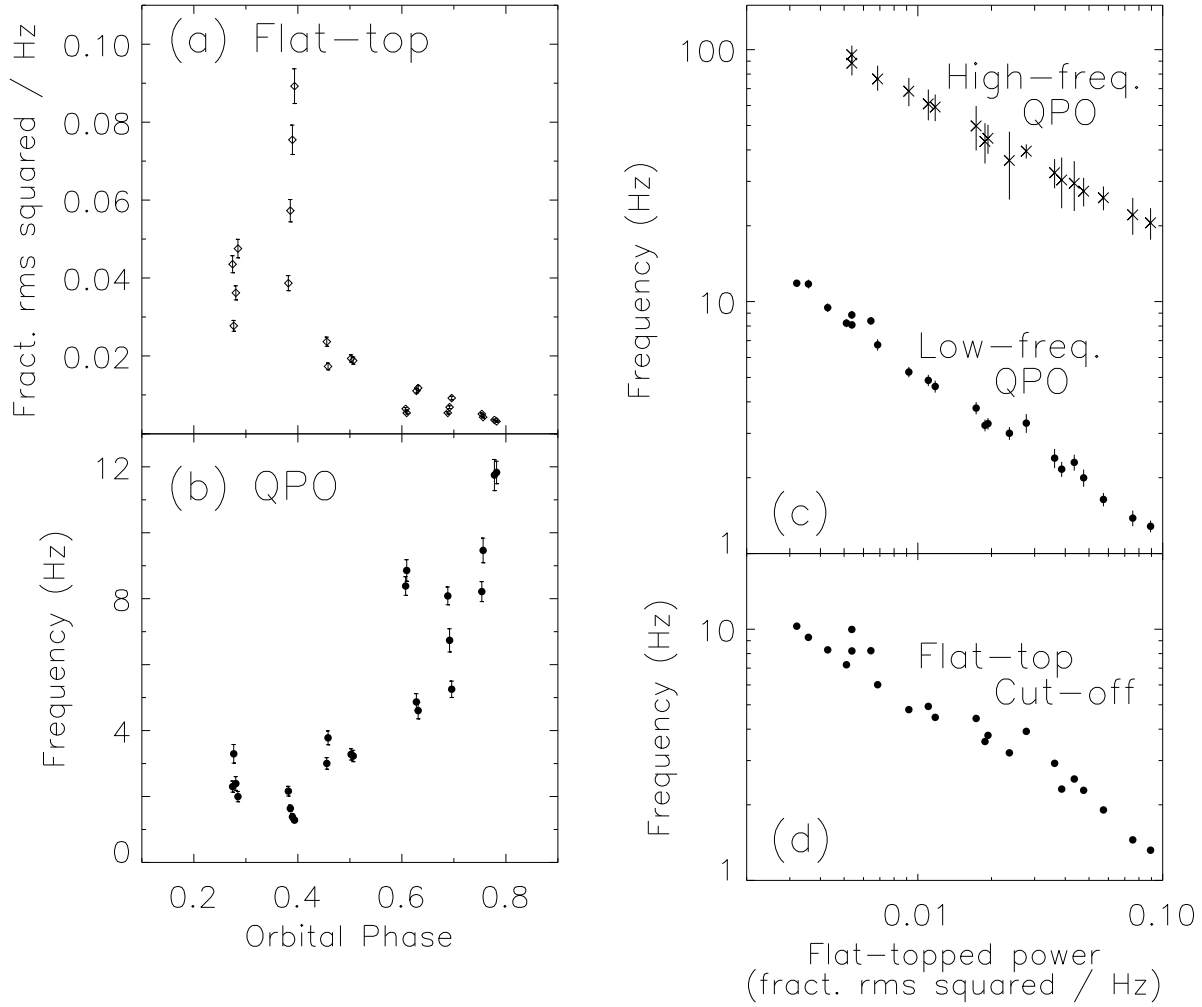


Figure 4-4: Flat-top power level (a) and QPO frequency (b) as a function of orbital phase over a single orbital cycle. (c) Frequency of the narrow low-frequency QPO and the broad high-frequency QPO vs. the flat-top power level. (d) Cut-off frequency of the flat-topped power vs. flat-top power level.

narrow QPO peak (Figure 4-4d). These two frequencies agree within 20% for all observations.

4.3 Discussion

The 1.4 and 5-17 Hz QPO reported by Tennant et al. [69, 70] were found during observations near phase zero. It was suggested that the QPO were bimodal, with the 1.4 Hz QPO independent of luminosity and the 5-17 Hz component correlated with the estimated 2-10 keV unabsorbed energy flux [69, 70]. Our observations show a gradual evolution of the QPO from 1.3 to 12 Hz over the *non-flaring* phases. Some of the phase zero *EXOSAT* observations which exhibited 5-17 Hz QPO

also had a QPO peak at 100–200 Hz [69]. This low/high frequency QPO pair is likely to be the evolving QPO pair we have observed, but extended to higher frequencies.

The correlation between the flat-topped power level and the cut-off frequency (Figure 4-4d) is similar to the effect observed by Belloni and Hasinger [6] in the black hole candidate Cyg X-1 and also observed in the neutron star 4U 1608-522 [87] by Yoshida et al. In fact, several properties of 4U 1608-522 show correlations similar to those we have observed in Cir X-1. In two of the three observations of 4U 1608-522 by Yoshida et al. [87], QPO were seen (at 0.4 and 2.0 Hz respectively) just above the knee in the power spectrum, and a broader peaked noise feature was observed at higher frequencies of 1.0 and 5.1 Hz respectively [87]. We note that the ratio of the two peaks is the same in both observations, just as the two peaks in our Cir X-1 observations move to higher frequency with a nearly constant frequency ratio (although the ratio is different for the two sources). In both sources, the spectrum generally (but not always) hardens as these features move out to higher frequencies and the flat-topped power level decreases.

The *RXTE* observations of Cir X-1 have (1) confirmed a general hardening of the spectrum during the non-flaring phases 0.2–0.7, (2) demonstrated a trend (with moderate scatter) for the power density features to shift to higher frequency and the amplitude of the low-frequency power to decrease with increasing orbital phase during the non-flaring phases, and (3) demonstrated extremely tight correlations among the QPO features and the flat-topped power. In the eccentric-orbit model, these characteristics may reflect the evolving state of the accretion disk while it is being depleted with little or no replenishment. For example, the leveling of the hardness ratios after phase 0.6-0.8 may reflect a time constant (of order 10 days) of the disk structure.

Chapter 5

QPOs Associated with Spectral Branches

This chapter is scheduled to be published (in a slightly modified form) in the October 10, 1998 issue of The Astrophysical Journal (Vol. 506) [63].

5.1 Overview

We present *Rossi X-ray Timing Explorer (RXTE)* All-Sky Monitor observations of the X-ray binary Circinus X-1 which illustrate the variety of intensity profiles associated with the 16.55 d flaring cycle of the source. We also present eight observations of Cir X-1 made with the *RXTE* Proportional Counter Array over the course of a cycle wherein the average intensity of the flaring state decreased gradually over ~ 12 days (study E, see Figure 3-5). This unusually slow transition allows us to demonstrate how the time-variability properties of the source are related to its intensity and its spectral properties (In Chapter 4, we characterized only the quiescent phases of a typical cycle). Fourier power density spectra for these observations show a narrow quasi-periodic oscillation (QPO) peak which shifts in frequency between 6.8 Hz and 32 Hz, as well as a broad QPO peak that remains roughly stationary at ~ 4 Hz. We identify these as Z-source horizontal and normal branch oscillations (HBOs/NBOs) respectively. Color-color and hardness-intensity diagrams (CDs/HIDs) show curvilinear tracks for each of the observations. The properties of the QPOs and very low frequency noise allow us to identify segments of these tracks with Z-source horizontal, normal, and flaring branches which shift location in the CDs and HIDs over the course of the 16.55 d cycle. These results contradict a previous prediction, based on the hypothesis that Cir X-1 is a high- \dot{M}

Obs.	Julian Date ¹	Phase	Mean Intensity (Crab) ²
I	2450497.90	0.10	2.3
II	2450499.98	0.23	1.8
III	2450501.69	0.33	1.6
IV	2450503.66	0.45	1.5
V	2450505.80	0.58	1.2
VI	2450507.31	0.67	1.3
VII	2450509.35	0.79	1.1
VIII	2450511.62	0.93	1.0

Table 5.1: PCA observations of Cir X-1 during 1997 February 18 – March 4.

atoll source, that HBOs should never occur in this source [54, 77].

5.2 Observations

The *RXTE* ASM has provided 2–12 keV light curves of Cir X-1 since 1996 February (see Figure 3-1). Throughout the ASM observations, the baseline intensity of Cir X-1 has remained near 1.0 Crab. However, the profile of each 16.55-d flaring cycle can vary considerably. The variety of intensity profiles is illustrated in Figure 5-1, which shows ASM light curves and hardness ratios for three individual cycles. In many cycles, after 3–5 days in the flaring state, the intensity is quite steady for the remainder of the cycle (e.g., Figure 5-1a). In addition to the main flaring episode, some cycles show a mid-phase flare (not always at the same phase) to as high as 2 Crab (Figure 5-1b). Occasionally, the flaring state begins after phase zero and continues for most of the cycle with a gradually decreasing intensity (Figure 5-1c). Despite the variety of intensity profiles, all cycles observed with the ASM show the general pattern of spectral hardening mentioned in section 2.4. During the half day before phase zero, and continuing intermittently for up to two days, brief dips occur in many cycles (perhaps in all cycles, since the ASM coverage is incomplete). These dips are seen as isolated low points in the ASM light curves of Figure 5-1.

Eight PCA observations (~ 6 ksec each) were carried out at roughly two-day intervals (Table 5.1) during 1997 February 18 – March 4 to sample the 16.55 day cycle shown in Figure 5-1c. The very gradual decline of the flaring-state intensity in this cycle serendipitously provided an opportunity to study intensity-related source properties. All five proportional counter units (PCUs) of the PCA operated normally during each observation, except during the first few minutes of the first

¹Midpoint of 2–3 hr observation (~ 6 ksec of data per observation).

²1.0 Crab $\approx 13,000$ counts/s (2–32 keV, all 5 PCUs)

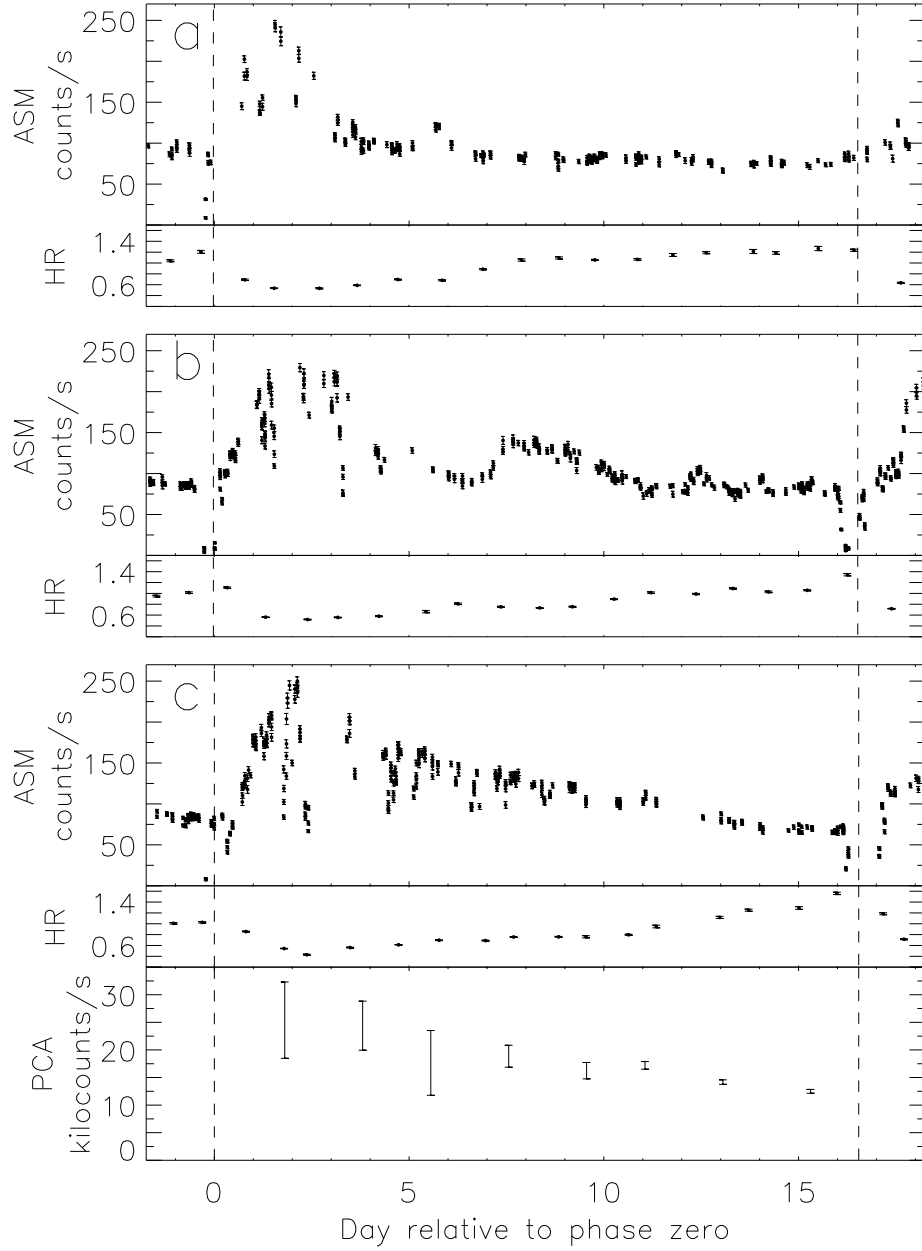


Figure 5-1: *RXTE* ASM light curves (1.5–12 keV) for three 16.55 d cycles of Cir X-1 showing different flaring profiles. Each intensity point corresponds to a 90-s exposure by one of the three ASM cameras, and the hardness ratio (HR), defined as the ratio of counting rates for 5–12 keV to 3–5 keV, is shown in one-day averages. The 3–5 keV to 1.5–3 keV hardness ratio exhibits very similar behavior and is not shown here. The intensities are for Cir X-1 after background and other sources in the field of view have been subtracted. The Crab nebula yields ~ 75 c/s. Vertical dashed lines indicate phase zero based on the radio ephemeris of Stewart et al. 1991. Day zero corresponds to (a) 1997 April 23.87 (b) 1996 August 2.14 and (c) 1997 February 16.69. For cycle (c), the intensity ranges (I[2.0–18 keV]) seen in the eight *RXTE* PCA observations (I–VIII in time order) are also shown.

observation when only three PCUs were on. All intensities for that period have been adjusted by a factor of 5/3, but these data are not used in color-color and hardness-intensity diagrams due to gain differences between detectors.

Figure 5-2 shows the light curves and hardness ratios (with 16 s time resolution) for each of the PCA observations (I–VIII in time order), made as the intensity declined from 2.5 Crab to 1.0 Crab. On time-scales of hundreds of seconds, the observations made at high intensities show strong variability, while observations at 1.0 Crab (~ 13 kilocounts/s) show quite steady count rates. As expected from the ASM hardness ratios, the PCA hardness ratio gradually increases from a low value during the early observations when the source was in the flaring state to a factor four higher as it reached the quiescent level. The relationship between intensity and spectral changes is discussed in detail below.

5.3 Analysis and Results

5.3.1 Color-color and Hardness-intensity Diagrams

For the eight PCA observations of 1997 February–March, 16 s intensity and hardness-ratio measurements were used to construct color-color and hardness-intensity diagrams (CDs/HIDs, Figure 5-3). The hardness ratios were defined as the ratio of count rates in selected energy bands: a soft color ($I[4.8\text{--}6.3\text{ keV}] / I[2.0\text{--}4.8\text{ keV}]$) and hard color ($I[13\text{--}18\text{ keV}] / I[8.5\text{--}13\text{ keV}]$) for the CD, and a broad color ($I[6.3\text{--}13\text{ keV}] / I[2.0\text{--}6.3\text{ keV}]$) for the HID. The evolution from flaring to quiescent state produced a large range of colors and intensities over the entire cycle. In contrast, each individual observation yielded a localized cluster or track within the CDs and HIDs. The spectral branches for each of the observations are easier to distinguish in the HID than the CD. The long tracks in the HID associated with observations I–V show the color changes associated with the large intensity variations during the flaring phases. The intensity variations are smaller for observations VI–VIII, but significant color changes do occur during these observations as well.

The choice of energy bands used in constructing these diagrams can affect the appearance of spectral tracks. For observations showing a single branch, only the length and slope of the branch is affected. Observations V and VI each show two branches. The orientation of these branches is discussed in more detail below.

The tracks in the CD and HID are reminiscent of the correlated spectral/intensity behavior of Z and atoll class LMXBs (see Figure 1-1), which also show correlations of temporal properties with position along tracks or branches in CDs and HIDs [27]. Thus, we have investigated how the temporal properties of Cir X-1 are related to position in the CD or HID. For this purpose, we divided the

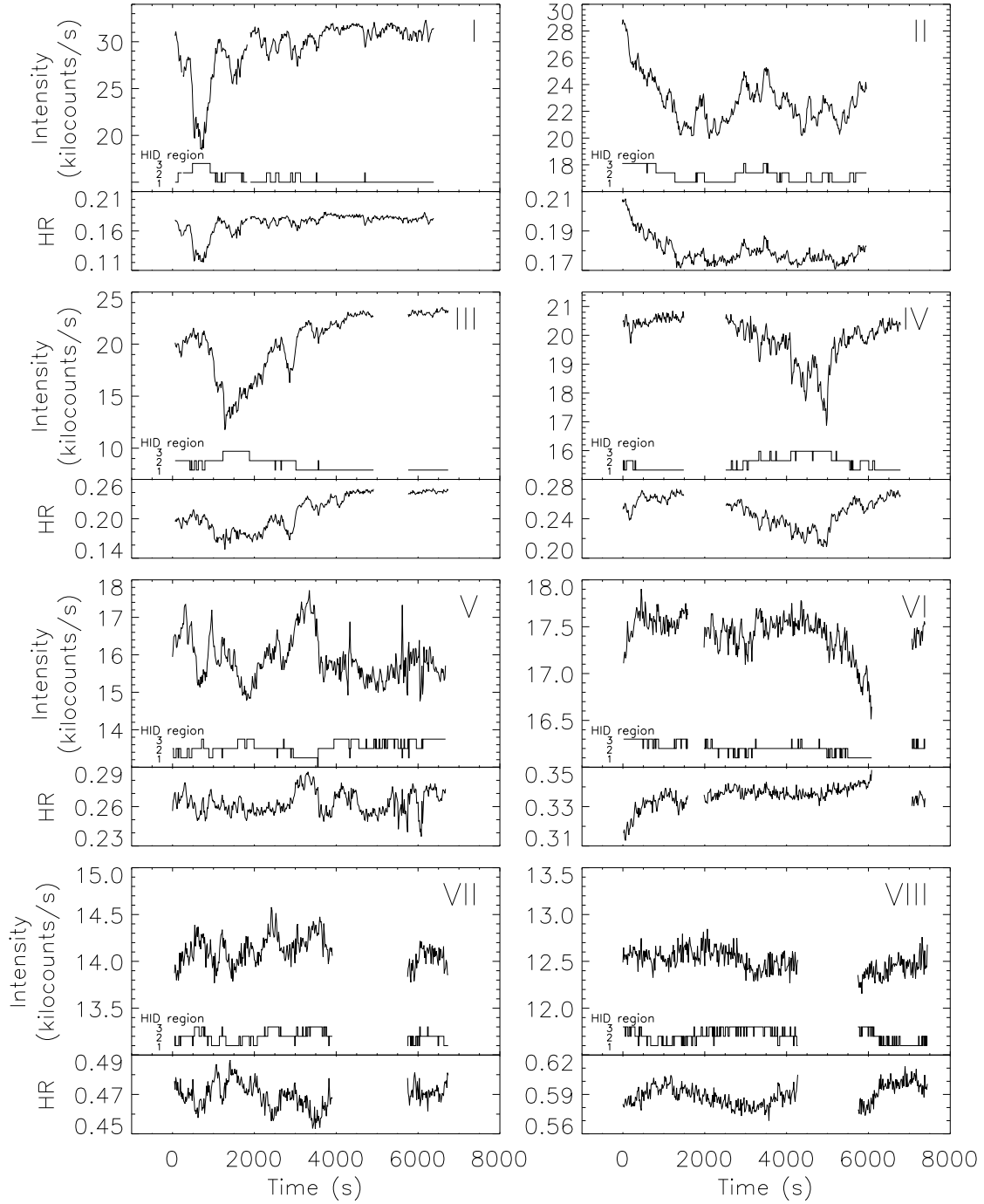


Figure 5-2: PCA light curves (2–18 keV, 5 PCUs) and hardness ratios ($HR = I[6.3\text{--}13\text{ keV}] / I[2.0\text{--}6.3\text{ keV}]$) in 16 s time bins for the eight observations made during 1997 February 18 – March 4. A count rate of 13 kcts/s \approx 1.0 Crab. The data gaps in Obs. VI were longer than as shown here; the second segment of the observation has been shifted left by 4000 s and the third segment by 5000 s. These data were used to construct the hardness-intensity diagram in Figure 5-3. The association with specific regions of that diagram is indicated below each light curve.

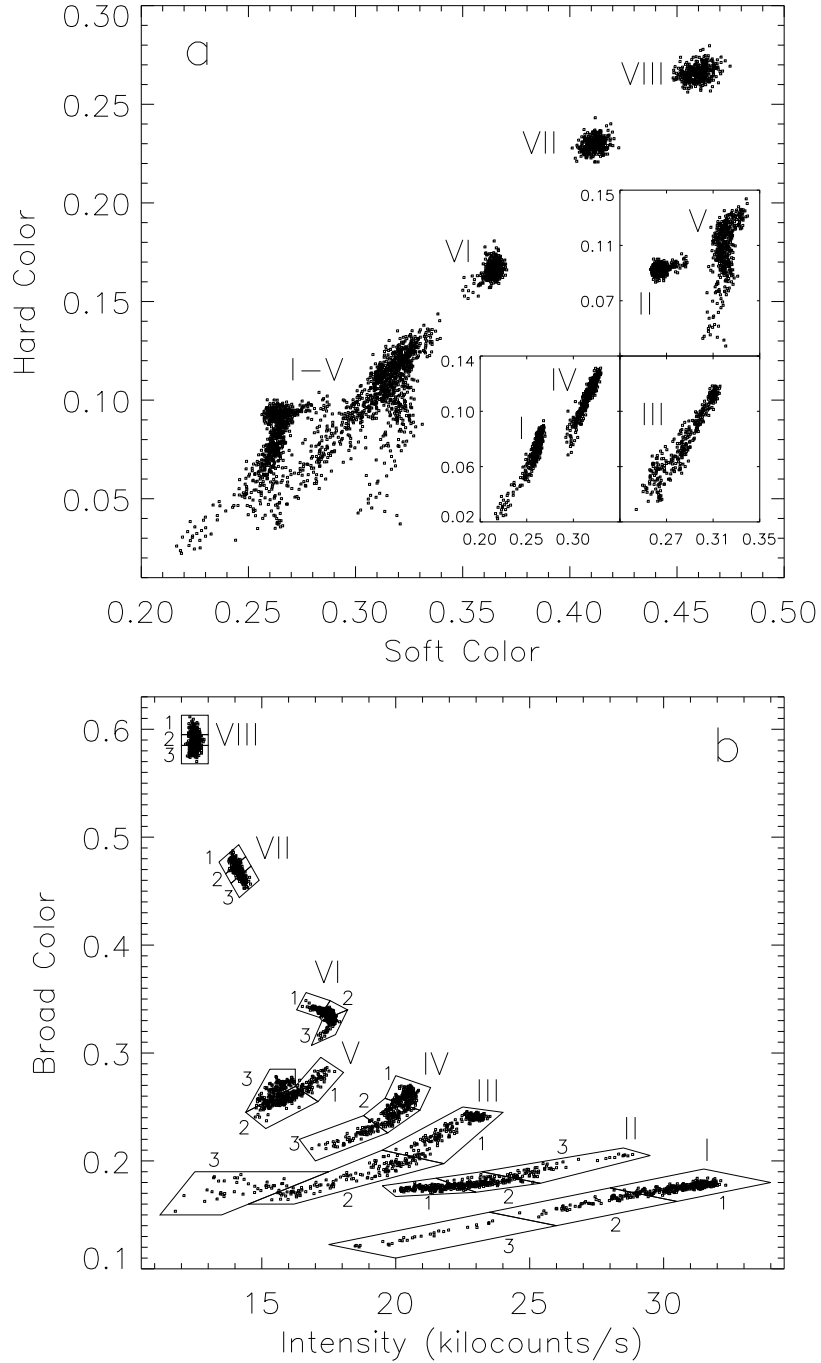


Figure 5-3: Color-color diagram (a) and hardness-intensity diagram (b) for all eight observations (I–VIII). In the CD, soft color is defined as $I[4.8\text{--}6.3\text{ keV}] / I[2.0\text{--}4.8\text{ keV}]$ and hard color as $I[13\text{--}18\text{ keV}] / I[8.5\text{--}13\text{ keV}]$. In the HID, the intensity, $I[2.0\text{--}18\text{ keV}]$, is from all five PCUs and the hardness ratio is a “broad” color: $I[6.3\text{--}13\text{ keV}] / I[2.0\text{--}6.3\text{ keV}]$. Each point corresponds to 16 s of data. Background has been subtracted, but it does not affect the intensity or soft color and only slightly affects the hard color. The three insets in the CD separate overlapping points from observations I–V. The HID track for each observation has been divided into three regions (1–3) for timing analysis.

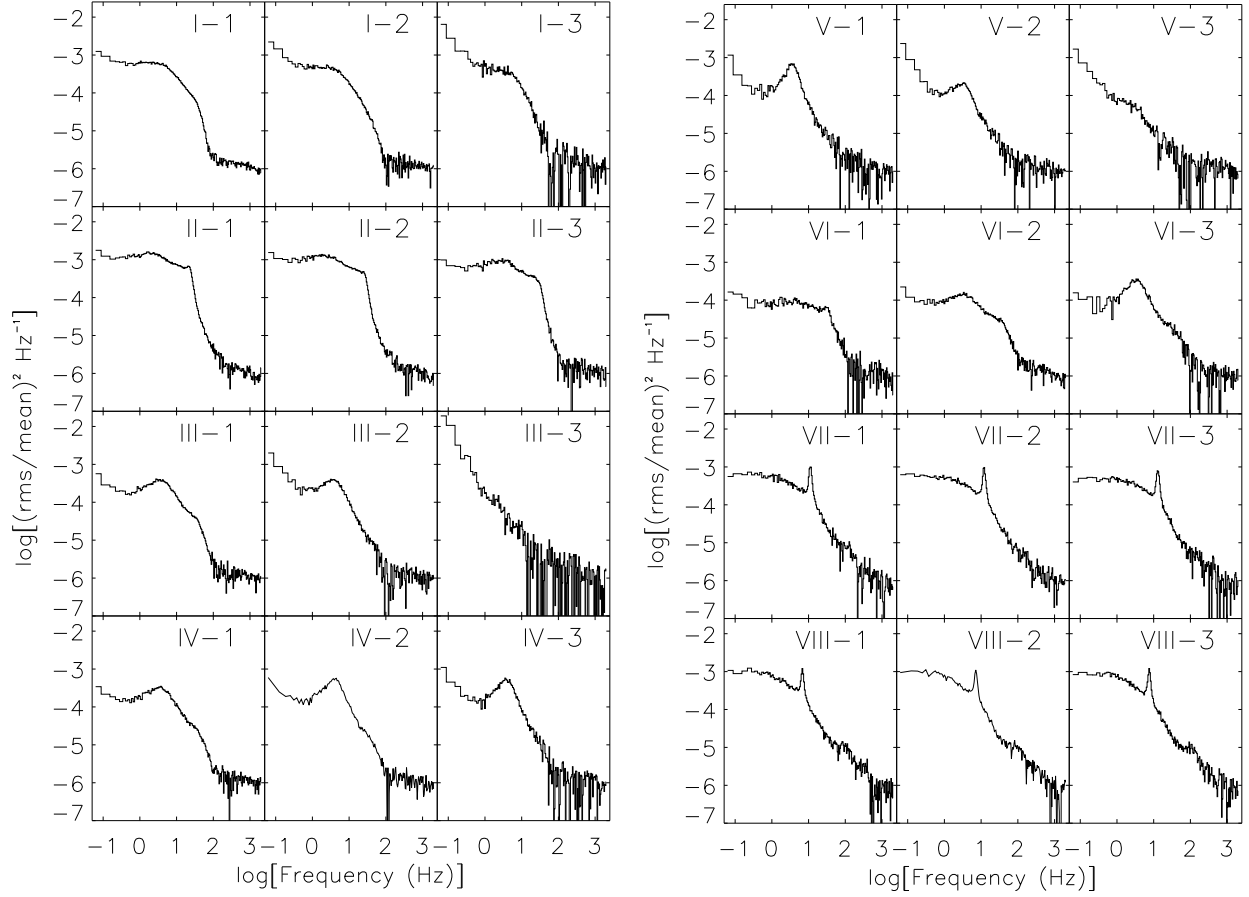


Figure 5-4: Averaged and rebinned power density spectra (2–32 keV) for each of the three HID regions for each observation. Poisson noise has been subtracted from each PDS (see text).

HID track for each of the eight observations into three regions (Figure 5-3b). The choice of numbers for each region was motivated in part by the timing results discussed below, but the numbers serve mainly as reference labels rather than as meaningful quantities (such as Z "rank number").

5.3.2 Power Density Spectra

Fourier power density spectra (PDSs) were computed using 16 s segments with $244 \mu\text{s}$ (2^{-12} s) time bins. This was done for both the full 2–32 keV energy range and for four energy channels: 2.0–4.8 keV, 4.8–13 keV, 13–18 keV, and 18–32 keV. The Leahy-normalized power spectra [40] were converted to the fractional rms normalization by dividing by the background-subtracted count rate in the selected band. The expected Poisson level, i.e. the level of white noise due to counting statistics, was estimated taking into account the effects of deadtime [51, 88, 89] and subtracted from each PDS; this method tends to slightly underestimate the actual Poisson level. For each of the 24 HID

regions defined in Figure 5-3, an average PDS was calculated from the power spectra corresponding to points in that region. The PDSs were then logarithmically rebinned.

The average PDS (2–32 keV) for each HID region is shown in Figure 5-4. During the extended active state (observations I–VI), a broad peak is often observed near 4 Hz; this feature is prominent in PDSs from observations III–VI, weak in observation II, and indistinguishable from a flat-topped component in observation I (see below). A strong narrow QPO feature is seen at frequencies from 6.8 to 13 Hz in observations VII and VIII. In some cases, especially at higher photon energy (see Figure 5-5), a harmonic peak is observed at twice the frequency of this QPO. A weak narrow QPO feature is present at frequencies above 20 Hz in regions II-1 and VI-1. A sharp “knee” is present at similar frequencies in regions II-2, II-3, III-1, IV-1, VI-2, VI-3, and possibly I-1. Broad high-frequency noise is sometimes seen, e.g. at ~ 100 Hz in observation VIII (Figure 5-5b). There is an underlying red continuum spectrum of noise in all of the regions of the HID, but the shape and low frequency slope of the continuum vary over a wide range.

The narrow QPO peaks and the low frequency noise in the PDSs from the “quiescent” 1 Crab observations (VII and VIII) resemble previously observed PDSs (Chapter 4, [62, 54, 69]). Those PDSs also contained narrow QPO features, with centroid frequencies in the range 1.3–20 Hz, and similarly shaped low-frequency noise (e.g. see Figure 4-3). The broad high-frequency component that we detect in the present observations is similar to the 20–100 Hz QPO seen in earlier PCA observations (Chapter 4, [62]) and to the 100–200 Hz QPO observed with *EXOSAT* [69].

The weak narrow QPO feature above 20–30 Hz in regions II-1 and VI-1 occurs near the knee of the low-frequency noise component. This similarity to the LFN and prominent QPO at lower frequency in observations VII and VIII suggests these higher frequency oscillations are produced by the same physical process as the lower frequency QPOs. In observations II and VI, this QPO feature is visible in region 1 as a small peak that fades in region 2 and becomes only a “knee” in region 3 (see Figure 5-4). Thus we assume that this knee is related to the QPO. Similar knees are present in regions III-1, IV-1, and possibly I-1. We include a narrow QPO component in fits of PDSs which show a knee above 20 Hz, but identify these cases as “unpeaked” in the discussion below.

Likewise, although no peak appears in the PDSs from observation I, a broad noise component has roughly constant power below about 4 Hz and drops off above that frequency, forming a “knee” which might indicate the presence of the 4 Hz QPO component. The PDS for region I-1 somewhat resembles those of regions III-1 and IV-1, in that all show a break in the power spectrum near 4 Hz and a second knee or change in slope near 30 Hz. We include a broad QPO component in fits of the PDSs for observation I, but we identify these cases as “unpeaked”.

The PDSs were fit with models comprising both broad-band and QPO components: a power-law

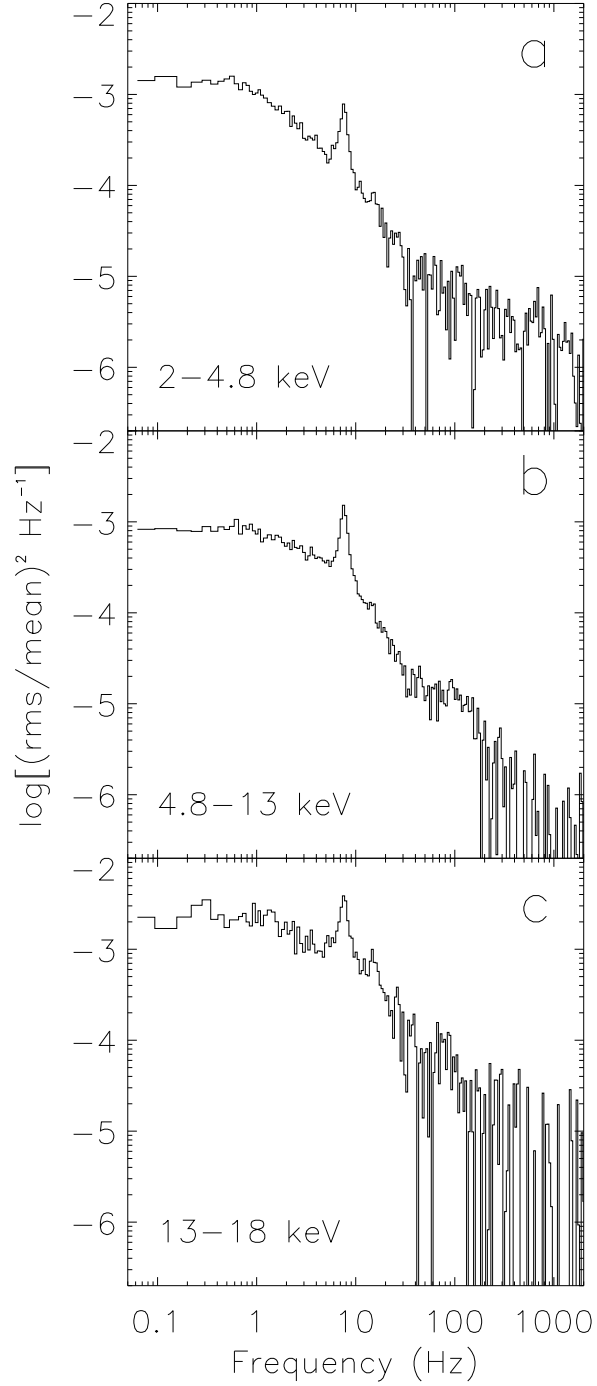


Figure 5-5: Averaged and rebinned power density spectra for HID region VIII-3 in three energy bands. A harmonic peak of the 7.6 Hz QPO is clearly visible in the high-energy channel (c). The broad high-frequency peak, most clear in (b), occurs near ~ 100 Hz in this observation. The low-frequency noise cuts off less sharply as energy increases.

for the very low frequency noise (VLFN), an exponentially cut-off power-law for the broad low-frequency noise, a Lorentzian for the broad QPO near 4 Hz, Lorentzians for the narrow QPO and its first harmonic, a broad Lorentzian for the high-frequency peak, and a second power-law to fit the residual Poisson noise at high frequency. The model for each PDS consisted of two to five of these components, depending on which components were necessary for an acceptable fit. The frequency of the harmonic (when present) of the narrow QPO was fixed at twice the fundamental frequency. For the fits of the PDSs from the four narrower energy channels, the QPO centroid frequencies were fixed at the values determined from the 2–32 keV PDSs. There were generally not enough counts to obtain useful PDS fits for the 18–32 keV channel. For use in performing the fits, we estimated the variance of each power in each binned and averaged PDS by calculating the sample variance of the powers in the individual PDSs that were averaged to obtain each point, and dividing the result by the number of the powers used in computing the sample variance.

The centroids of the narrow variable-frequency QPO and the ~ 4 Hz QPO were measured accurately whenever a clear peak was visible. However, in cases where these components are weak or unpeaked, the centroids were less well-constrained. The centroid of the broad high-frequency peak and the cut-off frequency of the LFN were often poorly constrained.

Figure 5-6 shows the frequency of the broad and narrow QPOs versus intensity (2–18 keV). The frequency of the narrow peak is generally correlated with intensity, starting at 6.8 Hz at 1 Crab and reaching 32 Hz at 1.3 Crab. At higher intensity, this QPO is sometimes present above 20 Hz and is often unpeaked (i.e., a knee). In observations III–VI, the broad QPO is clearly present at 3.3 to 4.3 Hz. This QPO component was included in the fits of the PDSs from observations I and II, and the resulting frequencies (2.1–4.5 Hz) are shown as unfilled squares (indicating a weak peak or a knee) above 20 kcts/s in Figure 5-6.

The ratio of the width of the narrow QPO peak to its centroid frequency ($\Delta\nu/\nu$) is about 0.15 when at 6.8 to 13 Hz. At higher frequency this QPO becomes broader, with $\Delta\nu/\nu \sim 0.4$. When the broad QPO near 4 Hz is strong, we find that $\Delta\nu/\nu \sim 1$, and when it is weak $\Delta\nu/\nu \sim 2$ to 3.

Figure 5-7 illustrates the dependence of the rms amplitude of the QPOs upon photon energy. Typical values for the rms amplitude of the 6.8–13.1 Hz QPO at 2–4.8 keV, 4.8–13 keV, and 13–18 keV are 4%, 5%, and 8% respectively (Figure 5-7a), indicating a weak trend of increasing rms amplitude at higher photon energy. The amplitude of the broad QPO increases significantly at higher photon energy. For clearly peaked 4 Hz QPOs, the rms amplitude is typically about 3%, 8%, and 18% in these three energy bands (Figure 5-7b). The rms values vary considerably when these components are weak or unpeaked but their amplitudes still generally increase with energy (Figure 5-7c).

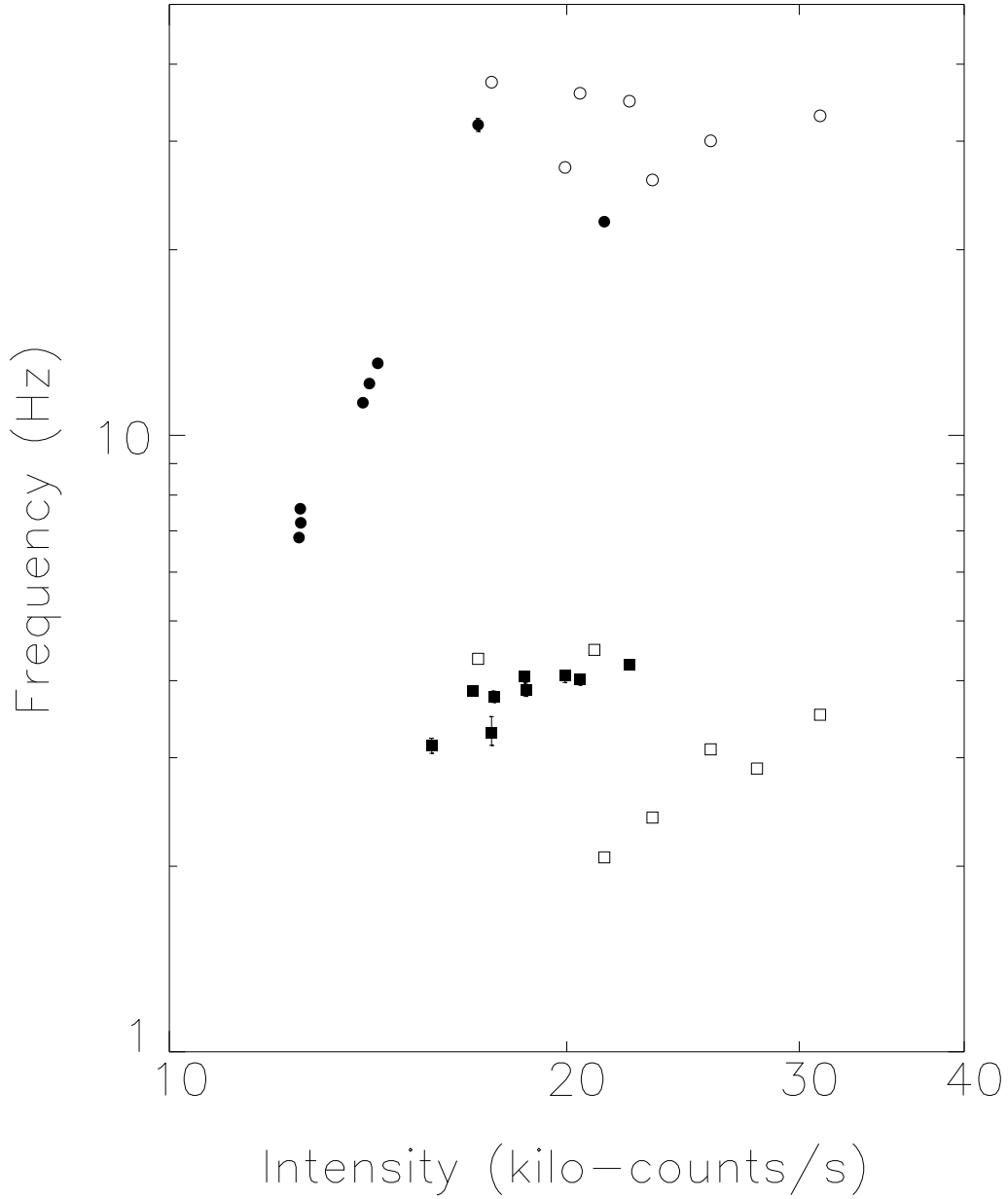


Figure 5-6: Centroid frequency of the QPOs versus intensity ($I[2.0-18 \text{ keV}]$). A filled circle represents the narrow QPO and a filled square represents the broad $\sim 4 \text{ Hz}$ QPO (all points below 5 Hz are the broad QPO). Unfilled circles and squares indicate the approximate frequency of a knee or very weak peak that may be associated with the narrow and broad QPO respectively. Error bars on frequency measurements (filled points only) represent 90% confidence intervals for a single parameter ($\Delta\chi^2=2.7$). In many cases, the error bar for the QPO frequency is smaller than the plot symbol.

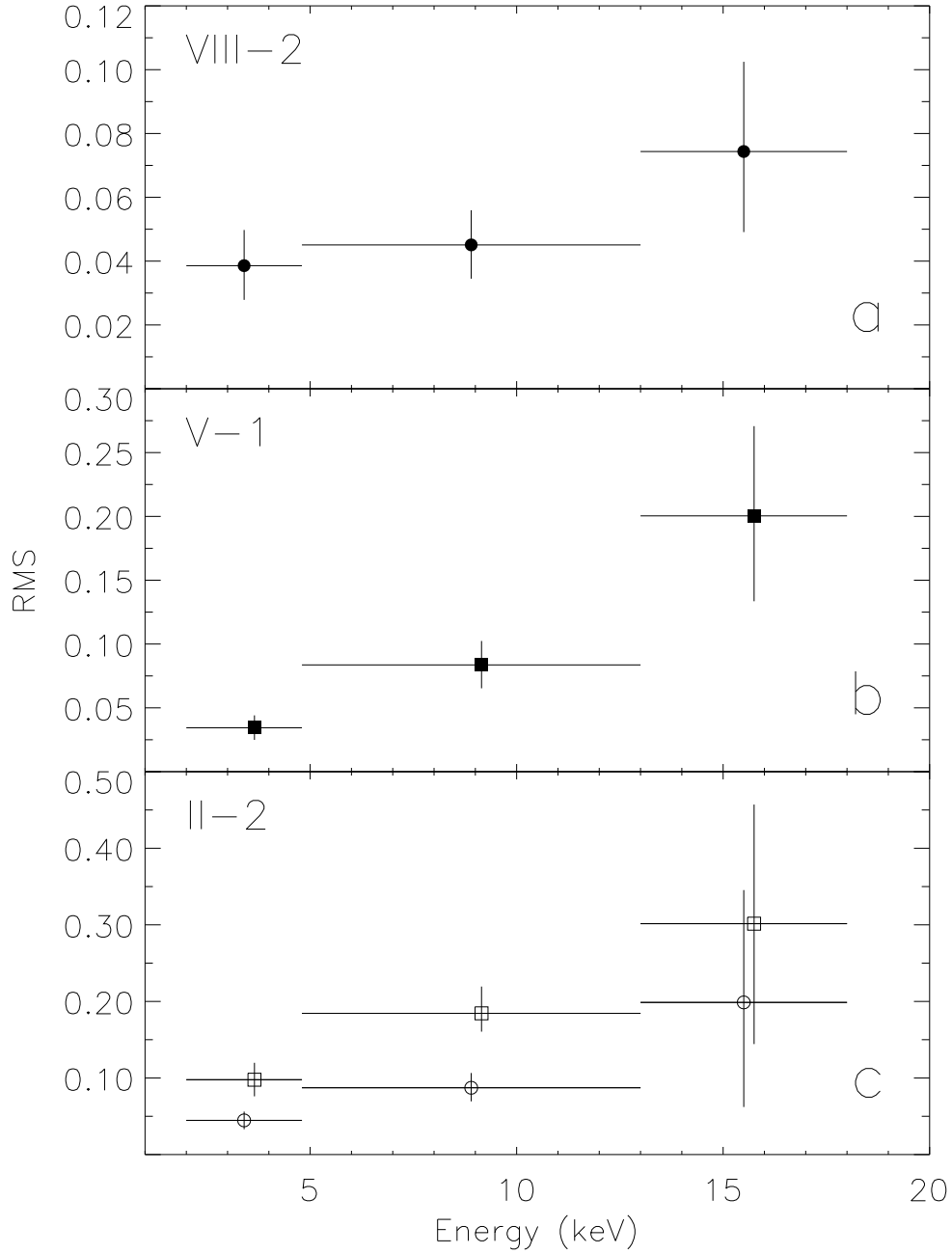


Figure 5-7: Rms amplitude of QPOs versus photon energy. Panel (a) shows the rms for the narrow QPO at 7.2 Hz (solid dot) and (b) for an example of the broad 4 Hz QPO (solid box). In panel (c), unfilled circles and boxes indicate the rms amplitude of a component forming a knee or very weak peak that may be associated with the narrow and broad QPOs respectively. The broad QPO points have been offset slightly to the right in energy for clarity. Errors on QPO amplitudes represent 90% confidence intervals.

5.3.3 Temporal Behavior versus Position on Spectral Branches

The outlines of the HID regions of Figure 5-3b are reproduced in Figure 5-8 with labels summarizing the observed QPO properties. As the hardness ratio decreases and the intensity increases along the HID tracks for observations VIII, VII, and VI, the frequency of the narrow QPO feature increases from 6.8 Hz to 32 Hz. The feature is rather weak and knee-like in observation VI, but it appears to have a width consistent with the width of the prominent QPO peak in observations VII and VIII. A similar weak and somewhat knee-like feature is also present in observation II, where it increases in frequency from 22 Hz to 30 Hz as the intensity increases. The PDSs from observations I, III, and IV all show a knee above 30 Hz at the high-intensity, hard end of their HID tracks; these knees may be related to the narrow QPO features seen in the other observations.

The broad 4 Hz QPO is not present in the “quiescent” observations (VII and VIII). This QPO is strongest in portions of the intermediate-intensity observations (III–VI) and is weakly present in the soft, high-intensity observations (II and possibly I).

Very low frequency noise dominates the power spectrum of regions V-3 and III-3. Both of these regions appear to begin upturned branches at the low-intensity, soft end of branches showing the more pronounced 4 Hz QPOs.

5.4 Discussion

The combined temporal and spectral-branch properties of the observations presented here suggest Z-like behavior. We identify the 6.8–32 Hz QPOs as horizontal-branch oscillations (HBOs), the 4 Hz QPO as normal-branch oscillations (NBOs), and the strong VLFN as flaring-branch behavior (see discussion below). These identifications of characteristic time-variability patterns then help to identify the tracks in the HID as horizontal, normal, and flaring branches (HB/NB/FB), where each 6 ks observation of Cir X-1 appears to have captured a snapshot of portions of one or two of the branches. The spectral branches appear to shift around as the flaring gradually subsides, rather than forming a stable Z pattern. It is likely that the shapes of the spectral branches become distorted somewhat during these large shifts. We now describe the inferred properties of each of the spectral branches in more detail.

5.4.1 Horizontal Branch

HID regions VIII, VII, and VI-1 show a narrow QPO peak or knee at 6.8–7.6 Hz, 11.3–13.1 Hz, and 32 Hz respectively. This frequency range overlaps the 13–60 Hz range of typical horizontal branch QPOs [78]. The associated low-frequency noise and harmonic peak are also typical of horizontal

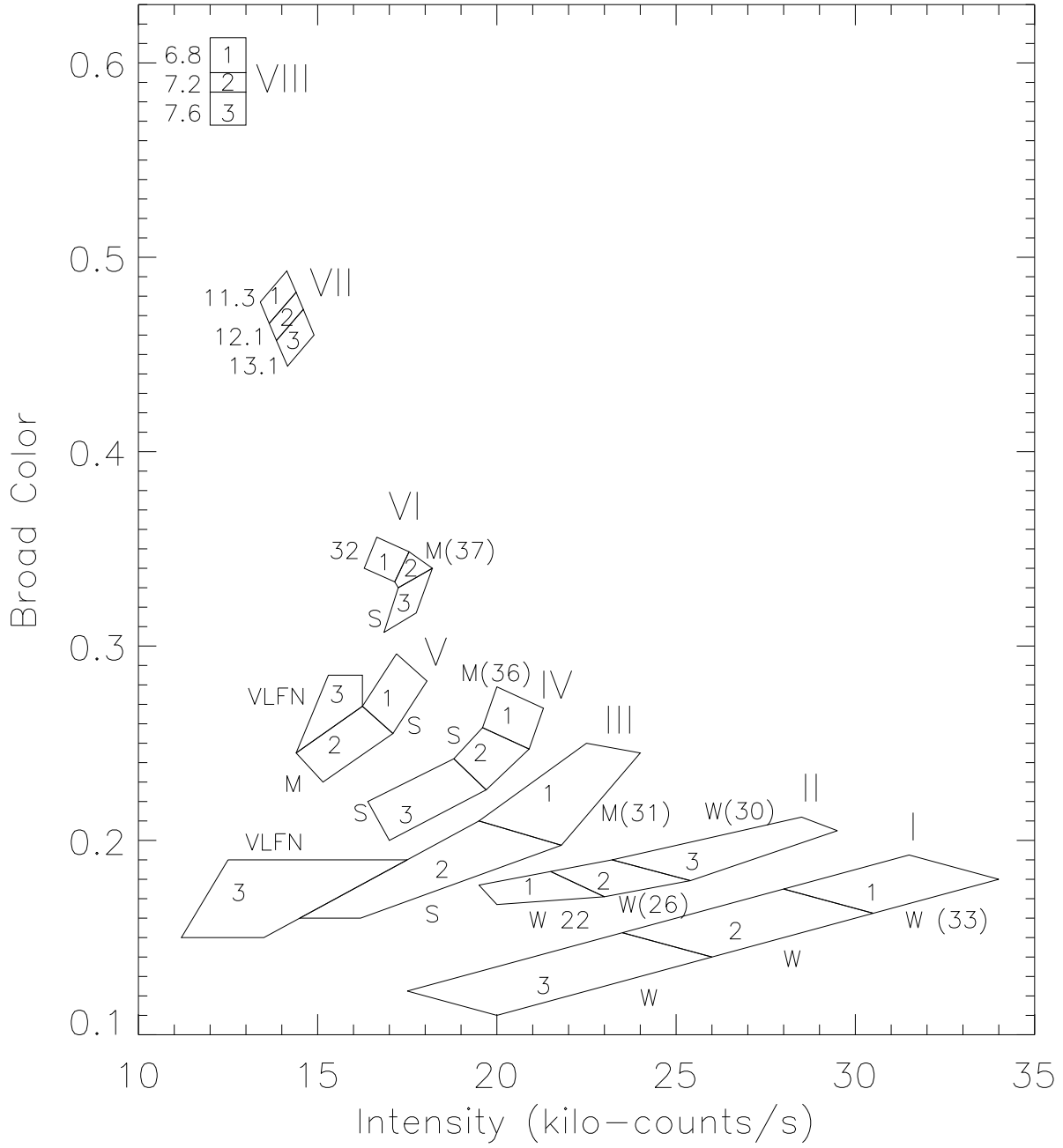


Figure 5-8: Hardness-intensity diagram showing QPO properties for the regions from Figure 5-3b. The frequency of the 6.8 to 32 Hz QPO is labeled (in Hz) beside each region where it is present. Parenthesized frequencies indicate that this component was unpeaked, i.e., a knee. Letters indicate the strength of the broad 4 Hz QPO: S—strong, M—medium, and W—weak or unpeaked.

branch power spectra. The broad high frequency peak in Cir X-1 may be related to the high frequency noise component often observed on the horizontal branch.

The HID track for observation VI shows the narrow QPO at 32 Hz on a roughly horizontal segment (region VI-1) and a knee at 37 Hz on the right end of this segment (region VI-2). The apex of region VI-2 brings a transition to the 4 Hz QPO, which is dominant on the downward branch of this track (region VI-3). This is very similar to the HB/NB transition in Z sources.

When Cir X-1 is in “quiescence” in observations VII and VIII, the “horizontal branch” turns upward and becomes vertical in the HID. For comparison, *RXTE* PCA observations of Cir X-1 from 1996 March 10–19 which show a narrow QPO peak at 1.3–12 Hz [62] (Chapter 4) are almost entirely confined to the 12.3–14.7 kcts/s (2–21 keV) intensity range. The HID tracks for those observations lie along a nearly vertical line, and probably represent sections of the “horizontal” branch.

Observation II may also be on part of the HB, since a weak narrow QPO appears to evolve into a knee and increase in frequency from 22 to 30 Hz as the intensity increases. However, the broad QPO is also weakly visible in PDSs for this observation. The fact that observations II, VI, VII, and VIII all show little variation of the hard color used in Figure 5-3a suggests that observation II may be associated with the other HB observations.

5.4.2 Normal Branch

The 4 Hz QPO is observed when the source intensity rises above the “quiescent” 1-Crab level (~ 13 kcts/s). It is roughly stationary in frequency (3.3–4.3 Hz when clearly peaked) and broader than the HBO. The feature is easily seen in observations III–VI; at these times the location in the HID moves along diagonal tracks. The ~ 4 Hz frequency and motion along diagonal tracks in the HID is consistent with the 4–7 Hz NBOs observed at nearly constant frequency on the NB of typical Z sources [27]. We therefore identify the broad 4 Hz QPO as a normal branch oscillation, and the diagonal tracks for observations III–VI as shifted normal branches.

The broad QPO component may be also present in the highest intensity observations, as a weak feature in observation II and in the form of a break near the 4 Hz QPO frequency in observation I. We also note that at the top of the normal branch (regions I-1, III-1, IV-1, VI-2) a knee above 30 Hz is present in addition to the NBO component.

A similar broad 4 Hz QPO is present in observations from 1996 March 5–6 (Obs. 1 in Table 4.1) made immediately before phase zero of the cycle showing the 1.3–12 Hz narrow QPO.

5.4.3 Flaring Branch

Beyond the left apex of the normal branch a short upturned branch is observed in HID region V-3 and possibly III-3. The PDS for these regions are dominated by very low frequency noise, which is typical for flaring branches, and no QPO peaks are obviously apparent. We note that in the well-established Z sources neither NBOs nor HBOs are present on the flaring branch, except for Sco X-1 and GX 17+2, in which the NBO evolves into a 6–20 Hz QPO (see [78] and references therein).

The left end of the spectral track for observation V bends upward in the HID shown in Figure 5-3b, but bends downward in the CD in Figure 5-3a. This behavior is demonstrated more clearly in Figure 5-9, which shows CDs and HIDs for observations V and VI. When a broad color ($I[6.3\text{--}13\text{ keV}] / I[2.0\text{--}6.3\text{ keV}]$) is used as the ordinate of the diagrams (Figure 5-9a,b), the track for observation V turns upward on the left end. When a harder color ($I[13\text{--}18\text{ keV}] / I[8.5\text{--}13\text{ keV}]$) is used as the ordinate (Figure 5-9c,d), this branch turns downward. The CD and particularly the HID version based on the harder color show the most clear similarity to canonical Z diagrams, with the temporal behavior of observations V and VI being generally consistent with horizontal, normal, and flaring branches. The broad-color HID (Figure 5-9b) shows evidence for a shift of the normal branch that does not show up in the other three diagrams of that figure.

5.4.4 Relation to Other Sources

Our observations reveal spectral branches which shift in the CD and HID as Cir X-1 evolves from a soft, high-intensity state to a hard, lower-intensity state. The ASM light curves and hardness ratios (Figure 5-1) show that this evolution occurs periodically with the 16.55 day cycle, thus suggesting that the CD/HID shifts may also be periodic. Shifts of the “Z” pattern in CDs and HIDs have been observed in the so-called Cyg-like Z sources: Cyg X-2 [35], GX 5-1 [34], and GX 340+0 [33]. However, the shifts do not occur periodically in those sources, nor do they have the magnitude of the shifts observed in Cir X-1.

The flaring branch of Cir X-1 turns upward when a soft or broad color is used on the vertical axis. When a harder color is used, this branch turns downward but then bends to the left. In the Cyg-like Z sources, the flaring branch sometimes turns upward or starts toward higher intensity and then loops back to lower intensity [35, 34, 33, 55]). In some cases, these sources are observed to “dip” while on the flaring branch [34, 55, 84]), with tracks which turn down and then to the left, similar to that of Cir X-1 in Figure 5-9c.

The left end of the horizontal branch in Cir X-1 turns upward and becomes vertical at low intensity (Figure 5-8). On this section of the branch, HBO frequencies are low: 6.8–13 Hz in

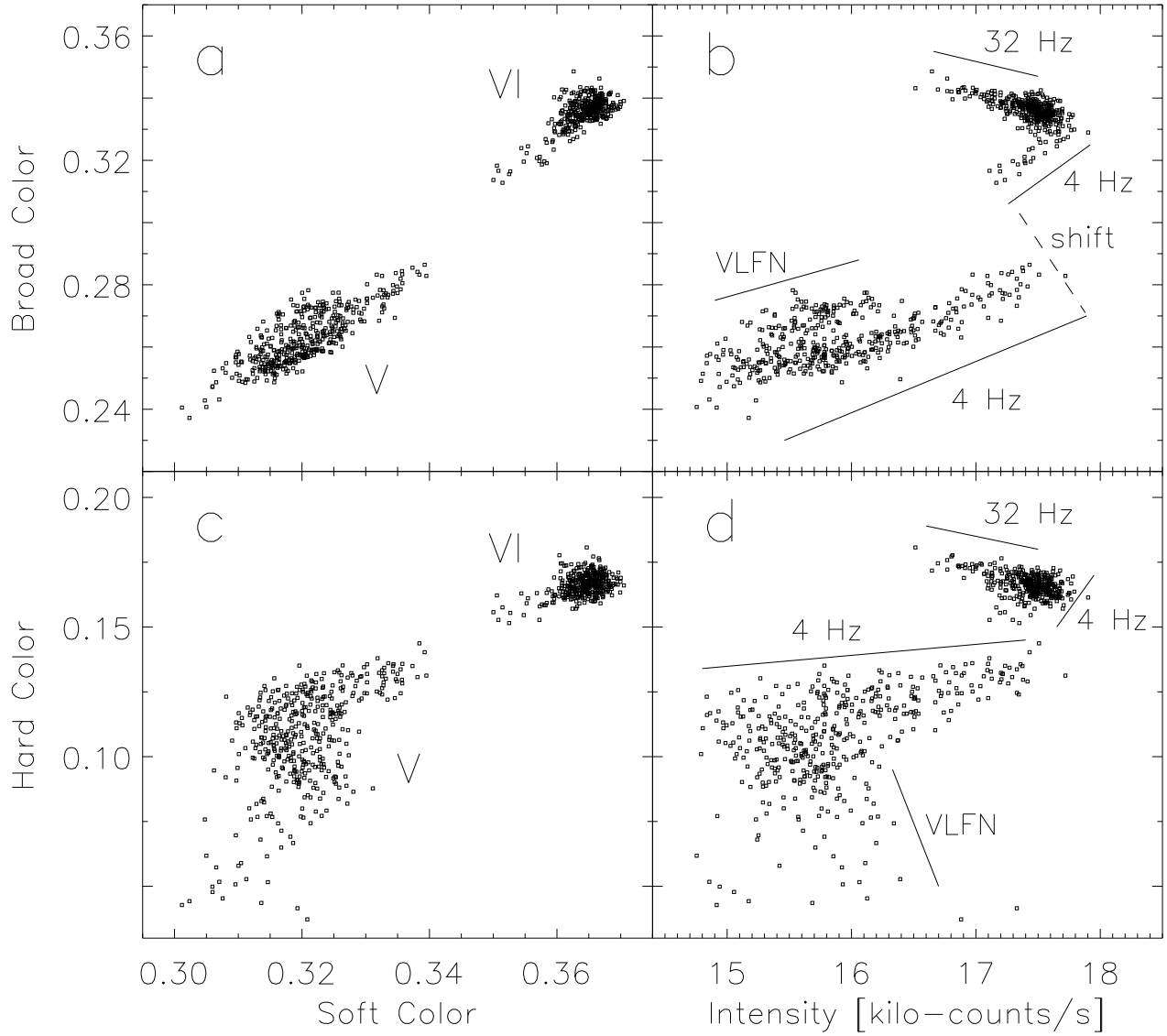


Figure 5-9: Broad-color and hard-color CDs and HIDs for observations V and VI. In all four diagrams, Obs. V is in the lower left and Obs. VI in the upper right. The CD and HID tracks for Obs. V both turn upward at the left end in the broad-color diagrams (a,b) but turn downward in the hard-color diagrams (c,d). In the HIDs, presence of the 32 Hz HBO, 4 Hz NBO, and VLFN is indicated along the branches. An apparent shift of the normal branch between observations V and VI is labeled in (b). The intensity, $I[2.0-18 \text{ keV}]$, is from all five PCUs. The soft color is defined as $I[4.8-6.3 \text{ keV}] / I[2.0-4.8 \text{ keV}]$, the broad color as $I[6.3-13 \text{ keV}] / I[2.0-6.3 \text{ keV}]$, and the hard color as $I[13-18 \text{ keV}] / I[8.5-13 \text{ keV}]$. Each point corresponds to 16 s of background-subtracted data.

observations VII and VIII and 1.3–12 Hz in the earlier 1996 March observations. A similar effect was reported in GX 5-1 [44, 34], in which the HB turns upward at the low-intensity end while HBOs are observed at relatively low frequency (13–17 Hz). Lewin et al. [44] suggested that other Z sources might show such an upward turn of the HB if their intensities and QPO frequencies became sufficiently low. Recent *RXTE* observations of Cyg X-2 [65] show a long vertical extension of the horizontal branch in an HID.

The 5–20 Hz narrow QPO was detected with *EXOSAT* at an intensity similar to the quiescent level observed by *RXTE*. We note that absorption dips are responsible for much of the structure seen in the CD shown for that observation; however, the HIDs show that the narrow QPO occurred on an upturned left end of a horizontally oriented track as in our data (see Figures 2–4, 8, & 10 in [54]). At higher intensity during the same observation, the narrow QPO was not present, and we note that some of the high-intensity PDSs show hints of a broad peak near 4 Hz. We thus conclude that the behavior observed by *EXOSAT* during that observation is related to the Z-like behavior we observe with *RXTE*.

Most of the other *EXOSAT* observations took place when Cir X-1 was significantly lower in intensity than the “quiescent” level of the current observations. The CDs and HIDs for these *EXOSAT* observations did not show tracks which could clearly be identified as Z or atoll. Their power spectra were generally dominated by VLFN, typical of atoll sources in the banana state, and sometimes also showed a broad red noise component resembling atoll high-frequency noise [54]. However, these power-spectral shapes are not unique to atoll sources: power spectra for black hole candidates in the high state are dominated by VLFN, as are those of the current observations on the low-intensity end of the normal branch and on the flaring branch (i.e., regions III-3 and V-3).

Cir X-1 was expected to never show HBOs since atoll-like behavior was taken as evidence that the magnetic field is not strong enough to allow the magnetospheric beat frequency mechanism (MBFM) to operate [77, 54]. (However, it is also possible that the HBOs are not produced by the MBFM.) The results presented here demonstrate both HBOs and NBOs in Cir X-1 and show no evidence for atoll behavior. Since the atoll-like behavior observed with *EXOSAT* occurred at lower intensity than in the present observations, it is possible that they do represent a different state of the source. If Cir X-1 actually can show atoll behavior as well as the Z-like behavior shown here, then we would have new clues to the differences between the two types of sources. Such observations would challenge the hypothesis that differences in both \dot{M} and magnetic field distinguish these two classes.

5.5 Summary

Our results from an analysis of *RXTE* observations of Cir X-1 reveal behavior similar to that of Z sources, and, in particular, allow us to identify temporal and spectral signatures of the horizontal, normal, and flaring branches. The spectral variability of Cir X-1 is seen to correspond to tracks in a HID which are similar in direction to the typical direction in the HID of Z sources in general, but the locations of the tracks corresponding to each branch move from observation to observation in a systematic manner.

To be specific, in the current observations of Cir X-1 the horizontal branch is characterized by the presence of relatively narrow 6.8–32 Hz QPO features in the PDS. The track in the HID of the horizontal branch is horizontal at the high intensity end and becomes vertical at the low intensity end, where the source is “quiescent”, i.e., has an intensity near 1 Crab and is characterized by a relatively low degree of variability on time scales longer than 1 s. The normal branch is characterized by broad 4 Hz QPOs, and by motion in the HID which generally falls along tracks which run diagonally from hard high-intensity locations to soft low-intensity locations. There are also time intervals when the PDS is dominated by very low frequency noise. We identify these intervals as excursions onto the flaring branch.

The large amplitude intensity variations associated with the active/flaring state of Cir X-1 can be divided into three categories: (1) motion across the horizontal portion of the horizontal branch and along the normal and flaring branches, (2) shifts of the spectral branches, and (3) absorption dips. While our *RXTE* observations have allowed us to recognize and distinguish these different types of variability, there is still much to be understood about the physical mechanisms responsible.

Chapter 6

Correlated Timing and Spectral Behavior

6.1 Overview

The eight observations presented in Chapter 5 (study E) were characterized by well-separated spectral tracks in color-color and hardness-intensity diagrams. Based on timing characteristics, the spectral branches were identified with Z-source horizontal, normal, and flaring branches (HB/NB/FB). However, due to the short duration of the observations and the large shifts of the tracks between them, the complete spectral-branch pattern for could only be inferred from fragmented pieces.

Those results indicated that the transition between the quiescent and flaring states of Cir X-1 is at least partially related to motion around the “Z” track. In 1997 June, we carried out an extensive *RXTE* campaign to study in detail the transition to active state, including 7 days of 56% coverage beginning before the phase zero dips (study G, see Figure 3-5). The excellent coverage provided by those observations allowed us to find portions of the transition which clearly demonstrate the full spectral track of Cir X-1. The evolution of the timing characteristics and energy spectrum were studied as a function of position along the track. We found a continuous evolution of the power density spectrum between the different states defined by the spectral branches. We also found that each branch of the spectral track is associated with a specific type of evolution of the energy spectrum (e.g., pivoting about 7 keV in one case and increasing at low energy while remaining constant at high energy in another case). We explored various physical models for the energy spectrum and parameterized the evolution of the spectrum in terms of a two-component model consisting of a multi-temperature “disk blackbody” and a higher-temperature isothermal blackbody.

6.2 1997 June PCA Observations

The PCA light curves and hardness ratios for the 1997 June observations are shown in Figure 6-1. These data show only moderate variability before phase zero until entering a phase of significant dipping during the half day before phase zero. The hardness ratios show that significant spectral evolution (both hardening and softening) occurs during these dips. Similar dip behavior from another set of PCA observations was studied in detail and is presented in Chapter 7.

By phase zero (day 611.5), the main dipping episode ends, and the climb to the flaring state begins. While the intensity increases by more than a factor of three in the lowest energy band (2–4.8 keV), the intensity between 6.3 keV and 13 keV does not climb at all, and above 13 keV the intensity actually decreases by a factor of about 10 over the first 1.5 days following phase zero. This anti-correlation of the low and high-energy intensity during the transition results in decreased hardness ratios after phase zero, as is observed by the ASM (section 2.4). After a relatively smooth transition toward high total intensity during the first day following phase zero, the intensity becomes highly variable (i.e., the “active” or “flaring” state) for the remainder of the observations (about a week).

6.3 Complete Spectral Track

The color-color and hardness-intensity diagrams (CDs/HIDs) for all data in Figure 6-1 are shown in Figure 6-2. These data cover a significant portion (10 d) of an entire 16.55 d cycle. The dips seen in Figure 6-1 appear as prominent light tracks with two sharp bends in the CD (initially toward the right of the main arc-shaped locus) and one sharp bend in the HID ($I < 2.3$ kilocounts/s/PCU). I show in Chapter 7 that tracks with these shapes are indicative of highly variable absorption of a bright spectral component and only moderate, fixed absorption of a fainter component. Having identified absorption dip signatures, I will now focus on non-dip spectral behavior (presumably more directly related to the X-ray source) for the remainder of this chapter.

Most of the data fall along a single arc-shaped locus in the CD and a more complicated curved structure in the HID. This behavior is quite similar to that shown for the eight brief sampling observations from 1997 February–March presented in Chapter 5 (see the CD and HID in Figure 5-3). However, the high-efficiency coverage of the current observations has filled in many of the gaps that occurred between the tracks of the earlier observations.

In order to examine the detailed structure with the overall locus of CD/HID points, the data were divided into shorter time segments (of order hours) and plotted separately in CDs and HIDs. In general, each segment produced a fragmented track or tracks, similar to the 1997 February–March

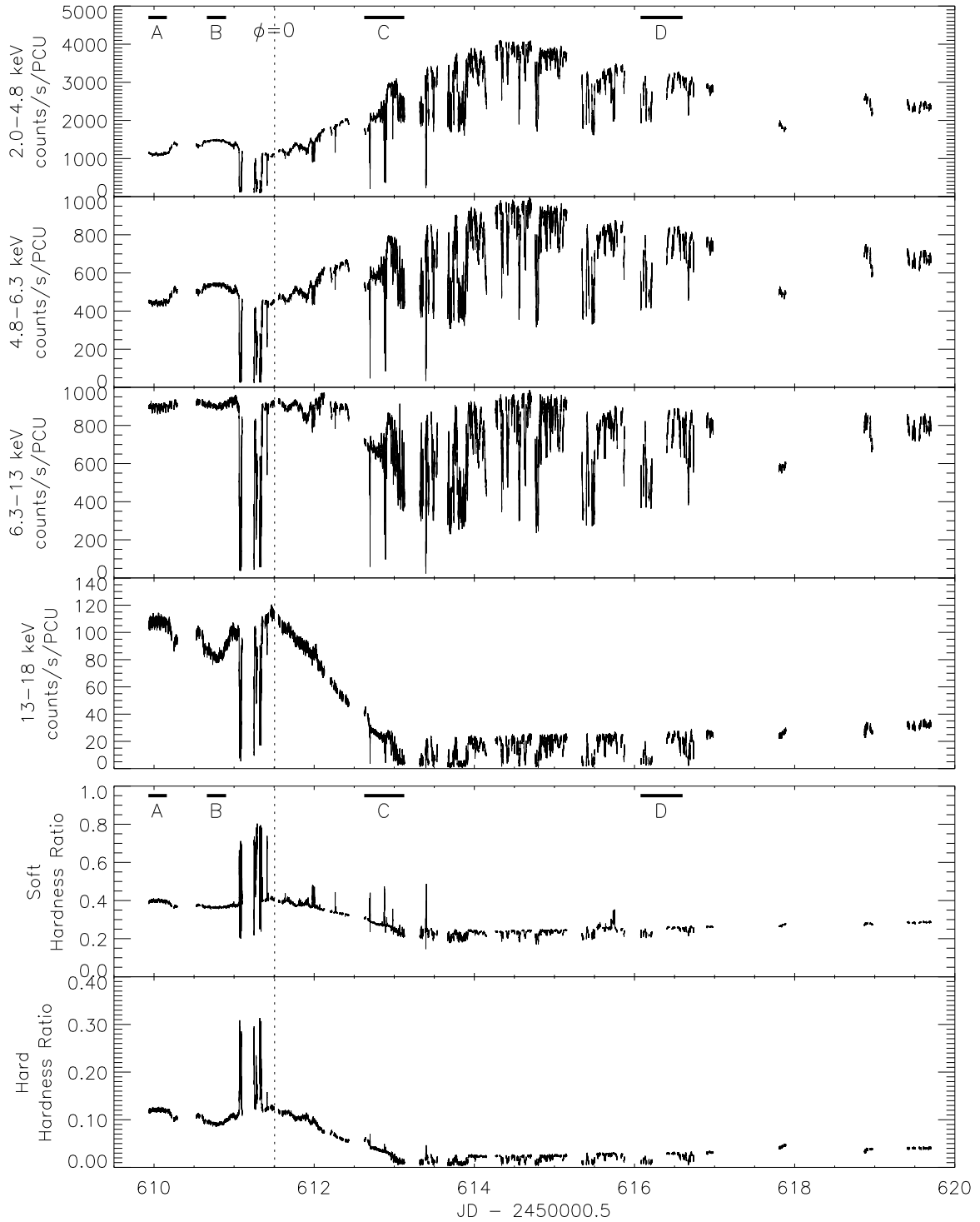


Figure 6-1: Light curves in four energy bands and two hardness ratios for PCA observations of Cir X-1 from 1997 June 10–20, covering a 10-day period around phase zero ($\phi = 0$). The intensities at the beginning of these observations (day 610) are typical “quiescent” levels. Each point represents 16 s of background-subtracted data from PCUs 0, 1, and 2. Ratios of the intensities in the four bands produce soft ($I[4.8\text{--}6.3\text{ keV}] / I[2.0\text{--}4.8\text{ keV}]$) and hard ($I[13\text{--}18\text{ keV}] / I[6.3\text{--}13\text{ keV}]$) hardness ratios. Segments labeled A, B, C & D were used for spectral studies.

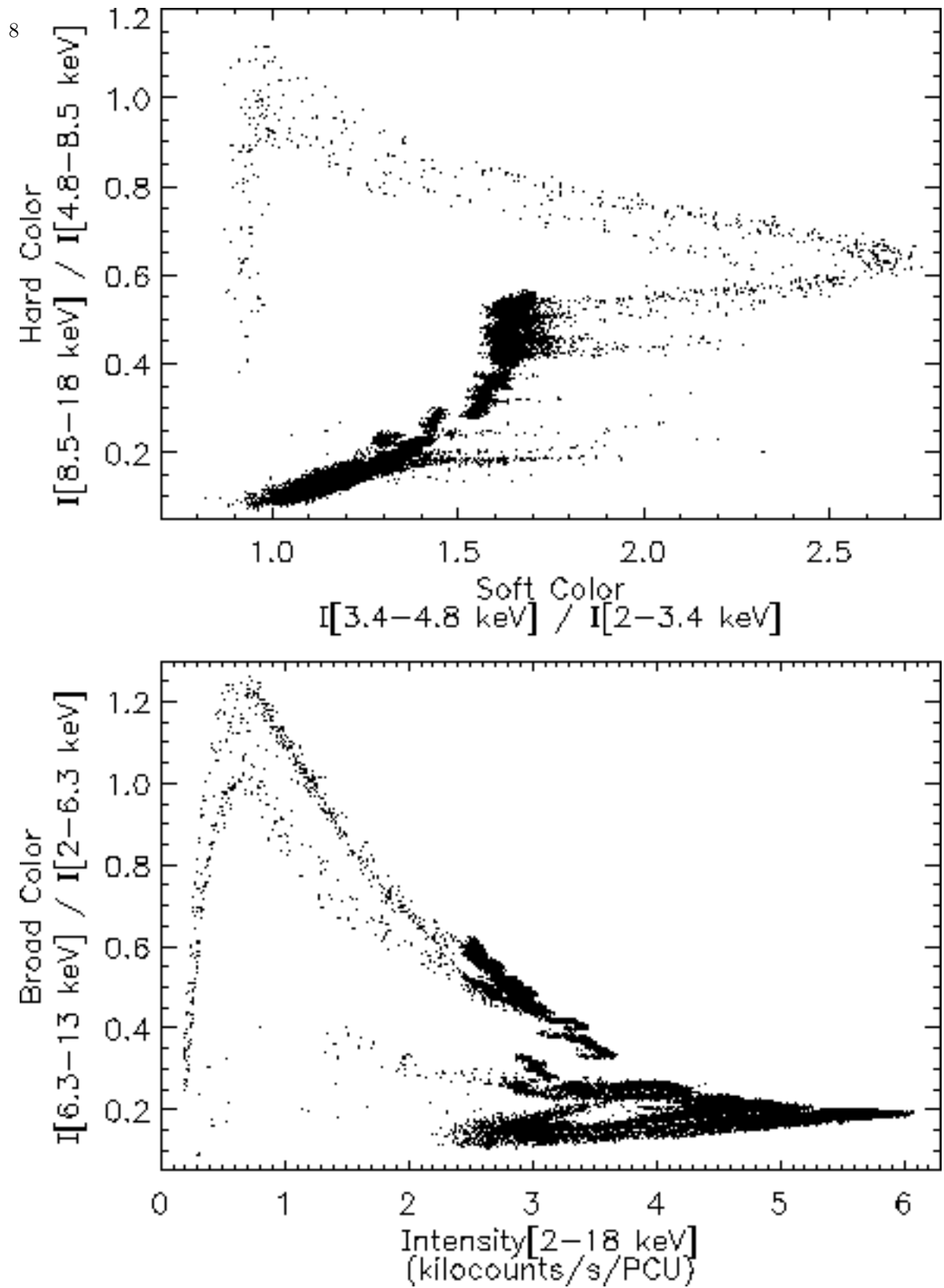


Figure 6-2: Color-color and hardness-intensity diagrams from PCA observations during 1997 June 10-21 (the entire period covered by Figure 6-1). Each point represents 16 s of background-subtracted data from PCUs 0, 1, and 2.

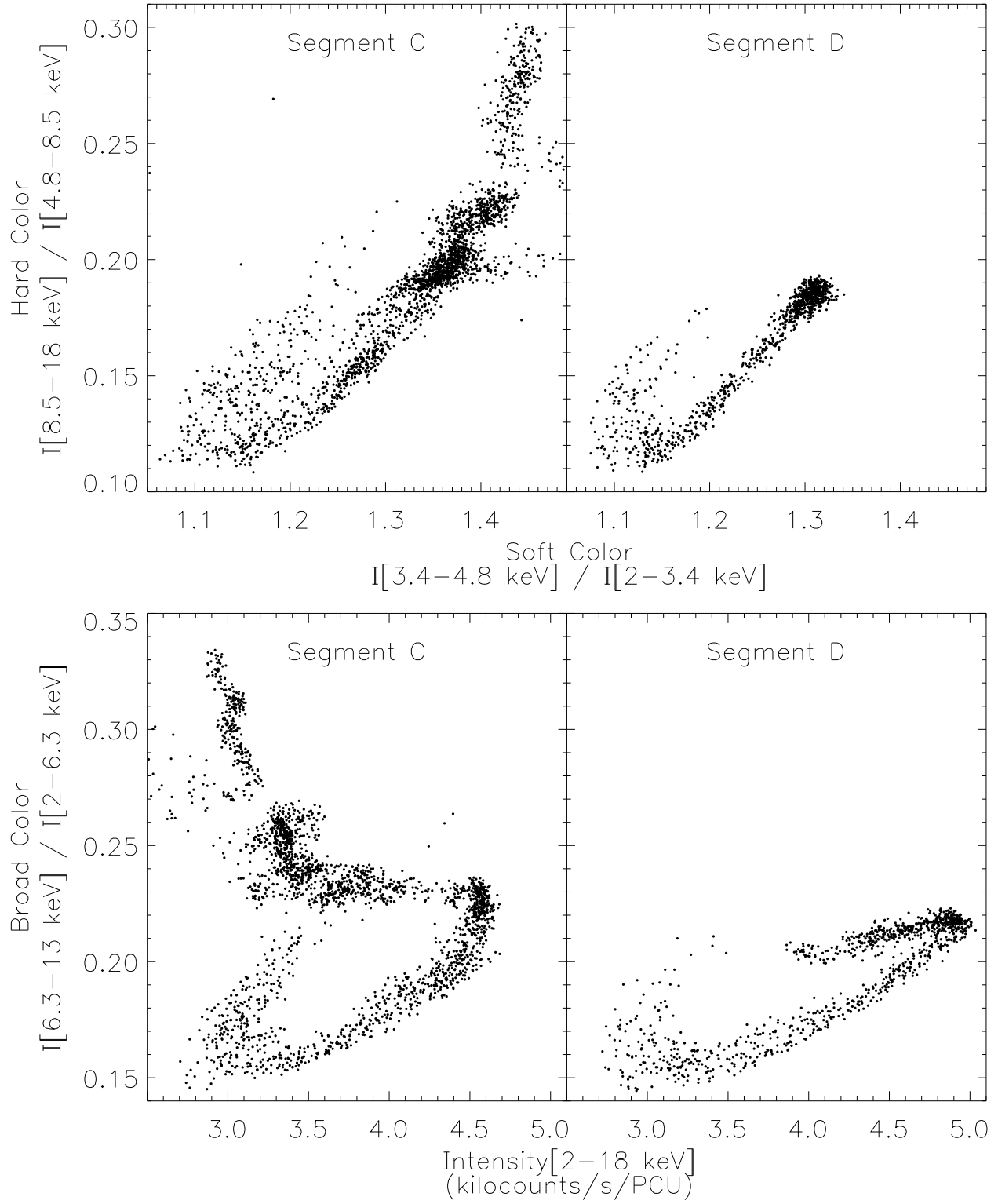


Figure 6-3: Color-color and hardness-intensity diagrams from time segments “C” (left panels) and “D” (right panels) of Figure 6-1 (1997 June 13.625–14.125 and 1997 June 17.075–17.600 respectively). Each point represents 16 s of background-subtracted data from PCUs 0, 1, and 2.

observations. In Figure 6-3, the CDs and HIDs are shown for two time segments (labeled “C” and “D” in Figure 6-1), during which the source traced out a significant portion of several connected branches. These time segments were each about 12 hours in duration and separated by several days. Tracks of other time segments generally each resembled some portion of the entire pattern shown in Figure 6-3, but often with a shifted position in the diagrams.

The location of the tracks for segments C and D in the HID for the total 10 d observation set is such that the “hole” produced by the looped branches is visible between 3 and 4 kilocounts/s/PCU in Figure 6-2. The data from the segment C included some absorption dips, resulting in tracks moving off the right side of the CD and the left side of the HID (and far beyond the limits of the plot in both cases). The HID patterns are consistent with the shape of the full “Z” track as inferred by the fragmented tracks in Chapter 5. For segment C, there is a large upturned left extension of the horizontal branch, the horizontal portion of the HB, the diagonal normal branch, and a flaring branch that turns above rather than below the NB. Similar tracks are also present in the HID for segment D, except there is only a small hint an upward turn at the left end of the HB. The plots for the two segments have the same limits and show a significant shift of the HB and upper NB between the two time segments. The HID for segment D is remarkably similar to that derived from *RXTE* PCA observations of the Z source Cyg X-2 [65]. The Cyg X-2 HID shows a very prominent vertical extension of the HB.

The branches in Figure 6-3 are less well separated in the color-color diagrams, as noted in Chapter 5. However, the flaring branch clearly turns above the normal branch in the current diagrams, and the upturned left extension of HID horizontal branch of segment C appears to also have an increased slope in the CD. The upturned flaring branch is very similar to the flaring branch observed in the color-color diagram for the Z source GX 349+2 in recent *RXTE* PCA observations [90].

Twenty regions along the HID track of time segment C, shown in the lower left panel of Figure 6-3, were selected for further timing and spectral analysis. These regions are shown in Figure 6-4 and labeled with increasing numbers from the left HB, through the NB, to the FB. We will refer to this label as the “rank number” after similar work done by other authors on the standard Z sources; however, the numbers at the various apexes have no special significance. It should also be noted that region 6 does not fit in with the monotonic increase of rank number around the spectral track, and may be an indication of a shifted horizontal portion of the HB.

The light curves, hardness ratio, and HID regions versus time for the data in Figure 6-4 (time segment C) are shown in Figure 6-5. During this half-day segment, the source generally moves toward higher rank number around the spectral track as the observation progresses. Thus, the data have been divided into four sub-segments which predominantly correspond to each portion of the

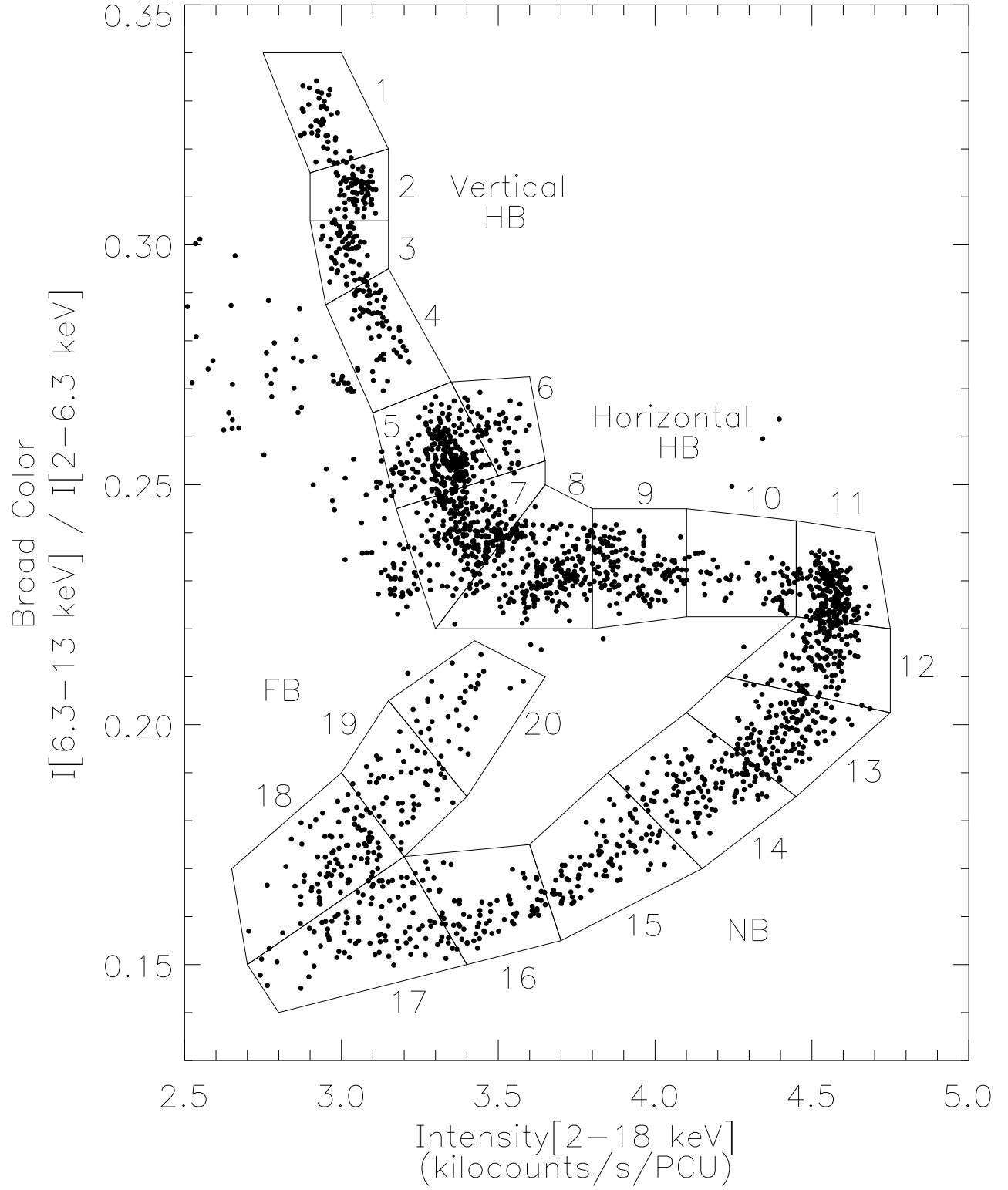


Figure 6-4: Hardness-intensity diagram from time segment C (1997 June 13.625–14.125; day 12.625–13.125). The HID track has been divided into 20 regions from which power density spectra and energy spectra were constructed.

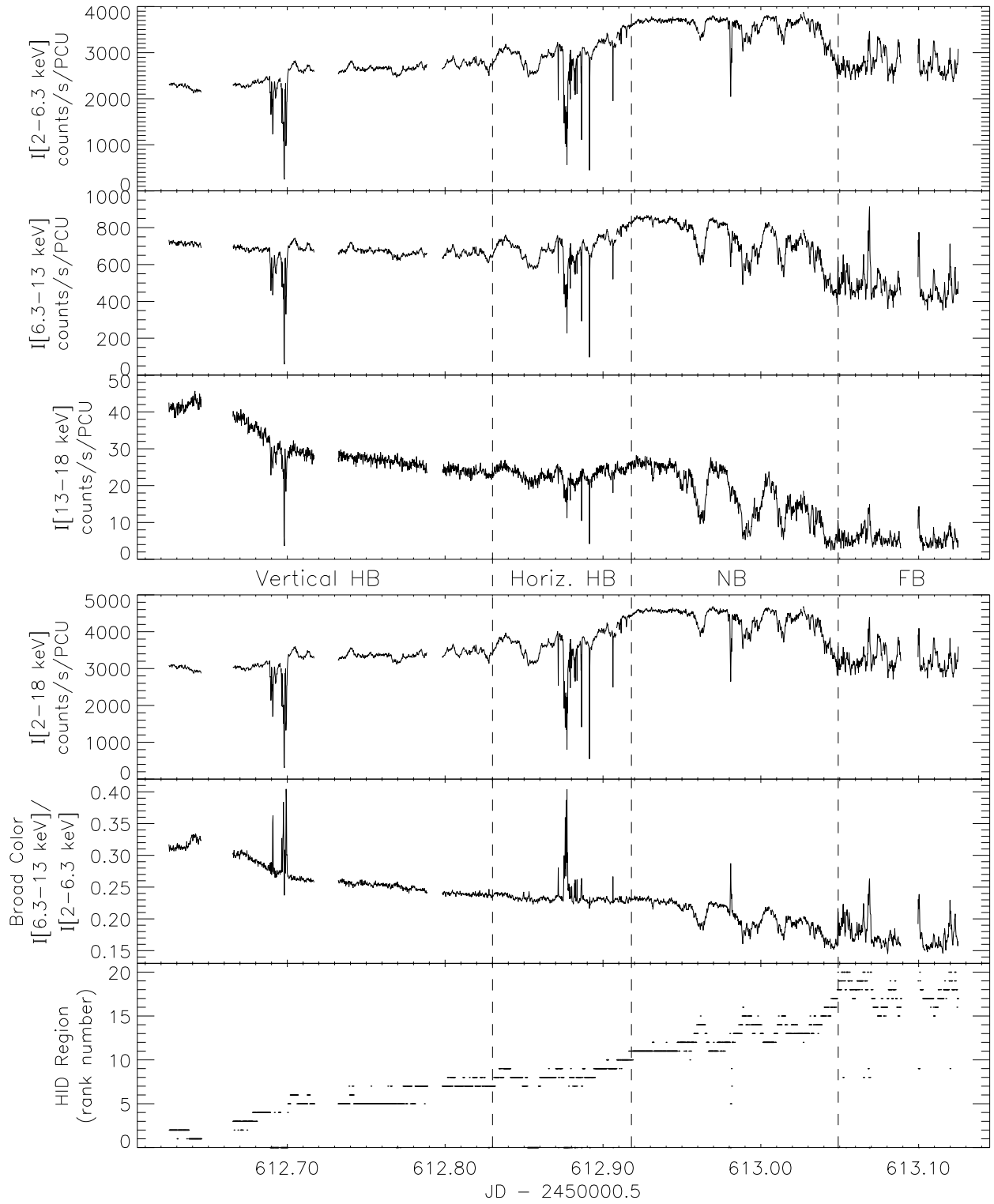


Figure 6-5: Top: light curves in 3 energy channels and bottom: total 2–18 keV light curve, broad color, and HID regions for time segment C (1997 June 13.625–14.125; see Figure 6-1). Based on HID region numbers, the predominant spectral branch is identified for each portion of the data. Absorption dips (omitted from HID regions) are clearly identified by decreased intensity coupled with upward broad-color spikes.

HID track: the horizontal and vertical portions of the HB, the NB, and the FB. Brief absorption dips occur in all but the flaring branch during this particular data set; these are easily identified by sharp intensity dips coupled with a spiked increase in broad color.

The different branches are characterized by the following characteristics, excluding the behavior associated with the dips: The upturned left portion of the HB evolves relatively smoothly, with a slight increase in 2–6.3 keV intensity and a decrease of almost a factor of two in the 13–18 keV band. The horizontal portion of the HB shows a substantial increase in soft intensity and on average shows relatively steady hard intensity. The normal branch shows increased variability; it is bright in the soft bands but shows a decrease in the hard band. The NB/FB transition occurs at lower intensity in all bands compared to most of the NB. The flaring branch itself is then produced by high-variability “mini-flares” or bursts above the NB/FB apex level.

Although the HID regions were defined in Figure 6-4 such that obvious absorption tracks were avoided, one brief dip, on day 612.98, occurred from region 12 on the normal branch and placed a few points artificially across regions 9, 7, and 5. These points are easily identified in Figure 6-5 and are thus not included in subsequent timing and spectral analysis.

Likewise, the highest mini-flares on the flaring branch actually extend beyond region 20 and cross regions 8 and 9. In fact a few such points can even be seen above region 10 in Figure 6-4. The FB points that fell into HB regions can also be clearly identified as points with rank numbers of 8 or 9 in the FB portion of Figure 6-5. These are not included in subsequent timing and spectral analysis.

6.4 Evolution of the Power Density Spectrum

Fourier power density spectra (PDSs) were computed for each 16 s of time segment C (1997 June 13.625–14.125). Each transform used 2^{16} 244- μ s (2^{-12} s) time bins and covered the full 2–32 keV energy range. The expected Poisson level, i.e. the level of white noise due to counting statistics, was estimated taking into account the effects of deadtime [51, 88, 89] and subtracted from each PDS; this method tends to slightly underestimate the actual Poisson level. For each of the 20 HID regions defined in Figure 6-4, an average PDS was calculated from the power spectra corresponding to points in that region. The PDSs were then logarithmically rebinned and are shown in Figure 6-6.

The general features of the power spectra are similar to those observed in previous PCA observations (see Figures 4-3 and 5-4), although here a continuous evolution is observed between each timing state in a single observation. The narrow QPO is observed to evolve from 12–25 Hz moving down the upturned left extension of the HB (regions 1–5 and 7; region 6 may be a shifted version of 8). Across the horizontal portion of the HB (8–11), the narrow QPO remains close to 30 Hz and

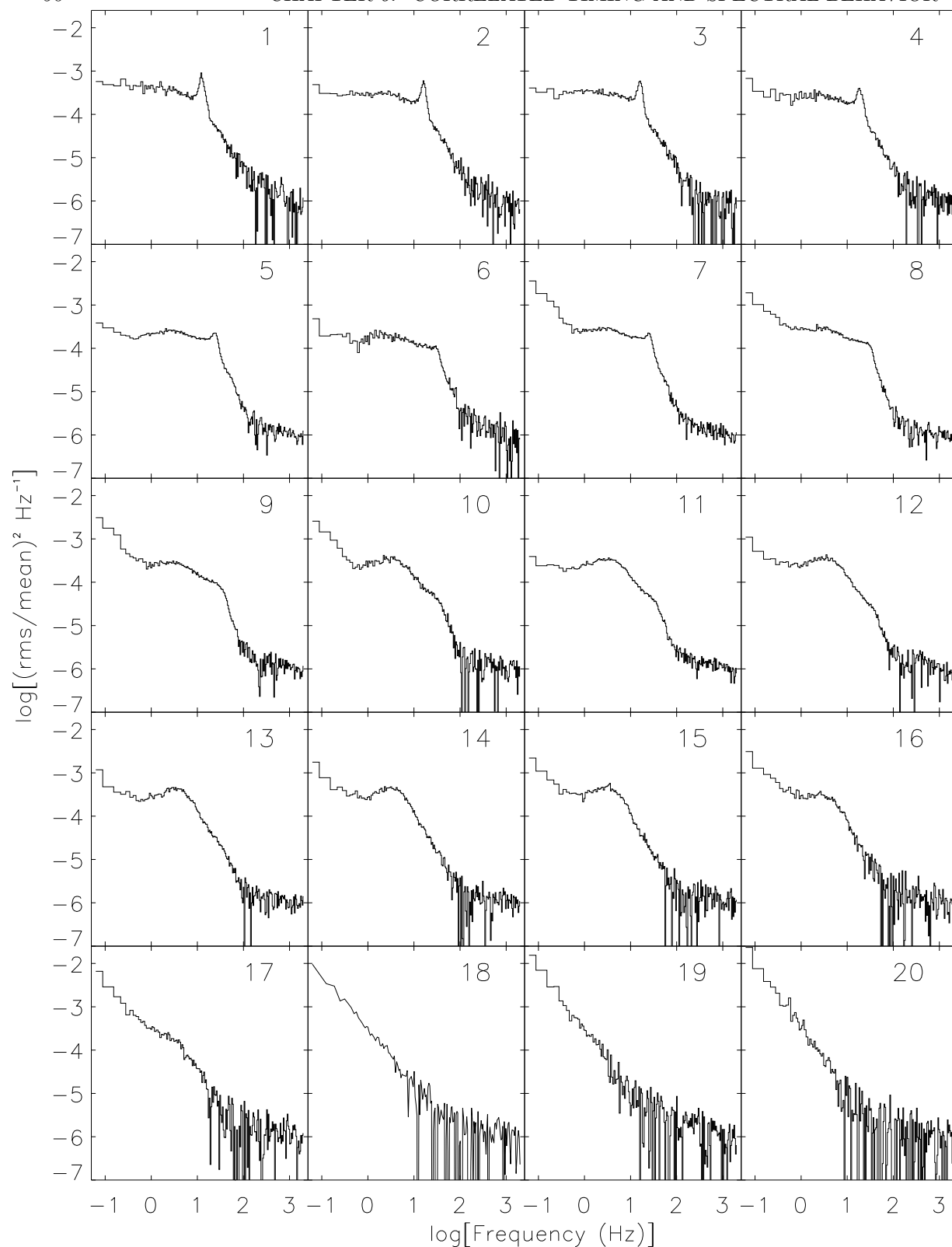


Figure 6-6: Averaged and rebinned power density spectra (2–32 keV) for each of the 20 regions along the HID track in Figure 6-4. The estimated Poisson noise level has been subtracted from each PDS.

fades into a knee, while the broad QPO gradually rises up near 4 Hz. The broad QPO is present all along the normal branch (regions 8–16) but is most prominently peaked in the middle of the branch. On the flaring branch (regions 18–20), no QPOs are present and the power spectrum shows only strong very low frequency noise.

6.5 Evolution of the Energy Spectrum

The Standard2 data mode of the PCA produces 129-channel energy spectra every 16 s. A parallel background file was constructed using the “pcabackest” program provided with the FTOOLS analysis package (version 4.0) and three background model files provided by the PCA instrument team at NASA/GSFC (`pca_bkgd_q6_e03v01.mdl`, `pca_bkgd_xray_e03v02.mdl`, `pca_bkgd_activ_e03v03.mdl`). Average energy spectra (and background spectra) were constructed for each of the 20 HID regions, separately for each of the five PCUs. A 1% systematic error estimate was added to each channel of the spectra to account for calibration uncertainties.

Representative energy spectra for each segment of the HID track are shown in Figure 6-7. They demonstrate how the spectrum evolves along each branch. One spectrum in each panel is included in the next (since it is derived from the intersection of branches), allowing the comparison to be boot-strapped around the entire HID track. The region numbers in the figures are ordered vertically to aid the comparison.

The spectrum is hardest in region 1, at the top of the vertical extension of the horizontal branch. Motion down the branch (softening, regions 1–7) is due to pivoting of the spectrum about ~ 7 keV, i.e., increasing intensity below ~ 7 keV and decreasing intensity above that energy. Motion to the right across the horizontal portion of the HB (regions 8–11) is due to continued increasing low-energy intensity, but with a nearly constant spectrum above 12 keV. The numerator of the hardness ratio ($I[6.3\text{--}13\text{ keV}] / I[2\text{--}6.3\text{ keV}]$) does not extend very far into this band of nearly constant flux and furthermore is dominated by photons with energies at the low end of the 6.3–13 keV band where the intensity increases by a factor more similar to that of the denominator. So, although the 2.5–25 keV spectrum softens significantly (e.g., comparing the intensity at 5 keV to 18 keV), the hardness ratio in Figure 6-7 decreases only slightly from region 7 to region 11.

While moving down the normal branch (regions 11–17), the spectrum decreases across the entire 2.5–25 keV band, but most strongly at high energy (thus further softening). Towards the bottom of the NB, the spectrum begins to show an abrupt steepening in slope above 10 keV. Motion up the FB (regions 18–20) is produced by increasing intensity above ~ 4 keV and a relatively constant spectrum below that energy (thus hardening). The change in slope above 10 keV evolves into a

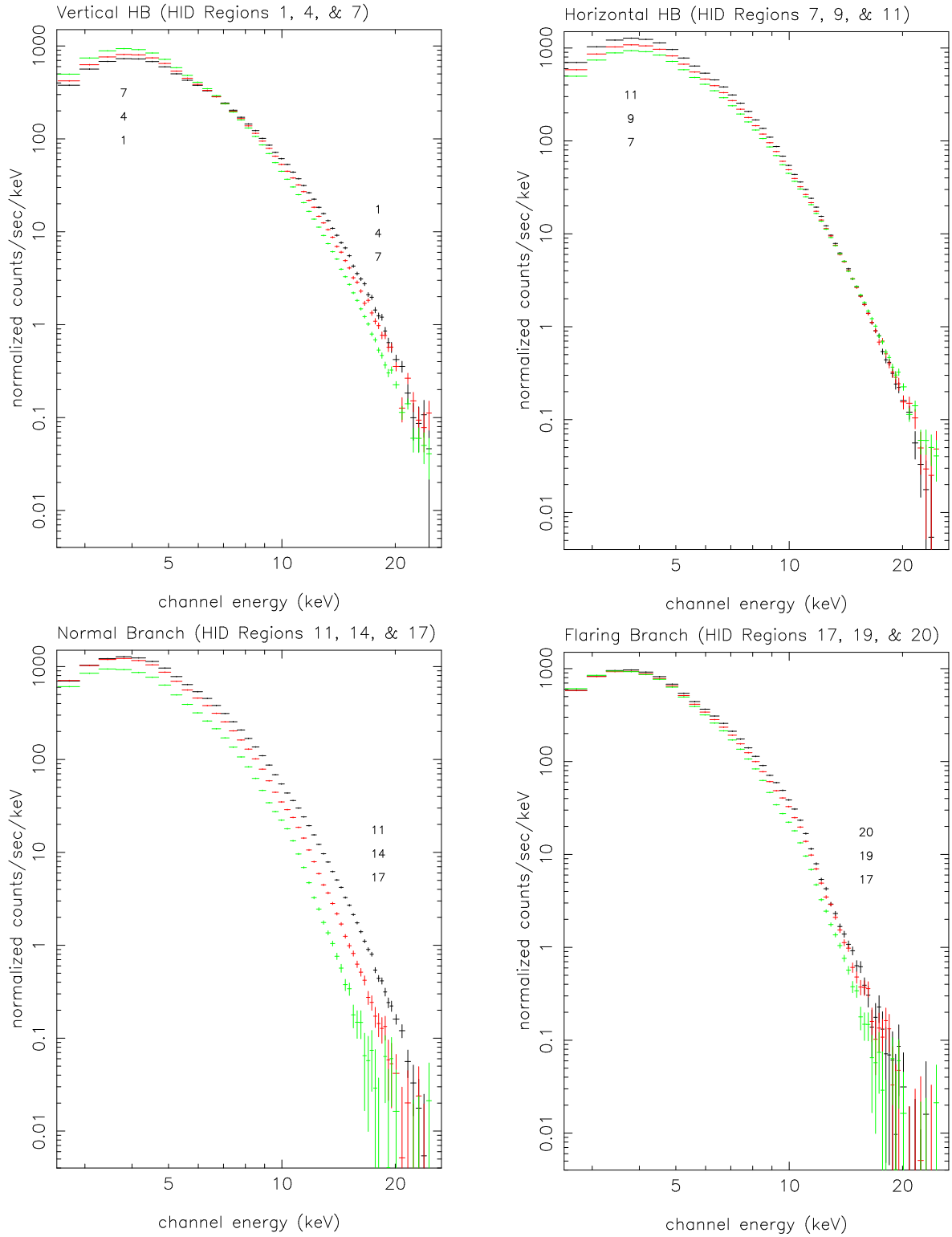


Figure 6-7: Cir X-1 energy spectra (2.5–25 keV; PCU 0 only) for several regions on each segment of the HID track in Figure 6-4. The region numbers within the figures are ordered vertically to match the relative intensities at the low and/or high-energy ends of the spectra.

much more prominent step feature, with structure more complicated than merely a change in slope (see below).

6.6 Selection of Spectral Models

In order to explore possible models for use in fitting the spectra from the HID regions, two high-quality spectra were constructed from long steady segments (17–19 ks) at the beginning of the 1997 June observations (time segments A and B in Figure 6-1, from days 609.93–610.16 and 610.66–610.90 respectively). Based on timing properties measured throughout these data sets, time segment A falls on the vertical portion of the HB (strong narrow QPO at 8.4–11.5 Hz) and time segment B falls near the HB/NB apex (weak narrow QPO above 30 Hz and/or the broad 4 Hz QPO). Variability in both of these segments was limited to less than 10% in all energy bands between 2.5–18 keV. We thus constructed a single (averaged) spectrum for each segment, and we will refer to them as spectrum A and spectrum B. Errors in these spectra are dominated by the 1% systematics at all energies up to ~ 20 keV.

Based on a study of the PCA response matrices using Crab nebula data, R. Remillard has recommended limiting fits to 2.5–25 keV and using only PCUs 0, 1, and 4 (pvt. comm., currently available at <http://lheawww.gsfc.nasa.gov/users/keith/ronr.txt>). Spectra from each of these detectors are fit separately. Fit parameters reported are the average values for PCUs 0, 1, and when possible 4 (see below), and errors are conservatively estimated from the entire range allowed by 90% confidence intervals from each of the detectors. PCU 4 consistently gives lower normalizations for fitted spectral components, so normalizations and flux values from that detector are not included when computing the average values and their errors. Furthermore, spectrum B was not constructed for PCU 4 since that detector was turned off during part of time segment B.

Several single-component models were fit to spectra A and B (all models included an additional component for interstellar absorption). Blackbody and power-law models fit very poorly in both cases, as did a multi-temperature “disk blackbody” spectrum (summed emission from various radii of an accretion disk [49, 46]; model “diskbb” in XSPEC), with reduced χ^2 (χ_r^2) values of 22–545. A thermal bremsstrahlung model (emission due to acceleration of electrons by protons or ions in an optically thin plasma cloud) provided a better fit to spectrum B ($\chi_r^2 = 4.0$), but fit spectrum A poorly ($\chi_r^2 = 34$). A relatively good fit was achieved for both spectra with a modified bremsstrahlung model (see Table 6.1), which includes the self-Comptonization of bremsstrahlung photons to higher energy due to interactions with electrons in an optically thick plasma cloud [38] (model “compLS” in XSPEC).

$N_H/10^{22} \text{ }^1$ (cm^{-2})		Model Components ²			Flux/ 10^{-8} ^3 $\text{erg cm}^{-2} \text{ s}^{-1}$	$\chi_r^2 \text{ }^4$
Self-Comptonized Bremsstrahlung						
		T (keV)	Optical depth	norm		
A	$2.80^{+0.22}_{-0.23}$	$2.78^{+0.04}_{-0.05}$	$11.05^{+0.47}_{-0.36}$	$4.54^{+0.24}_{-0.23}$	$2.73^{+0.02}_{-0.02}$	1.16–1.55
B	$3.94^{+0.18}_{-0.21}$	$2.89^{+0.12}_{-0.11}$	$7.20^{+0.71}_{-0.69}$	$9.67^{+0.37}_{-0.43}$	$3.04^{+0.02}_{-0.02}$	1.51–2.02
Cutoff Power Law ⁵ Blackbody ⁶						
		Photon index	E_{cut} (keV)	norm	T (keV)	R (km)
A	$0.27^{+0.94}_{-0.27}$	$-0.65^{+0.72}_{-0.30}$	$1.73^{+0.58}_{-0.24}$	$2.24^{+1.53}_{-0.47}$	$2.44^{+0.10}_{-0.05}$	$4.40^{+0.34}_{-0.87}$
B	$1.95^{+0.74}_{-0.86}$	$-0.34^{+0.46}_{-0.60}$	$1.67^{+0.31}_{-0.27}$	$5.97^{+2.70}_{-2.29}$	$2.29^{+0.09}_{-0.07}$	$4.61^{+0.67}_{-0.73}$
Blackbody ⁶ Blackbody ⁶						
		T (keV)	R (km)	T (keV)	R (km)	
A	$0.00^{+0.02}_{-0.00}$	$1.16^{+0.02}_{-0.02}$	$24.13^{+0.38}_{-0.37}$	$2.33^{+0.02}_{-0.03}$	$5.38^{+0.16}_{-0.15}$	$2.72^{+0.02}_{-0.02}$
B	$0.01^{+0.21}_{-0.01}$	$1.12^{+0.01}_{-0.02}$	$30.46^{+0.92}_{-0.40}$	$2.20^{+0.03}_{-0.03}$	$5.59^{+0.27}_{-0.25}$	$3.04^{+0.02}_{-0.02}$
Disk Blackbody ⁷ Blackbody ⁶						
		T_{in} (keV)	$R_{in} \cos^{1/2} \theta$ (km)	T (keV)	R (km)	
A	$1.44^{+0.26}_{-0.27}$	$1.81^{+0.08}_{-0.06}$	$9.39^{+0.64}_{-0.64}$	$2.47^{+0.04}_{-0.04}$	$4.10^{+0.25}_{-0.25}$	$2.73^{+0.02}_{-0.02}$
B	$2.49^{+0.23}_{-0.23}$	$1.54^{+0.04}_{-0.04}$	$15.63^{+0.93}_{-0.84}$	$2.28^{+0.05}_{-0.05}$	$4.66^{+0.37}_{-0.37}$	$3.04^{+0.02}_{-0.02}$

Table 6.1: Fit parameters for spectra A & B for four models.

A number of two-component models were also fit to these two spectra. A model using a disk blackbody and power law did not fit well ($\chi_r^2=3-5$), mainly because the spectrum does not flatten to a single slope at high energy. A hard (high-temperature, $\gtrsim 2$ keV) blackbody is often used to fit the spectra of LMXBs thought to contain a neutron star, where emission near the surface might produce a high-temperature blackbody with small effective area. A power law with high-energy exponential cutoff plus a hard blackbody fit well (see Table 6.1) but parameters for the cutoff power law were poorly constrained since the cutoff energy ($E_{cut} \approx 1.7$ keV) was below the PCA bandpass.

Two blackbodies (~ 1.1 keV and ~ 2.2 keV) fit moderately well (see Table 6.1), but required negligible interstellar absorption. The low absorption is inconsistent with previous measurements from *ASCA* and *ROSAT* (both sensitive below 2 keV where the absorption is most easily constrained) which estimated the interstellar column density to be $N_H = (1.8-2.4) \times 10^{22}$ cm⁻² [12, 56].

¹Absorption column density (Hydrogen atoms per cm²).²Errors quoted are 90% confidence limits for a single parameter ($\Delta\chi^2 = 2.7$).³Total 2.5–25 keV flux.⁴Reduced $\chi^2 = \chi^2/dof$, where dof = degrees of freedom = the number of spectral bins (52–54/spectrum) minus the number of fit parameters (4–6).⁵High-energy exponential cut-off.⁶Blackbody radius assumes a distance of 8 kpc.⁷For the disk blackbody, the inner radius of the accretion disk (times $\cos^{1/2} \theta$, where θ is the disk inclination angle and $\theta = 0$ is parallel to the line of sight) is given for a distance of 8 kpc.

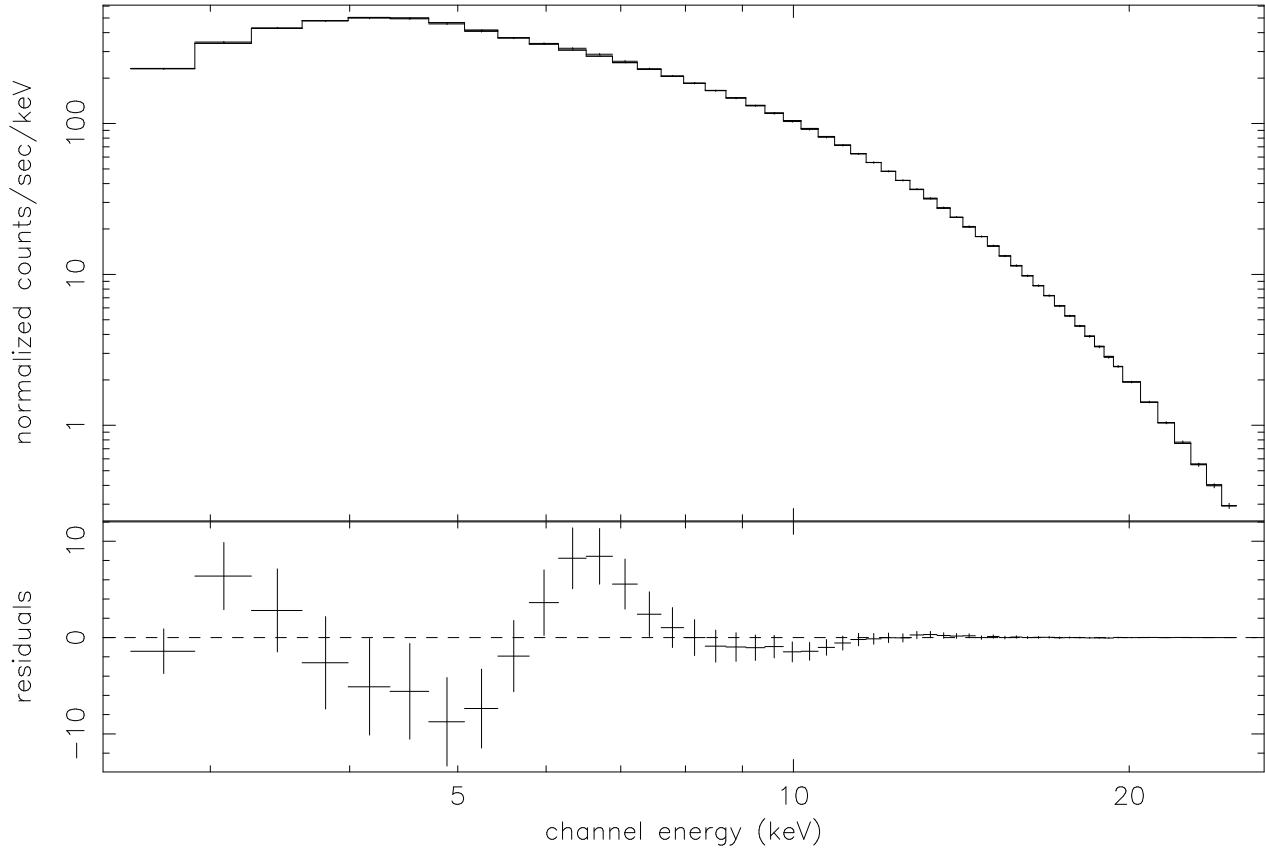


Figure 6-8: Spectrum A and model (histogram) consisting of a disk blackbody and blackbody (see Table 6.1). The residuals show a peak at 6–7 keV that may be due to an iron emission line.

A soft disk blackbody, with temperatures at the inner edge of the disk of 1.5–1.8 keV, plus the hard blackbody fit both spectra quite well (see Table 6.1). This gave absorption column densities roughly consistent with the *ASCA* and *ROSAT* values. Other two-component models could also produce similar fits to those describe above. Thus, the spectrum cannot be uniquely deconvolved into separate components. However, for purposes of fitting the HID regions, the model composed of a disk blackbody and blackbody was used. This model is physically motivated (a component from an accretion disk and a harder component from near the surface of a neutron star) and provides good fits with interstellar column densities roughly consistent with previously measured values.

The spectral fit for spectrum A for a disk blackbody plus blackbody is shown in Figure 6-8. This plot illustrates the good fit of the model over the entire 2.5–25 keV band. Peaked residuals at 6–7 keV suggest the presence of an emission line, probably iron $K\alpha$. Very similar residuals appear in most of the fits discussed above for both spectra A and B. Addition of a Gaussian line to the models does in fact improve the fits in almost all cases; however, the best-fitting line often has an extremely

large Gaussian width ($\sigma > 1$ keV). The energy resolution of the PCA is about 1 keV FWHM at 6 keV; thus it is difficult to place reliable constraints on the parameters (such as centroid and width) of a narrow component such as an emission line. We have not included an emission line in the fits reported in Table 6.1. The presence of an emission line near 6.4 keV is discussed in more detail in Chapter 7 in conjunction with spectra of absorption dips, which show the line more prominently.

6.7 Fits to Spectra from 20 HID Regions

A disk blackbody plus blackbody was fit to the spectra from each of the 20 HID regions. The resulting fit parameters are listed in Table 6.2, and several representative fits are shown in Figures 6-9 and 6-10. We estimated the distance to Cir X-1 to be 8 kpc (see section 1.3) in converting blackbody and disk blackbody normalizations to radii.

The spectra along the horizontal branch (regions 1–11) were all fit relatively well, with residuals similar to those for spectra A and B above, suggesting a possible emission line from iron. These spectra all show column densities of $1.8\text{--}2.3 \times 10^{22} \text{ cm}^{-2}$, consistent with the *ASCA* and *ROSAT* values discussed above. The temperatures of both components (~ 1.3 keV for the inner disk and ~ 2.0 keV for the hard blackbody) are quite stable on the HB, with only slight evidence for cooling down the vertical portion of the branch (i.e., higher temperatures in regions 1–4). The pivoting spectrum on the vertical portion of the HB may be related to these temperature changes. The inner radius of the disk blackbody component (times a factor of order unity involving the inclination angle of the disk) increases from 19 to 33 km, while the radius of hard blackbody remains between 3 and 4 km. Thus, it is mainly changes in the (soft) disk blackbody radius that produce the HB track. These size scales are consistent with the hypothesis that these components arise from emission close to a neutron star, which has a radius of order 10 km. From region 1 to 11, the total 2.5–25 keV flux increases monotonically (with the exception of region 6) from $2.89\text{--}4.35 \times 10^{-8} \text{ erg cm}^{-2} \text{ s}^{-1}$ (corresponding to 1.2–1.8 times the Eddington luminosity limit for a $1.4 M_{\odot}$ neutron star at 8 kpc).

Moving down the normal branch, the quality of the fits decrease, as indicated by the increasing χ^2 values in Table 6.2. The absorption column density gradually decreases by a factor of two, but may be related to the decreasing fit quality. The inner radius and temperature of the disk blackbody change only slightly on the normal branch. In contrast, the hard blackbody begins to fade on the upper portion of the normal branch (regions 12–14), as indicated by a decreasing radius for the emission area. In fact, by the middle of the normal branch, the hard blackbody has faded entirely and fits have lower χ^2 values without it. Thus, the hard blackbody is omitted from the fits for regions 15–20. The 2.5–6 keV residuals continue to appear similar to those on the HB, but the

HID ¹ region	$N_H/10^{22}$ ² (cm ⁻²)	T_{in} (keV)	$R_{in} \cos^{1/2} \theta$ ³ (km)	T (keV)	R ⁴ (km)	Flux/ 10^{-8} ⁵ erg cm ⁻² s ⁻¹	χ_r^2 ⁶
1	$1.83^{+0.28}_{-0.32}$	$1.45^{+0.05}_{-0.05}$	$19.29^{+1.31}_{-1.22}$	$2.16^{+0.09}_{-0.07}$	$3.65^{+0.50}_{-0.52}$	$2.89^{+0.03}_{-0.02}$	1.41–2.14
2	$1.97^{+0.30}_{-0.28}$	$1.41^{+0.04}_{-0.05}$	$20.87^{+1.46}_{-1.29}$	$2.15^{+0.09}_{-0.10}$	$3.71^{+0.68}_{-0.64}$	$2.99^{+0.02}_{-0.02}$	1.40–1.70
3	$2.04^{+0.27}_{-0.35}$	$1.38^{+0.04}_{-0.04}$	$22.24^{+1.30}_{-1.16}$	$2.08^{+0.09}_{-0.08}$	$4.00^{+0.56}_{-0.52}$	$2.96^{+0.02}_{-0.02}$	1.32–1.81
4	$2.18^{+0.37}_{-0.32}$	$1.36^{+0.05}_{-0.06}$	$23.46^{+2.27}_{-1.85}$	$2.07^{+0.18}_{-0.17}$	$3.89^{+1.27}_{-1.18}$	$3.02^{+0.03}_{-0.02}$	2.21–3.47
5	$2.29^{+0.33}_{-0.27}$	$1.31^{+0.03}_{-0.05}$	$27.22^{+1.97}_{-1.74}$	$2.02^{+0.11}_{-0.14}$	$3.78^{+0.97}_{-0.94}$	$3.21^{+0.02}_{-0.02}$	2.51–3.24
6	$2.35^{+0.30}_{-0.24}$	$1.34^{+0.03}_{-0.04}$	$26.21^{+1.33}_{-1.19}$	$2.02^{+0.11}_{-0.13}$	$3.31^{+0.58}_{-0.53}$	$3.37^{+0.02}_{-0.02}$	1.41–1.55
7	$2.31^{+0.24}_{-0.25}$	$1.30^{+0.02}_{-0.03}$	$28.67^{+1.20}_{-1.05}$	$2.03^{+0.09}_{-0.11}$	$3.30^{+0.65}_{-0.57}$	$3.27^{+0.02}_{-0.02}$	2.22–2.76
8	$2.27^{+0.29}_{-0.25}$	$1.29^{+0.02}_{-0.03}$	$30.06^{+1.70}_{-1.48}$	$2.01^{+0.12}_{-0.14}$	$3.34^{+0.91}_{-0.83}$	$3.46^{+0.03}_{-0.02}$	2.41–2.70
9	$2.18^{+0.21}_{-0.24}$	$1.30^{+0.03}_{-0.03}$	$30.68^{+1.15}_{-1.07}$	$2.01^{+0.14}_{-0.14}$	$3.36^{+0.85}_{-0.69}$	$3.75^{+0.02}_{-0.02}$	2.29–2.44
10	$2.01^{+0.23}_{-0.24}$	$1.31^{+0.02}_{-0.03}$	$31.35^{+1.31}_{-1.10}$	$2.01^{+0.12}_{-0.11}$	$3.02^{+0.86}_{-0.67}$	$4.15^{+0.02}_{-0.03}$	1.82–2.56
11	$1.98^{+0.19}_{-0.22}$	$1.30^{+0.02}_{-0.02}$	$32.90^{+1.24}_{-1.17}$	$1.93^{+0.08}_{-0.08}$	$3.52^{+0.67}_{-0.54}$	$4.39^{+0.03}_{-0.03}$	2.55–3.05
12	$1.78^{+0.22}_{-0.21}$	$1.29^{+0.02}_{-0.02}$	$33.41^{+1.51}_{-1.34}$	$1.94^{+0.17}_{-0.12}$	$3.09^{+0.82}_{-0.72}$	$4.35^{+0.03}_{-0.03}$	2.87–3.06
13	$1.63^{+0.21}_{-0.25}$	$1.28^{+0.02}_{-0.02}$	$34.02^{+1.09}_{-0.92}$	$2.12^{+0.22}_{-0.19}$	$1.51^{+0.70}_{-0.47}$	$4.21^{+0.03}_{-0.03}$	3.74–4.66
14	$1.53^{+0.18}_{-0.17}$	$1.26^{+0.01}_{-0.02}$	$33.94^{+1.28}_{-1.06}$	$2.34^{+0.53}_{-0.40}$	$0.84^{+0.77}_{-0.46}$	$3.98^{+0.03}_{-0.03}$	4.19–5.11
15	$1.48^{+0.15}_{-0.16}$	$1.22^{+0.00}_{-0.00}$	$35.30^{+0.51}_{-0.49}$			$3.68^{+0.02}_{-0.02}$	5.15–6.34
16	$1.43^{+0.19}_{-0.17}$	$1.19^{+0.00}_{-0.00}$	$35.88^{+0.50}_{-0.48}$			$3.32^{+0.02}_{-0.02}$	5.91–7.52
17	$0.94^{+0.17}_{-0.15}$	$1.20^{+0.00}_{-0.00}$	$32.69^{+0.23}_{-0.53}$			$3.00^{+0.02}_{-0.01}$	5.87–7.16
18	$0.56^{+0.16}_{-0.18}$	$1.26^{+0.01}_{-0.01}$	$28.22^{+0.49}_{-0.48}$			$2.94^{+0.02}_{-0.02}$	9.59–11.39
19	$0.64^{+0.17}_{-0.16}$	$1.29^{+0.01}_{-0.01}$	$27.02^{+0.35}_{-0.36}$			$3.08^{+0.02}_{-0.02}$	9.36–10.45
20	$0.81^{+0.15}_{-0.19}$	$1.33^{+0.01}_{-0.01}$	$26.25^{+0.38}_{-0.37}$			$3.24^{+0.02}_{-0.02}$	14.67–17.01

Table 6.2: Fit parameters for HID regions 1–20 using a model consisting of a disk blackbody and a blackbody.

peaked ~ 6.5 keV residual on the left HB becomes broader and more complicated for higher rank numbers.

On the flaring branch (regions 18–20), the fit quality decreases further, accompanied by very low values for the absorption column density. A significant contribution to the high χ^2 values on the flaring branch is due to the feature above 10 keV that was mentioned above in section 6.5. This feature actually begins to develop on the lower NB, as early as region 14 and is illustrated by two spectra shown Figure 6-11. The residuals shown for each bin have been divided by the size of the error bar for that bin. The feature resembles a narrow line or absorption edge but its location above 10 keV rules out even hydrogen-like iron as a possible source.

A number of other spectral models were fit to the HID-region spectra, and all failed to satis-

¹ Errors quoted are 90% confidence limits for a single parameter ($\Delta\chi^2 = 2.7$).

² Absorption column density (Hydrogen atoms per cm²).

³ Inner radius of the accretion disk (times $\cos^{1/2} \theta$, where θ is the disk inclination angle and $\theta = 0$ is parallel to the line of sight) assuming a distance of 8 kpc.

⁴ Blackbody radius assuming a distance of 8 kpc.

⁵ Total 2.5–25 keV flux.

⁶ Reduced $\chi^2 = \chi^2/dof$, where dof = degrees of freedom = the number of spectral bins (52–54/spectrum) minus the number of fit parameters (4–6).

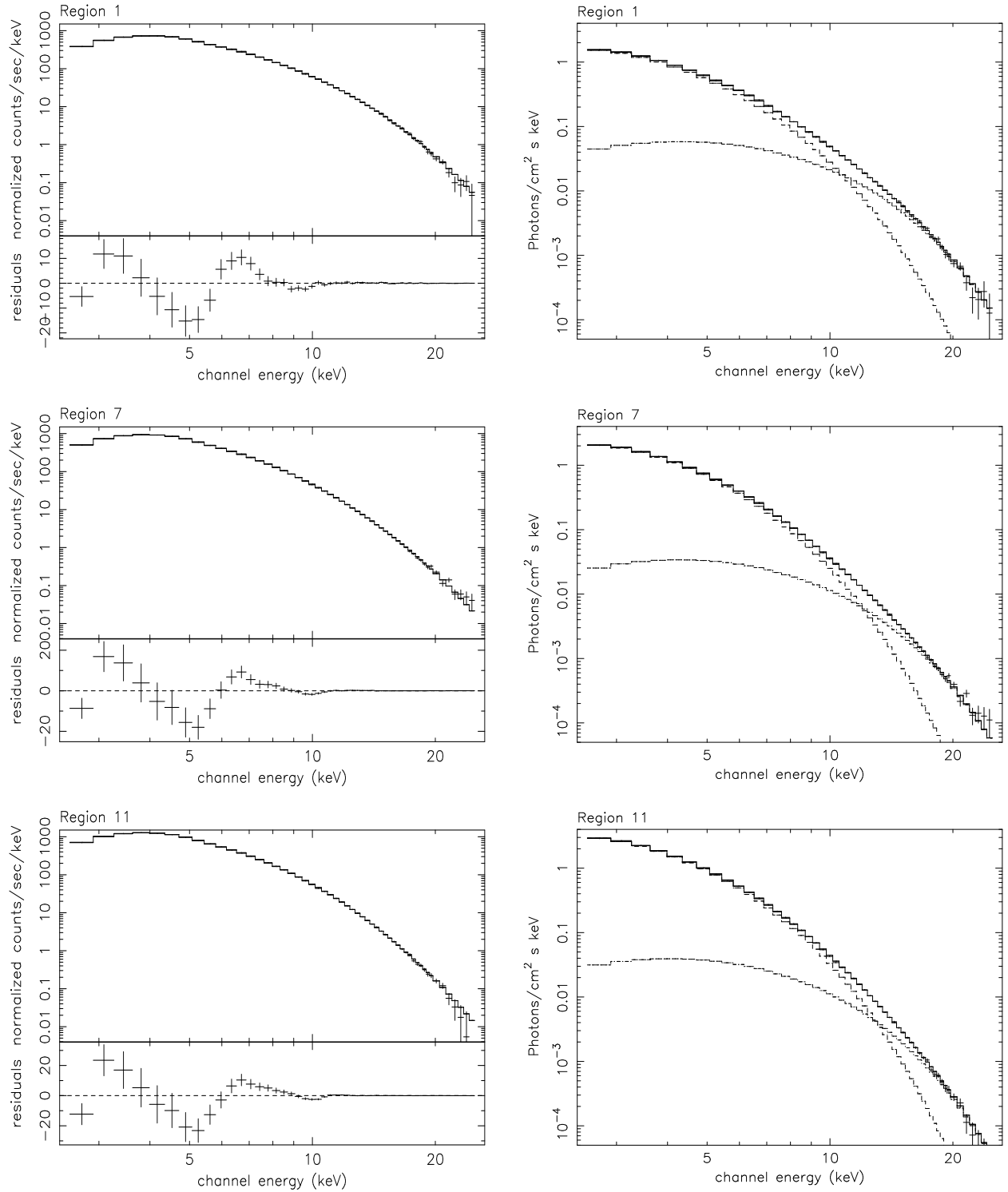


Figure 6-9: Fitted energy spectra (2.5–25 keV; PCU 0 only) and model components (disk blackbody and blackbody) for HID regions 1, 7, and 11 of Figure 6-4. The disk blackbody dominates at low energy and the blackbody dominates at high energy. Fit parameters are listed in Table 6.2.

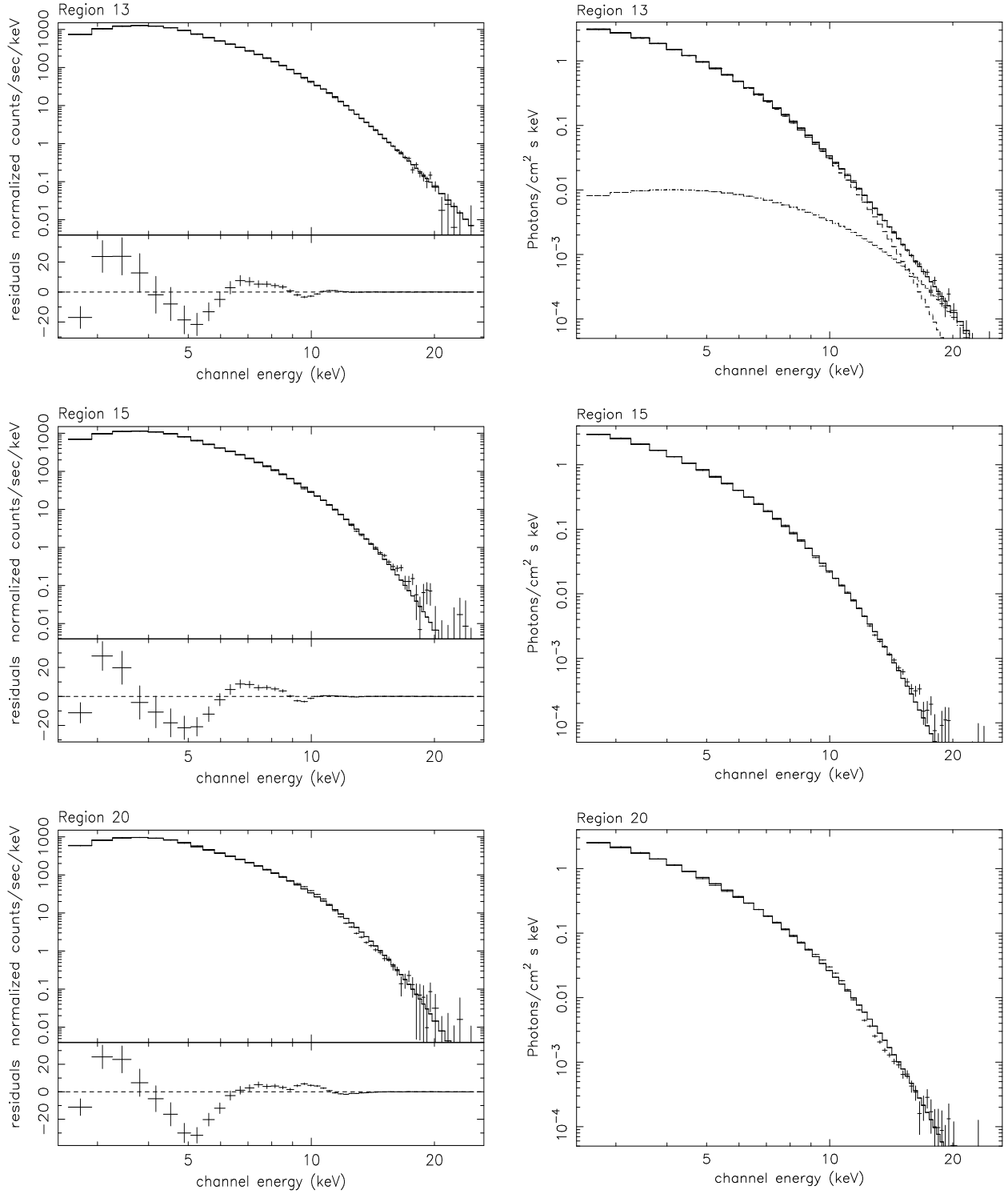


Figure 6-10: Fitted energy spectra (2.5–25 keV; PCU 0 only) and model components (disk blackbody and blackbody) for HID regions 13, 15, and 20 of Figure 6-4. The blackbody only contributes to the high-energy end of the spectrum in region 13, and has faded away entirely in regions 15 and 20. Fit parameters are listed in Table 6.2.

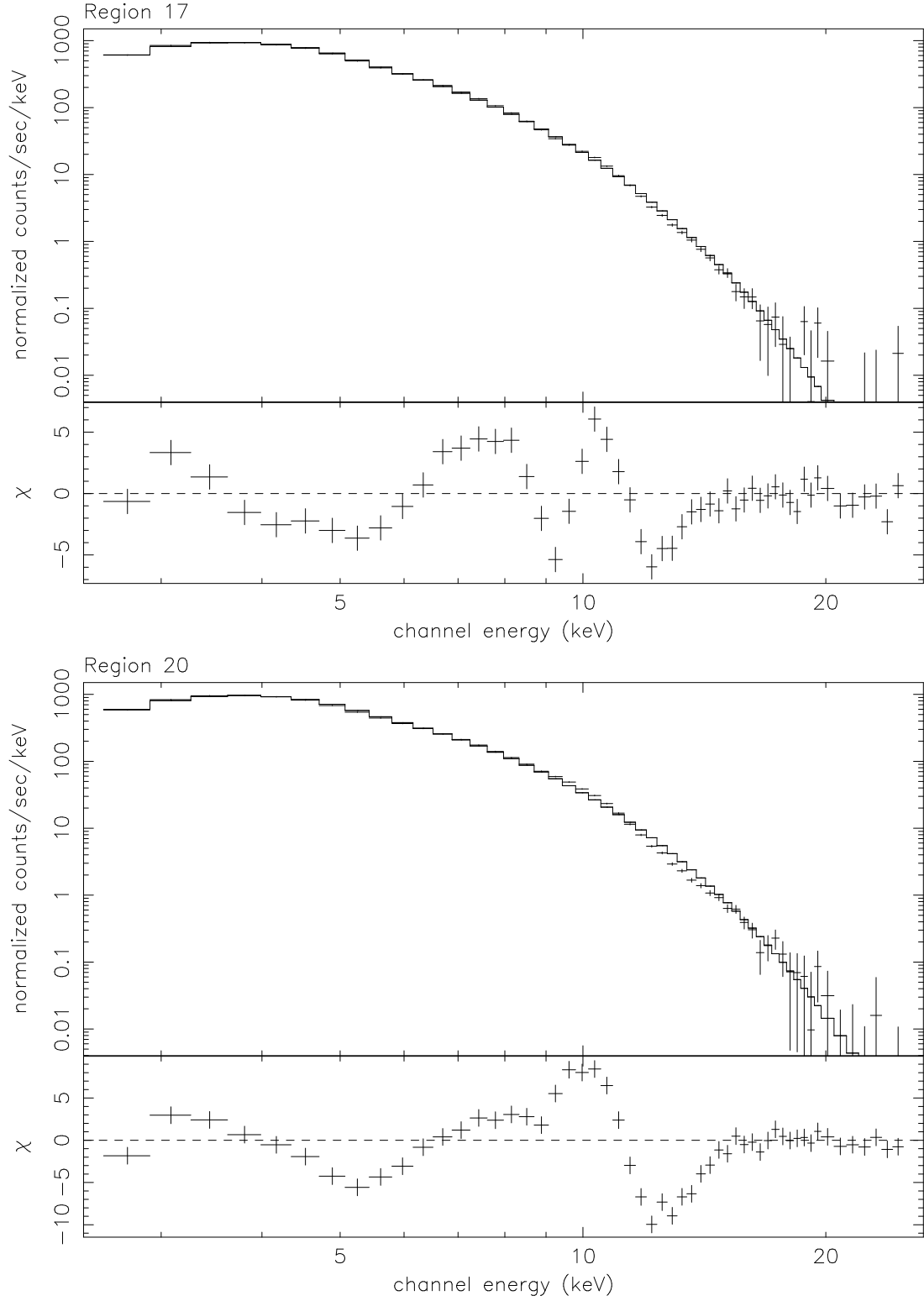


Figure 6-11: Spectra from HID regions 17 and 20 (crosses) and fitted models (histograms) consisting of a disk blackbody and blackbody. The ratio of residuals to error bars shows a narrow edge or line-like feature above 10 keV.

factorally fit the lower portion of the track (rank number 14 and greater). In addition no single or double-component model was found that could reproduce the unusual feature above 10 keV. For example, a broken power law (model with two different slopes above and below a cutoff energy) fails to account for the more step-like nature of the feature.

6.8 Summary

Although color-color and hardness-intensity diagrams for Cir X-1 are complicated by absorption dips and shifting spectral tracks, the source clearly traces out a complete Z-source track during short time segments (hours). Power spectra taken from regions of the HID track show continuous evolution from the narrow QPO (increasing in frequency from 12–30 Hz) on the horizontal branch, to the broad 4 Hz QPO on the normal branch, to only very low frequency noise on the flaring branch. Flaring-branch light curves show high levels of variability due to “mini-flares”.

The energy spectrum on the horizontal branch is fit well with a two-component model consisting of a soft disk blackbody and a harder blackbody (presumably from closer to the surface). In this model, motion along the HB is mainly associated with an increasing inner radius of the disk (increasing disk blackbody normalization). This would imply that, as the luminosity increases across the HB, the inner edge of the disk is pushed further away from the surface. It is not clear how this is related to the increasing QPO frequency, which would typically be expected to require a *decreasing* radius if the QPOs were related to Keplerian motion at the inner edge of the disk. Energy spectra on the normal branch indicate that the hard blackbody fades away, leaving only the disk blackbody. On the lower NB, a feature in the spectrum develops above 10 keV. This feature becomes more prominent on the flaring branch. Although, there is still much to be understood about the physical mechanisms responsible for the spectral and timing evolution of Cir X-1 around the HID diagram, these results have demonstrated the specific timing and spectral properties associated with each branch.

Chapter 7

Absorption Dips

7.1 Overview

RXTE All-Sky Monitor light curves of Cir X-1 show that dips occur near phase zero of the 16.55-day cycle of the source (Chapter 3). *RXTE* Proportional Counter Array observations carried out between 1996 September 20–22 provided 60% observing efficiency for 48 hours around phase zero (study D, see Figure 3-5). These observations showed significant dipping activity during much of those two days. We have studied the dramatic spectral evolution associated with the dips, and show that the spectrum throughout the dips is well-fit by variable and at times heavy absorption of a bright component, plus a faint component that is only weakly absorbed. We also show that an iron emission line near 6.5 keV present during dips maintains a constant absolute flux level outside the dips as well, indicating that the line is associated with the faint component. We suggest that these results are consistent with a model in which the bright component is reprocessed by a scattering medium, only slightly modifying the spectral shape, but adding an iron line due to fluorescence. These results are also generally consistent with a spectral study based on *ASCA* observations of a low-to-high transition in Cir X-1 [12], where the spectrum was fit with a partial-covering model.

7.2 Dips in RXTE Light Curves

Light curves from the ASM and PCA show that the intensity of Cir X-1 drops below the 1 Crab baseline near phase zero of most (possibly all) cycles. These low-intensity episodes, which we refer to as “dips”, are brief compared to the 16.55-d cycle, lasting as short as seconds (e.g., Figure 6-5) and as long as half a day (e.g., Figure 7-1). They often show abrupt transitions (rise or fall times

much smaller than the total duration), and are characterized by specific spectral evolution which we describe in detail below. During the strongest dips observed in PCA observations, the intensity dropped to levels more than a factor of 10 below the baseline level (2–90 keV). Dips in the ASM light curves (2–12 keV) reached similar levels (i.e., as low as ~ 80 mCrab).

The dips most often occurred during the half day before and after phase zero, but also sometimes continued through day 1.5 in ASM data and day 2.5 in PCA data. On a couple of occasions, dips also occurred at later phases in the ASM light curve, e.g., near day 4 of the cycle. Dips occurred in all six cycles of Cir X-1 for which we obtained PCA observations during the half day before phase zero (see Figure 3-5). All-Sky Monitor light curves of Cir X-1 show intensity points below the 1 Crab baseline in about half of the cycles observed (see section 2.4). Because ASM coverage is incomplete (about ten to twelve 90-s exposures per day), it is possible that dips might actually occur in all cycles.

The PCA observations (study D) made during 1996 September 20–22 (Figure 7-1) covered a 48-hour period around phase zero (with $\sim 60\%$ observing efficiency) and showed significant dipping for about half of the observed time. These observations provided the opportunity to study dipping behavior in detail, and are thus the focus of this chapter. Dips in other cycles have also been examined and show similar behavior to that presented below.

The observations shown in Figure 7-1 began about a half day before phase zero. The intensity of Cir X-1 was very low (an extended dip) during the first half day of the observations, and then returned to the much higher “quiescent” level shortly after phase zero. During the half day immediately following phase zero, the intensity underwent shorter intermittent dips. The strongest dips all reached similar minimum levels of about 200–350 counts/s/PCU (2–18 keV) after background (~ 10 c/s/PCU) was subtracted. A second episode of significant extended dipping occurred from about 0.5 to 0.9 days after phase zero, followed by flaring-state activity for the remaining half day of the observation. The flaring state is characterized by (1) a gradual increase of the average intensity in the low-energy PCA bands (which then dominate the total PCA count rate) accompanied by a significant drop in the high-energy bands and (2) individual flares on shorter timescales (less than a few hours) which show increased intensity in all PCA energy bands. The spectral and timing evolution during the flaring state of Cir X-1 was discussed in Chapters 5 and 6.

7.3 Evolution of Hardness Ratios During Dips

Three dips in Figure 7-1 have been identified for further study (Dips 1–3). A 4000-s segment of Figure 7-1 is shown for each of these dips in Figures 7-2, 7-3, and 7-4. The light curves in multiple

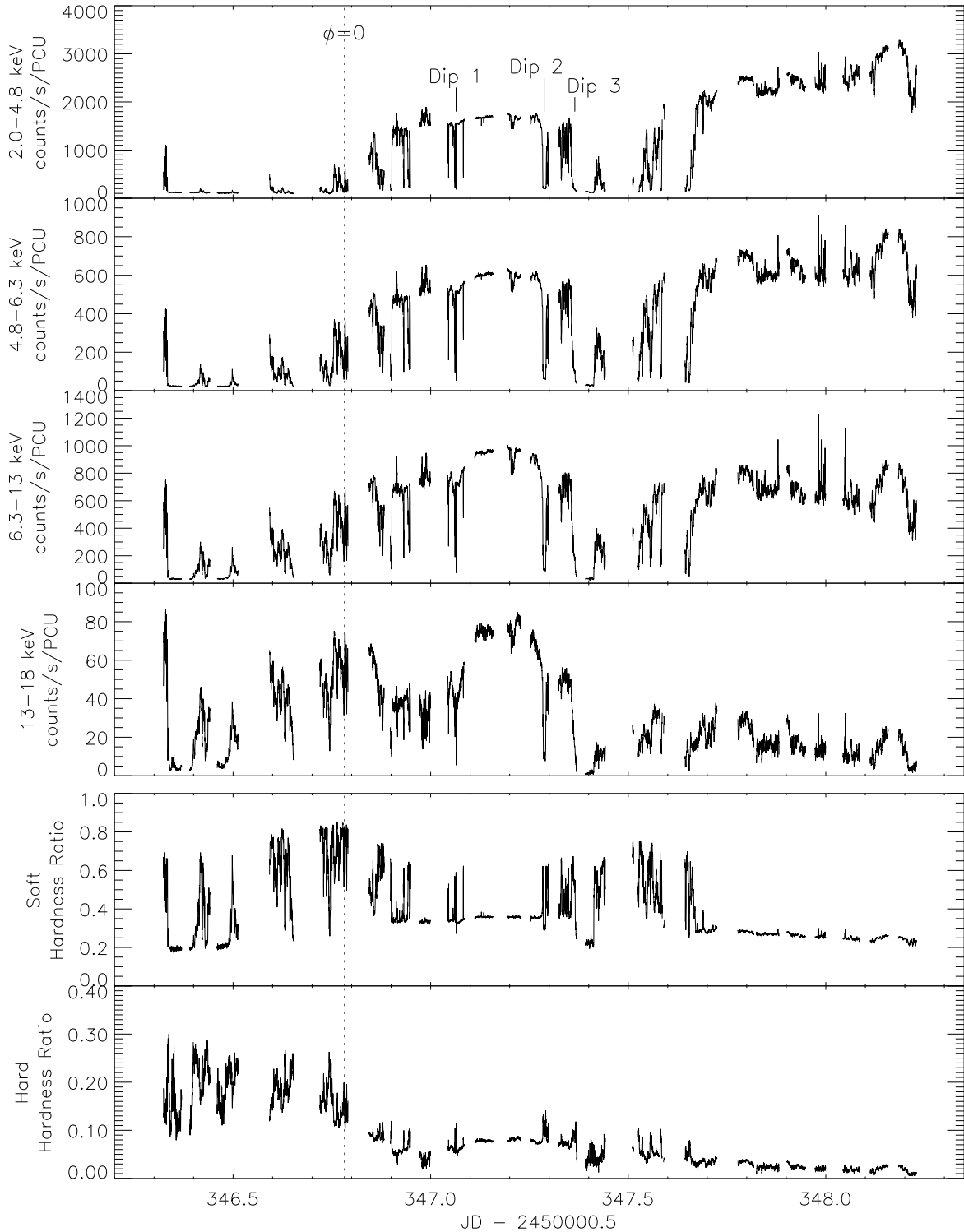


Figure 7-1: Light curves in four energy channels and two hardness ratios for PCA observations of Cir X-1 from 1996 September 20–22, covering a two-day period around phase zero ($\phi = 0$). Three dips have been identified for further study. Each point represents 16 s of background-subtracted data from PCUs 0, 1, and 2. Ratios of the intensities produce soft ($I[4.8\text{--}6.3\text{ keV}] / I[2.0\text{--}4.8\text{ keV}]$) and hard ($I[13\text{--}18\text{ keV}] / I[6.3\text{--}13\text{ keV}]$) hardness ratios. The intensity levels of the segment at day ~ 347.2 (after Dip 1) are close to the level in each band during the quiescent phases of the orbit.

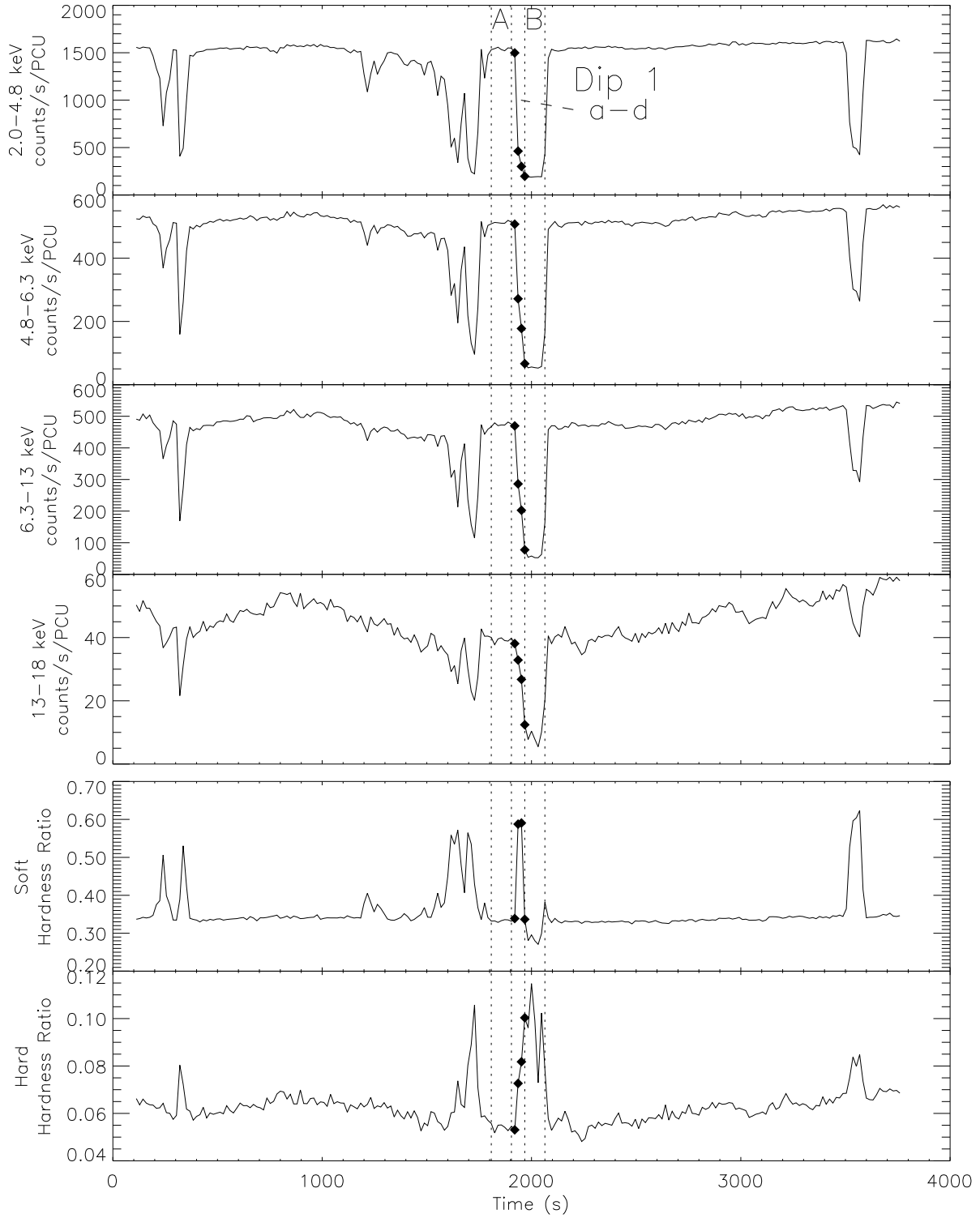


Figure 7-2: Light curves in four energy channels and two hardness ratios spanning 4000 s including Dip 1. Time zero corresponds to day 347.041 in Figure 7-1. The intensity and hardness ratio points are the same as in Figure 7-1. Energy spectra were extracted from two 96-s time segments (A and B), indicated by dotted vertical lines, and four 16-s segments (a–d) indicated by diamonds.

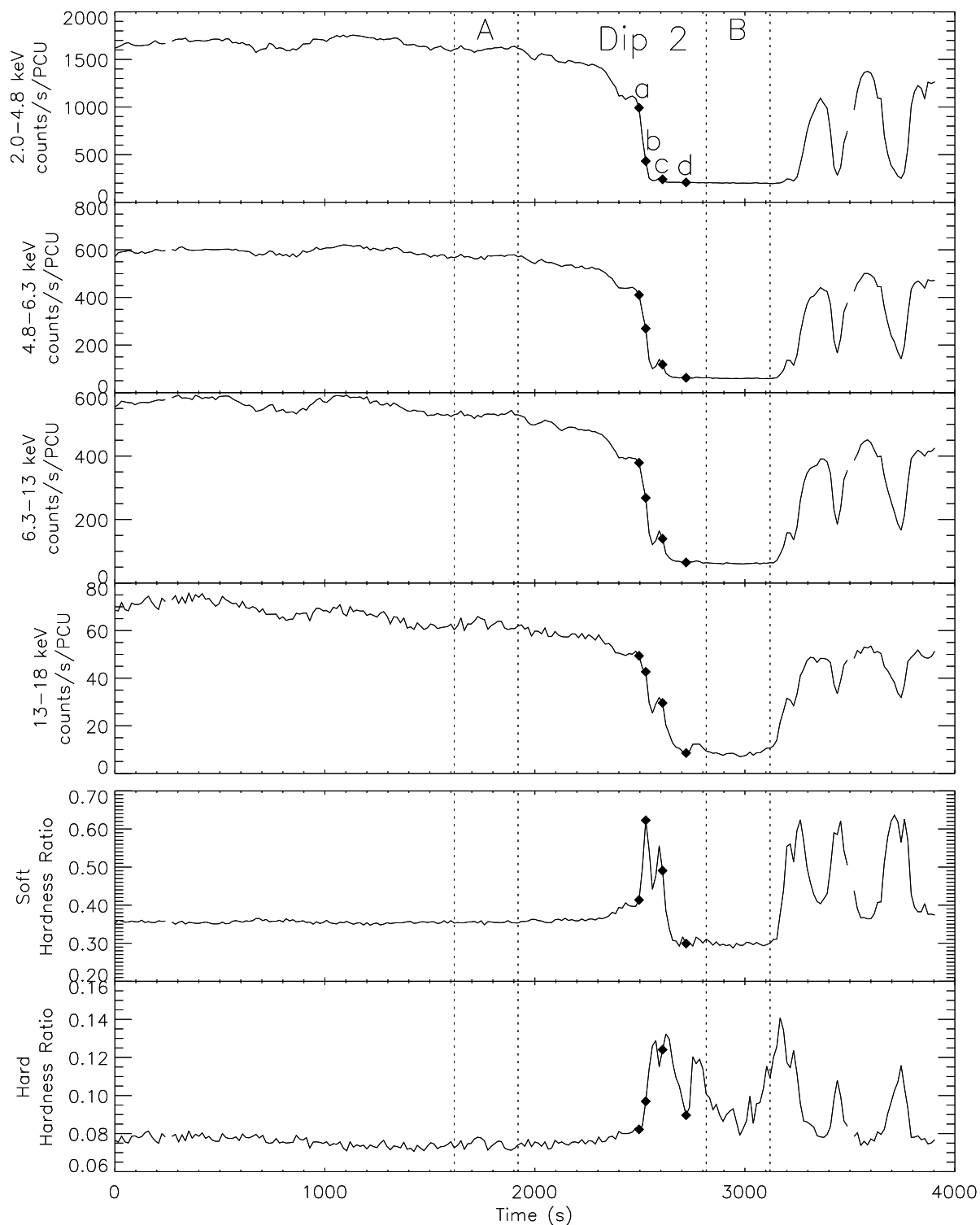


Figure 7-3: Light curves in four energy channels and two hardness ratios spanning 4000 s including Dip 2. Time zero corresponds to day 347.254 in Figure 7-1. The intensity and hardness ratio points are the same as in Figure 7-1. Energy spectra were extracted from two 304-s time segments (A and B), indicated by dotted vertical lines, and four 16-s segments (a–d), indicated by diamonds.

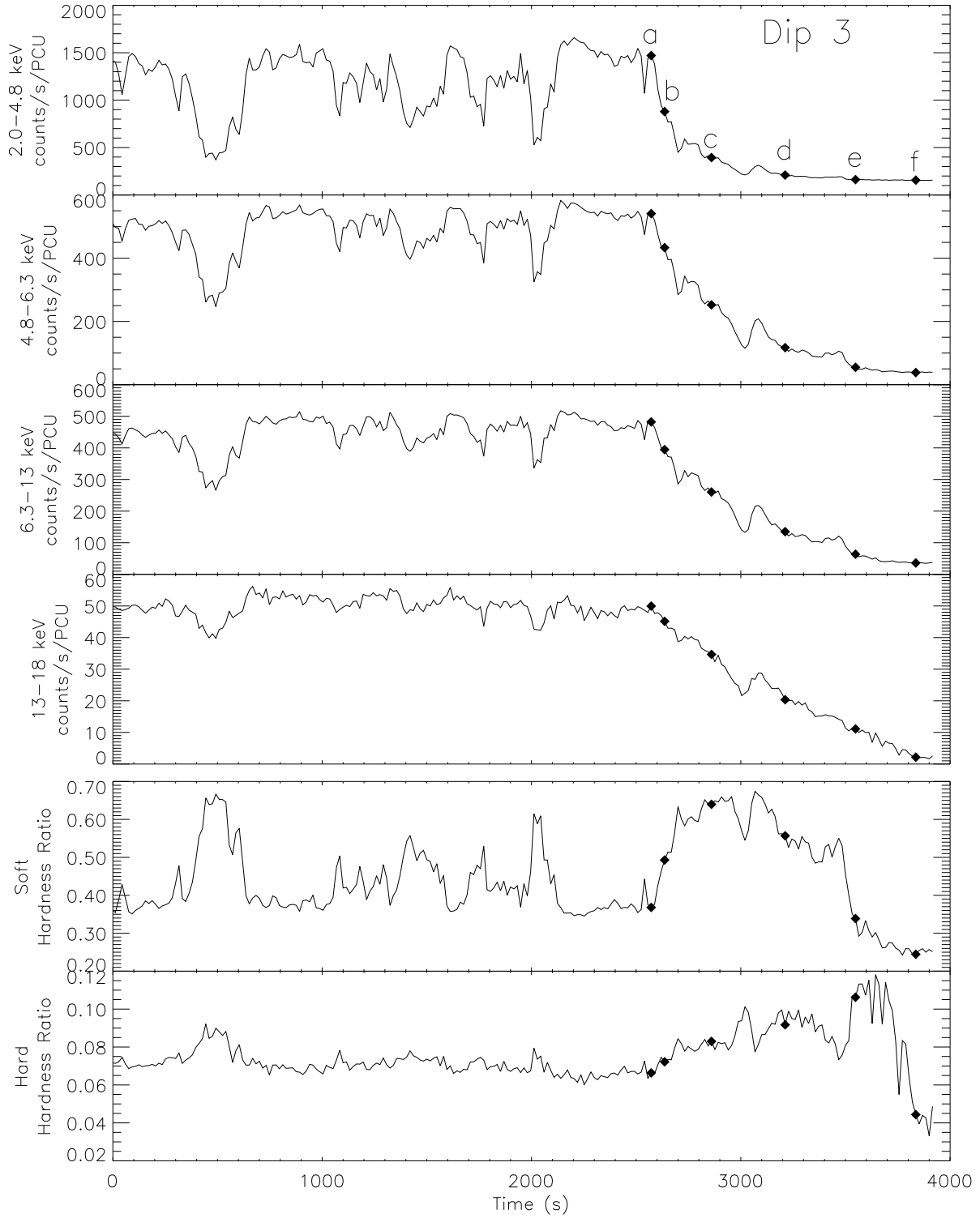


Figure 7-4: Light curves in four energy channels and two hardness ratios spanning 4000 s including Dip 3. Time zero corresponds to day 347.325 in Figure 7-1. The intensity and hardness ratio points are the same as in Figure 7-1. Energy spectra were extracted from six 16-s time segments (a–f), indicated by diamonds.

PCA energy channels show that the transitions into and out of dips occur more rapidly at low energy than in higher energy bands (best demonstrated by the gradual ingress of Dip 3 in Figure 7-4), thus hardness ratios initially increase (harden) as the denominator falls more quickly than the numerator. Low energy count rates are also the first to reach a fixed bottom level. This causes hardness ratios to decrease (soften) since the denominator approaches a constant while the numerator continues to decrease.

The intensity and hardness ratios from Dip 3 (the last 1716 s of data in Figure 7-4) have been used to produce color-color and hardness-intensity diagrams (CDs/HIDs), shown in Figure 7-5. The spectral evolution during the dip produces tracks with dramatic bends in both the CD and the HID. A similar CD and HID has also been produced for the first three segments of Figure 7-1 (day 346.31–346.52), during which the intensity was mostly in an extended low/dip state (Figure 7-6).

In the HIDs of Figures 7-5 and 7-6, dips produce motion to the left (toward lower intensity) and initially upward (harder), but turn downward (softer) when the count rate in the denominator reaches its bottom level. In the CDs (most prominently in Figure 7-6), since two hardness ratios are employed (hard and soft color), motion is initially to the right and upward (harder in both colors but mostly in the lower channels). When the lowest channel reaches the bottom level, the track turns to the left but continues upward. When intermediate channels stop decreasing and only the highest channels still drop, the track finally turns downward. The intensity of the second lowest energy band rapidly drops by a factor of two (at time 3500 s in Figure 7-4) just before settling to its lowest level; this resulted in a gap in the the middle CD branch in Figure 7-5.

Evolution of the position in CDs and HIDs apart from dips is interpreted in Chapters 5 and 6 as motion around a “Z” track as well as shifts of the entire “Z” pattern. The exact position of a dip track in the diagrams depends on its starting point, i.e., the baseline intensity and spectrum. Although starting from different positions, all dips we have observed in *RXTE* light curves of Cir X-1 produce the same general shape in CDs and HIDs (but not always complete tracks if dips are weak).

7.4 Evolution of Energy Spectra During Dips

7.4.1 Spectral Model

Cold (neutral) matter most effectively absorbs photons at lower energies, so obscuration by cold matter produces dips that are more gradual at high energy than at low energy, as we observe in Cir X-1. However the fact that strong dips in Cir X-1 appear to “bottom-out” well above background suggests the presence of a faint component unaffected by the dips. Thus, in modeling spectra of dips in Cir X-1, at least two components are necessary: (1) a bright component modified by variable and

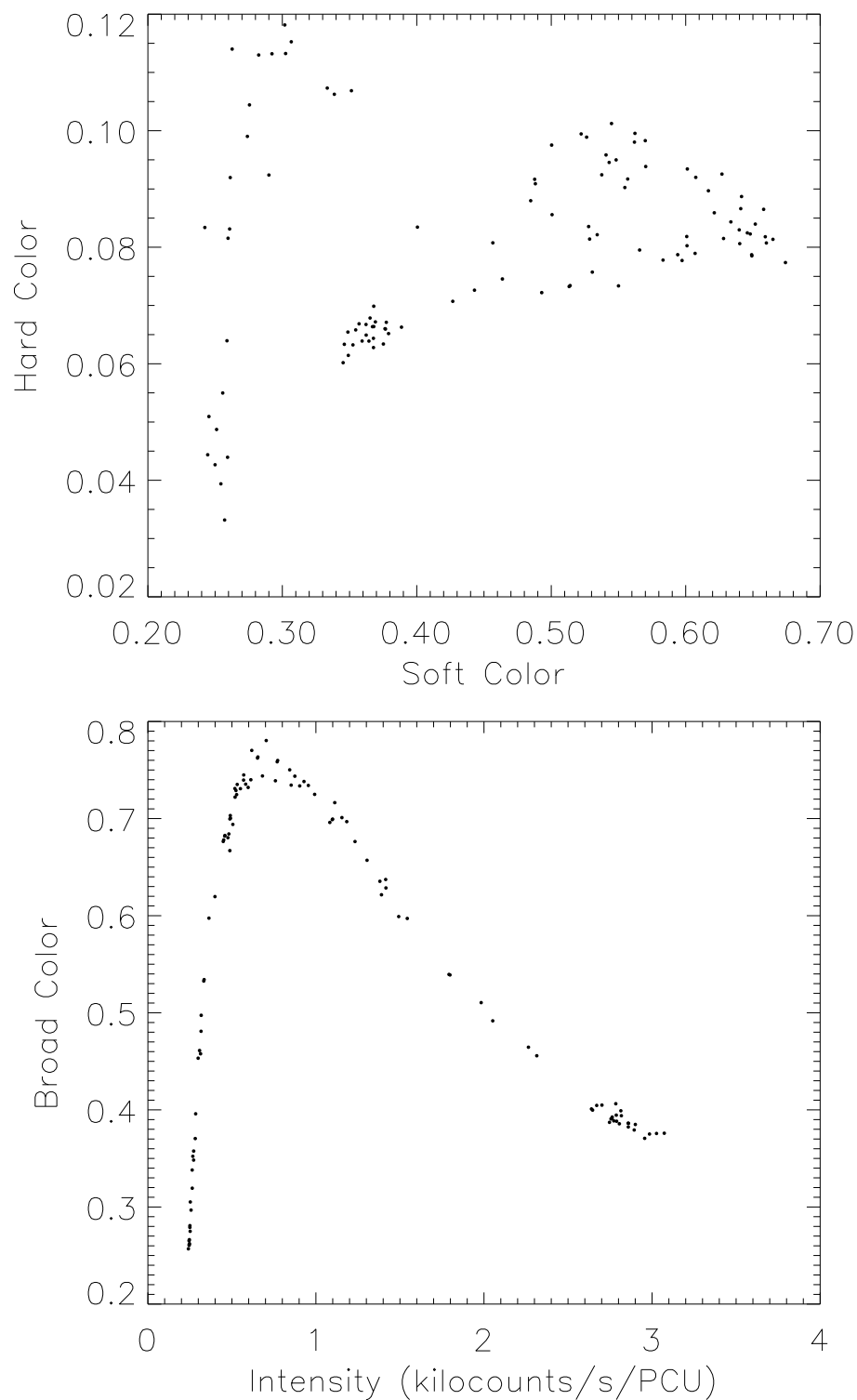


Figure 7-5: Color-color and hardness-intensity diagrams for the last 1716 s of data in Figure 7-4, during which the intensity gradually transitioned from the non-dip baseline to the bottom of a dip. Intensity is $I[2.0-18 \text{ keV}]$, and the hardness ratios are defined as soft color: $I[4.8-6.3 \text{ keV}] / I[2.0-4.8 \text{ keV}]$, hard color: $I[13-18 \text{ keV}] / I[6.3-13 \text{ keV}]$, and broad color: $I[6.3-18 \text{ keV}] / I[2.0-6.3 \text{ keV}]$. Each point represents 16 s of background-subtracted data from PCUs 0, 1, and 2.

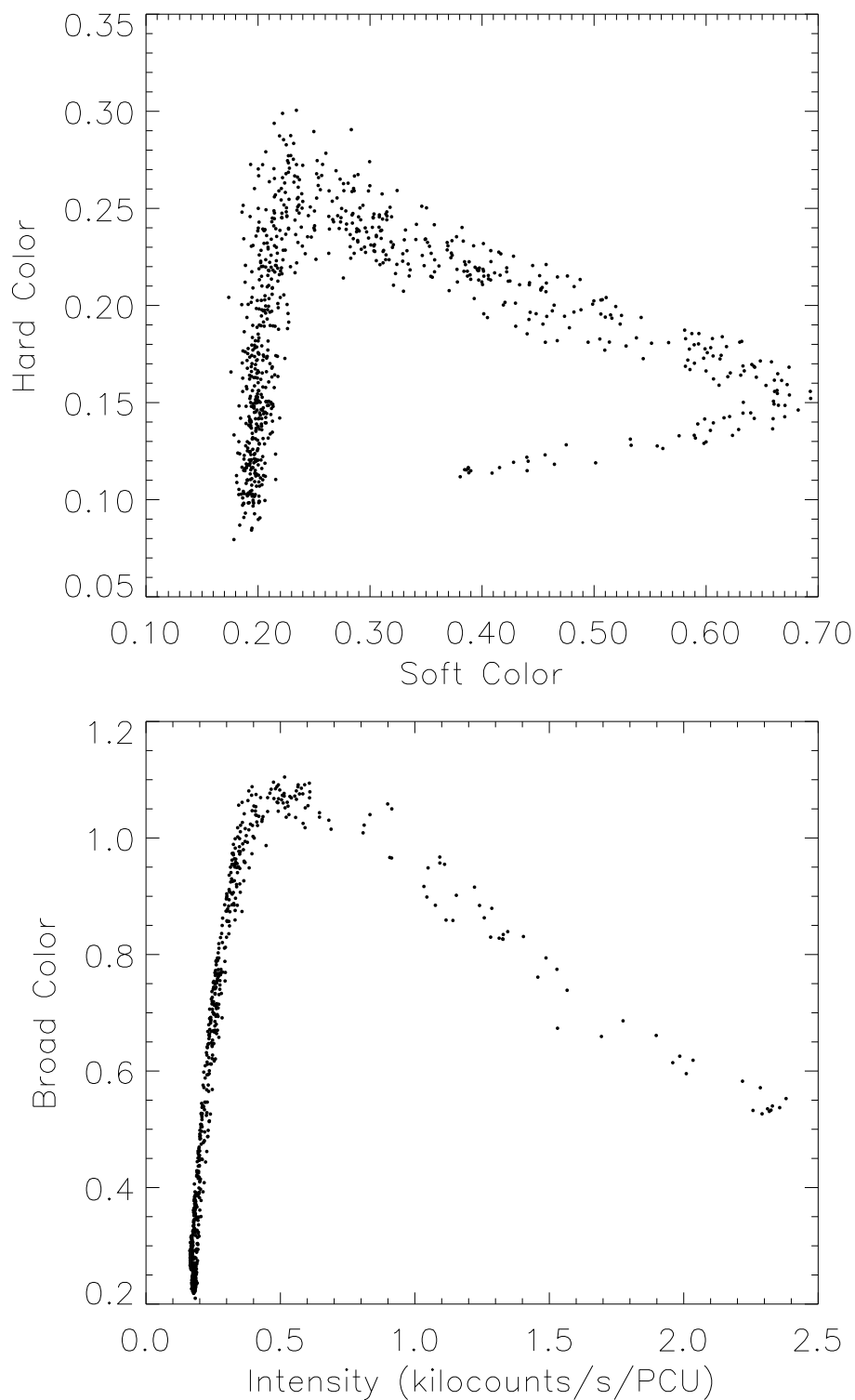


Figure 7-6: Color-color and hardness-intensity diagrams for the first three segments in Figure 7-1 (day 346.31–346.52), during which Cir X-1 was in an extended low/dip state. Intensity is $I[2.0\text{--}18\text{ keV}]$, and the hardness ratios are defined as soft color: $I[4.8\text{--}6.3\text{ keV}] / I[2.0\text{--}4.8\text{ keV}]$, hard color: $I[13\text{--}18\text{ keV}] / I[6.3\text{--}13\text{ keV}]$, and broad color: $I[6.3\text{--}18\text{ keV}] / I[2.0\text{--}6.3\text{ keV}]$. Each point represents 16 s of background-subtracted data from PCUs 0, 1, and 2.

at times very heavy absorption and (2) a faint component seen through a constant and relatively low column density. For simplicity, we assume that the spectral shape of the two components are similar, as might be the case if the faint component is due to scattering (e.g., by a corona, stellar wind, etc.) of the main bright component back into the line of sight from other initial emission directions. (Although the terms “direct” and “scattered” components would be more physical, we will continue to use the terms “bright” and “faint” since they do not tie the discussion to a particular assumed model.)

From a study of the energy spectrum during non-dip observations (Chapter 6), we found that the 2.5–25 keV spectrum of Cir X-1 was generally fit well with a model consisting of a multi-temperature “disk blackbody” plus a hard blackbody. Thus, we adopt this model for the bright component during dips and constrain the faint component to use the same model parameters, but with the flux multiplied by a constant factor f which is less than unity.

The absorption column density for the faint component is assumed to remain constant throughout a dip, but the column density for the bright component is allowed to vary to produce the dips. The light curves during strong dips show a significant reduction in intensity even at high energy (13–18 keV), indicating very high column densities ($N_H > 10^{24} \text{ cm}^{-2}$). Photo-electric absorption is the dominant process responsible for dips at low energy, but the photo-electric cross-section decreases with energy. Thus, above about 10 keV, Thomson scattering (with an approximately energy-independent cross section) becomes important. Both photo-electric and Thomson cross-sections are included in the absorption calculation for the bright component. The complete model used can then be expressed as:

$$F = \left[\exp(-\sigma_{ph} N_H^{(1)}) \exp(-\sigma_{Th} N_H^{(1)}) + \exp(-\sigma_{ph} N_H^{(2)}) f \right] M, \quad (7.1)$$

where F is the observed flux, σ_{ph} and σ_{Th} are the photo-electric and Thomson cross-sections, $N_H^{(1)}$ and $N_H^{(2)}$ are the effective hydrogen column densities of the bright and faint components respectively, f is the ratio of the flux of the faint component to that of bright component, and M is the disk blackbody plus blackbody model.

7.4.2 Spectral Fitting Strategy

Because dip spectra are composed of multiple components (variably absorbed and faint manifestations of the disk blackbody and blackbody) we make use of joint fits of spectra from inside and outside dips to simultaneously constrain the parameters of the various components. The combined χ^2 value obtained when the model is fit to multiple spectra is minimized by varying the model pa-

rameters, but allowing only the absorption column density of the bright component to vary between spectra. Since the disk blackbody and blackbody parameters typically evolve on timescales of hours (see Chapter 6), it is important to compare spectra during a dip to spectra immediately outside the dip.

In order to perform joint spectral fits, we extracted PCA energy spectra from time segments before and during the three dips shown in Figures 7-2, 7-3, and 7-4. The same procedure for constructing and fitting PCA spectra presented in sections 6.5 and 6.6 is used here as well (comparing results from PCUs 0, 1, and 4).

7.4.3 Energy Spectra Inside and Outside Dips

We compiled spectra from a 96-s time segments immediately prior to Dip 1 and from another 96-s segment during the lowest portion of Dip 1 (segments labeled “A” and “B” in Figure 7-2). Likewise, we selected a 304-s segment from before Dip 2, and other segment of the same duration from the lowest portion of that dip (segments “A” and “B” in Figure 7-3). These spectra are shown in Figures 7-7 and 7-8 (top panels), along with fitted curves using the model described above (equation 7.1). The best-fitting parameters for the bright and faint component of each fit are listed in the first two lines of Table 7.1. The column density ($N_H^{(2)}$) of the faint component is given in the table. The column density ($N_H^{(1)}$) of the bright component differs for spectra A and B of each fit and is thus given separately in Table 7.2.

The disk blackbody and blackbody parameters for both dips are similar to those obtained for non-dip spectra in Chapter 6 (temperatures of 1.5 keV and 2.2 keV respectively). The flux of the faint component is 10–11% that of the bright component (f). The column density of the faint component is very low, and consistent with zero. This low value is inconsistent with estimates of the interstellar column density measured with *ASCA* and *ROSAT* ($N_H = 1.8\text{--}2.4 \times 10^{22} \text{ cm}^{-2}$) [12, 56]. This may indicate that the spectral shape of the faint component is not exactly the same as that of the bright component. If scattering is responsible for the faint component, then this process might distort the spectrum slightly toward lower energy, thereby giving the appearance of reduced interstellar absorption. The use of different spectral models for the bright and faint components becomes unproductive due to the large number of parameters involved, so we allow the column density of the faint component to account for small difference in spectral shape.

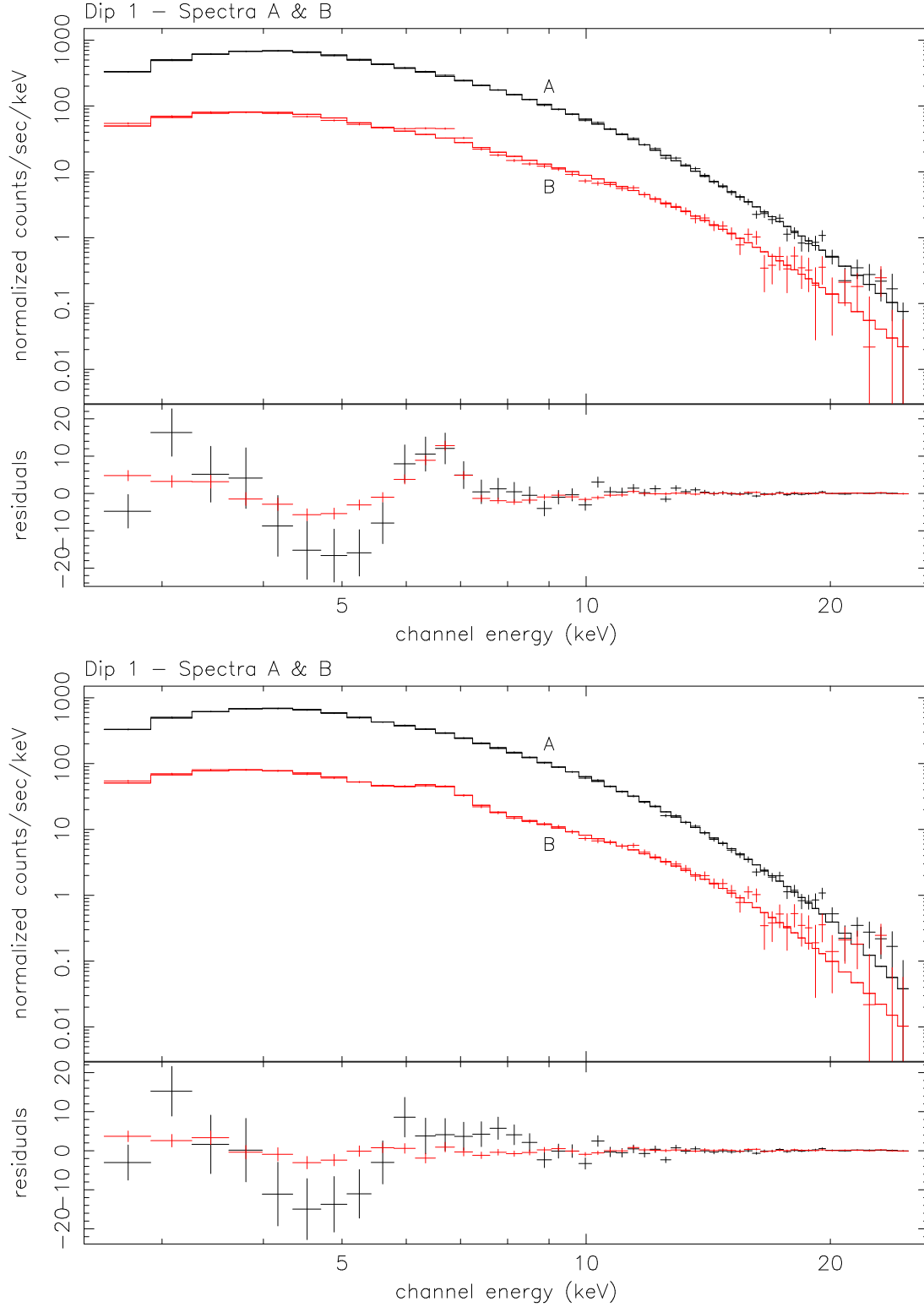


Figure 7-7: Top: Spectral fits for 96-s segments prior to Dip 1 (spectrum A) and during Dip 1 (spectrum B). Bottom: same spectra and model (see text), but with a Gaussian emission-line component included to fit the peaked residuals near 6.5 keV. The data shown are from PCU 0 only.

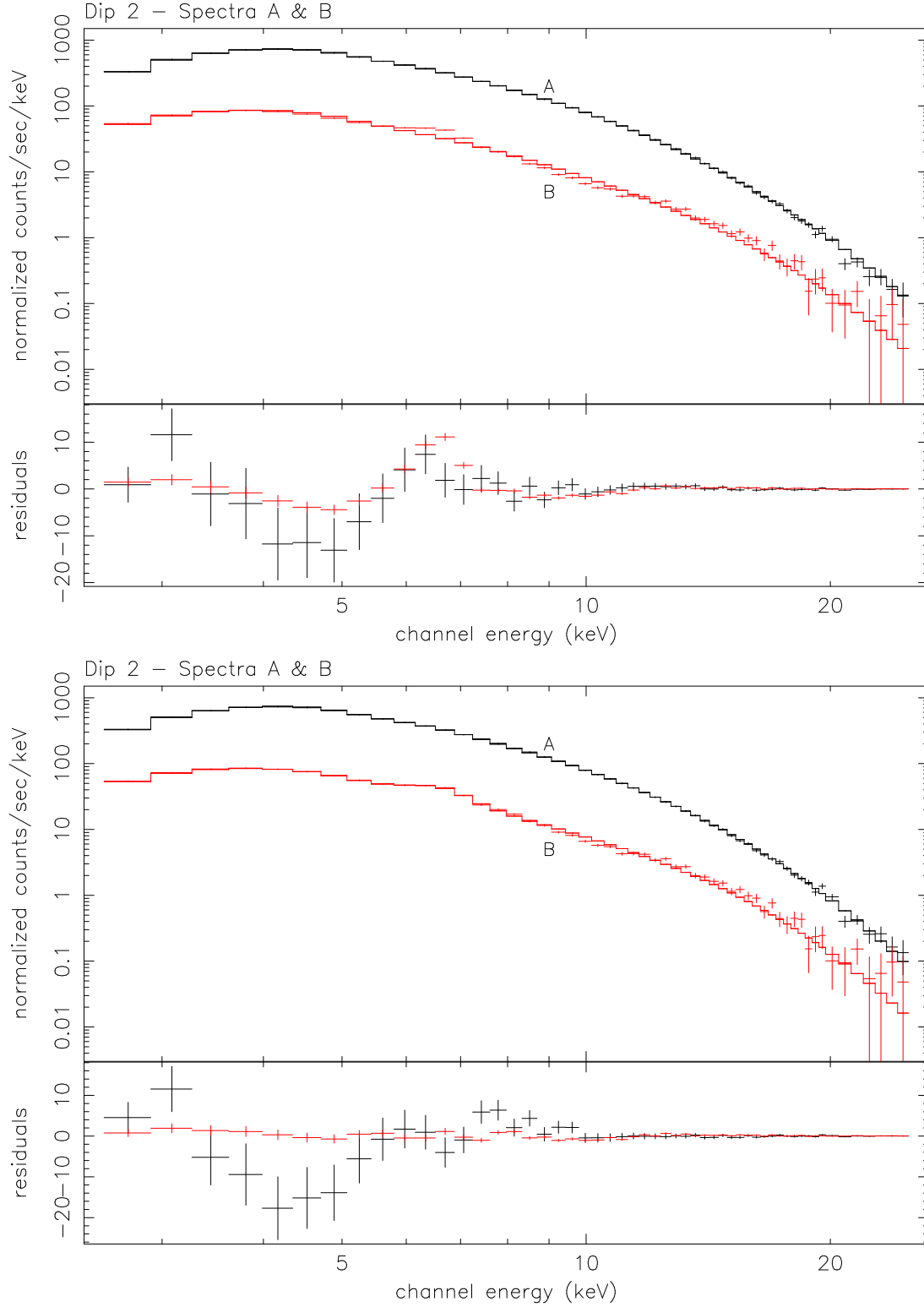


Figure 7-8: Top: Spectral fits for 304-s segments prior to Dip 2 (spectrum A) and during Dip 2 (spectrum B). Bottom: same spectra and model (see text), but with a Gaussian emission-line component included to fit the peaked residuals near 6.5 keV. The data shown are from PCU 0 only.

Joint fit ¹	Iron Line ²	Disk Blackbody ³		Blackbody ⁴		Faint Component		
		T_{in} (keV)	$R_{in} \cos^{1/2} \theta$ (km)	T (keV)	R (km)	f ⁵	$N_H^{(2)}/10^{22}$ ⁶ (cm ⁻²)	χ_r^2 ⁷
1A-B	no	$1.51^{+0.10}_{-0.17}$	$16.94^{+3.96}_{-2.20}$	$2.20^{+0.62}_{-0.42}$	$3.77^{+3.33}_{-2.55}$	$0.107^{+0.005}_{-0.006}$	$0.00^{+0.07}_{-0.00}$	3.89-4.07
2A-B	no	$1.51^{+0.04}_{-0.06}$	$17.54^{+1.25}_{-0.87}$	$2.32^{+0.16}_{-0.15}$	$3.47^{+0.86}_{-0.76}$	$0.103^{+0.003}_{-0.003}$	$0.03^{+0.28}_{-0.03}$	7.58-7.84
1A-B	yes	$1.23^{+0.22}_{-0.15}$	$25.32^{+8.56}_{-7.03}$	$1.79^{+0.33}_{-0.16}$	$7.87^{+3.34}_{-4.14}$	$0.096^{+0.007}_{-0.006}$	$0.00^{+0.10}_{-0.00}$	1.44-1.62
2A-B	yes	$1.35^{+0.06}_{-0.05}$	$22.45^{+1.83}_{-1.69}$	$2.10^{+0.12}_{-0.09}$	$5.23^{+0.92}_{-0.93}$	$0.092^{+0.002}_{-0.002}$	$0.00^{+0.10}_{-0.00}$	1.87-2.15
1a-d	yes	$1.18^{+0.19}_{-0.16}$	$27.04^{+9.39}_{-6.33}$	$1.72^{+0.22}_{-0.12}$	$8.22^{+2.69}_{-3.03}$	$0.103^{+0.009}_{-0.011}$	$0.00^{+0.44}_{-0.00}$	0.99-1.20
2a-d	yes	$1.26^{+0.14}_{-0.14}$	$25.12^{+7.66}_{-5.20}$	$2.08^{+0.25}_{-0.15}$	$5.46^{+1.08}_{-1.08}$	$0.117^{+0.013}_{-0.014}$	$0.15^{+0.70}_{-0.15}$	0.80-1.12
3a-f	yes	$1.07^{+0.08}_{-0.09}$	$42.66^{+8.34}_{-6.60}$	$1.74^{+0.09}_{-0.09}$	$9.23^{+1.41}_{-1.32}$	$0.054^{+0.005}_{-0.005}$	$0.00^{+0.14}_{-0.00}$	1.27-1.34

Table 7.1: Top group: joint fit parameters of the bright and faint components of spectra from outside (A) and inside (B) dips 1 and 2. Middle group: the same, but with an added Gaussian line. Third group: joint fit parameters for the four to six 16-s spectra for dips 1, 2, and 3. The absorption parameters ($N_H^{(1)}$) for the bright component are given in Tables 7.2 (A-B) & 7.4 (a-f) and the iron line parameters are given in Table 7.3.

$N_H^{(1)}/10^{22}$		$N_H^{(1)}/10^{22}$	
Spectrum	(cm ⁻²)	Spectrum	(cm ⁻²)
No Gaussian			
1A	$2.83^{+0.57}_{-0.43}$	2A	$3.50^{+0.29}_{-0.34}$
1B	176^{+12}_{-13}	2B	306^{+21}_{-19}
With Gaussian			
1A	$3.81^{+0.71}_{-0.81}$	2A	$4.30^{+0.26}_{-0.26}$
1B	184^{+15}_{-14}	2B	283^{+16}_{-14}

Table 7.2: Effective hydrogen column density of the bright component outside (A) and inside (B) Dips 1 and 2 (from fits with and without a ~ 6.5 keV Gaussian emission line).

¹ In joint fits (using the model given in equation 7.1), only the column density ($N_H^{(1)}$) of the bright component is allowed to vary between spectra (see Tables 7.2 and 7.4). Errors quoted are 90% confidence limits for a single parameter ($\Delta\chi^2 = 2.7$).

² A Gaussian emission line (~ 6.5 keV) was included in the final five fits (see Table 7.3).

³ For the disk blackbody, the inner radius of the accretion disk (times $\cos^{1/2} \theta$, where θ is the disk inclination angle and $\theta = 0$ is parallel to the line of sight) is given for a distance of 8 kpc.

⁴ The blackbody radius is given assuming a distance of 8 kpc.

⁵ The bright and faint components are assumed to have the same disk blackbody and blackbody parameters, but the faint component is scaled down by a factor f .

⁶ Absorption column density on the faint component (Hydrogen atoms per cm²).

⁷ Reduced $\chi^2 = \chi^2/dof$, where dof = degrees of freedom = the number of spectral bins ($\sim 54/\text{spectrum}$) minus the number of fit parameters.

The column density of the bright component outside dips (spectra 1A and 2A; see Table 7.2) is about $3 \times 10^{22} \text{ cm}^{-2}$, just slightly above the interstellar value. The column density during the low segments of dips (spectra 1B and 2B) is extremely high: $184 \times 10^{22} \text{ cm}^{-2}$ for spectrum 1B and $283 \times 10^{22} \text{ cm}^{-2}$ for spectrum 2B. This high column density value is required to produce the observed reduction in flux at 20 keV and is sufficient to render the absorbed component totally negligible at lower energies. Thus, the flux in spectra 1B and 2B below 5 keV is due entirely to the faint component.

7.4.4 Iron Emission Line

The fits for both dips show similar residuals for the spectra from outside and inside the dip (Figures 7-7 and 7-8). These residuals are also similar to those obtained in fits of spectra from the horizontal branch or upper normal branch in the study in Chapter 6. In particular, the fits of these spectra all show peaked residuals near 6.5 keV. In the two spectra from the bottom of dips (spectra 1B and 2B), the feature is prominently visible as a “bump” in the spectra themselves (see Figures 7-7 and 7-8). The parameters of this feature are best constrained when only the faint component is present. The line component is probably from iron $K\alpha$ emission, which occurs at 6.4 keV for neutral iron and higher energy for ionized iron. The fact that these residuals in the dip spectra are very similar in absolute flux level to the residuals immediately outside the dips strongly suggests that the line feature is associated with the faint component. For example, iron fluorescence might occur during the scattering process.

Based on the similar peaked residuals inside and outside the dips, a Gaussian emission line component was added near 6.5 keV (see the bottom panels of Figures 7-7 and 7-8). The addition of the line does reduce the peaked residuals near 6.5 keV, but does not improve the residuals (of similar strength but indicating data *below* the model) between 4–5 keV. The results of the joint fits, now including the Gaussian line, are listed in the second group in Tables 7.1 and 7.2, showing that the other model parameters are generally consistent with the previous fits within the 90% confidence limits. Table 7.1 also shows that a significant improvement in the reduced χ^2 value was achieved in both cases. We will continue to include a Gaussian line in all subsequent fits.

The parameters for the Gaussian line are shown in Table 7.3. Although the best-fitting centroid energy of the line is close to 6.6 keV, the Gaussian width is large (probably due to the relatively coarse energy resolution of the PCA: $\sim 1 \text{ keV}$ FWHM at 6 keV), so that we cannot confirm whether the line is from neutral or partially ionized iron or whether it is actually composed of multiple unresolved narrow lines.

Joint Fit	E (keV)	σ (keV)	normalization (photons cm ⁻² s ⁻¹)
1A-B	$6.59^{+0.12}_{-0.13}$	$0.18^{+0.28}_{-0.18}$	$0.018^{+0.007}_{-0.004}$
2A-B	$6.58^{+0.06}_{-0.07}$	$0.29^{+0.10}_{-0.13}$	$0.016^{+0.002}_{-0.002}$
1a-d	$6.59^{+0.16}_{-0.15}$	$0.13^{+0.29}_{-0.13}$	$0.015^{+0.002}_{-0.002}$
2a-d	$6.45^{+0.16}_{-0.20}$	$0.47^{+0.29}_{-0.32}$	$0.025^{+0.012}_{-0.008}$
3a-f	$6.46^{+0.23}_{-0.27}$	$0.39^{+0.32}_{-0.39}$	$0.012^{+0.004}_{-0.003}$

Table 7.3: Gaussian emission-line parameters for the joint fits of spectra outside and inside dips (A-B) and during entry into a dip (a-d, a-f). In each case, the same Gaussian line parameters were used for each spectrum in a joint fit.

7.4.5 Spectral Evolution During Dip Transitions

Through its large collecting area, the PCA provides good-quality spectra of bright sources such as Cir X-1 every 16 s. This enables us to study the detailed evolution of the spectrum during the transitions between the high and low states outside and inside dips. We selected four to six 16-s segments from the ingress of Dips 1, 2 and 3 (indicated as diamonds on Figures 7-2, 7-3, and 7-4). The 16-s spectra from each of these dips are shown in Figures 7-9, 7-10, and 7-11, along with the model curves from joint fits of the 4–6 spectra of each dip.

As expected from the light curves of the dips (Figures 7-2, 7-3, and 7-4), the intensity in each case initially decreases at low energy, but then reaches a fixed level while the intensity at higher energy continues to decrease. Intermediate spectra in each figure show a “step” near 7.1 keV, which cannot be accounted for solely by the emission line, but is naturally fit by the iron K absorption edge of the absorption component and indicates a column density of $N_H > \text{few} \times 10^{23}$. As discussed above, the intensity at the bottom of the dip is significantly reduced (relative to outside the dip) even at 20 keV due to Thomson scattering,

The fit parameters for the bright and faint components in each joint fit of the 16-s spectra (1a-d, 2a-d, and 3a-f) are shown in Table 7.1. The flux in the faint component relative to the bright component ranges from 5% and 12% in these fits, and the column density for the faint component is again consistent with zero. The Gaussian line parameters for these fits are listed in Table 7.3, and indicate a line centered at 6.4–6.6 keV. The best-fitting normalization (absolute flux) of the line differs by a factor of two among the three dips but is consistent with no change within the errors. For each set of spectra, the variable absorption column density of the bright component is shown in Table 7.4. In each case the column density increases from a relatively low value ($N_H = 4\text{--}9 \times 10^{22}$) at the start of a dip to very high values ($N_H > 10^{24}$) at the lowest part of the dips.

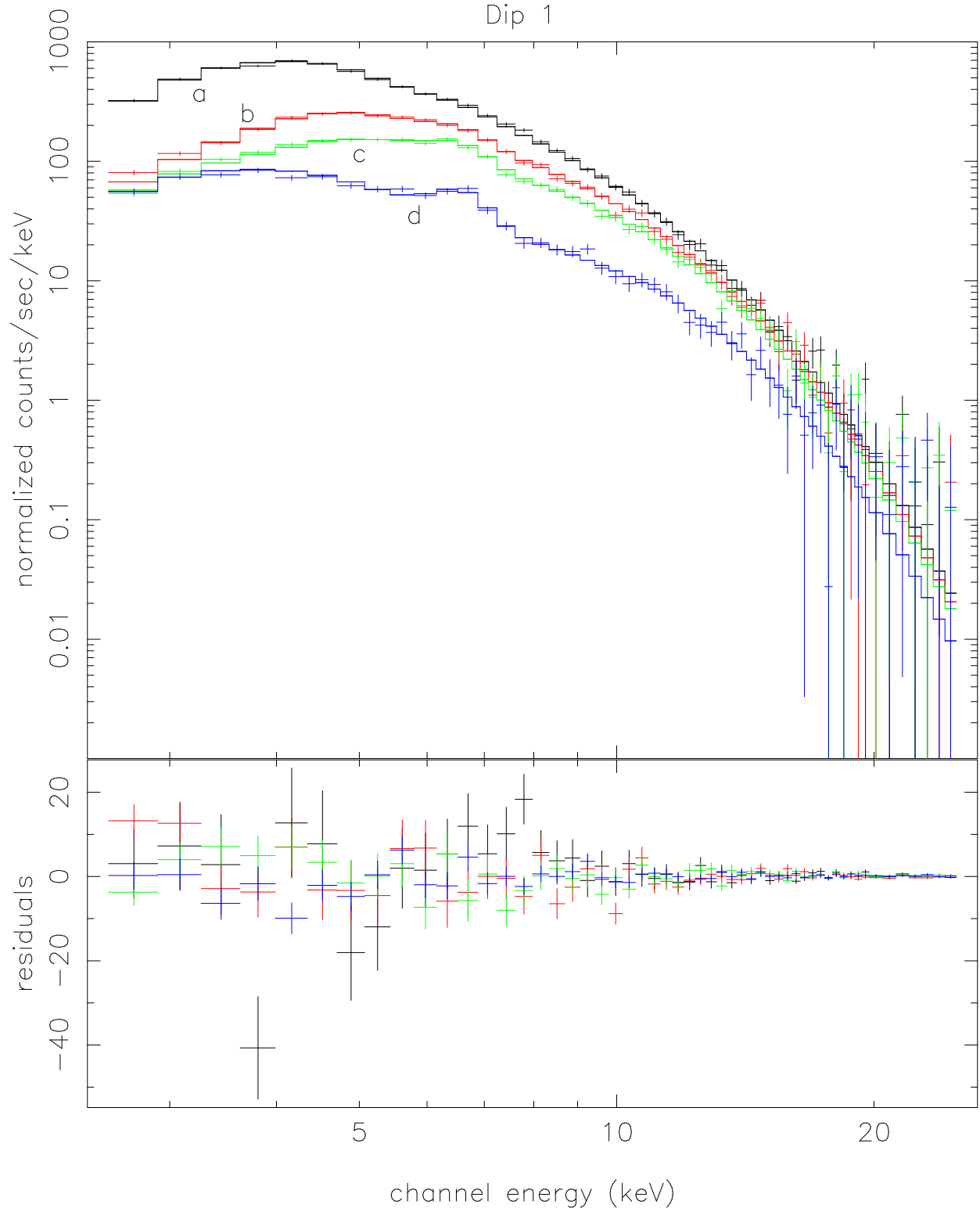


Figure 7-9: Spectral fits for four 16-s segments (a-d) during the decline into Dip 1. Only the column density of the bright component varies between the four jointly-fit curves. The data shown are from PCU 0 only.

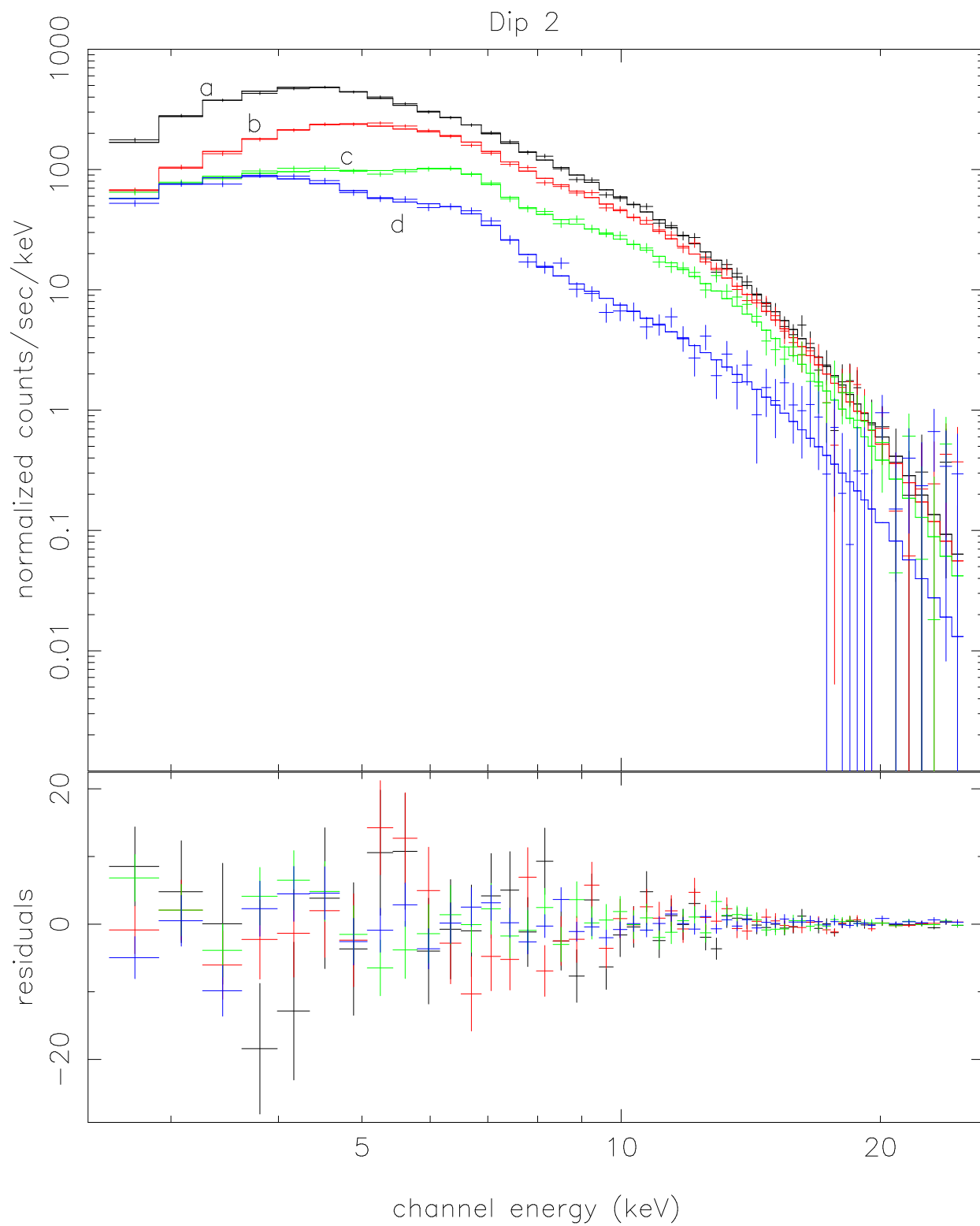


Figure 7-10: Spectral fits for four 16-s segments (a–d) during the decline into Dip 2. Only the column density of the bright component varies between the four jointly-fit curves. The data shown are from PCU 0 only.

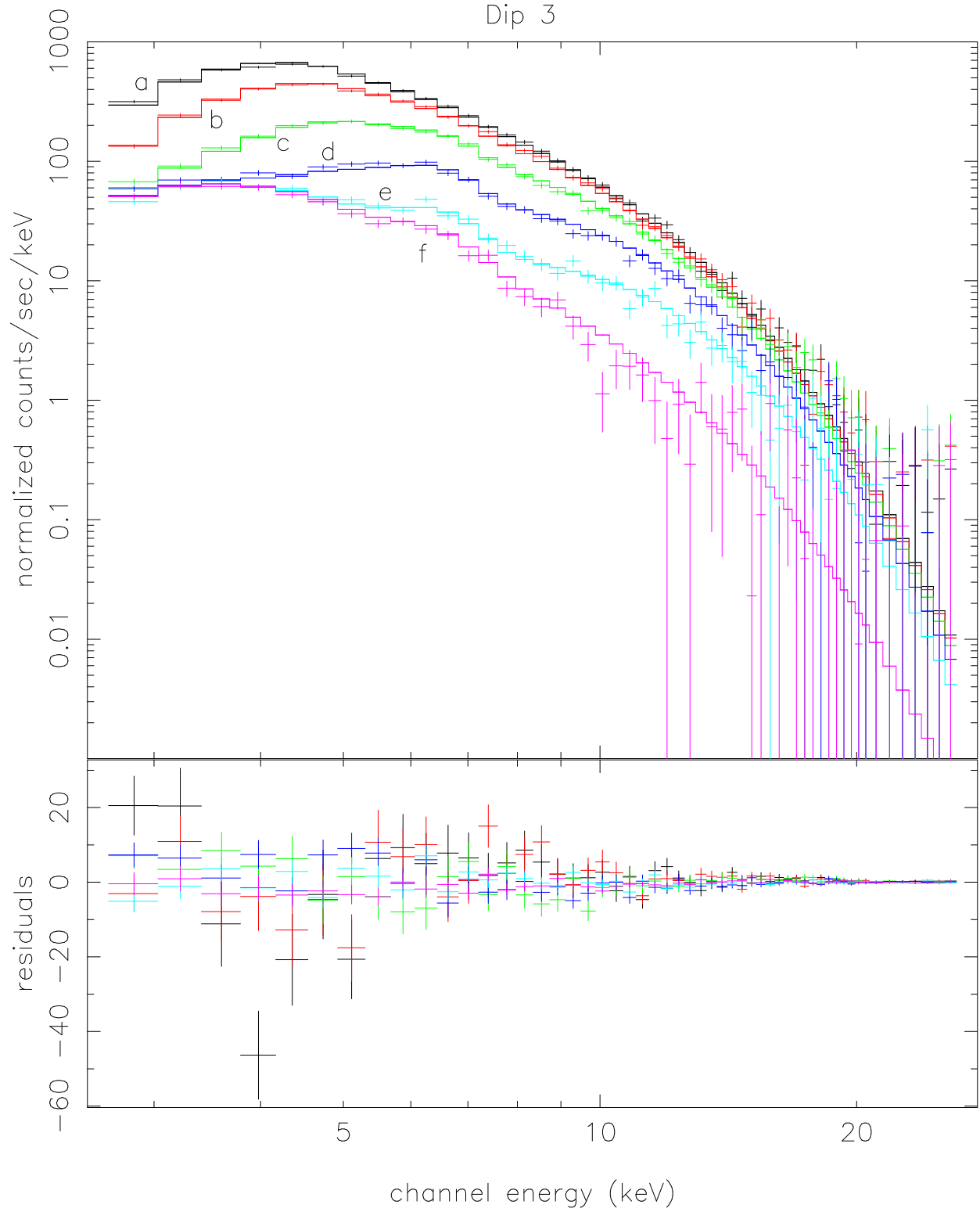


Figure 7-11: Spectral fits for six 16-s segments (a-f) during the decline into Dip 3. Only the column density of the bright component varies between the six jointly-fit curves. The data shown are from PCU 0 only.

Spectrum	$N_H^{(1)}/10^{22}$ (cm^{-2})	Spectrum	$N_H^{(1)}/10^{22}$ (cm^{-2})	Spectrum	$N_H^{(1)}/10^{22}$ (cm^{-2})
1a	$4.16^{+1.10}_{-0.75}$	2a	$8.84^{+1.37}_{-1.09}$	3a	$8.31^{+1.09}_{-0.96}$
1b	$25.8^{+1.6}_{-1.3}$	2b	$25.8^{+1.4}_{-1.5}$	3b	$15.7^{+1.0}_{-1.1}$
1c	$43.6^{+1.7}_{-2.1}$	2c	$64.0^{+2.4}_{-2.5}$	3c	$33.2^{+1.4}_{-1.5}$
1d	129^{+8}_{-8}	2d	242^{+83}_{-52}	3d	$66.7^{+1.6}_{-1.5}$
				3e	127^{+8}_{-7}
				3f	$> 2 \times 10^4$

Table 7.4: Effective hydrogen column density responsible for the variable absorption in the bright component, due to photo-electric absorption and Thompson scattering, during 16-s spectra from Dips 1, 2, and 3.

These fits show that the model developed above, where only the absorption column density on the bright component varies between all spectra of a given dip, is quite successful in reproducing the evolution of the spectrum throughout the dips.

7.5 Discussion

The spectral evolution during dips in Cir X-1 produces curved tracks in CDs and HIDs. By identifying these tracks we can exclude absorption dip behavior from analysis intended to study Z-source spectral tracks, as we have done in Chapter 6.

Similar absorption-dip behavior was recently observed in *RXTE* observations of the black-hole candidates GRO J1655-40 and 4U 1630-47 [36, 74]. Dips in these sources show evidence for a faint unabsorbed component and produced curved tracks in CDs and HIDs similar to those we observe in Cir X-1.

Spectral analysis from an *ASCA* observation of Cir X-1 during an intensity transition also showed evidence for an unabsorbed component [12]. A partial-covering model was used to fit the energy spectrum (with two blackbodies), but it was noted that the model could be interpreted as a direct component plus a scattered component. The *ASCA* spectra also showed an iron K edge due to absorption with column densities near 10^{24} cm^{-2} . Thus our results are generally consistent with the *ASCA* results, but we are able to demonstrate how the continuum spectrum evolves throughout dips.

An iron line at 6.4 keV was seen in the low-state *ASCA* spectrum, but no line was detected at a similar flux level in the high-state spectrum [12]. Our analysis shows that an iron emission line appears to be associated with the faint component, and is present outside dips at the same flux level.

Since scattering by an extended cloud of material is probably responsible for the faint component, it is likely that the iron $K\alpha$ emission is also produced as a result of the scattering process.

The fact that absorption dips in Cir X-1 mainly occur within a day of phase zero and are then followed by significant flaring, suggests that the dips are associated with the mass transfer process. Thus, absorption might be due to the mass transfer stream itself or due to a bulge on the disk produced by the addition of matter. The intermittent nature of the PCA light curves near phase zero (Figure 7-1) indicate that we are observing the fine structure (temporal or geometrical) of the obscuring material.

Chapter 8

Multi-frequency Observations

8.1 Overview

The 16.55-d X-ray period of Cir X-1 is also seen in the radio, infrared, and optical bands (see Chapter 1). We organized two multi-frequency campaigns, in 1996 May and 1997 June, to study correlated variability in different frequency bands. Such observations have the potential to constrain emission mechanisms and provide information about the mass accretion rate. For example, in Z source LMXBs the optical flux is believed to result from higher energy photons being reprocessed in the accretion disk. Thus optical intensity is taken as a measure of mass accretion rate, and has been used to argue that mass accretion rate increases along Z source spectral tracks from the horizontal branch, down the normal branch, and onto the flaring branch [28, 2].

8.2 May 1996 Campaign

The first campaign (see Table 8.1) occurred during 1996 May 7–14, covering a week including phase zero on May 11.413 UT (JD 2450214.913). Radio observations were made from South Africa with the 28-m dish at Hartebeeshoek Radio Astronomical Observatory (HartRAO) by George Nicolson. Infrared observations were made with the 1.9-m telescope at the South African Astronomical Observatory (SAAO) by Ian Glass. In addition to the ongoing All-Sky Monitor observations, seven *RXTE* PCA (and *HEXTE*) observations were made with a combined exposure time of 54 kiloseconds.

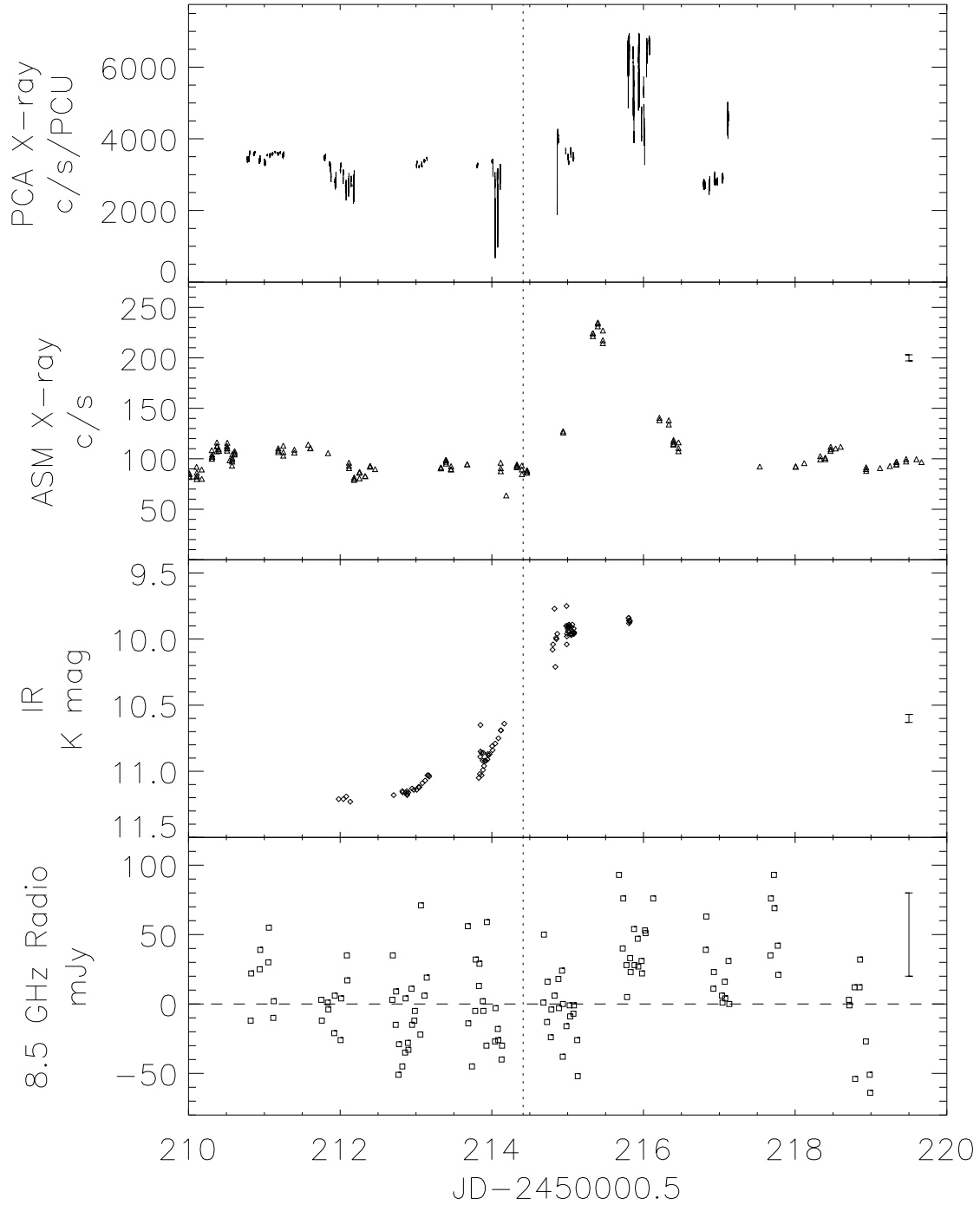


Figure 8-1: X-ray, IR, and radio light curves of Cir X-1 from 1996 May 7–17. Phase zero is indicated by the vertical dotted line at day 214.413 (1997 May 11.413). PCA intensity is from the 2–32 keV band (16-s bins) and ASM intensity is from 2–12 keV (90-s exposures). Errors on the PCA data are negligible. Typical error bars are shown for the ASM, IR, and radio data: errors on the ASM data are typically 2–5 c/s, on the IR data are typically about 0.03 magnitudes (worse on days 214 & 215), and on the radio data are about 30 mJy. The average quiescent level of 29 mJy has been subtracted from the radio data. (Data provided by I. Glass (IR), G. Nicolson (radio), and the *RXTE*/ASM team.)

Frequency Band	Observatory	Type of Observation	Dates
Radio	HartRAO	8.5 GHz (3 samples/d)	ongoing
		8.5 GHz & 5.0 GHz	May 10–15
IR	SAAO (1.9 m)	K-band photometry	May (7),8–12,(13)
X-ray	RXTE	ASM	ongoing
X-ray	RXTE	PCA	May 7–14

Table 8.1: Multi-frequency Observations of Cir X-1 from 1996 May. Dates in parentheses were cancelled due to poor weather conditions.

8.2.1 Radio (HartRAO)

Radio intensity measurements of Cir X-1 at 8.5 GHz (3.5 cm) are routinely carried out as often as several times daily at HartRAO. In recent years the periodic flares have been weak, i.e. no flares above 100 mJy, compared to 200 mJy – 2 Jy between 1976–1986 ($1 \text{ Jansky} = 1 \text{ Jy} = 10^{-26} \text{ W m}^{-2} \text{ Hz}^{-1}$). In fact, radio flares since 1986 have not been strong enough to update the radio ephemeris.

In conjunction with our multi-frequency campaign, HartRAO observations were made 12–20 times per day at both 8.5 GHz and 5.0 GHz from 1996 May 10–15 and 5–7 times per day at 8.5 GHz for several days prior to and after that period. Each measurement takes about 8 minutes. The observations are made as drift scans, i.e., the telescope is stationary during a scan, which begins pointing ahead of the source. Because Cir X-1 lies in the Galactic plane, there is strong confusion from other sources such as H II regions and the supernova remnant with which Cir X-1 is associated. A quiescent average scan is subtracted from the data and then fit the telescope beam pattern at the position of Cir X-1. This method gives a residual flux relative to the quiescent background rather than the absolute flux, but is sufficient to monitor the flaring behavior.

The 8.5 GHz data from JD-2450000.5 = 210–219 are shown in Figure 8-1. The error on a typical point is about 30 mJy (1σ). The average flux from observations between phase 0.2 to 1.0 is 29 mJy, and has been subtracted from the data. There is no evidence for variability during that phase interval. Between days 215.5–218.0 (phase ~ 0.05 –0.2) the flux is higher. After subtracting the 29 mJy quiescent level from the data, then 66% of the data points lie between 2–5 sigma above the noise of 19 mJy. This is consistent with weak flaring observed in other cycles from earlier in 1996, but flaring may be occurring earlier in the cycle than the corresponding period in 1995, when the flaring was between phases 0.2–0.3.

8.2.2 Infrared Photometry (SAAO)

The infrared observations at SAAO provided K band ($2.2 \mu\text{m}$) photometry measurements 4–32 times per night for five nights from 1996 May 8–12 (see Figure 8-1). An aperture of 9 arcsec diameter was used. The K magnitude was 11.2 on May 8–9 (day 211–212) and gradually brightened by about 1 magnitude during May 10–12 (day 213–215) to 10.15 (K = 0 mag corresponds to a flux density of $6.3 \times 10^{-23} \text{ W m}^{-2} \text{ Hz}^{-1}$, and other magnitudes are related to flux through $m_2 - m_1 = -2.5 \log[F_2/F_1]$). The quiescent and flaring magnitudes are similar to those obtained by Glass during 1980–1993, but are somewhat lower than the high values (K=9.5 to 7.7) observed in the late 1970's [24]. Observing conditions during the first two and last nights were good and the errors are 0.03 mag or better. The data suggest a possible precursor event during day 214; however the observing conditions were not as good during the third and fourth nights. When the conditions were bad, Cir X-1 was measured relative to star J from the image in Whelan et al. [83], which was used as a standard taken to be K=9.82.

8.2.3 Correlated Multi-frequency Variability

The X-ray and radio light curves in Figure 8-1 reach a peak value during the second day after phase zero, while the IR reaches a peak value only 0.5 d after phase zero. The PCA and IR data both show evidence for increasing variability before phase zero. Furthermore, both show a gradual rise in intensity during the period from day 213.0 to 213.15, shown in more detail in Figure 8-2. Fourier power spectra from each of the five PCA segments in Figure 8-2 show a narrow quasi-periodic oscillation peak at 26.0 Hz, 24.2 Hz, 25.4 Hz, 31.54 Hz, and 37.61 Hz (in time order of the five segments). This timing behavior indicates that increasing X-ray intensity corresponds to motion to the right or down the horizontal branch in a hardness-intensity diagram (see Chapters 5 & 6 and [63]). Thus, this segment shows IR flux increasing from the horizontal branch toward the normal branch, similar to the optical trend in Z sources [28, 2].

8.3 June 1997 Campaign

The second campaign (see Table 8.2) occurred during 1997 June 4–22, covering a half cycle before and after phase zero on June 12.506 UT (JD 2450612.006). Radio observations were made from South Africa at Hartebeeshoek Radio Astronomical Observatory (HartRAO) by George Nicolson. Infrared photometry measurements were made with the 1.9-m telescope at the South African Astronomical Observatory (SAAO) by Ian Glass. IR spectroscopy at the the ANU 2.3 m telescope in Siding Springs, Australia and optical spectroscopy at the Anglo-Australian Telescope (AAT, 3.9 m) were

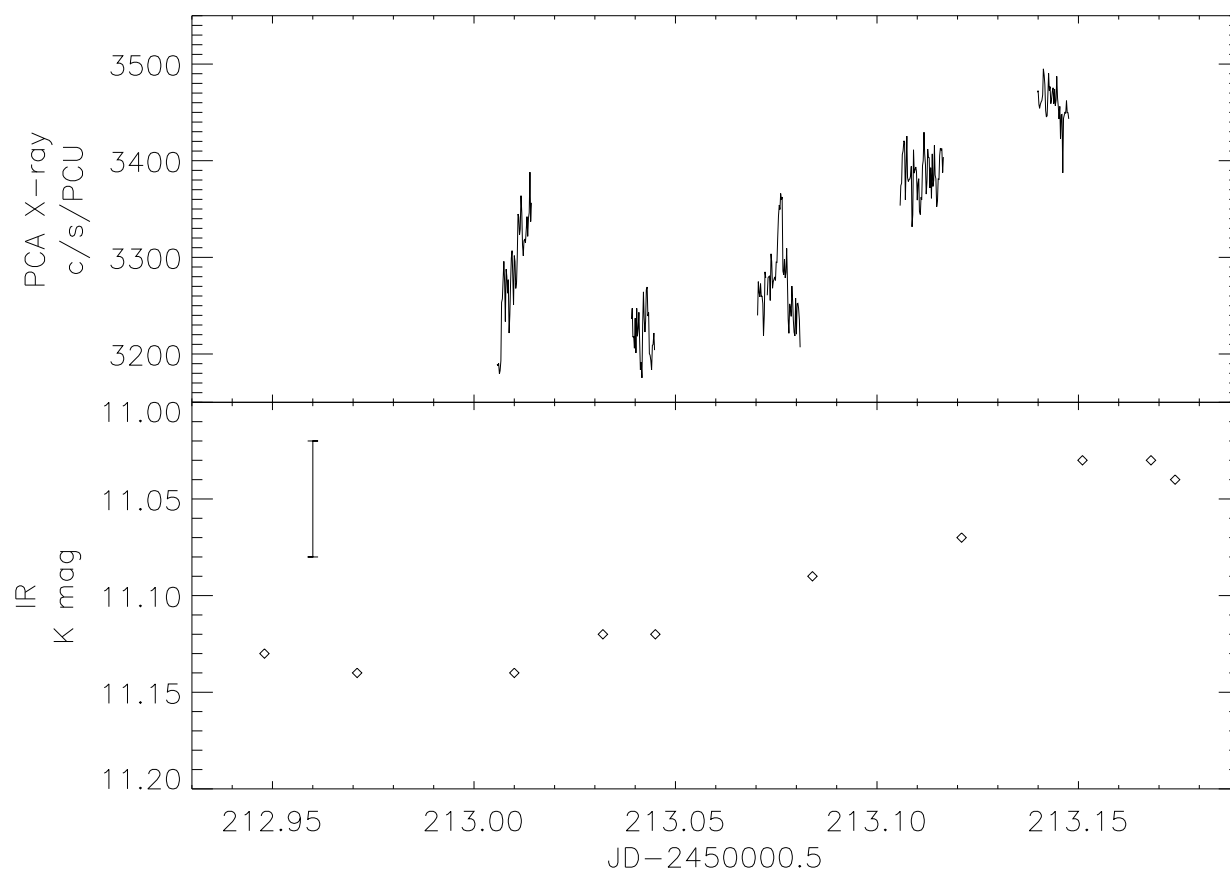


Figure 8-2: X-ray and IR light curves of Cir X-1 from day 212.93–213.19. X-ray intensity is from the 2–32 keV PCA band (16-s bins). A typical IR error bar of ± 0.03 magnitudes is shown. (IR data courtesy of I. Glass.)

Frequency Band	Observatory	Type of Observation	Dates
Radio	HartRAO	8.5 GHz & 5.0 GHz	ongoing
IR	SAAO (1.9 m)	K-band photometry	June (10–14),15–16
	ANU (2.3 m)	K-band spectroscopy	June (12),20
Optical	AAT (3.9 m)	spectroscopy	June 4,(12)
X-ray	RXTE	ASM	ongoing
		PCA (samples)	June 4,6,8,18,19,20
		PCA (\sim continuous)	June 11–17

Table 8.2: Multi-frequency Observations of Cir X-1 from 1997 June. Dates in parentheses were cancelled due to poor weather conditions.

carried out by Rob Fender, Kinwah Wu, and Helen Johnston. In addition to the ongoing All-Sky Monitor observations, extensive *RXTE* PCA (and *HEXTE*) observations were made, with 56% coverage over 7 days around phase zero, and shorter observations before and after that week. The X-ray observations for this campaign are discussed in Chapter 6.

8.3.1 Radio (HartRAO)

In conjunction with our multi-frequency campaign, coverage during the ongoing radio (8.5 GHz and 5.0 GHz) monitoring at HartRAO was increased. The 5.0 GHz radio data for 1997 May – August are shown in Figure 8-3, along with the ASM light curve and the PCA data from the 1997 June observations (study G) and the brief observations from 1997 May (study F). As in the previous year, the radio intensity was faint with only minimal variability (a constant DC bias level has again been subtracted). However, in at least two cycles (starting at days 611 and 661), including the cycle that was the main focus of this multi-frequency campaign, there does appear to be weak evidence for flaring at about the same time as the X-ray flaring observed with the PCA and ASM.

8.3.2 IR Photometry (SAAO)

Infrared photometry observations (see section 8.2.2) were scheduled at SAAO for seven nights, from 1997 June 10–16 (JD-2450000.5 = 609–615). Due to poor weather conditions, only limited data were obtained, shown in Table 8.3. On June 14, the JHK magnitudes are similar to typical peak values observed since 1980. On June 15, the K magnitude is about 0.5 mag lower, but still well above the typical quiescent value of $K \approx 11.5$.

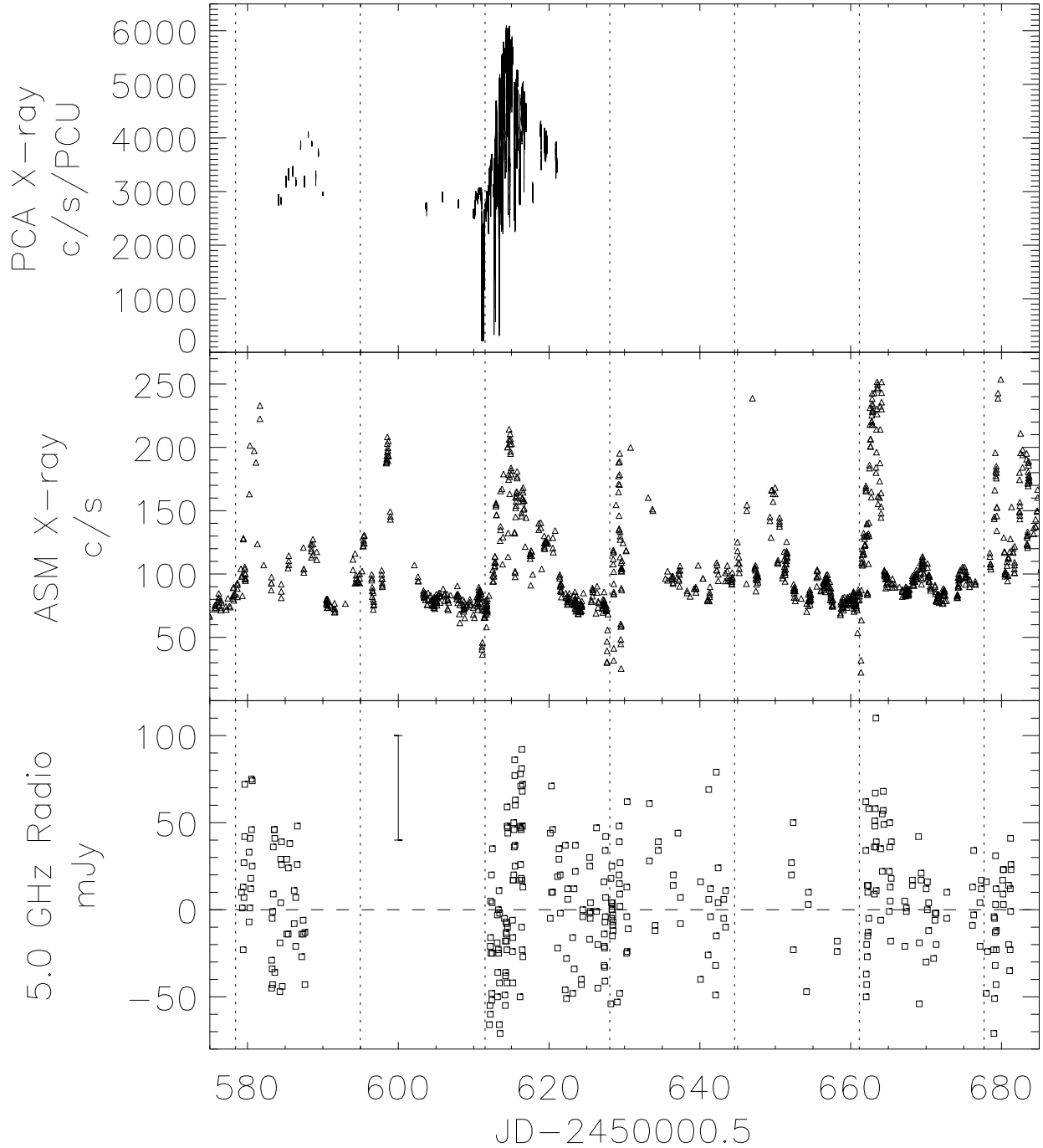


Figure 8-3: X-ray (PCA and ASM) and radio (5.0 GHz) light curves of Cir X-1 from 1997 May 7 – August 25. Phase zero is indicated by the vertical dotted lines. PCA intensity is from the 2–32 keV band (16-s bins) and ASM intensity is from 2–12 keV (90-s exposures). Errors on the PCA data are negligible and errors on the ASM data are typically 2–5 c/s. For each 16.55-d cycle, the average radio flux for the phase interval 0.3 to 0.9 of that cycle was subtracted from the data; the bias removed was typically 50–60 mJy and a typical error bar is shown. (The radio data was provided by G. Nicolson, and ASM data by the *RXTE*/ASM team. The PCA data are from studies F and G; see Table 3.1.)

JD	J	H	K	L
2450614.35	11.97	10.68	9.88	8.98
.42			9.88	
.48			9.85	
2450615.41			10.34	

Table 8.3: Infrared JHKL photometry measurements from 1997 June 14 & 15. Errors are $+/- 0.03$, except on the L magnitude the error is $+/- 0.05$.

8.3.3 IR Spectroscopy (ANU)

Infrared K-band spectroscopy was carried out at the ANU 2.3 m telescope at Siding Spring, Australia. Two nights were scheduled, near phase 0.0 on June 12 and near phase 0.5 on June 20. Observations on the first night were cancelled due to bad weather, but conditions were more favorable on June 20 and good quality K-band spectra of Cir X-1 were obtained (see Figure 8-4). The spectrum shows H Brackett γ and HeI emission lines. Both lines are red-shifted by about +430 km/s, and there is a hint of asymmetry on the blue (shorter wavelength) wing.

8.3.4 Optical Spectroscopy (AAT)

Optical spectroscopy at the H α region (6100–7200 Å) was carried out with the AAT 3.9 m telescope. Observations were scheduled on two nights, near phase 0.5 on June 4 and near phase 0.0 on June 12. Like the ANU observations on June 12, the AAT observations on that night were cancelled due to bad weather. The observations on June 4 were successful, and six good-quality spectra were obtained. The average spectrum, normalized by the continuum, is shown in Figure 8-5. This spectrum shows a prominent H α emission line, as well as weaker HeI(6678 Å) and HeI(7065 Å) lines. The H α line is asymmetric, as suggested by previous observations [17, 47, 53, 83], and can be fit well by two Gaussians lines: a broad component blue-shifted from the rest wavelength by -300 km/s and a narrow component red-shifted from the rest wavelength by +375 km/s. The two narrow HeI lines are red-shifted by an amount similar to the narrow H α line, and thus all three show a similar red-shift to the lines in the IR spectrum in section 8.3.3. All three narrow lines have widths of about 9.5 Å, or ~ 400 km/s, while the width of the broad H α component is 46 Å, or 2100 km/s.

8.3.5 Comparison of the AAT Optical Spectrum to HST Results

The optical spectrum obtained with AAT during our 1997 June campaign is comparable to the spectrum of Cir X-1 obtained with the Hubble Space Telescope (HST) Faint Object Spectrograph (FOS) in 1995 June by Mignani, Caraveo, & Bignami [47]. The HST spectrum also showed an

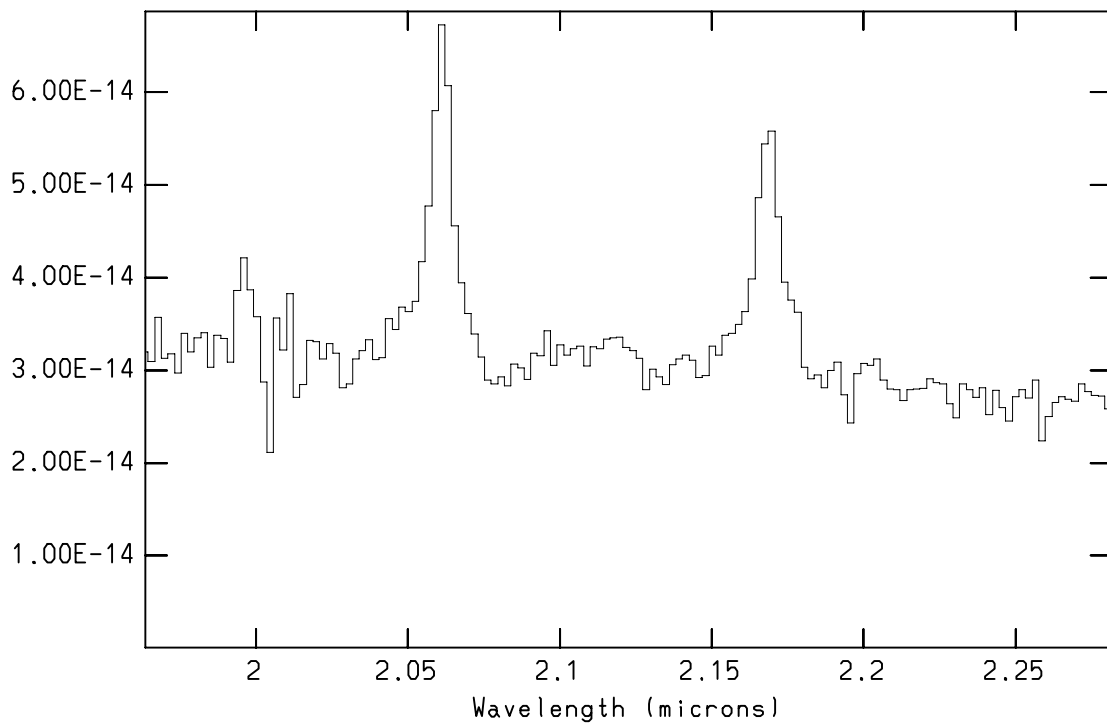


Figure 8-4: Infrared spectrum of Cir X-1 from ANU on 1997 June 20 (about phase 0.5), showing He I ($2.06\ \mu\text{m}$) and H Brackett γ ($2.165\ \mu\text{m}$) emission lines. This spectrum was compiled from the sum of 16 120-s exposures. (Figure courtesy of H. Johnston.)

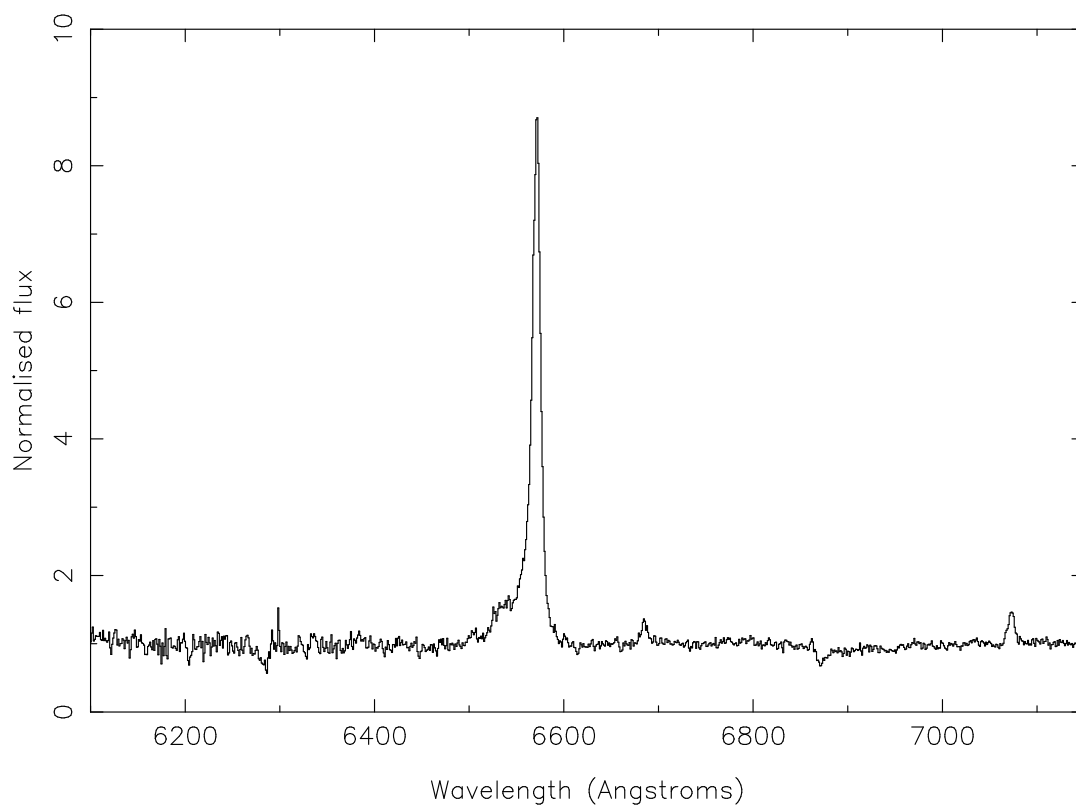


Figure 8-5: Optical spectrum of Cir X-1 from AAT on 1997 June 4 (about phase 0.5), showing a prominent $H\alpha$ emission line, as well as weaker He I(6678 Å) and He I(7065 Å) lines. (Figure courtesy of H. Johnston.)

asymmetric $H\alpha$ emission line, and was likewise fit by a broad and a narrow Gaussian line. The broad line is centered on the $H\alpha$ rest wavelength and has a width of 11.4 \AA . The narrow component is red-shifted by 380 km/s and has a width of 3.32 \AA . Based on the HST results, the authors suggested that the broad line originates in the accretion disk, with temperatures of order $\sim 20000 \text{ K}$ responsible for its large width. They further suggest that the narrow line arises from a “hot spot” where the accretion stream from the companion impacts the disk. Thus the narrow line, observed at phase zero with HST, was expected to be observed at varying blue/red-shifts at other orbital phases.

The interpretation suggested for the HST spectrum is not compatible with the additional results obtained with AAT, which show the narrow line at almost the same wavelength as HST, but at phase 0.5. Furthermore, it is the *broad* component which has shifted, from the rest wavelength to -300 km/s blue-shifted. Clearly, further observations at various orbital phases are needed. If the narrow $H\alpha$ component, and the other optical and IR lines, prove to be fixed at about $+400 \text{ km/s}$, then that velocity might reflect the radial velocity of the system, providing further support for the hypothesis that Cir X-1 is a high-velocity runaway from SNR 321.9-0.3. Measuring the velocity of the shifting broad component might help map the binary orbit, about which very little is securely known.

8.4 Conclusions

The X-ray light curves of Cir X-1 show significant variability on all time scales down to seconds (and even shorter time scales including the QPOs). Unfortunately, most observations at other wavelengths typically provide measurements on timescales of hours, allowing only coarse correlations to be studied. Yet even those measurement can be quite valuable. For instance, our multi-frequency campaign from 1996 has shown that according to the ephemeris equation currently in use (equation 1.1), the X-ray, IR, and radio bands all show enhanced emission within a day of phase zero (all peaking after phase zero). The 1997 radio data also show weak evidence for flares after phase zero, coincident with those in the X-ray band. The correlated increase in IR and X-ray intensity over several hours shown in Figure 8-2 demonstrates the need for observations with improved time-resolution.

Clearly a return of the radio intensity to its previous bright levels would be very useful in improving the orbital ephemeris equation (i.e., testing the change in period implied by the current quadratic term.) Bright radio flares would also be able to be studied in much greater detail than the current marginal detections, allowing short-term correlation with other wavelengths to be explored. Delays of specific events between wavebands would provide information on how photons are being

reprocessed from one band into another. We continue to maintain a Target of Opportunity proposal with *RXTE* to provide X-ray coverage, should bright radio flares return.

As mentioned above, one promising follow-up project to these campaigns is to study the shifting optical/IR emission lines. If such work can provide information about the binary orbit (through Doppler mapping), then the X-ray data can be re-examined with more consideration of the geometry of the system. This work may begin as early as this summer.

A promising radio-interferometry imaging project is the attempt to detect proper motion of Cir X-1 away from the nearby supernova remnant (SNR), as is expected in the runaway binary scenario (see Chapter 1). Based on the 700–2000 km/s velocity implied by its distance from the SNR, and assuming a distance of 8 kpc, suggests that proper motion might be of order $1''$ in 20 yr [67], which could be detected in only a few years of precise measurements. Confirmation of association with the SNR, and thus of a young age, would be highly significant to our understanding of the evolution of the system. Preliminary work has recently been started on this project (by R. Fender et al.), with Australia Telescope Compact Array (ATCA) images taken to establish the location of an appropriate point source to use as a reference for proper motion measurements. Such radio imaging may also provide further information on the jet-like structures seen inside the synchrotron nebula surrounding Cir X-1.

Chapter 9

Mass Transfer in an Eccentric Binary

9.1 Overview

Mass transfer in X-ray binaries generally occurs through Roche-lobe overflow or via a stellar wind. Significant stellar winds only occur in high-mass donor (O or B) stars. Although the X-ray properties of Cir X-1 most resemble those of a low-mass X-ray binary, the true nature of the donor star and the mechanism for mass transfer remain uncertain (see section 1.3.6). Furthermore, the high eccentricity inferred from the 16.55-d intensity cycle of Cir X-1 will have a significant effect on how mass transfer occurs. In this chapter, I explore the effect of eccentricity on mass transfer through both Roche-lobe overflow and a stellar wind.

9.2 Mass Transfer via Roche-Lobe Overflow

Mass transfer in most low-mass X-ray binaries is believed to occur through Roche-lobe overflow, wherein one star fills its critical equipotential surface and matter from the stellar surface streams through the inner Lagrange (L1) point (a saddle point in the net gravitational and centrifugal potential between the stars) toward the other star. As matter flows in, the Coriolis force causes it to orbit the compact object, forming an accretion disk wherein matter loses angular momentum through viscosity and spirals inward. In an eccentric orbit, the situation is much more complicated, with such mass transfer limited to the time near periastron passages. To help understand the behavior of mass transfer in an eccentric binary, I developed a computer code to follow the trajectory of a

test particle started from the surface of a donor star and moving in an eccentric binary system. The particle was followed until it reaches the neutron-star accretion disk, returns to the donor, or leaves the system.

9.2.1 Equipotential Surfaces in an Eccentric Binary Orbit

The standard Roche-lobe framework describes the potential of a binary pair of stars in circular orbit, co-rotating at the orbital frequency. In an eccentric orbit, not only does the separation between the stars vary, but so does the instantaneous angular frequency of the orbit, making co-rotation impossible. A generalized Roche potential for centrally condensed stars in an eccentric binary orbit has been derived by Avni [3]. A Cartesian coordinate system was used, with the origin at the center of mass of star 1, of mass M_1 , which rotates with an angular velocity ($\vec{\omega}_{rot}$) along the Z axis. The reference frame rotates about the center of mass of star 1 such that star 2 (of mass M_2), always lies on the +X axis. The potential at a point (X,Y) is:

$$\psi = -\frac{GM_1}{d_1} - \frac{GM_2}{d_2} + \frac{GM_2}{D^2}X - \frac{1}{2}\omega_{rot}^2(X^2 + Y^2) \quad (9.1)$$

where d_1 and d_2 are the distances from (X,Y) to the center of mass of each star and D is the instantaneous separation of the stars. To determine the location of the instantaneous inner Lagrange point, this potential is maximized along the line connecting the centers of the two stars. Although this potential is derived for the frame rotating with the orbit (and thus with an angular frequency continuously changing to match the instantaneous Keplerian frequency) the location of the L1 point is specified by a distance from the center of mass of star 1 along the line between the stars, and is thus well-defined in an inertial frame. Likewise, the quantities in equation 9.1 necessary to calculate the location of the L1 point are distances and masses, which can be measured in inertial space, and the angular rotation frequency of star 1, which is also measured in the inertial frame. Thus, this equation can be used to locate the instantaneous L1 point in an inertial frame, which will prove convenient in the calculation below.

9.2.2 Keplerian Orbits

Keplerian orbits can be parameterized by a quantity known as the eccentric anomaly, u , which evolves in time according to Kepler's equation:

$$\frac{2\pi t}{P} = u - e \sin u, \quad (9.2)$$

where t is the time elapsed since periastron, P is the orbital period, and e is the eccentricity. The left-hand side of equation 9.2 is also known as the mean anomaly. The separation vector of the two stars is then given by:

$$\begin{aligned} x(u) &= a(\cos u - e) \\ y(u) &= a\sqrt{1 - e^2} \sin u, \end{aligned} \quad (9.3)$$

where a is the semimajor axis of the orbit (half of the maximum separation distance of the stars), and periastron lies along the $+x$ axis. For each time step, equation 9.2 is solved for u via Newton's method, and the positions of the two stars are calculated from equations 9.3. The velocities of the stars can be calculated by substituting du/dt , from the time derivative of equation 9.2, and u into the time derivatives of equations 9.3.

9.2.3 Trajectory of a Particle in the Binary Potential

The trajectory of a particle of negligible mass m moving in the potential of a binary system can be calculated by integrating the instantaneous velocity and acceleration of the particle in the inertial (non-rotating) frame of reference as the stars move in their orbits. The instantaneous velocity (\vec{v}_m) and acceleration are given by:

$$\frac{d\vec{r}_m}{dt} = \vec{v}_m, \quad (9.4)$$

and

$$\frac{d\vec{v}_m}{dt} = \frac{\vec{F}_m}{m} = -\frac{GM_1m(\vec{r}_m - \vec{r}_1)}{|\vec{r}_m - \vec{r}_1|^3} - \frac{GM_2m(\vec{r}_m - \vec{r}_2)}{|\vec{r}_m - \vec{r}_2|^3}, \quad (9.5)$$

where the subscripts 1, 2, and m refer to the two stars and the particle respectively, \vec{F}_m is the gravitational force on the particle, M is the mass of a star, and \vec{r} is a position vector. The x and y components of equations 9.4 and 9.5 are integrated by a Runge-Kutta algorithm [57] to obtain the trajectory of the particle. The initial coordinate of the particle is taken to be a point on the surface of the donor (whose radius is defined to be the size of its critical lobe at periastron and held constant around the orbit) on the line between the centers of the two stars. The initial velocity of the particle is the vector sum of the instantaneous orbital velocity of the donor, the velocity of a particle on the surface due to rotation of the donor, and possibly an additional radial velocity away from the surface (see below).

9.2.4 Final Outcome of Particle Trajectories

The possible final outcomes of the particle trajectory are as follows:

1. It is assumed that the accretion disk almost fills the instantaneous critical lobe of the neutron

star at periastron (i.e., 80% of the distance between the neutron star and the L1 point at periastron), and that the disk maintains that size at all other orbital phases. The particle is assumed to have **entered the disk** if it passes closer than this distance from the neutron star at any point in the orbit.

2. The donor is likewise assumed to fill its critical lobe at periastron and maintain that radius throughout the orbit. The particle is considered to be **recaptured** if it re-enters that radius relative to the donor at any point in the orbit.
3. The particle is assumed to be **ejected** from the binary (or at least no longer a likely contributor to mass transfer) if its distance from the CM exceeds twice the semimajor axis of the orbit.
4. After two full binary orbits, if none of the above three cases have occurred, the outcome is **undetermined**.

In all cases, the orbital period was taken to be that of Cir X-1, 16.55 days, and the mass of the neutron star was taken to be $1.4 M_{\odot}$. For simplicity, the donor star is assumed to rotate uniformly at the average Keplerian frequency ($\omega_{rot} = 2\pi/16.55$ days). Also, a donor mass of $1 M_{\odot}$ has been adopted for the discussion below, where results are shown for two eccentricities: 0.5 and 0.8. Such values might be close to actual values for Cir X-1, but are mainly chosen for illustrative purposes.

Figure 9-1 shows the final outcome of particles which were released from the surface of the donor at different orbital phases (evenly spaced in time) of a system with $e = 0.5$. The top panels (Figures 9-1a, b) are for an initial radial velocity off the surface of 30 km/s, or about 15% of the escape velocity from the star (if it were isolated). In Figure 9-1a, one can see the arrival time as a function of start time, where the different symbols indicate where the particle entered the accretion disk and where it was recaptured by the donor. Only particles that begin transfer during the interval -0.9 to $+0.3$ days relative to periastron eventually enter the disk, and most of the particles arrive at the disk (Figure 9-1b) closely spaced in time near day 0.3 or shortly after. Figures 9-1c and 9-1d show that similar behavior occurs for particles with a larger radial velocity from the surface of 60 km/s ($\sim 30\%$ of the escape velocity from the donor). The larger initial velocity allows particles to reach the disk over a somewhat longer portion of the orbit, and also results in most of the particles reaching the disk *before* periastron.

The fact that mass transfer is most effective for particles released before periastron is related to the relative velocity of the stars in their eccentric orbit. Particles released as the stars approach periastron naturally move toward the neutron star, and are more likely to be captured by the disk. Particles released after periastron have to try to “catch up” to a receding neutron star, and after a certain point will simply be recaptured by the donor. The asymmetric profile of particles entering

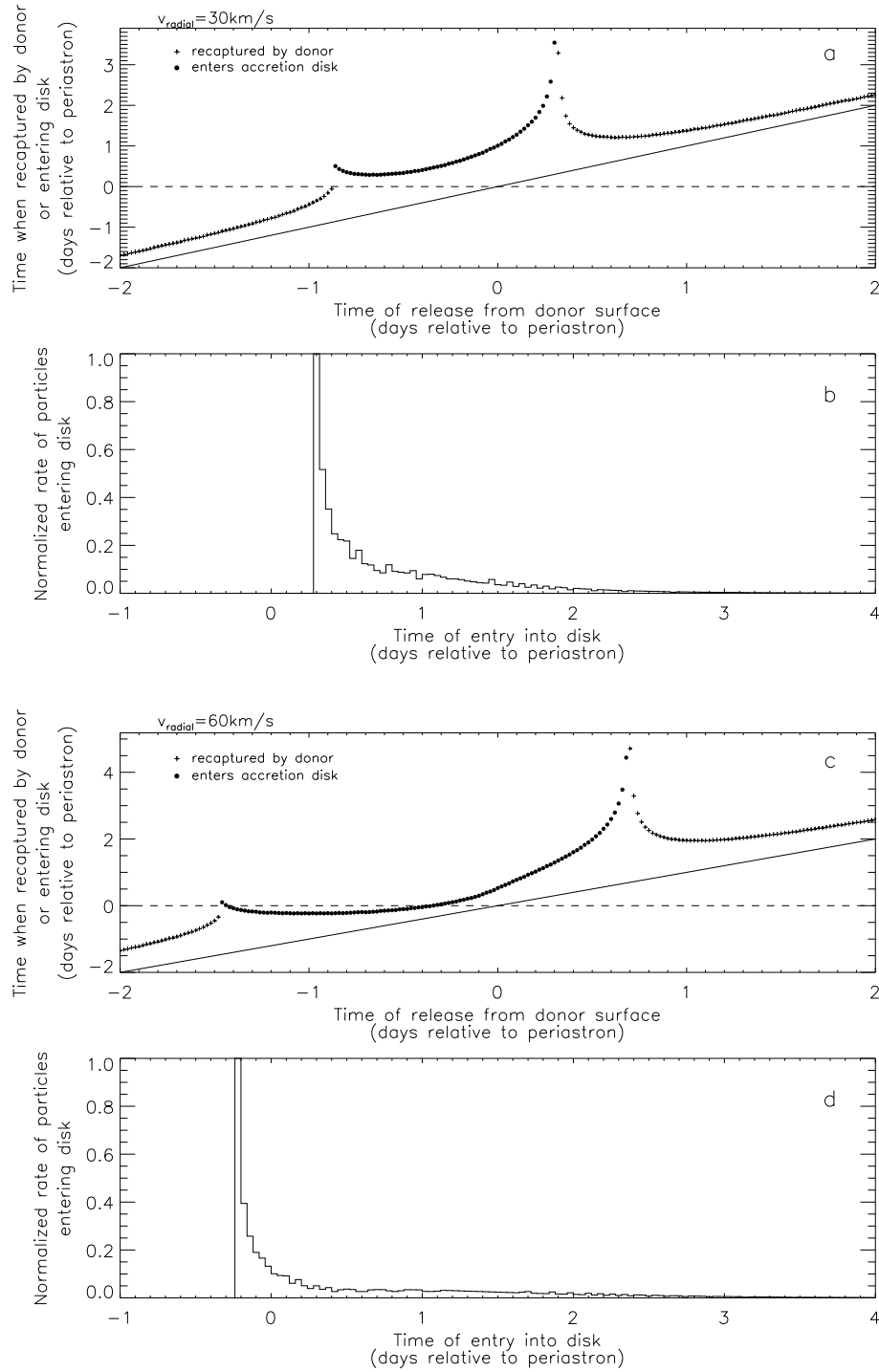


Figure 9-1: Panels (a) and (c): stop time of particles in a system with $e=0.5$ (and $P=16.55 \text{ d}$) versus time of release from donor ($1 M_{\odot}$), with the final outcome (recapture or entry into disk) indicated. Panels (b) and (d): normalized rate of particles entering the accretion disk versus their arrival time relative to periastron. The top panels, (a) and (b), are for an initial radial velocity from the surface of 30 km/s , and the bottom panels, (c) and (d), are for 60 km/s . In (a) and (c), the solid diagonal line has a slope of unity and indicates zero elapsed time between release and the final outcome; the horizontal dashed line indicates a final outcome occurring at periastron.

the disk is also related to the relative motion of the stars. Particles released shortly before periastron are carried along the orbit of the donor and their arrival times are thus focussed near the time of periastron.

Figures 9-2a and 9-2b show the outcome of a similar transfer scenario as Figure 9-1, but with a larger eccentricity ($e = 0.8$) and with each particle receiving an initial release velocity of 50 km/s radially away from the surface of the donor (again about 15% of the escape velocity). The higher eccentricity confines mass transfer to a narrower range of orbital phase, mainly a release within 0.15 d prior to periastron passage.

Figures 9-2c and 9-2d also show the outcome of transfer in a system with $e = 0.8$, but with a larger radial velocity of 100 km/s ($\sim 30\%$ of the escape velocity from the donor). In this case the accretion rate shows two sharp peaks after periastron passage, separated by only 0.25 d (Figure 9-2d). The combined high orbital velocity approaching periastron in the eccentric orbit and the high initial velocity from the surface cause some particles to initially “overshoot” the neutron star, eventually to be captured in the disk, but only after a delay that concentrates the arrival time of many particles near day 0.4

Eight illustrative trajectories for some of the test particles shown in Figure 9-1c ($e = 0.5$), released at various orbital phases with $v_{radial} = 60$ km/s, are shown in Figure 9-3. These plots show how the motion of the two stars in their eccentric orbits can produce a wide variety of trajectories for a particle transferred from the surface of the donor.

9.2.5 Comparison to the X-ray Intensity Profile

The sharp rise time of the number of particles entering the accretion disk in Figures 9-1 and 9-2 resembles the sharp rise in X-ray intensity from Cir X-1 after phase zero (not necessarily periastron) in the ASM light curve (see Chapter 3). These peaks are quite narrow (generally only a fraction of a day) compared to the ~ 3 -5 days typically observed in the X-ray light curve. However, the actual intensity profile depends on additional factors, such as the duration of time that matter spends in the disk before falling onto the neutron star. These results serve primarily as an example of what can be done once more is known about the parameters of the Cir X-1 system, such as the actual eccentricity and the mass and stellar type of the donor.

9.3 Mass Transfer via a Stellar Wind

When the donor star in an X-ray binary does not fill its Roche lobe, a stellar wind or other outflow must be responsible for mass transfer. This is the case in some high-mass X-ray binaries, where

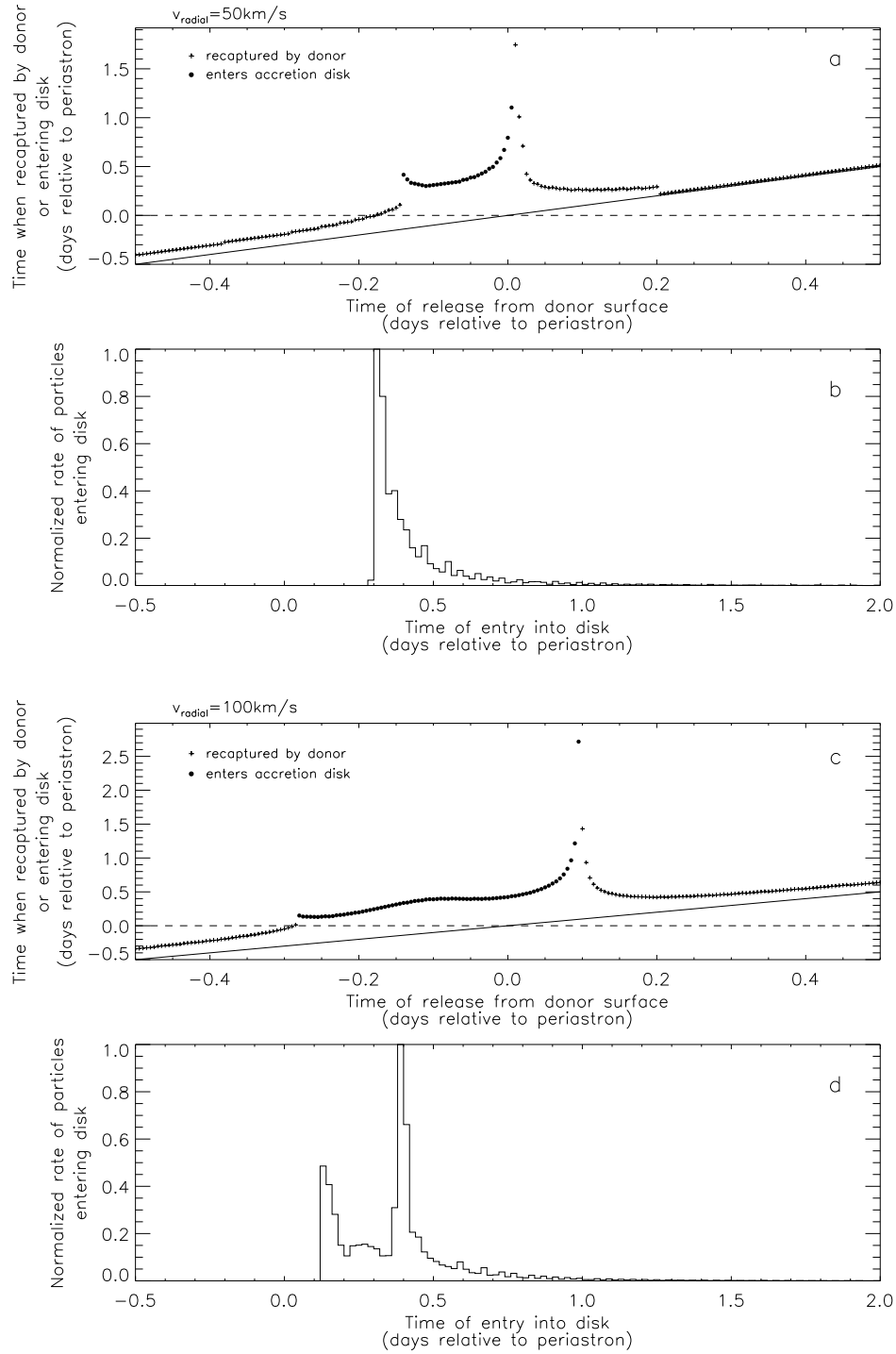


Figure 9-2: Panels (a) and (c): stop time of particles in a system with $e=0.8$ (and $P=16.55 \text{ d}$) versus time of release from donor ($1 M_{\odot}$), with the final outcome (recapture or entry into disk) indicated. Panels (b) and (d): normalized rate of particles entering the accretion disk versus their arrival time relative to periastron. The top panels, (a) and (b), are for an initial radial velocity from the surface of 50 km/s , and the bottom panels, (c) and (d), are for 100 km/s . In (a) and (c), the solid diagonal line has a slope of unity and indicates zero elapsed time between release and the final outcome; the horizontal dashed line indicates a final outcome occurring at periastron.

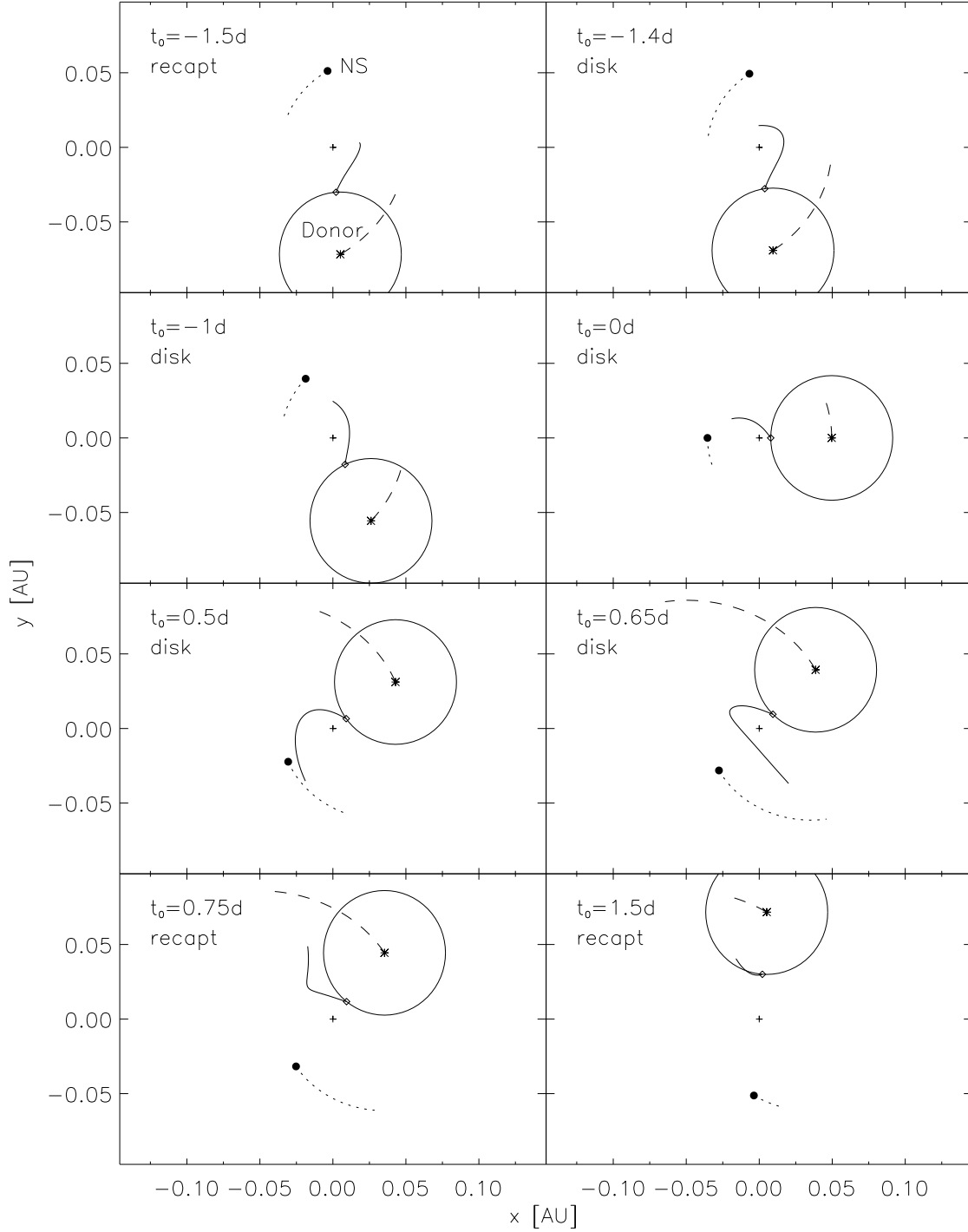


Figure 9-3: Trajectory of a particle moving in an eccentric binary system ($M_{don}=1 M_{\odot}$, $e=0.5$), where the particle starts with an initial radial velocity of 60 km/s off the surface of the donor at a time t_0 relative to periastron. The plot is in a non-rotating frame with the CM at the origin (+). The location of the particle, donor star, and neutron star at t_0 are indicated by the diamond, asterisk, and solid dot respectively. The subsequent motion of the particle until enters the accretion disk or is recaptured is shown as a solid curve, and the motion of the donor and neutron star in their orbits during that time is indicated by a dashed or dotted ellipse segment respectively.

the donor star experiences significant mass loss via a wind from the surface. Since a high-mass companion for Cir X-1 cannot yet be ruled out, I also studied wind transfer in an eccentric binary. I developed a computer code to study the mass transfer rate as a function of orbital phase. The resulting theoretical mass accretion profiles can be compared with the observed X-ray intensity profiles, which at least in some circumstances may be a measure of the accretion rate.

9.3.1 Bondi-Hoyle Accretion

Material in the stellar wind passing within a critical radius of the neutron star is sufficiently deflected by the gravitational field of the neutron star to eventually be captured and accrete onto the surface (first presented by Bondi & Hoyle in 1944 [9]). Since the wind material flows around both sides of the neutron star (in the orbital plane; the problem is actually three-dimensional) the net angular momentum of the captured matter is small and accretion occurs without forming an accretion disk. The critical radius, i.e., the maximum accretion radius (r_{acc}), is the radius inside which the gravitational potential energy due to the neutron star exceeds the kinetic energy of the particles in the wind due to the relative velocity of the wind and neutron star ($\vec{v}_{rel} = \vec{v}_{wind} - \vec{v}_{orb}$) and the thermal particle motion (related to the sound speed v_s):

$$\frac{GM_{ns}m}{r_{acc}} \simeq \frac{1}{2}mv_{rel}^2 + \frac{1}{2}mv_s^2, \quad (9.6)$$

where M_{ns} is the mass of the neutron star and m is the mass of a wind particle (mainly protons). Solving equation 9.6 for the critical accretion radius gives

$$r_{acc} \simeq \frac{2GM_{ns}}{v_{rel}^2 + v_s^2}. \quad (9.7)$$

The mass accretion rate is then

$$\dot{M}_{acc} = \rho(r)v_{rel}\pi r_{acc}^2, \quad (9.8)$$

where $\rho(r)$ is the density of the wind at a distance r from the center of the donor star, i.e., the separation between the stars. Conservation of mass provides an expression that relates the mass loss rate of the donor due to wind (\dot{M}_w), v_{wind} , and $\rho(r)$:

$$\dot{M}_w = \rho(r)v_{wind}4\pi r^2. \quad (9.9)$$

Combining equations 9.7, 9.8, and 9.9 gives the fraction of the wind captured by the neutron star:

$$\frac{\dot{M}_{acc}}{\dot{M}_w} = \frac{G^2 M_{ns}^2}{r^2} \frac{v_{rel}}{v_{wind}} \frac{1}{(v_{rel}^2 + v_s^2)^2}. \quad (9.10)$$

9.3.2 Wind Accretion Profile in an Eccentric Binary

For a given set of binary parameters (masses, orbital period, and eccentricity), the positions and velocities of the two stars around their orbits can be calculated according to the expressions given in section 9.2.2. The mass of the neutron star is taken to be $1.4 M_\odot$ and a period of 16.55 days is used.

High-mass stars such as OB supergiants typically have high wind speeds of 1000-2000 km/s. A wind speed of 1000 km/s is used in the case discussed below. The relative velocity between the wind and the neutron star is calculated from the wind speed and the relative orbital velocity of the stars.

For a wind temperature T , the sound speed is given by $v_s = \sqrt{\gamma k T / m}$, where k is Boltzmann's constant and $\gamma = 5/3$ for a monatomic gas. A typical wind temperature of 10000 K thus corresponds to a sound speed of about 12 km/s. This is much less than the wind speeds in this calculation. So, the wind temperature does not contribute significantly to the final results, but a value of 10000 K has been adopted for concreteness.

In this calculation, wind propagation delays are ignored, i.e. the wind velocity vector is calculated using the *current* position and velocity of the donor star. This simplification is valid when the wind speed is significantly larger than the orbital velocity of the donor. In the limit of very high wind speed, $v_{rel} \approx v_w \gg v_s$, and so equation 9.10 reduces to

$$\frac{\dot{M}_{acc}}{\dot{M}_w} = \frac{G^2 M_{ns}^2}{r^2} \frac{1}{v_w^4}. \quad (9.11)$$

Thus, for a given wind speed, it is primarily the distance between the stars that determines the fraction of the wind captured. However, equation 9.10 is still used in the code, since the orbital motion of the neutron star will produce an asymmetry of the profile relative to phase zero.

In an eccentric orbit the separation between the stars changes with orbital phase (θ) according to

$$r(\theta) = a \frac{1 - e^2}{1 + e \cos \theta} = \left(\frac{P}{2\pi} \right)^{2/3} G^{1/3} (M_{ns} + M_{don})^{1/3} \frac{1 - e^2}{1 + e \cos \theta}, \quad (9.12)$$

where the Kepler's third law was used in the second equality. Thus for a fixed orbital period and high wind speed, the wind capture fraction is weakly dependent on the mass of the donor star, strongly dependent on eccentricity, and varies with orbital phase as $(1 + e \cos \theta)^2$. Thus, only the normalization, and not the shape, of the wind accretion profiles change significantly with different

donor masses or (high) wind speeds.

The profile of mass accretion rate versus orbital phase for a $5 M_{\odot}$ donor is shown in Figure 9-4 for three values of eccentricity (0.2, 0.5, 0.8) and three wind speeds (500, 1000, 2000 km/s). As expected, a low eccentricity produces a broad profile, while a high eccentricity shows a much narrower peak. The peak value occurs slightly after phase zero due to the relative velocity of the wind and neutron star near periastron, and this shift is largest when the wind speed is slowest.

9.3.3 Comparison to the X-ray Intensity Profile

The X-ray light curve of Cir X-1 as observed by the ASM (see Chapter 3) shows that flaring is usually limited to a quarter to a third of each 16.55-d cycle, suggesting at least a moderate eccentricity. The flaring is complex and varies significantly from cycle to cycle. In contrast to the wind profiles in Figure 9-4, many X-ray cycles show an asymmetric profile, with the intensity declining more slowly than the rise. Some cycles even show a secondary peak well separated from the first. Such behavior cannot be accommodated in the simple wind model presented here. Moreover, the X-ray light curves show a substantial baseline intensity level that does not occur in simulations with a large eccentricity.

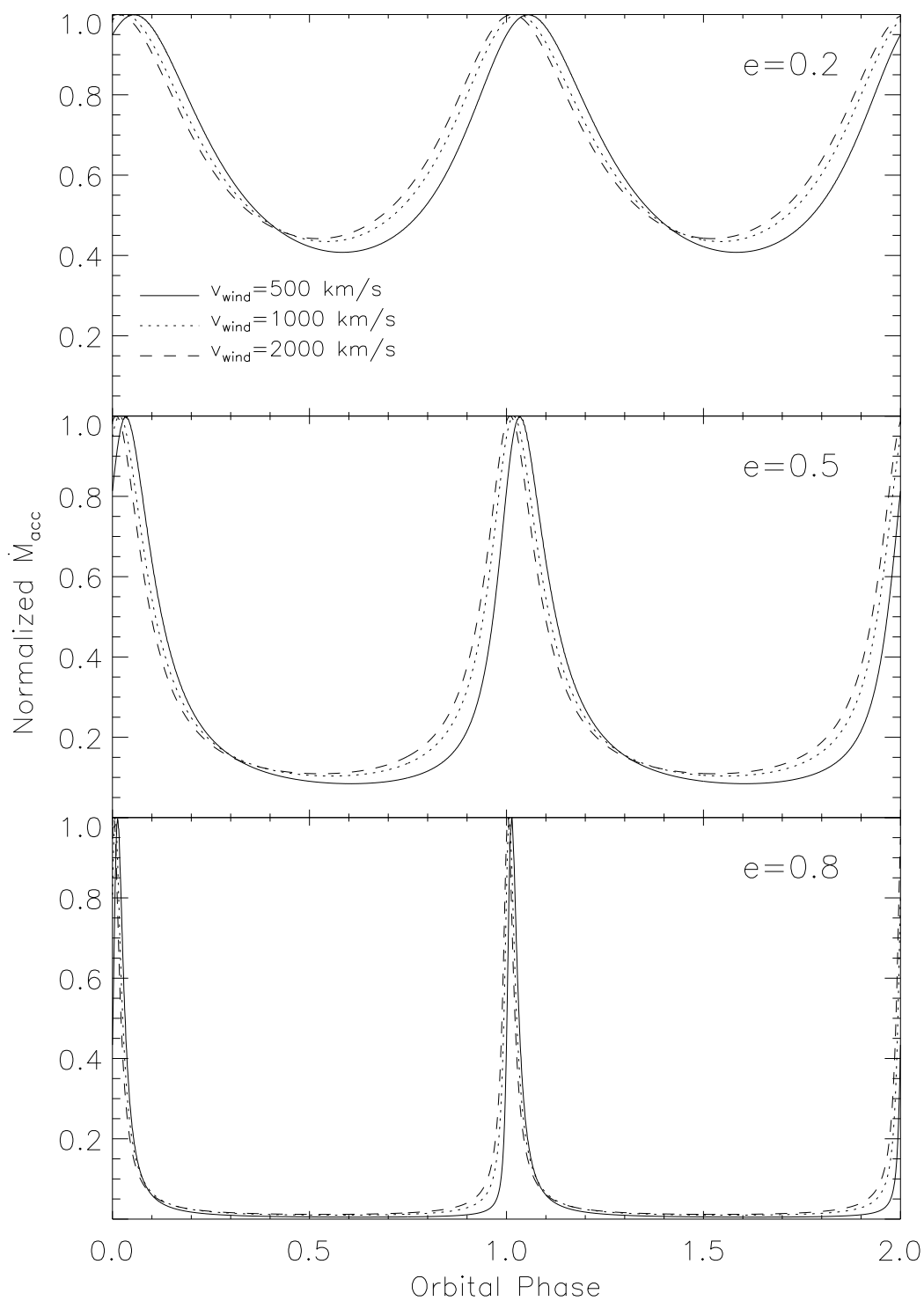


Figure 9-4: Wind accretion rate versus orbital phase for three eccentricities and wind speeds for a $5 M_{\odot}$ donor. Each curve is normalized by its peak value; the actual wind capture fraction (relative to the mass-loss rate of the donor) decreases significantly with higher velocity.

Chapter 10

Eccentric Binary Evolution

10.1 Overview

In order to explore the possible evolutionary history of Circinus X-1, I have developed a binary evolution code to model the evolution of a neutron-star and low-mass companion ($M < 3 M_{\odot}$) in an eccentric orbit. Although a high-mass companion cannot be ruled out based on the observed optical and infrared magnitudes (see section 1.3.6), the X-ray behavior is most consistent with a low-mass X-ray binary, and thus I only consider systems with a low-mass companion in this model. This code was originally developed by C. M. Becker to model accreting white dwarfs in circular binary orbits [4]. In order to keep the model simple, yet include eccentricity, I assumed that mass transfer (via Roche-lobe overflow) occurs only at periastron and that the transfer is conservative (no mass lost from the system). I have also added the effects of tidal dissipation on the orbit and allow a system to evolve even when not transferring mass. I then used this code as the basis for a Monte Carlo population synthesis study of low-mass X-ray binaries that might resemble Cir X-1. I show that the number of systems in the Galaxy with parameters similar to those of Cir X-1 should be of order unity, consistent with the unique status of the source as an eccentric LMXB with a high accretion rate.

10.2 Binary Evolution Theory

10.2.1 Evolution of Binary Parameters

The Keplerian elements of the binary system can be specified by the mass of the neutron star (M_{ns}), the mass of the donor star (M_{don}), the orbital angular momentum (J_{orb}), and the eccentricity (e).

The orbital period (P_{orb}), angular frequency (Ω_{orb}), and semimajor axis (a) are related to these four quantities by straightforward application of Kepler's third law

$$\left(\frac{P_{orb}}{2\pi}\right)^2 = \Omega_{orb}^{-2} = \frac{a^3}{GM_T} \quad (10.1)$$

and the expression for the orbital angular momentum

$$J_{orb} = G^{1/2} M_{ns} M_{don} M_T^{-1/2} a^{1/2} (1 - e^2)^{1/2}, \quad (10.2)$$

where $M_T = M_{ns} + M_{don}$.

Mass transfer will occur when the donor star fills its critical potential lobe. For simplicity, I assume that the mass transfer is conservative, i.e., all matter lost by the donor is accreted by the neutron star: $\delta M_{ns} = -\delta M_{don}$ and $\delta M_T = 0$. Furthermore, since the critical potential lobe will be smallest at periastron, it is assumed that mass transfer occurs *only* at periastron. This is likely to be a good approximation for large eccentricities but clearly cannot hold true in the limit of zero eccentricity. For the purpose of studying systems that resemble Cir X-1, systems with very low or zero eccentricity (i.e., $e \lesssim 0.01$) are not of interest.

Because mass transfer depends on the size of the donor relative to its critical potential lobe, it is necessary to follow the evolution of the donor star radius. There are several means by which the donor radius may change, each of which will be discussed in more detail below. At this point I will only mention what those mechanisms are: (1) The radius of the donor changes over time due to the nuclear evolution of its core. (2) The star responds adiabatically to the removal of mass. (3) The radius, if not at equilibrium, adjusts toward the equilibrium radius on a thermal time scale. The net effect of these contributions on radius evolution can be expressed as:

$$\frac{\delta R_{don}}{R_{don}} = \left(\frac{\delta R_{don}}{R_{don}}\right)_{nuc} + \left(\frac{\delta R_{don}}{R_{don}}\right)_{th} + \left(\frac{\delta R_{don}}{R_{don}}\right)_{ad}. \quad (10.3)$$

Orbital angular momentum is lost through tidal dissipation, magnetic braking, and gravitational radiation.

$$\frac{\delta J}{J} = \left(\frac{\delta J}{J}\right)_{tid} + \left(\frac{\delta J}{J}\right)_{mb} + \left(\frac{\delta J}{J}\right)_{gr}. \quad (10.4)$$

Likewise, these mechanisms produce a change in eccentricity. Unlike angular momentum (which is assumed to be conserved during mass transfer), the eccentricity changes due to mass transfer. Thus,

the total change in eccentricity is given by:

$$\frac{\delta e}{e} = \left(\frac{\delta e}{e}\right)_{\dot{m}} + \left(\frac{\delta e}{e}\right)_{tid} + \left(\frac{\delta e}{e}\right)_{mb} + \left(\frac{\delta e}{e}\right)_{gr}. \quad (10.5)$$

I will discuss each of these mechanisms in detail below. The final two terms in equation 10.5 are expected to occur on much longer time scales than the first two terms and are thus ignored.

10.2.2 Evolution of the Donor Star Radius

10.2.2.1 Nuclear Evolution

The equilibrium radius of a star depends on its total mass, as well as the mass of its core produced by nuclear evolution. An expression for this radius is given by Rappaport et al. [60]:

$$\frac{R_{eq}}{R_{\odot}} \simeq 0.85 \left(\frac{M_{don}}{M_{\odot}}\right)^{0.85} + \frac{4950 M_c^{4.5}}{(1 + 4M_c^4)}, \quad (10.6)$$

where M_c is the mass of the core expressed in solar units.

As the core mass grows through nuclear evolution, the radius of the donor will also increase. Taking the derivative of equation 10.6 and dividing by the donor radius gives the fractional change in the radius due to nuclear evolution:

$$\left(\frac{\delta R_{don}}{R_{don}}\right)_{nuc} = \frac{\delta R_{eq}}{R_{don}} = \frac{R_{eq} - 0.85(M_{don}/M_{\odot})^{0.85}}{R_{don}} \left[4.5 - \frac{16M_c^4}{(1 + 4M_c^4)}\right] \frac{\delta M_c}{M_c} \quad (10.7)$$

The nuclear evolution of the core is straightforward to compute since in a red giant the luminosity is generated from nuclear burning in a thin shell surrounding a helium core. The change in core mass is determined by the rate at which hydrogen is burned in a shell around the helium core. In the low-mass giants being considered here, hydrogen is fused into helium via the proton-proton chain, which converts 0.7% of the hydrogen mass into energy. Thus, the core gains mass at a rate proportional to the luminosity of the donor (L_{don}). Becker gives an expression for this rate [4]:

$$\dot{M}_c = 1.47 \times 10^{-11} f_c \left(\frac{L_{don}}{L_{\odot}}\right) \left(\frac{X}{0.7}\right)^{-1} M_{\odot} \text{ yr}^{-1}. \quad (10.8)$$

where X is the hydrogen abundance (mass fraction), taken to be ~ 0.75 and f_c is an ad hoc constant multiplicative factor of 2 to make this simple evolutionary model more consistent with the results of more sophisticated codes.

An approximate analytic formula for the luminosity of a star on the red giant branch is given by

the following expression, adapted from the result of Eggleton [19]:

$$\frac{L_{don}}{L_{\odot}} \simeq 2 \left(\frac{M_{don}}{M_{\odot}} \right)^4 + \frac{2 \times 10^5 (M_c/M_{\odot})^6}{1 + 2.5(M_c/M_{\odot})^4 + 3(M_c/M_{\odot})^5}. \quad (10.9)$$

10.2.2.2 Thermal Readjustment Toward Equilibrium

If the radius of the donor star differs from its thermal equilibrium radius, it will adjust toward the equilibrium radius on a thermal timescale. For example, if the critical potential lobe of the star restricts its radius to be smaller than it would be if it were in thermal equilibrium, the star will expand on a thermal time scale, driving mass transfer. The following relation is used to describe the readjustment of the stellar radius of the donor on a thermal (Kelvin-Helmholtz) timescale:

$$\left(\frac{\delta R_{don}}{R_{don}} \right)_{th} \simeq \frac{R_{eq} - R_{don}}{R_{don} \tau_{KH}} \delta t, \quad (10.10)$$

where

$$\tau_{KH} \simeq \frac{3GM^2}{7RL} \simeq 1.5 \times 10^7 \left(\frac{M_{don}}{M_{\odot}} \right)^2 \left(\frac{R_{don}}{R_{\odot}} \right)^{-1} \left(\frac{L_{don}}{L_{\odot}} \right)^{-1} \text{ yrs.} \quad (10.11)$$

10.2.2.3 Adiabatic Response to Mass Loss

A star will respond adiabatically to mass loss. Rappaport, Joss, and Webbink [59] relate the resulting change of the radius to the change in mass through a factor ξ_{ad} :

$$\left(\frac{\delta R_{don}}{R_{don}} \right)_{ad} = \xi_{ad} \frac{\delta M_{don}}{M_{don}}. \quad (10.12)$$

DiStefano et al. [15] performed detailed evolution studies with a Henyey-type code including mass loss. They found that for stars with a low core mass ($M_{cor} < 0.2M_{\odot}$), the radius shrinks when mass is removed, but for higher core mass, the mass loss causes the star to expand (resulting in unstable transfer). They parameterized their results for ξ_{ad} with respect to core mass:

$$\xi_{ad} = \tilde{\xi}_{ad} \left[1 - \left(\frac{M_c}{\tilde{M}_c} \right)^2 \right], \quad (10.13)$$

where $\tilde{\xi}_{ad} = 4.0$ and $\tilde{M}_c = 0.2 M_{\odot}$.

10.2.3 Evolution of Orbital Parameters

10.2.3.1 Tidal Evolution

In a binary system, tidal friction will dissipate energy while conserving the total angular momentum. In particular, in a system where one star is compact (e.g. a neutron star), the sum of the total orbital energy plus the rotational energy of the “donor” star (actually not necessarily donating matter in this discussion) will decrease while angular momentum is exchanged between the orbit and the rotation of the star. In the weak friction model, it is assumed that the star is tidally deformed into the equipotential surface it would have formed a constant time τ ago in the absence of the tidal friction, i.e., a tidal bulge that is offset from the line between the centers of the stars. The rate of change of the orbital and rotational parameters due to this tidal dissipation is given by Hut [29] (using variables as defined above):

$$\frac{da}{dt} = -6 \frac{GM_{don}k\tau}{R_{don}^3} \frac{1+q}{q^2} \left(\frac{R_{don}}{a} \right)^8 \frac{a}{(1-e^2)^{15/2}} \left[f_1(e^2) - (1-e^2)^{3/2} f_2(e^2) \frac{\Omega_{rot}}{\Omega_{orb}} \right], \quad (10.14)$$

$$\frac{de}{dt} = -27 \frac{GM_{don}k\tau}{R_{don}^3} \frac{1+q}{q^2} \left(\frac{R_{don}}{a} \right)^8 \frac{e}{(1-e^2)^{13/2}} \left[f_3(e^2) - \frac{11}{8} (1-e^2)^{3/2} f_4(e^2) \frac{\Omega_{rot}}{\Omega_{orb}} \right], \quad (10.15)$$

and

$$\frac{d\Omega_{rot}}{dt} = 3 \frac{GM_{don}k\tau}{R_{don}^3} \frac{1}{q^2 r_g^2} \left(\frac{R_{don}}{a} \right)^6 \frac{\Omega_{orb}}{(1-e^2)^{15/2}} \left[f_2(e^2) - (1-e^2)^{3/2} f_5(e^2) \frac{\Omega_{rot}}{\Omega_{orb}} \right], \quad (10.16)$$

where

$$\begin{aligned} f_1(e^2) &= 1 + \frac{31}{2}e^2 + \frac{255}{8}e^4 + \frac{185}{16}e^6 + \frac{25}{64}e^8 \\ f_2(e^2) &= 1 + \frac{15}{2}e^2 + \frac{45}{8}e^4 + \frac{15}{16}e^6 \\ f_3(e^2) &= 1 + \frac{15}{4}e^2 + \frac{15}{8}e^4 + \frac{5}{64}e^6 \\ f_4(e^2) &= 1 + \frac{3}{2}e^2 + \frac{1}{8}e^4 \\ f_5(e^2) &= 1 + 3e^2 + \frac{3}{8}e^4. \end{aligned}$$

Also, $q = M_{don}/M_{ns}$ is the mass ratio and Ω_{rot} and Ω_{orb} are the rotational and mean orbital angular velocities. The dimensionless radius of gyration, r_g , is related to the moment of inertia of the donor star by $I = r_g^2 M_{don} R_{don}^2$, and the apsidal motion constant k is also related to the structure of the donor. A typical value for the radius of gyration is $r_g^2 = 0.1$ for the low-mass relatively unevolved stars considered here.

For stars with an outer convective zone (i.e. low-mass stars with $M \lesssim 1-2 M_\odot$), Lecar gives an approximate expression for the product of the apsidal motion constant and the tidal time lag [41]:

$$k\tau \approx 25 \frac{\eta \lambda v_{conv} (\text{km/s})}{g/g_\odot} \text{ s}, \quad (10.17)$$

where $g = GM/R^2$ is the gravitational acceleration. The convective velocity, v_{conv} , is typically ~ 1 km/s for a wide range of convective stars. Furthermore, η and λ are the fractional mass and fractional depth respectively of the outer convection zone of the donor star. Lecar gives a table of these two quantities for main-sequence stars with effective temperatures of in the range of $T=5200$ – 7200 K [41]. To facilitate interpolation and extrapolation of values for $\eta\lambda$, an analytic function was fit to the table entries, resulting in the following relation:

$$\log_{10}(\eta\lambda) = \begin{cases} 10.66 - 2.7907 \times 10^{-6} T^2 + 7.5778 \times 10^{-10} T^3 - 5.899 \times 10^{-14} T^4 & T \geq 5000\text{K} \\ -1.25375 & T < 5000\text{K}. \end{cases} \quad (10.18)$$

For stars with effective temperatures below 5000 K, the tidal circularization time scale is very short and systems containing such stars will circularize before other mechanisms affect the orbital evolution. In contrast, for stars with effective temperatures above 7200 K, the time scale is very long and tidal dissipation will not play a significant role in the evolution of the orbital parameters.

10.2.3.2 Effect of Mass Transfer on the Orbit

The effect of mass transfer in a circular orbit is relatively simple to calculate: if angular momentum is conserved, then the change in the semimajor axis of the orbit depends uniquely on the change in the masses of the stars. Mass transfer onto a star less massive than the donor star will decrease their separation, and transfer onto a more massive star will increase the orbital separation. In an eccentric orbit, the angular momentum depends on both the eccentricity as well as the semimajor axis, and thus conservation of angular momentum is insufficient to determine how both orbital parameters change. So, Eggleton has derived a prescription for the effect of mass transfer on the orbital eccentricity [19]. Mass transfer that occurs at orbital angle θ (position angle of one star relative to the other, where $\theta = 0$ corresponds to periastron) results in a change in eccentricity given by:

$$\delta e = -2(1-q)(\cos \theta + e) \frac{\delta M_{don}}{M_{don}}. \quad (10.19)$$

When mass is transferred at a constant rate around the entire orbit, the average change in eccentricity is zero, since over a complete orbit $\langle \cos \theta \rangle = -e$. In the other extreme, when mass transfer occurs only at periastron (as in a highly eccentric orbit),

$$\delta e = -2(1-q)(1+e) \frac{\delta M_{don}}{M_{don}}. \quad (10.20)$$

Since $\delta M_{don} < 0$ during mass transfer and $q = M_{don}/M_{ns}$, equation 10.20 shows that mass

transfer will decrease the eccentricity when $M_{don} > M_{ns}$ and will increase the eccentricity when the mass ratio is reversed.

10.2.3.3 Magnetic Braking

This section on magnetic braking is reproduced from Becker [4].

Most stars have some magnetic field, and the interaction of the field lines with the ejected matter increases the effective “lever arm” and, therefore, the amount of specific angular momentum carried away by the stellar wind. Thus a small amount of mass loss can, in principle, extract a significant amount of angular momentum from the rotation of the star. If tidal interactions between the donor and companion keep the donor star co-rotating with the orbit, then magnetic braking can result in angular momentum losses from the orbit.

Skumanich [64] and Smith [66] independently determined a rotation rate/age relation for isolated stars, mostly with masses about $1 M_{\odot}$, in clusters of various ages. From this relation an empirical magnetic braking torque was inferred. Verbunt & Zwaan [82] applied this to binary systems as a way to drive angular momentum loss. I use a slightly modified version of this braking law as given by Rappaport et al. [58]:

$$\left(\frac{\delta J}{J}\right)_{mb} = -1.73 \times 10^{-27} f_{mb} \left[\frac{R_{\odot}^4 (R_{don}/R_{\odot})^{\gamma} M_T^{1/3}}{G^{2/3} M_{wd} P^{10/3}} \right] \delta t, \quad (10.21)$$

where γ is the parameterized magnetic braking index (typically $\gamma = 4$), f_{mb} is a multiplicative constant of order unity, and “cgs units” are used. In the process of applying magnetic braking to binaries, a number of liberties were taken in applying the results of Skumanich and Smith. The use of the magnetic braking law in binaries extends to shorter periods and different masses for stars than in the original data. The parameter γ is used in place of any real knowledge of how the braking depends on stellar radius since most of the stars used to develop the original relation were G stars with more or less the same radius.

10.2.3.4 Gravitational Radiation

This section on gravitational radiation is reproduced from Becker [4].

Gravitational radiation arises from a mass distribution with a time varying quadrupole moment, such as a pair of stars orbiting each other. For such a simple geometry (a circular orbit), the rate of angular momentum loss is given by the Einstein quadrupole radiation formula:

$$\left(\frac{\delta J}{J}\right)_{gr} = -\frac{32}{5} (4\pi^2)^{4/3} \frac{G^{5/3}}{c^5} \frac{M_{wd} M_{don}}{M_T^{1/3} P^{8/3}} \delta t, \quad (10.22)$$

where P is the orbital period [39]. For the systems we will consider, with periods typically larger than 10 hours, gravitational radiation alone drives mass transfer too slowly to have any significant effect.

10.2.4 Stable Mass Transfer

Mass transfer can act as a sort of regulator, preventing the donor radius from exceeding the critical potential lobe radius (stable transfer). If mass transfer is unable to prevent the donor from overfilling the critical potential lobe, transfer will be unstable. If mass transfer (or another mechanism) eventually results in the donor underfilling its critical potential lobe, mass transfer will stop. Thus, during stable mass transfer the donor radius can continuously adjust so that it always equals the Roche lobe radius. Based on the assumption of stable transfer, I will now derive the expression that governs the rate of mass transfer.

For the case of circular orbits, the Roche-lobe radius is related to the semimajor axis of the orbit through a function $f(q)$ of the mass ratio $q = M_{don}/M_{ns}$:

$$R_L = f(q) \cdot a. \quad (10.23)$$

An analytic approximation of this function has been derived by P. Eggleton [18]:

$$f(q) = \frac{0.49q^{2/3}}{0.6q^{2/3} + \ln(1 + q^{1/3})}. \quad (10.24)$$

For non-zero eccentricity, a plausible approximation to the effective critical potential lobe size is obtained by replacing the semimajor axis in equation 10.23 with the instantaneous separation d . A more precise measure for size of the critical potential lobe can be obtained by calculating the location of points on the critical surface of an effective potential that accounts for the eccentricity of the orbit, e.g., as given by Avni [3] (see section 9.2.1). However, for simplicity and speed in the evolution code, I will use equation 10.23 with the instantaneous separation.

In a Keplerian orbit, the separation as a function of angle (θ) from periastron is given by

$$d = \frac{a(1 - e^2)}{1 + e \cos \theta}. \quad (10.25)$$

Thus at periastron, $d = a(1 - e)$. As described above, mass transfer via Roche-lobe overflow requires that the radius of the donor star equal the radius of the critical potential lobe at periastron radius:

$$R_{don} \equiv R_L = f(q) \cdot a \cdot (1 - e). \quad (10.26)$$

Taking the logarithmic derivative of equation 10.26 shows how changes in these parameters are coupled:

$$\frac{\delta R_{don}}{R_{don}} = (1+q) \frac{d \ln f}{d \ln q} \frac{\delta M_{don}}{M_{don}} + \frac{\delta a}{a} - \frac{\delta e}{1-e}. \quad (10.27)$$

The logarithmic derivative of $f(q)$ is calculated from equation 10.24 to be:

$$\frac{d \ln f}{d \ln q} = \frac{2}{3} \left\{ \frac{\ln(1+q^{1/3}) - 0.5 \frac{q^{1/3}}{1+q^{1/3}}}{0.6q^{2/3} + \ln(1+q^{1/3})} \right\}. \quad (10.28)$$

Since I have chosen to work with orbital angular momentum rather than the semimajor axis, the logarithmic derivative of the orbital angular momentum (equation 10.2) is needed:

$$\frac{\delta J}{J} = \frac{\delta M_{ns}}{M_{ns}} + \frac{\delta M_{don}}{M_{don}} - \frac{1}{2} \frac{\delta M_T}{M_T} + \frac{1}{2} \frac{\delta a}{a} - \frac{e \delta e}{1-e^2}. \quad (10.29)$$

The masses in this relation can be re-expressed in terms of only the donor mass and the mass ratio:

$$\frac{\delta J}{J} = (1-q) \frac{\delta M_{don}}{M_{don}} + \frac{1}{2} \frac{\delta a}{a} - \frac{e \delta e}{1-e^2}. \quad (10.30)$$

Combining equations 10.27 and 10.30 to eliminate the semimajor axis gives:

$$\frac{\delta J}{J} = \left[1 - q - \frac{1+q}{2} \frac{d \ln f}{d \ln q} \right] \frac{\delta M_{don}}{M_{don}} + \frac{1}{2} \frac{\delta R_{don}}{R_{don}} + \frac{1}{2} \frac{e}{1+e} \frac{\delta e}{e}. \quad (10.31)$$

Using equations 10.3, 10.4, and 10.5 to explicitly include each source of evolution into 10.31:

$$\begin{aligned} 2 \left(\frac{\delta J}{J} \right)_{mb} + 2 \left(\frac{\delta J}{J} \right)_{gr} + 2 \left(\frac{\delta J}{J} \right)_{tid} - \frac{e}{(1+e)} \left(\frac{\delta e}{e} \right)_{tid} - \left(\frac{\delta R_{don}}{R_{don}} \right)_{nuc} - \left(\frac{\delta R_{don}}{R_{don}} \right)_{th} = \\ 2 \left[1 - q - \frac{1+q}{2} \frac{d \ln f}{d \ln q} \right] \frac{\delta M_{don}}{M_{don}} + \left(\frac{\delta R_{don}}{R_{don}} \right)_{ad} + \frac{e}{(1+e)} \left(\frac{\delta e}{e} \right)_{\dot{m}}, \end{aligned} \quad (10.32)$$

where all the explicitly time-dependent terms have been moved to the left hand side, and terms directly proportional to mass loss appear on the right hand side.

Now using equations 10.12 and 10.19 to replace the last two terms in equation 10.32 with their dependencies on mass transfer, we find

$$\begin{aligned} 2 \left(\frac{\delta J}{J} \right)_{mb} + 2 \left(\frac{\delta J}{J} \right)_{gr} + 2 \left(\frac{\delta J}{J} \right)_{tid} - \frac{e}{(1+e)} \left(\frac{\delta e}{e} \right)_{tid} - \left(\frac{\delta R_{don}}{R_{don}} \right)_{nuc} - \left(\frac{\delta R_{don}}{R_{don}} \right)_{th} = \\ \left[\xi_{ad} + 2(1-q) - 2 \frac{(\cos \theta) + e}{1+e} (1-q) - (1+q) \frac{d \ln f}{d \ln q} \right] \frac{\delta M_{don}}{M_{don}}. \end{aligned} \quad (10.33)$$

The time-dependent left-hand side of this equation, referred to as the “numerator”, governs the

time scale for mass transfer. The right-hand side depends on the mass transferred, rather than time. The term in square brackets on the right-hand side (the “denominator”), determines if mass transfer is stable. As mentioned in section 10.2.3.2, mass transfer limited to periastron results in $\langle \cos \theta \rangle = 1$, so that the second and third terms in the denominator cancel. For transfer around the entire orbit, when $\langle \cos \theta \rangle = -e$, the third term of the denominator vanishes.

All of the terms in the numerator are time dependent and can be calculated from the expressions given in the discussion above. The expressions given for gravitational radiation and magnetic braking are strictly correct only for circular orbits. However, these mechanisms of angular momentum loss are small in a system with a relatively long orbital period such as Cir X-1 (days), and thus the circular-orbit approximation is sufficient to estimate the magnitude of these quantities.

10.3 Binary Evolution Code

10.3.1 Code Algorithm

The parameters that need to be specified at the start of the evolution are the initial donor mass and the eccentricity and semimajor axis of the orbit. The initial core mass can be varied, but was generally taken to be zero and evolved as part of the code. The initial neutron star mass was taken to be $1.4 M_{\odot}$ in all cases. The initial spin of the donor was assumed to be slow relative to the orbital frequency ($\Omega_{rot}/\Omega_{orb} = 1 \times 10^{-3}$ for concreteness) and allowed to spin-up via tidal effects. The donor star was assumed to start in equilibrium ($R_{don} = R_{eq}$). It generally underfilled its initial periastron critical potential lobe, but in some cases just filled the critical lobe. Mass transfer started immediately in the latter case.

A minimum of 10 time steps are used per decade of time. Smaller time steps are chosen as necessary so that no parameter changes by more than 0.25% during each step, and 10^7 yr is the largest time step allowed. For each time step:

1. The new core mass is determined from the simplified stellar evolution code.
2. The equilibrium radius of the donor is determined from its total and core mass.
3. The change in donor radius due to nuclear evolution, thermal adjustment, and adiabatic response to mass loss is calculated.
4. The effects of tidal dissipation, magnetic braking, and gravitational radiation on the orbit are calculated.

5. If the donor star fills its critical potential lobe, determine the amount of mass transfer necessary to keep the donor radius no larger than the radius of critical potential lobe (calculate numerator and denominator from equation 10.33).
6. Update all the system parameters based on the above changes.

The evolution is stopped if any of the following conditions occur:

1. The donor star is stripped ($M_{don} - M_{cor} < 0.05 M_{\odot}$).
2. The mass of the donor star drops below $0.1 M_{\odot}$.
3. The denominator of equation 10.33 is negative (mass transfer is unstable).
4. The binary circularizes ($e < 0.01$), and thus is no longer a candidate to produce a system that resembles Cir X-1.
5. The binary comes close to being unbound. When a becomes extremely large and e approaches unity, the system has become nearly unbound or has unphysical parameters. Thus I stop the code when $e > 0.99$ and refer to such systems as being “unbound”.
6. More than 10 billion years have elapsed (longer than the age of most stars in the Galaxy).

10.3.2 Results

As mentioned in section 10.2.3.2, mass transfer tends to decrease the eccentricity while the donor star is more massive than the neutron star. In some cases, this can lead to circularization of the orbit. However, in many cases mass transfer eventually inverts the mass ratio (or $M_{don} < M_{ns}$ to begin with) so that the eccentricity and the semimajor axis are increased during continued mass transfer, often nearly unbinding the system. Systems that start with the donor star in contact with its critical potential lobe transfer mass at a high rate and usually unbind (see equation 10.20) in $\sim 10^8$ years.

Figure 10-1 shows the binary evolution calculation results for a $2 M_{\odot}$ donor that starts with donor star in contact with its critical potential lobe. In this situation, the thermal expansion of the donor towards the equilibrium radius dominates over other mechanisms, as is evident from the panel in Figure 10-1 showing the various time scales ($\tau_{th} \equiv R_{don}/(\dot{R}_{don})_{th}$, $\tau_{nuc} \equiv R_{don}/(\dot{R}_{don})_{nuc}$, $\tau_{circ} \equiv 1/\dot{e}_{tid}$, and τ_{KH} is given by equation 10.11). (The thermal expansion time scale is related to the Kelvin-Helmholtz time scale, but is longer by a factor shown in equation 10.10.)

Mass transfer initially decreases the eccentricity and semimajor axis (such that periastron separation remains unchanged since transfer occurs only at periastron). After 1.2×10^8 yr, $0.3 M_{\odot}$ has

been transferred, making the neutron star more massive than the donor. Continued mass transfer then gradually increases the eccentricity and semimajor axis (again such that periastron distance, $a(1-e)$, remains approximately constant) until the system is nearly unbound (after about 3×10^8 yr).

This system maintains a moderately high mass transfer rate during most of its entire lifetime, and its period increases to the level of Cir X-1 (16.55 d) and beyond (the time corresponding to a 16.55-d period is indicated with a dot on several of the curves in Figure 10-1). Thus this system might go through a phase that resembles Cir X-1. At the point where the period is near 16 days, its eccentricity is quite high, about 0.9, and the mass transfer rate is $3.5 \times 10^9 M_\odot/\text{yr}$.

The results of a calculation starting with a $1 M_\odot$ donor initially underfilling its critical potential lobe are shown in Figure 10-2. This system evolves uneventfully for over a billion years before the nuclear evolution of the core eventually brings the donor into contact with its critical potential lobe. (The time scales for magnetic braking and tides to affect the orbit are much longer than the nuclear time scale for most of the system's lifetime.) Once in contact, the donor begins mass transfer and continues for about 1.3×10^8 yr until the system is nearly unbound. This system would also go through a phase of moderate mass transfer ($\sim 10^{-9} M_\odot/\text{yr}$) and high eccentricity with a period near 16 days.

The results for mass transfer depend strongly on the size of the critical potential lobe, and thus depend on the separation of the stars at periastron ($a(1-e)$). Here I illustrate this effect by holding e constant and varying a . Figure 10-3 shows the evolution of eccentricity and mass transfer rate for four systems which differ only in their initial semimajor axes (initially, $M_{don} = 2 M_\odot$ and $e = 0.9$). For the system with the smallest orbit ($a = 37 R_\odot$), the donor star initially just fills its critical potential lobe, similar to the system in Figure 10-1, and thus transfers mass continuously until it unbinds after about 1.8×10^8 yr.

The second system in Figure 10-3 ($a = 40 R_\odot$) initially underfills its critical potential lobe, similar to that in Figure 10-2. Nuclear evolution eventually brings the donor into contact, at which point mass transfer begins. Unlike the system in Figure 10-2, the donor in this binary is initially more massive than the neutron star, so the eccentricity dips before ultimately increasing towards unity.

Skipping the third binary for the moment, the final system in Figure 10-3 has a large semimajor axis ($a = 128 R_\odot$) and the donor is far from filling its critical potential lobe. The radius of the donor increases due to nuclear evolution of the core, resulting in a cooler effective temperature. The tidal time scale strongly depends on the temperature through the convection-shell parameters η and λ (see section 10.2.3.1). Thus, the tidal time scale drops rather sharply after $\sim 2 \times 10^8$ yrs, resulting in rapid circularization of the orbit. The donor star never fills its critical potential lobe; thus, no mass

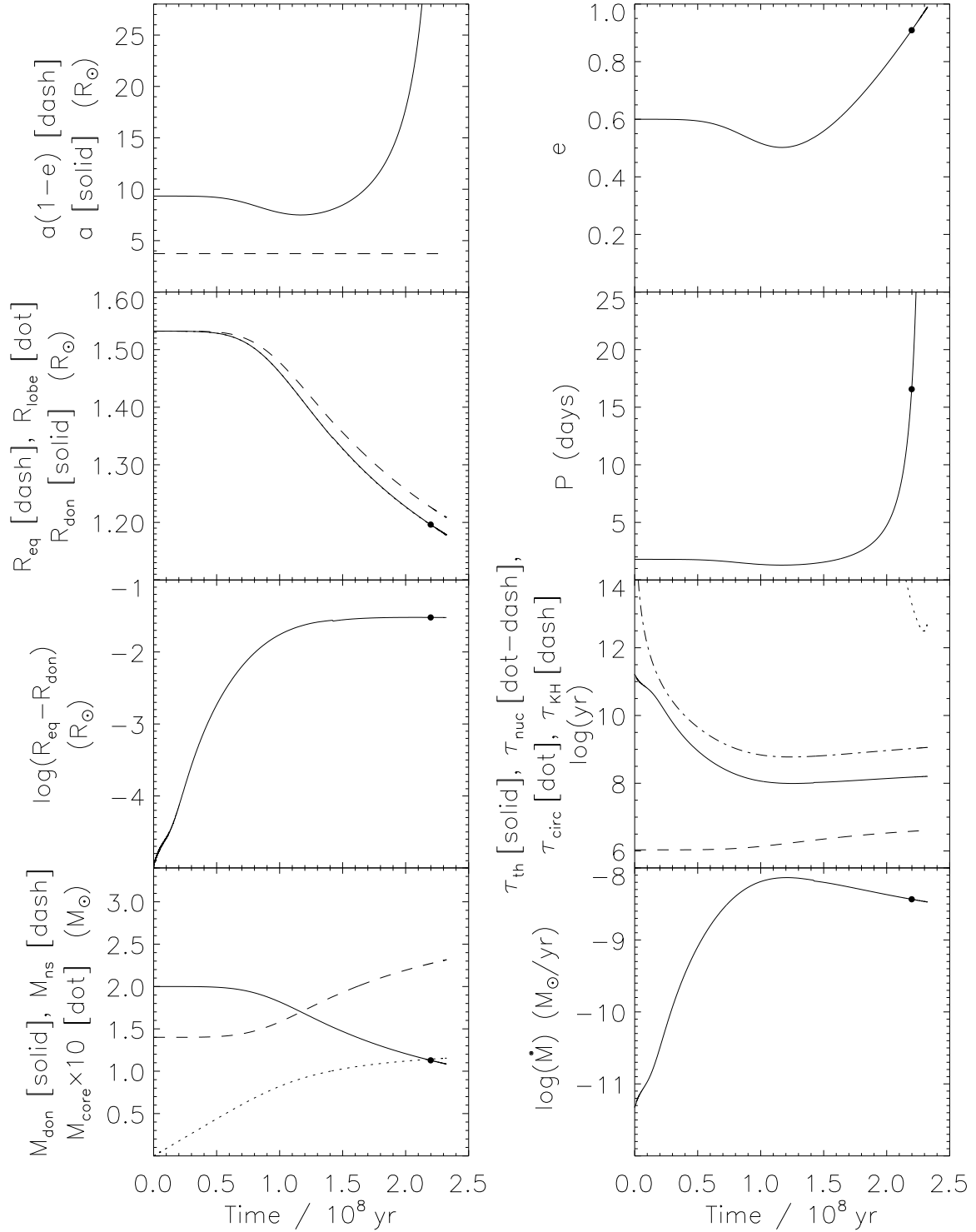


Figure 10-1: Results of a binary evolution calculation for a system started with the donor star just filling its critical potential lobe, with initial values: $M_{don} = 2 M_{\odot}$, $a = 9.34 R_{\odot}$, and $e = 0.6$. The donor remains in contact with its critical potential lobe throughout the evolution; thus, the curve for R_{lobe} coincides with the curve for R_{don} . A solid dot on some of the curves marks the time corresponding to an orbital period of 16.55 days.

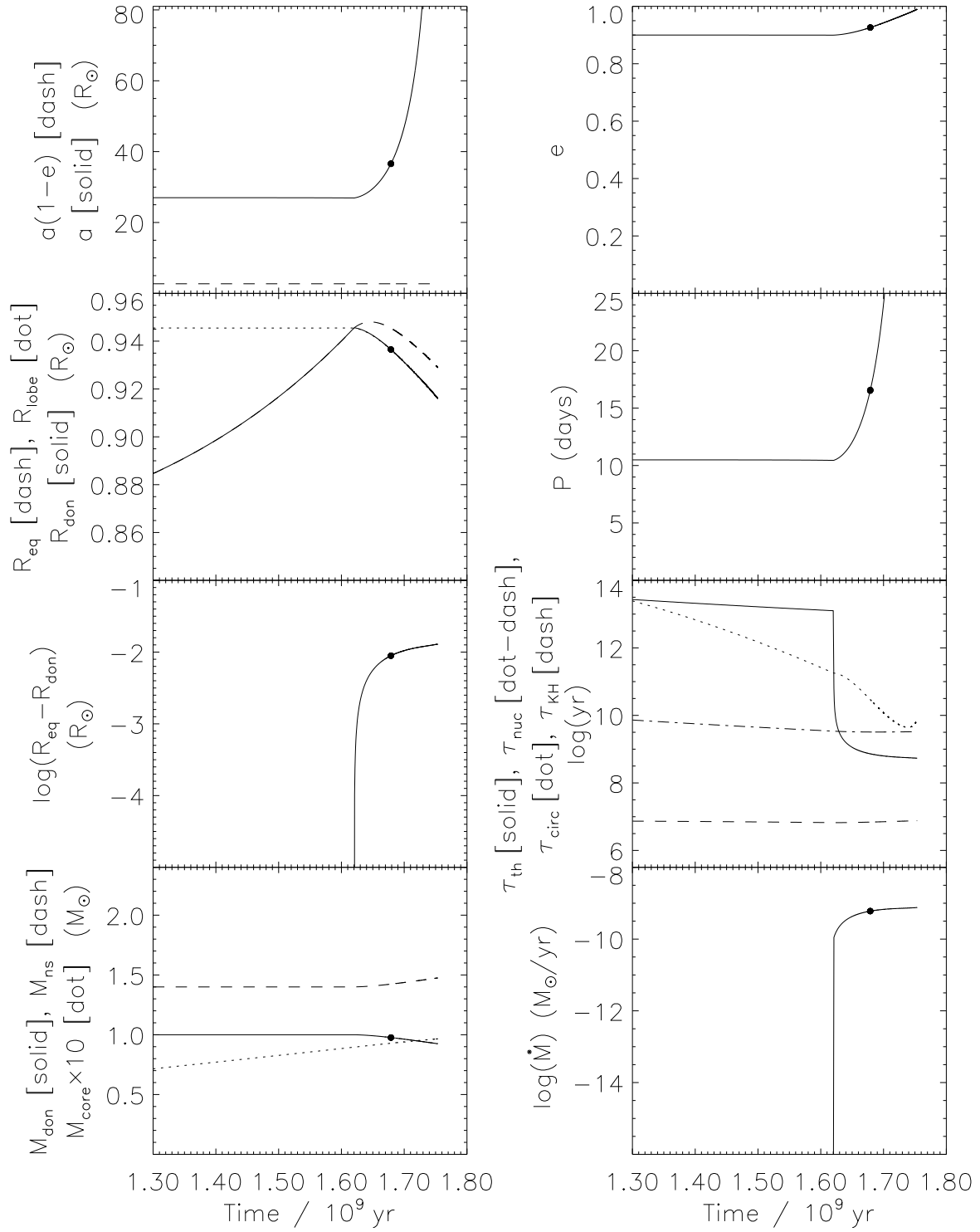


Figure 10-2: Results of binary evolution calculation for a system started with the donor underfilling its critical potential lobe, with initial values: $M_{\text{don}} = 1 M_\odot$, $a = 27 R_\odot$, and $e = 0.9$.

transfer occurs.

The third binary in Figure 10-3 ($a = 81 R_{\odot}$) is intermediate between the second and fourth. It initially underfills its critical potential lobe, but comes into contact though nuclear evolution. The eccentricity initially dips and then rises, as in the second system. However, the mass transfer eventually results in reduced tidal time scale (shorter than in the fourth system). Tidal effects then rapidly reduce the eccentricity and the orbit circularizes, as in the fourth system. Tidal circularization also approximately doubles the periastron separation, pulling the donor out of contact with its critical potential lobe and turning off mass transfer about 4×10^6 yrs after it began.

10.4 Monte-Carlo Population Synthesis

10.4.1 Systems Resembling Cir X-1

The results of individual binary evolution calculations show that systems resembling Cir X-1 can be produced. However, an entire population of LMXBs must be studied in order to determine the likelihood of actually observing such a system.

Terman, Taam, & Savage [73] have conducted a population synthesis study of LMXBs, following an initial distribution of zero-age binaries (with the more massive star $> 8 M_{\odot}$) from the main sequence, through a common-envelope phase, to just after the subsequent supernova explosion of the more evolved star. Systems that remain bound after the supernova explosion and do not immediately merge produce a population of low-mass main sequence stars ($\lesssim 3 M_{\odot}$) with a neutron-star companion (pre-LMXBs) that are expected to eventually transfer mass through evolution of the orbit and/or the companion star.

Using the binary evolution code described in the previous section, I have conducted a Monte-Carlo simulation of the evolution of pre-LMXBs throughout their entire lifetime as potential eccentric LMXBs. The initial population was drawn from the pre-LMXB population derived by Terman, Taam, & Savage [73], which yielded a relatively uniform distribution of systems in a specific range of e and $\log a$. Thus, I chose the eccentricity from a linear distribution in the range $e = 0.01$ to 0.99 , and the semimajor axis from a logarithmic distribution in the range $a = 1.25 R_{\odot}$ to $400 R_{\odot}$. Combinations outside the pre-LMXB distribution of Terman, Taam, & Savage were discarded. The initial neutron-star mass was fixed to be $1.4 M_{\odot}$ in all cases. Donor star masses were randomly chosen in the range $M_{don} = 0.8$ to $3 M_{\odot}$, and all donors were assumed to initially have zero core mass. Donor masses that corresponded to an equilibrium radius larger than the periastron critical potential lobe size were discarded as being systems that merge immediately or otherwise fail to contribute to the LMXB population.

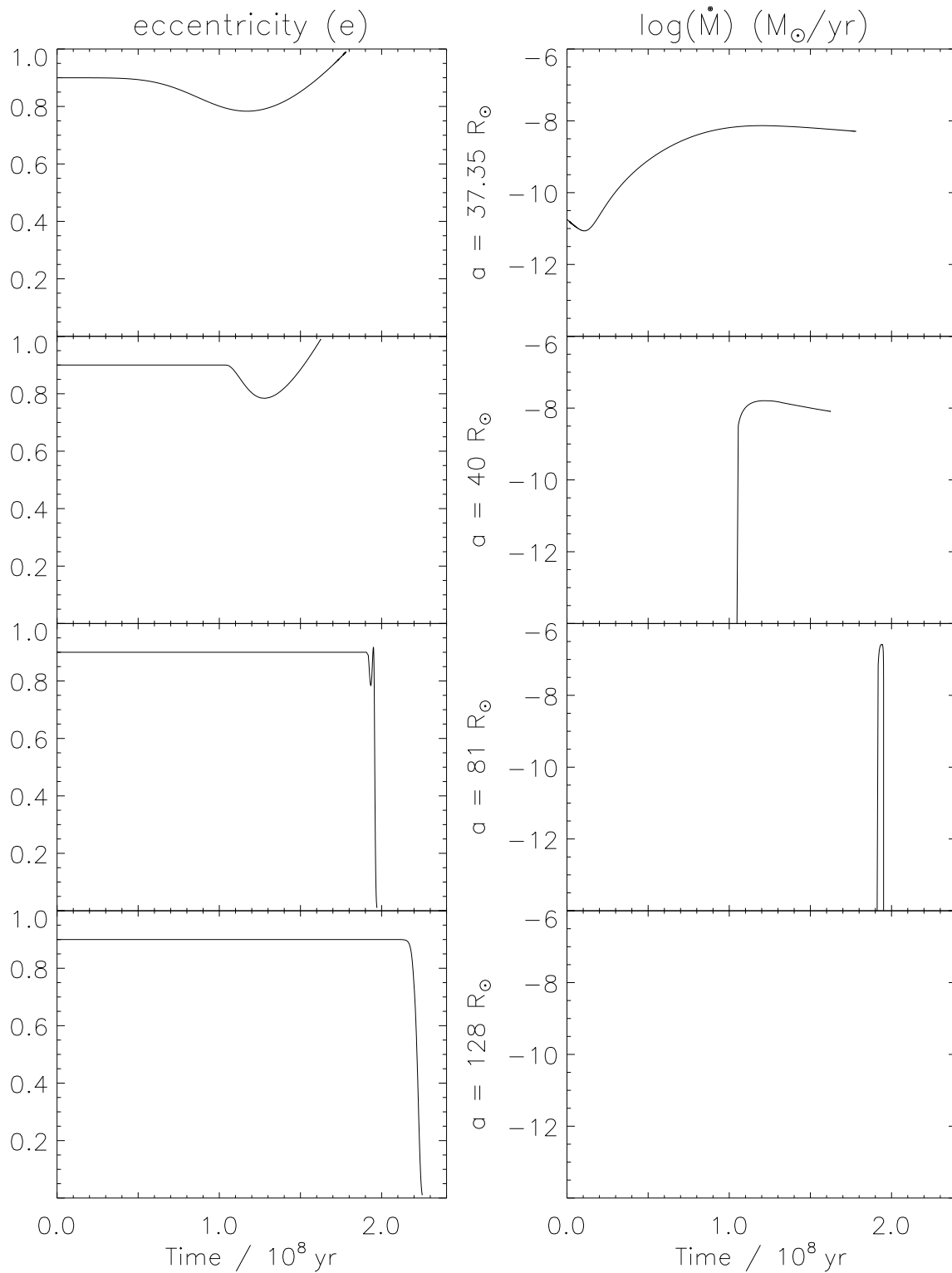


Figure 10-3: Eccentricity and mass transfer rate versus time for binaries with initial values $M_{don} = 2 R_{\odot}$, $e = 0.9$, and semimajor axes (a) between 37 and $128 R_{\odot}$.

For this study, 10^5 systems were evolved as described in the previous section. The following criteria were established to classify a system as one that resembled Cir X-1: an orbital period within $\sim 20\%$ of 16.55 days ($13 \text{ d} < P < 20 \text{ d}$), a high mass transfer rate ($10^{-9} \text{ M}_\odot/\text{yr} < \dot{M} < 10^{-7} \text{ M}_\odot/\text{yr}$), and at least a moderate eccentricity ($e > 0.1$).

Cir X-1 is 6–10 kpc away, yet still quite bright in X-rays, so any similar such system should also be visible from almost anywhere in the Galaxy. Since there is only one system detected with parameters meeting the above criteria, there is probably only about one such system in the Galaxy at this time.

Of the 10^5 systems, 42% were discarded immediately due to the donor being too large for the orbit. Of the remaining systems, (pre-LMXBs) 15% resembled Cir X-1 at some point in their lifetime. On average, each of the pre-LMXBs eventually resembled Cir X-1 for 4.0×10^5 yrs. Terman, Taam, & Savage [73] predict a pre-LMXB birth rate of $\sim 3 \times 10^{-6} - 10^{-5} \text{ yr}^{-1}$ in the Galaxy. Multiplying the predicted birth rate by the average lifetime in a state resembling Cir X-1 results in an expectation of 1–4 systems similar to Cir X-1 in the Galaxy at any given time. Thus, the fact that Cir X-1 exists but is unique is consistent with binary evolution calculations.

10.4.2 Predicted System Parameters for Cir X-1

In addition to determining the lifetime of systems that resemble Cir X-1, the Monte Carlo simulation was also used to study the distribution of system parameters corresponding to 16.55 day orbital periods and $10^{-9} \text{ M}_\odot/\text{yr} < \dot{M} < 10^{-7} \text{ M}_\odot/\text{yr}$.

Histograms of the number of binaries versus the *initial* donor mass and eccentricity for binaries that eventually reach $P = 16.55 \text{ d}$ and $10^{-9} \text{ M}_\odot/\text{yr} < \dot{M} < 10^{-7} \text{ M}_\odot/\text{yr}$ are shown in Figure 10-4. The initial donor mass distribution shows that most progenitors of systems resembling Cir X-1 have donor stars more massive than the neutron star. As I will show below, these systems come into contact and transfer mass due to the nuclear evolution of the donor. There is also smaller population of low-mass systems (the peak below 1 M_\odot) which evolve into contact through angular momentum losses (tides and magnetic braking). The initial eccentricity distribution includes all values above $e = 0.33$ and is skewed toward higher eccentricity, peaking near $e = 0.9$.

Figure 10-5 shows histograms of the number of systems versus various system parameters for binaries *at the time they reach a state resembling Cir X-1*: $P = 16.55 \text{ d}$ and $10^{-9} \text{ M}_\odot/\text{yr} < \dot{M} < 10^{-7} \text{ M}_\odot/\text{yr}$. The donor mass distribution peaks at about 1.25 M_\odot and is almost entirely confined to $M_{\text{don}} < 1.5 \text{ M}_\odot$. This is a reflection of the fact that most systems that reach 16.55 d periods during mass transfer are in the stage of increasing orbital period, which can occur only after the donor has become less massive than the neutron star. The core mass distribution shows that most

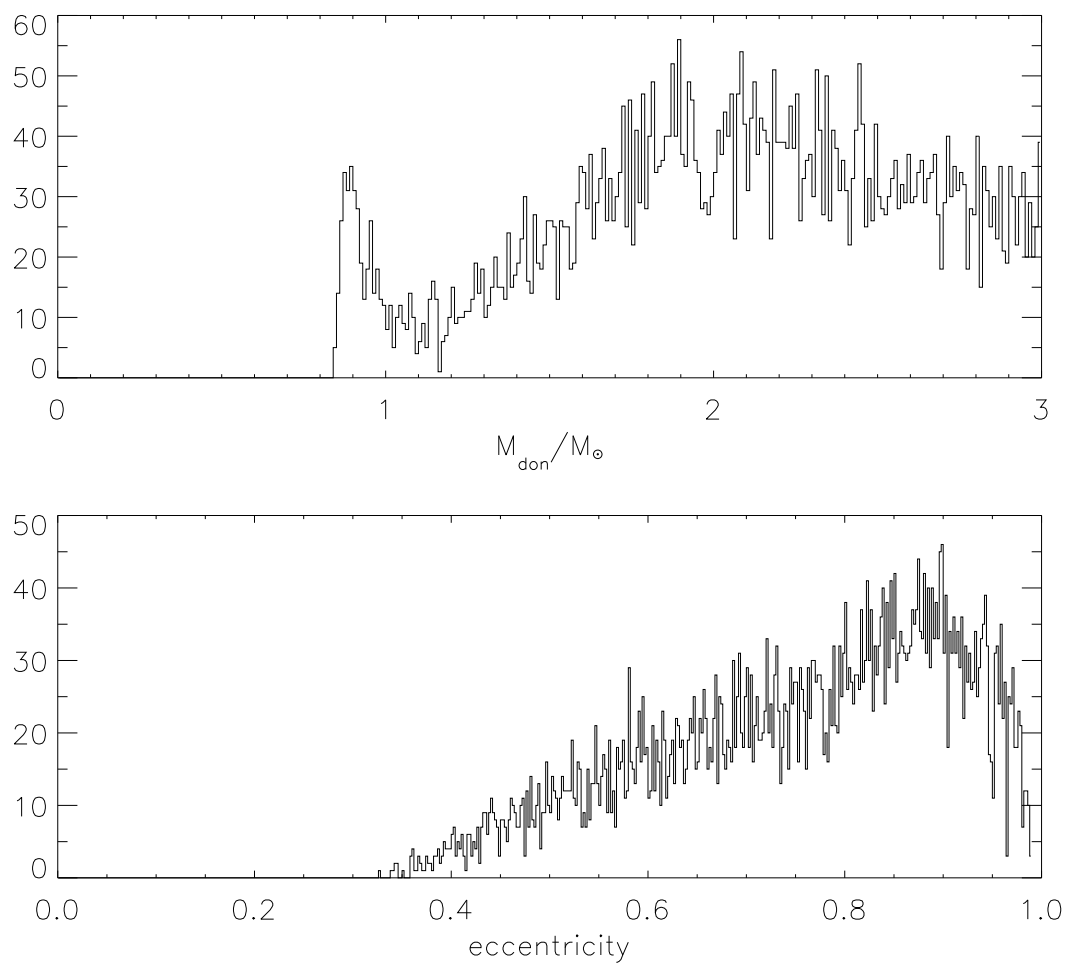


Figure 10-4: Histograms of number of binaries versus *initial* M_{don} and e which eventually reach $P = 16.55$ d and $1 \times 10^{-9} M_{\odot}/\text{yr} < \dot{M} < 1 \times 10^{-7} M_{\odot}/\text{yr}$. The y-axis normalization is arbitrary.

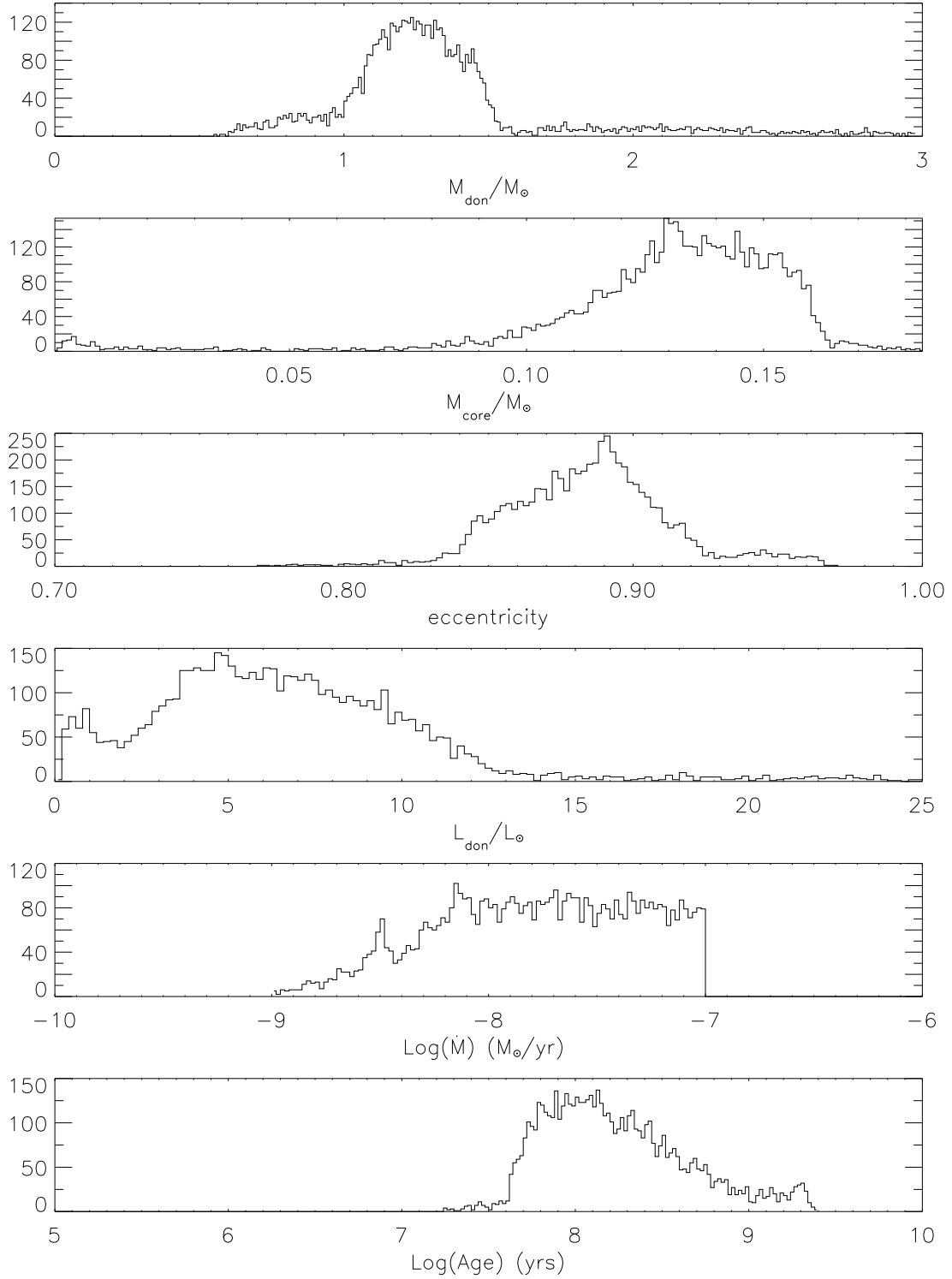


Figure 10-5: Histograms of the number of binaries versus various system parameters at the time when systems resemble Cir X-1, i.e., $P = 16.55$ d and $1 \times 10^{-9} M_{\odot}/\text{yr} < \dot{M} < 1 \times 10^{-7} M_{\odot}/\text{yr}$. The y-axis normalization is arbitrary.

systems have developed a moderate core of $0.10\text{--}0.16\text{ M}_\odot$, indicating that nuclear evolution is driving transfer in most of the systems. A small fraction of donor stars with a low core mass correspond to the lower-mass systems which evolve mainly through angular momentum losses.

The eccentricity distribution is constrained to high values, showing a peak between $e = 0.83 - 0.93$. A tail extending above $e = 0.93$ corresponds to the angular-momentum driven systems. The fact that no systems with low eccentricity have a 16.55-day orbit during mass transfer is due to the large periastron separation for a system with $a \approx 30\text{--}40\text{ R}_\odot$ (as required for two stars with nearly equal masses, $\sim 1\text{ M}_\odot$, and $P = 16.55\text{ d}$) and small eccentricity. For such systems, the critical lobe exceeds the donor size and no mass transfer will occur.

The luminosity of the donor star in most systems is less than about 13 L_\odot , as expected for a low-mass star that is not highly evolved. The optical and infrared magnitudes of the donor are discussed below.

The mass transfer rate is roughly uniform between $10^{-8}\text{--}10^{-7}\text{ M}_\odot/\text{yr}$ ($3 \times 10^{-8}\text{ M}_\odot/\text{yr}$ is approximately the Eddington limit for a 1.4 M_\odot neutron star) and falls off gradually below $10^{-8}\text{ M}_\odot/\text{yr}$. There is also a narrow peak in the distribution at about $3 \times 10^{-9}\text{ M}_\odot/\text{yr}$, corresponding to the angular-momentum driven systems.

The ages of systems when reaching a stage that resembles Cir X-1 are typically 4×10^7 to 1×10^9 . Systems older than about 1×10^9 are mainly the angular-momentum driven systems. All of the systems are significantly older than the young age ($\sim 30000\text{--}100000\text{ yr}$) that would be implied for Cir X-1 if it were associated with the nearby supernova remnant. Thus this model implies that association with the supernova remnant is inconsistent with the assumption that Cir X-1 has a low-mass companion.

The optical and infrared absolute magnitudes (V, R, I, J, & K) of the donor star the systems that resemble Cir X-1 are shown in Figure 10-6. Most donors have a V magnitude of 2–4. Assuming a distance of 8 kpc for Cir X-1 (see section 1.3.4), the distance modulus is -14.5 magnitudes. Using this and a visual extinction of $A_V \sim 4$ (see section 1.3.6), the mean absolute visual magnitude of $V \sim 3$ in Figure 10-6 corresponds to a apparent magnitude of $m_V \sim 21.5$, which is very similar to the non-flaring component of the observed visual magnitude [50]. A higher visual extinction would further increase the apparent visual magnitude, making the donor star fainter than the observed magnitude and requiring a contribution from the accretion disk.

The K-band absolute magnitude in Figure 10-6 is $\sim 1\text{--}3$ for most donors. Applying the same distance modulus correction as above (and ignoring the much smaller extinction in at this longer wavelength), gives an estimated apparent K magnitude of about 16.5, which is more than 4 magnitudes fainter than the observed non-flaring value [24]. Thus, the K-band flux of a low-mass

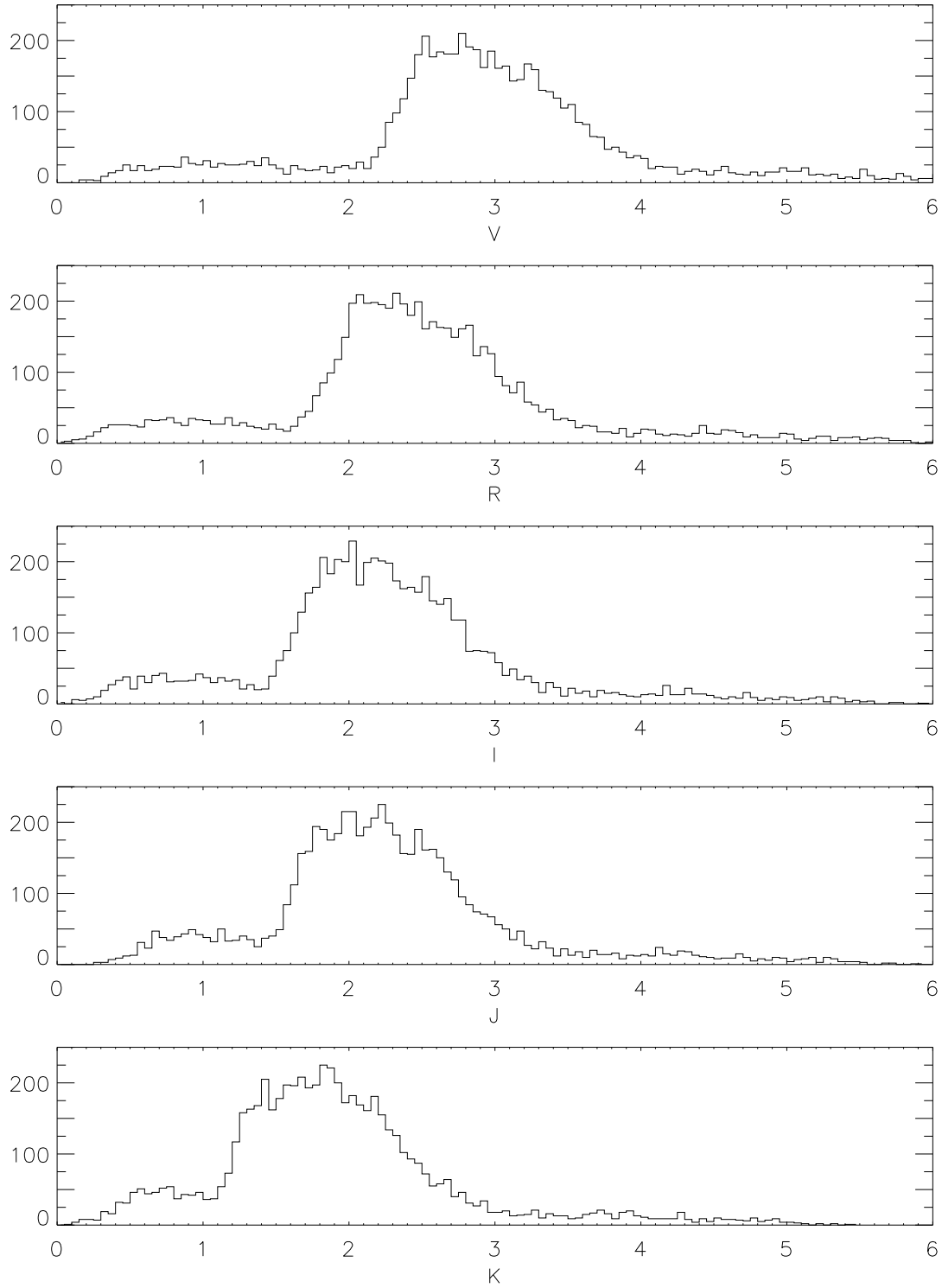


Figure 10-6: Optical and infrared absolute magnitudes (V,R,I,J,K) of the donor star in systems that resemble Cir X-1, i.e., those from Figure 10-5. The y-axis normalization of the histograms is arbitrary.

companion is much too faint to account for the observed flux, implying a significant contribution from the accretion disk (X-ray heating of the companion would be a variable contribution due to the different viewing angles around the orbit). Thus, the optical and infrared magnitudes of donor stars in the modeled systems are not inconsistent with (brighter than) the observed fluxes.

10.5 Conclusions

The eccentric binary evolution code developed for this chapter has shown that a system such as Cir X-1 can be naturally produced with a low-mass companion. A population synthesis study based on this code has shown that the number of systems expected to resemble Cir X-1 is consistent with its unique status in the Galaxy. These results also strongly favor a high eccentricity and donor less massive than the neutron star as current system parameters. Currently the orbital period is the only well-established orbital parameter of the system, making detailed comparison of the evolution results to actual values difficult. For example, in most cases, systems reached 16.55-d periods during mass transfer while unbinding (P increasing). However, if the current ephemeris equation (equation 1.1) is to be taken literally, the period may be decreasing rapidly. If such a change becomes well established, then this would be a significant constraint on models for the system. Furthermore, if Cir X-1 truly is a young LMXB (10^5 yr) associated with a nearby supernova remnant (see Chapter 1), then it must have evolved through a different scenario (i.e., $M_{don} > 3 M_{\odot}$) than the LMXB model developed here, which generally requires ages of at least 4×10^7 yr.

This evolution code (or a slightly modified version that allows circular orbits) can also be applied to other systems and can be used as the basis for a population synthesis study of LMXB properties in general. Some of this spin-off work is already in progress.

Chapter 11

Conclusions

The All-Sky Monitor light curve of Cir X-1 has shown consistent flaring above a steady, bright baseline, as well as significant variety among intensity profiles of each cycle. I have developed computer codes to calculate theoretical accretion-rate profiles for an eccentric binary in which mass transfer occurs via Roche-lobe overflow or via a stellar wind. These profiles generally show much less structure than the X-ray intensity profile. The theoretical profiles show that mass transfer is strongly peaked near periastron (in the case of a stellar wind and moderate eccentricity) or entirely confined to phases near periastron (for Roche-lobe overflow). The fact that the intensity of Cir X-1 maintains a high baseline level at all orbital phases might be related to the gradual emptying of the accretion disk (not included in the models). More difficult to understand is the strong mid-phase flares that sometimes occur in the X-ray light curve, when the neutron star and donor star are believed to be relatively far apart (near apastron).

I developed a binary evolution code for an eccentric low-mass X-ray binary. About 15% of systems drawn from a post-supernova population of pre-LMXBs [73] were found to possess parameters that might be similar to those of Cir X-1 during some stage of their evolution. On average, each LMXB system resembled Cir X-1 for 4×10^5 yrs. This result implies that the number of systems in the Galaxy that should currently resemble Cir X-1 should be of order a unity, consistent with its unique status as an eccentric LMXB with a high accretion rate.

Our multi-frequency campaigns showed that the current X-ray, radio, and infrared flaring all occur within a day of each other, shortly after phase zero. Unfortunately recent radio flares have been very weak, allowing only marginal detection of the flares. Clearly, a return of bright radio flares would be a welcomed opportunity to study correlated behavior in more detail. Infrared photometry on timescale shorter than hours might also prove useful in future campaigns. Optical and

IR spectroscopy carried out during our second multi-frequency campaign showed evidence for emission lines with high-velocity Doppler shifts ($\sim 300\text{--}400$ km/s). Compared with similar measurements made with the Hubble Space Telescope [47], these observations strongly suggest the need for a spectroscopy study around an entire 16.55-d cycle in order to search for evidence of the binary orbit. Another promising future project is the attempt to detect the angular velocity (proper motion) of the system away from the supernova remnant with which it might be associated [67], thus establishing that the system is young. This project will require precise radio astrometry using VLBI (very long baseline interferometry). Preliminary work for the proper motion study was recently carried out at ATCA by R. Fender.

In this project I have used extensive *RXTE* observations of Circinus X-1 to characterize much of the complex behavior exhibited by the source. Based on several timing and spectral studies, I classify the variability we have observed from Cir X-1 into three categories: (1) absorption dips, (2) motion *along* a Z-source hardness-intensity track, and (3) shifts *of* the Z-source hardness-intensity track. I will now summarize the main characteristics associated with each type of variability.

Absorption dips generally occur within the 0.5 d before to 1.5 d after phase zero and last seconds to hours in duration. During dips, the intensity drops below the baseline intensity level while hardness ratios initially increase, but then return to a low value during strong dips. A faint component ($\sim 10\%$ of the total flux) remains unaffected by the heavy absorption, and is probably due to scattering by material distributed over a larger region than the X-ray source itself. This conclusion is similar to that presented by Brandt et al. [12] based on *ASCA* observations of a single low-to-high transition. Here I have shown that multiple dips occur near phase zero in a complex and cycle-dependent manner, as might be expected for obscuration due to inhomogeneities in the mass transfer stream or intermittent “bumps” on the outer edge of the accretion disk. I have shown that the evolution of the energy spectrum throughout transitions into dips is consistent with a variably absorbed bright component and faint unobscured component, and that an iron emission line present both inside and outside dips appears to be associated with the faint (scattered) component. I have also identified the curved tracks that absorption dips produce in color-color and hardness intensity diagrams. The tracks are similar to those due to dips in the black-hole candidates GRO J1655-40 and 4U 1630-47 [36, 74]. Having recognized spectral tracks due to absorption, I was able to focus other studies on other behavior that may be more intrinsic to the source.

I have identified much of the current behavior of Cir X-1 as that of a Z-source low-mass X-ray binary. Hardness-intensity diagrams show that the track for Cir X-1 (e.g., Figure 6-4) differs somewhat from the canonical “Z” track (see Figure 1-1), but the timing characteristics on the branches strongly support the Z-source interpretation. In hardness-intensity diagrams, the “horizontal branch” (HB)

in Cir X-1 becomes almost vertical on the left end. Power density spectra of Cir X-1 from times corresponding to the vertical portion of the HB show horizontal-branch QPOs that evolve in frequency between 1.3 Hz and 30 Hz (increasing in frequency moving down the branch). On the horizontal portion of the HB, this QPO occurs at $\sim 30\text{--}35$ Hz and fades in strength, becoming only a “knee” in the power spectrum. A broad peak begins to arise near 4 Hz in power spectra from the horizontal portion of the HB. This peak becomes a prominent normal-branch QPO on the NB, and remains centered near 4 Hz. The flaring branch for Cir X-1 generally turns above rather than below the normal branch (although it’s orientation depends on the energy bands used in the hardness ratio). No QPOs are present in power spectra from the flaring branch.

The energy spectrum on the horizontal branch of Cir X-1 is fit well with a two-component model consisting of a soft disk blackbody and a higher-temperature blackbody (presumably from closer to the surface). In this model, motion along the HB is mainly associated with an increasing inner radius of the disk, implying that as the luminosity increases across the HB, the inner edge of the disk moves further away from the surface (contrary to expectations that the higher luminosity, and thus probably higher mass accretion rate, should result in a *decrease* in the radius of the inner edge of the disk). Energy spectra on the normal branch indicate that the hard blackbody fades away, leaving only the disk blackbody. On the lower NB, a feature in the spectrum develops above 10 keV. This feature becomes more prominent on the flaring branch.

When the intensity of Cir X-1 is at the “quiescent” (1.0 Crab) level, it is generally on the vertical portion of the HB. Much of the “flaring” activity above the “quiescent” level corresponds to motion across the HB. From the HB/NB apex, the intensity can decrease either down the normal branch (with hardness correlated with intensity) or back across the HB. The lower end of the normal branch is often at a similar intensity level to that of the vertical HB; however, from the low-intensity end of the normal branch, small bursts or “mini-flares” occur, resulting in motion up the flaring branch and producing very low frequency noise (VLFN) in the power spectrum. Bildsten [7, 8] has proposed that VLFN in low mass X-ray binaries is produced by small patches on the neutron-star surface burning intermittently due to slow non-convective combustion, rather than the rapid ignition of the entire surface which occurs in type I bursts. The “flares” or “bursts” seen on the flaring branch in Z sources, and Cir X-1 in particular, may be part of a continuous range from weak VLFN bursts, to small flares, to type I bursts.

I have shown that some of the variability in Cir X-1 is due to shifts of the “Z” track in hardness-intensity diagrams. These shifts are at least in part related to the cycling hardness ratios we observe with the All-Sky Monitor, i.e., gradual hardening of the spectrum during much of the 16.55-d cycle and more rapid hardening of the spectrum at the onset of the flaring state. There is a tendency for

horizontal-branch behavior to occur at the low-intensity, hard portion of the cycle, and normal or flaring-branch behavior to occur during high-intensity, soft portions of the cycle. Thus, evolution of the timing properties versus orbital phase is related to both the shifting Z-track and motion around the Z track. Clearly this can produce behavior more complicated than we observed in our first set of observations, presented in Chapter 4.

Although there is still much to be understood about the physical mechanisms responsible for the correlated spectral and timing behavior in Cir X-1, this project has demonstrated that these unanswered questions for Cir X-1 are related to similar issues in an entire class of systems (Z sources). In fact, some of the unique features of the behavior of Cir X-1 may prove useful in future studies of the Z and atoll classes of low-mass X-ray binaries.

If the baseline intensity level of Cir X-1 decreases from its current bright level, it will provide an opportunity to test the hypothesis that Cir X-1 shows atoll-source behavior at lower mass-accretion rates. Establishing the existence of a source showing the behavior of both classes under different conditions would be helpful in determining the physical distinctions between the classes (e.g., different magnetic fields would be ruled out).

Aspects of the behavior of Cir X-1 that differ from that of typical Z sources may also provide important constraints on models for Z-source behavior. For example, models of horizontal-branch oscillations (typically observed at 13–60 Hz) will have to address what physical property (e.g., mass, spin, or magnetic field of the compact object) of Cir X-1 results in significantly lower-frequency HBOs (1.3–35 Hz). Also, the large shifts of the Z-track in hardness-intensity diagrams for Cir X-1, and the fact that such shifts are associated with the 16.55-d orbital cycle of Cir X-1, are not explained by the hypothesis that mass accretion rate increases along the Z track. Kuulkers et al. [33, 35, 34] have suggested that secular shifts in several Z sources are due to inclination effects. However, the shifts in those sources were not observed to occur periodically as in Cir X-1, nor were the shifts as large (see section 5.4.4). Another possibility is, if accretion occurs both through a disk *and* through a spherical inflow (or other means), then the accretion rate of each component may be responsible for one aspect of the observed behavior.

In the past, the unique status of Cir X-1 among X-ray binaries has often resulted in its being relegated to the discussion of “other sources”. The results presented here show that Cir X-1 has much in common with other low-mass X-ray binaries and that its unusual features may provide the opportunity to study a system with somewhat atypical physical parameters.

Appendix A

Fourier Timing Techniques

A.1 Introduction

Temporal analysis in X-ray astronomy is generally accomplished through examination of the Fourier power density spectrum (PDS) and complex cross spectrum. The following is a brief review of some of the standard techniques that are directly applicable to RXTE data (see van der Klis [76], e.g., for a more complete discussion of standard techniques). In addition, specific formulae are derived to show how the analysis software handles such complications as data gaps and variable number of detectors.

The analysis software we developed at M.I.T. operates on time series data stored in “DS (DataStream)” format, which dynamically changes storage format to reduce file sizes, and allows data to be piped between programs to chain together several tasks. These features result in smaller files and faster processing than the standard FTOOLS package provided by NASA. Useful information can be stored as keywords in header blocks of DS files. Since the timing programs in particular rely heavily on using keyword parameters, keyword names will be referenced in the throughout this appendix, which is intended to provide documentation to our software.

A.2 Power Density Spectra

A.2.1 Leahy Normalization

The discrete Fourier transform of a time series of N bins (keyword NUMPOINT) containing counts x_k ($k = 0, \dots, N-1$) is

$$a_j = \sum_{k=0}^{N-1} x_k e^{2\pi i j k / N}, \quad j = -N/2, \dots, N/2 - 1. \quad (\text{A.1})$$

Frequency bin j corresponds to a frequency of $\nu = j/T = j/Nt_b$, where T is the total duration of the time series and t_b is the duration of a single time bin. The normalization used by Leahy et al. [40] defines the power in frequency bin j to be

$$P_j = \frac{2}{N_{ph}} |a_j|^2, \quad j = 0, \dots, N/2 \quad (\text{A.2})$$

where N_{ph} is the total number of photons in the transform. In this normalization, the distribution of powers for Poisson counting noise has a mean value of 2 and obeys the χ^2 distribution with 2 degrees of freedom. This has the advantage of straightforward estimation of the significance of high points in the PDS.

A.2.2 Estimate of the Poisson Noise Level

Real time series data always contains counting noise ($x = x_{source} + x_{noise}$). This adds power $P = P_{source} + P_{noise}$.

In the absence of detector effects, Poisson counting noise produces a constant power equal to 2 in the Leahy normalization. However, detector dead-time effects result in a Poisson-level that varies with Fourier frequency. Zhang et al. [88, 89] (see also [51]) have calculated this effect to be

$$\langle P_{noise}(\nu) \rangle = 2[1 - 2r_0\tau_d(1 - \frac{\tau_d}{2t_b})] - 2\frac{N-1}{N}r_0\tau_d(\frac{\tau_d}{t_b})\cos(2\pi t_b\nu) + 2r_{vle}r_0\tau_{vle}^2[\frac{\sin(\pi\tau_{vle}\nu)}{\pi\tau_{vle}\nu}]^2, \quad (\text{A.3})$$

where r_0 is the count rate per PCU detector, τ_d is the dead time per event (10 μs for the PCA), t_b is the time bin size, and N is the number of time bins in the transformed segment. The last term accounts for dead time due to very large events (VLEs), occurring at a rate r_{vle} per PCU with a dead-time window (τ_{vle}) of 55 μs or 155 μs for each VLE [89].

A.2.3 Fractional RMS Variability

Dividing a Leahy-normalized PDS by the mean count rate from the source results in a normalization giving the square of the fractional root-mean-squared variability per Hz. In this normalization, the square root of the integrated power under a PDS feature (such as a QPO peak) gives the fractional rms variability of the intensity due to that feature.

The average *total* count rate per second (keyword RATE) is

$$R = \frac{1}{t_b} \frac{\sum_{k=1}^N x_k}{N} = \frac{\bar{x}}{t_b}. \quad (\text{A.4})$$

However, to obtain the mean rate of the *source* R' , the background b must be subtracted:

$$R' = \frac{1}{t_b} \frac{\sum_{k=1}^N (x_k - b_k)}{N} = \frac{1}{t_b} (\bar{x} - \bar{b}) = R - B, \quad (\text{A.5})$$

where B is the average background rate per second (keyword BKGD). Generally, the average background rate is estimated from slew data or other means modeled with software provided with the FTOOLS package.

A.2.4 Estimates of Power Variance

The variance of powers in the Leahy normalization is 4 (so $\sigma = 2 = \mu$). The variance of the mean power from M consecutive frequency bins or from W PDSs is:

$$\sigma_\mu = \frac{2}{\sqrt{MW}}. \quad (\text{A.6})$$

However, intrinsic noise from the source often causes the actual variance of the averaged powers to exceed the theoretical variance. Thus, a useful error estimate is derived from the *sample* variance resulting from averaging MW powers $P_i, i = 1, \dots, MW$ (dropping the frequency index for clarity):

$$s^2 = \frac{1}{MW - 1} \sum_{i=1}^{MW} (P_i^2 - \langle P \rangle^2) \quad (\text{A.7})$$

The sample variance of the mean power is

$$s_\mu^2 = \frac{s^2}{MW} = \frac{1}{MW(MW - 1)} \sum_{i=1}^{MW} (P_i^2 - \langle P \rangle^2) \quad (\text{A.8})$$

A.2.5 Data Gaps

Ideally, each PDS should be derived from a continuous time series with no gaps. However, gaps are common in real data, making it necessary to work with partially filled (but not sparse) time series'. The simplest way to handle data gaps is to fill the empty bins with the mean number of counts per bin. (In practice the mean is subtracted from the data to suppress the DC term in the PDS, so unoccupied bins are filled with zeros.) To compensate for an incomplete time series, averages should be weighted by the fraction exposure f , the fraction of occupied bins in the time series (keyword FILL). I.e., in averaging M frequency bins from each of W power spectra, each with fractional exposure f_w ,

$$\langle P \rangle = \frac{\sum_{m=1}^M \sum_{w=1}^W f_w P_{mw}}{\sum_{m=1}^M \sum_{w=1}^W f_w} \quad (\text{A.9})$$

Likewise, the sample variance is

$$s^2 = \frac{1}{\sum_{m=1}^M \sum_{w=1}^W f_w - 1} \sum_{m=1}^M \sum_{w=1}^W (P_{mw}^2 - \langle P \rangle^2) \quad (\text{A.10})$$

which can be re-expressed as

$$s^2 = \frac{\sum_{m=1}^M \sum_{w=1}^W f_w}{\sum_{m=1}^M \sum_{w=1}^W f_w - 1} (\langle P^2 \rangle - \langle P \rangle^2) \quad (\text{A.11})$$

where $\langle P^2 \rangle = \frac{\sum_{m=1}^M \sum_{w=1}^W f_w P_{mw}^2}{\sum_{m=1}^M \sum_{w=1}^W f_w}$. Finally, the sample variance of the mean power is

$$s_\mu^2 = \frac{s^2}{\sum_{m=1}^M \sum_{w=1}^W f_w} = \frac{\langle P^2 \rangle - \langle P \rangle^2}{\sum_{m=1}^M \sum_{w=1}^W f_w - 1} \quad (\text{A.12})$$

Both $\langle P \rangle$ and $\langle P^2 \rangle$ are saved in the PDS files and used in error estimates (COL keywords with PDS and PDS^2 labels).

A.2.6 Variable Number of Detectors

For instrument safety, one or more of the five proportional counter units (PCUs) of the PCA may be shut off during an observation. Transforms are not performed for time segments which include a discontinuous detector turn-on/turn-off. However, separate PDSs with different numbers of PCUs turned on, \bar{p}_w (keyword NUMPCU), can still be averaged if care is taken to handle the various parameters properly. When averaging W PDSs the combined average of the number of PCUs on, \bar{p}_w (keyword NUMPCU), is weighted by the total number of occupied bins $n_w = W_w N_w f_w$ (from

keywords NUMFFT \times NUMPOINT \times FILL):

$$\bar{p} = \frac{\sum_{w=1}^W n_w \bar{p}_w}{\sum_{w=1}^W n_w} = \frac{\sum_{w=1}^W n_w \bar{p}_w}{n_{tot}} \quad (\text{A.13})$$

where n_{tot} is the total number of occupied bins. Alternately, the PCU average can be expressed as $\bar{p} = \sum_{p=1}^5 n_p p / n_{tot}$, where n_p is the number of bins with p PCUs on.

For the rms normalization, the relevant rates are those actually observed, regardless of the number of detectors involved. Thus, the combined average rate and background rate from W PDSs, each with average rate \bar{x}_w and background rate \bar{b}_w , are simply weighted by the number of occupied bins:

$$\bar{x} = \frac{\sum_{w=1}^W n_w \bar{x}_w}{n_{tot}}, \quad \bar{b} = \frac{\sum_{w=1}^W n_w \bar{b}_w}{n_{tot}}. \quad (\text{A.14})$$

Deadtime effects in each PCU are independent of the other PCUs, so the average rate per PCU r_0 used in the Poisson-level estimate (equation A.3) should be weighted by the number of PCUs on:

$$r_0 = \frac{1}{t_b} \frac{\sum_{p=1}^5 n_p p \frac{\bar{x}_p}{p}}{\sum_{p=1}^5 n_p p} = \frac{1}{t_b} \frac{\sum_{p=1}^5 n_p \bar{x}_p}{n_{tot} \bar{p}} \quad (\text{A.15})$$

where \bar{x}_p is the average number of counts in all time bins having p PCUs on. The numerator of the last term above is simply the total number of counts, which is equal to $n_{tot} \bar{x}$. Thus, the average rate per PCU reduces to

$$r_0 = \frac{1}{t_b} \frac{\bar{x}}{\bar{p}} = \frac{R}{\bar{p}}. \quad (\text{A.16})$$

The Poisson-level estimate also requires the average product per PCU of the VLE rate and the good count rate. For a constant number of PCUs p :

$$\langle r_{vle} r_0 \rangle_p = \frac{1}{t_b^2} \frac{\sum_{k=1}^{n_{tot}} p \frac{v_k}{p} \frac{x_k}{p}}{\sum_{k=1}^{n_{tot}} p} = \frac{1}{t_b^2} \frac{\sum_{k=1}^{n_{tot}} v_k x_k}{n_{tot} p^2}, \quad (\text{A.17})$$

where v_k is the VLE rate per bin. The average over different numbers of PCUs must be based on the number of occupied bins for each p :

$$\langle r_{vle} r_0 \rangle = \frac{\sum_{p=1}^5 n_p p \langle r_{vle} r_0 \rangle_p}{\sum_{p=1}^5 n_p p} = \frac{\sum_{p=1}^5 n_p p \langle r_{vle} r_0 \rangle_p}{n_{tot} \bar{p}}. \quad (\text{A.18})$$

(The keyword VLEP saves this VLE product as $\bar{p}^2 \langle r_{vle} r_0 \rangle$ to be consistent with the RATE and BKGD keywords, which are not per PCU.)

A.3 Complex Cross Spectra

The Fourier transforms of a time series in two energy channels can be used to produce a complex cross spectrum in addition to the two power density spectra. Using the same notation as for the PDS (see above), the cross spectrum derived from two Fourier transforms a_j and b_j is defined as

$$C_j = a_j^* b_j, \quad j = 0, \dots, N/2. \quad (\text{A.19})$$

A.3.1 Time Lags

The argument of the complex-valued cross spectrum is the phase delay (in radians) between intensity fluctuations in the two channels (once again dropping the frequency subscript):

$$\delta\phi = \arctan\left(\frac{\text{Im}(C)}{\text{Re}(C)}\right) = \arctan\left(\frac{\text{Re}(a)\text{Im}(b) - \text{Im}(a)\text{Re}(b)}{\text{Re}(a)\text{Re}(b) + \text{Im}(a)\text{Im}(b)}\right). \quad (\text{A.20})$$

This is easily converted to a time delay via $\delta t = \delta\phi/2\pi\nu$. A positive value of δt indicates that intensity fluctuations in the second channel lag those in the first.

A.3.2 Coherence Function

The magnitude of the cross spectrum can be used to derive the coherence function between two channels. The coherence function is a measure of the degree of linear correlation between the two time series at each Fourier frequency [81]. For noiseless signals, the coherence function is defined as

$$\gamma^2 = \frac{|\langle a^* b \rangle|^2}{\langle |a^* a| \rangle \langle |b^* b| \rangle} = \frac{|\langle C \rangle|^2}{\langle P_1 \rangle \langle P_2 \rangle} \quad (\text{A.21})$$

where P_1 and P_2 are the power spectra derived from a and b respectively and the angle brackets denote an average over m independent measurements (ideally $m \rightarrow \infty$).

For signals with Poisson counting noise, the quantities used in equation A.21 should be for the source only, thus

$$\gamma^2 = \frac{|\langle (a - a_{\text{noise}})^* (b - b_{\text{noise}}) \rangle|^2}{\langle P_1 - P_{1,\text{noise}} \rangle \langle P_2 - P_{2,\text{noise}} \rangle} \quad (\text{A.22})$$

$$\gamma^2 = \frac{|\langle a^* b \rangle - \langle a^* b_{\text{noise}} \rangle - \langle a_{\text{noise}}^* b \rangle + \langle a_{\text{noise}}^* b_{\text{noise}} \rangle|^2}{\langle P_1 - P_{1,\text{noise}} \rangle \langle P_2 - P_{2,\text{noise}} \rangle} \quad (\text{A.23})$$

$$\gamma^2 = \frac{|\langle C \rangle - \langle a^* b_{\text{noise}} \rangle - \langle a_{\text{noise}}^* b \rangle + \langle C_{\text{noise}} \rangle|^2}{\langle P_1 - P_{1,\text{noise}} \rangle \langle P_2 - P_{2,\text{noise}} \rangle}. \quad (\text{A.24})$$

According to Vaughan and Nowak [81], in the Gaussian limit the numerator in equation A.24

can be expressed as

$$| \langle C_{source} \rangle |^2 = | \langle C \rangle |^2 - \langle n^2 \rangle, \quad (\text{A.25})$$

where $n^2 \equiv (P_{1,source}P_{2,noise} + P_{1,noise}P_{2,source} + P_{1,noise}P_{2,noise})/m$. Thus, the intrinsic source coherence function can be expressed in terms of the observed powers and cross spectra and the estimated Poisson noise powers:

$$\gamma^2 = \frac{| \langle C \rangle |^2 - (P_{1,source}P_{2,noise} + P_{1,noise}P_{2,source} + P_{1,noise}P_{2,noise})/m}{\langle P_1 - P_{1,noise} \rangle \langle P_2 - P_{2,noise} \rangle}. \quad (\text{A.26})$$

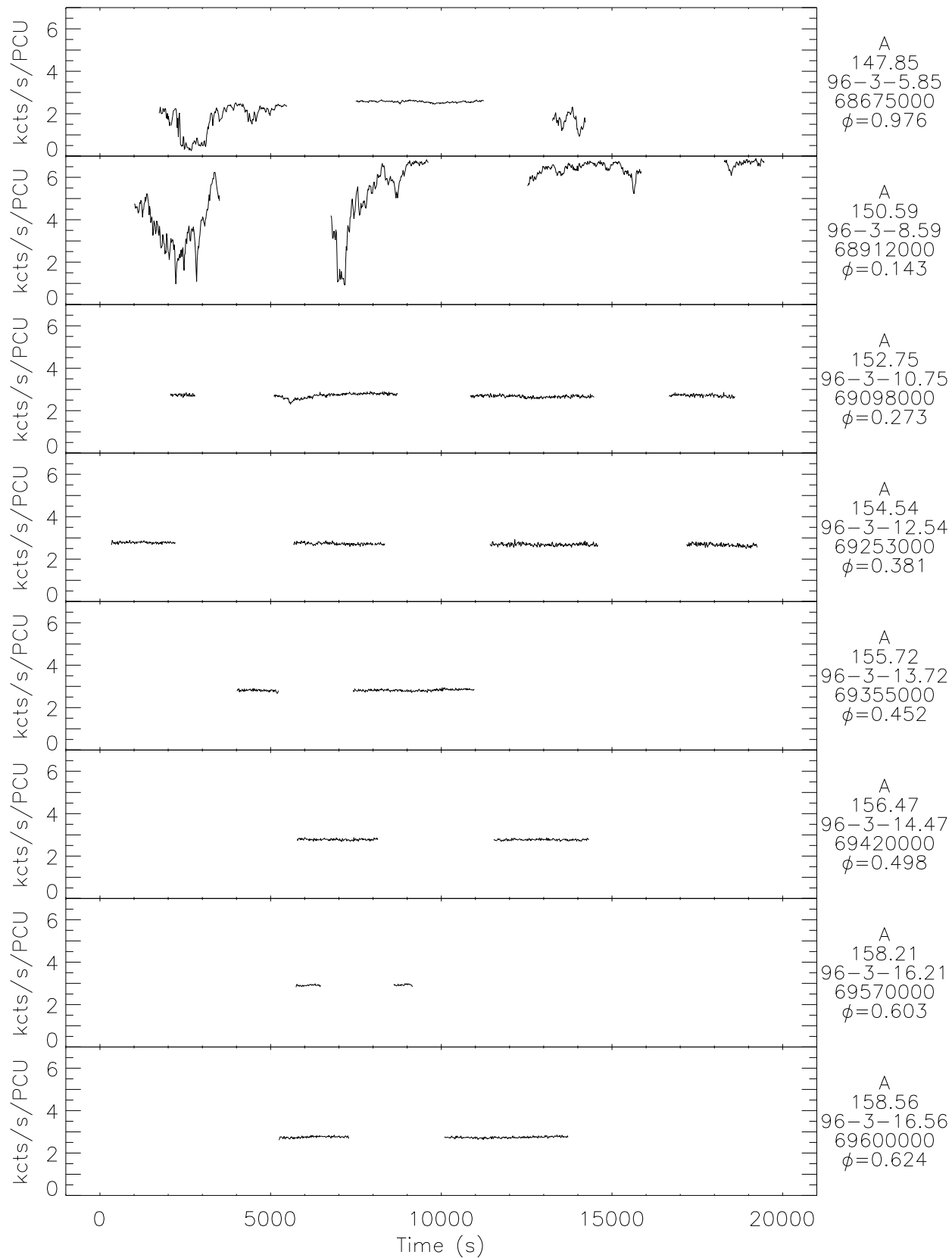
Appendix B

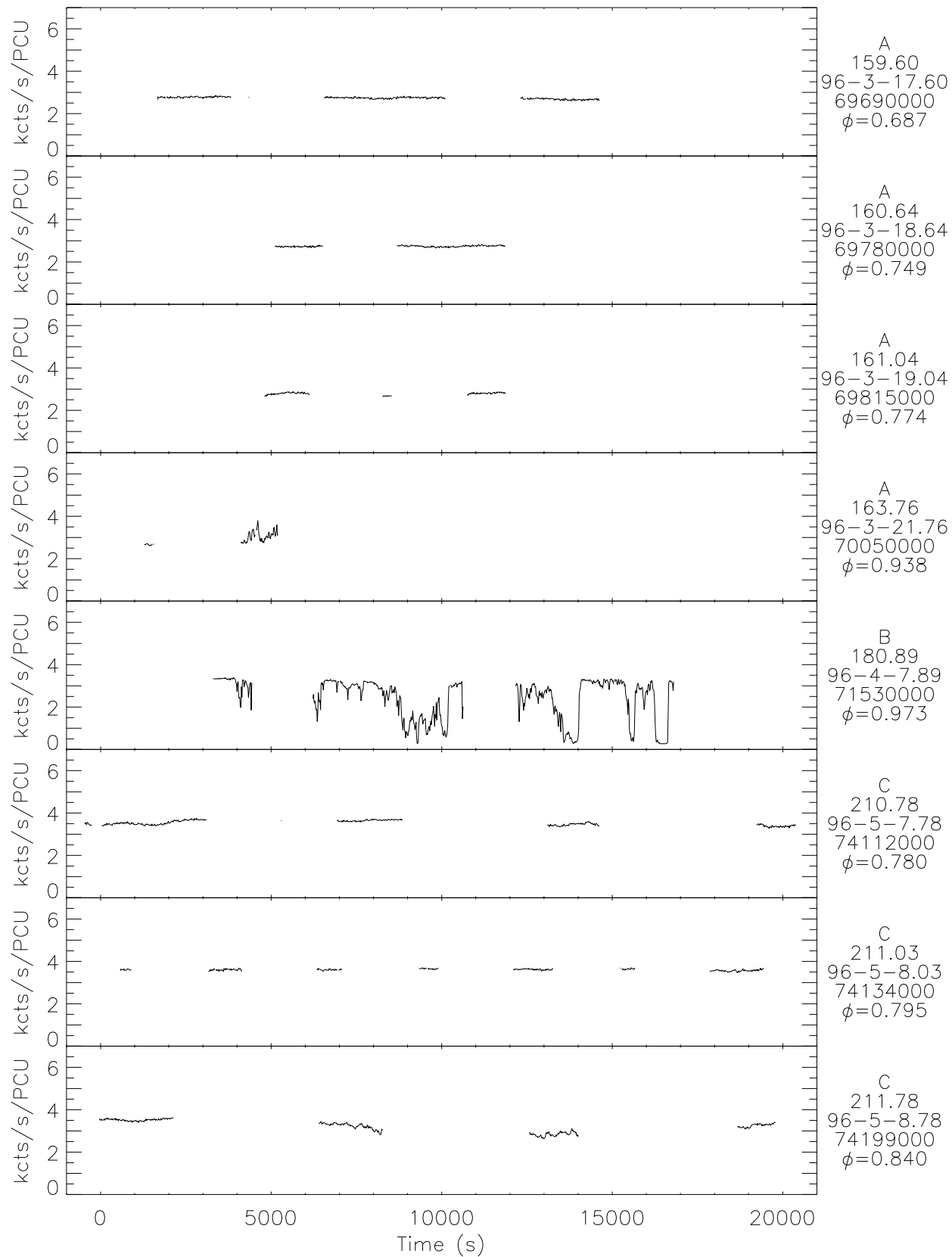
Standard PCA Light Curves

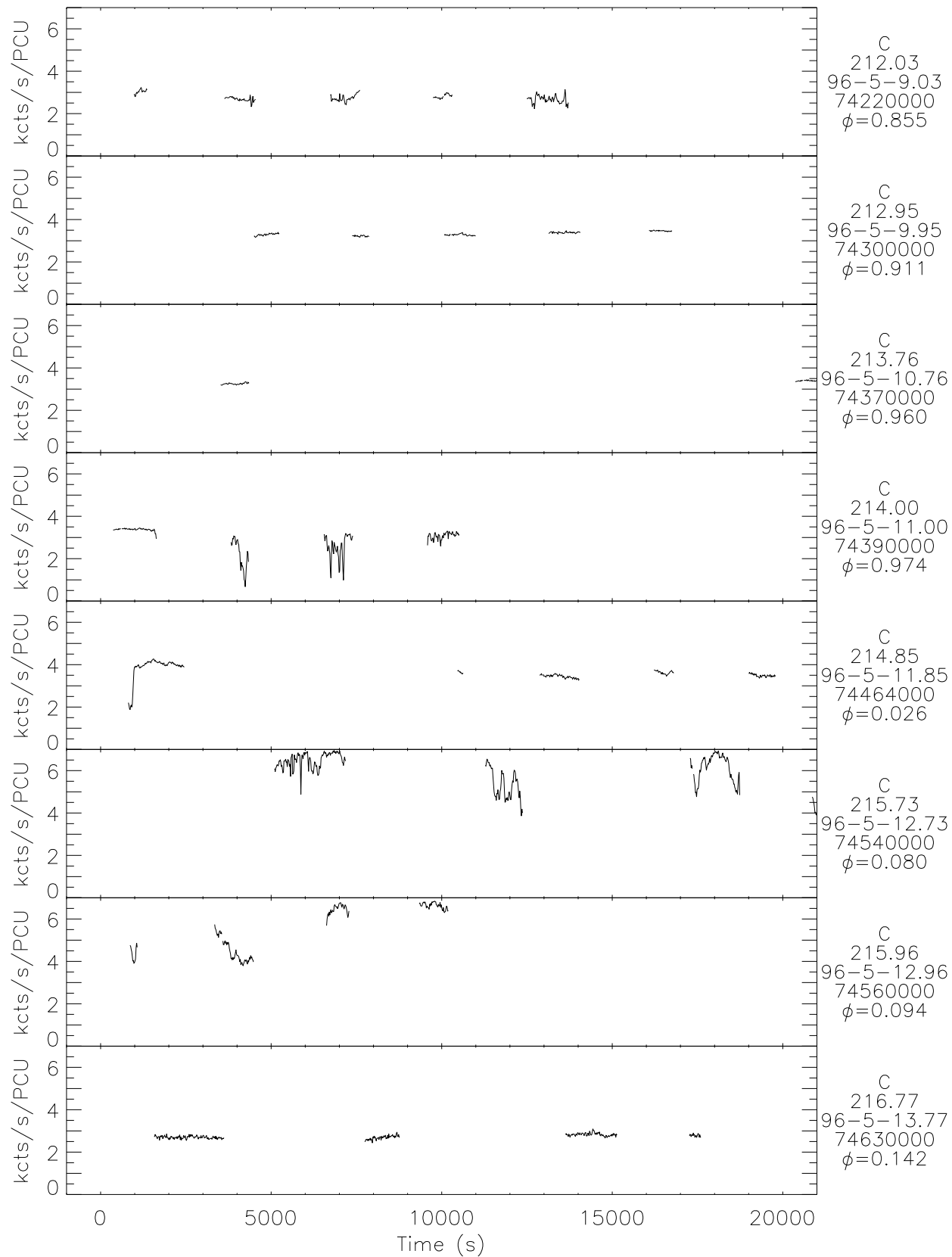
This appendix contains standard 20-kilosecond light curves of all our 1996–1997 PCA observations of Cir X-1. By displaying all data with a uniform scale, the wide range of variability and intensity levels is apparent.

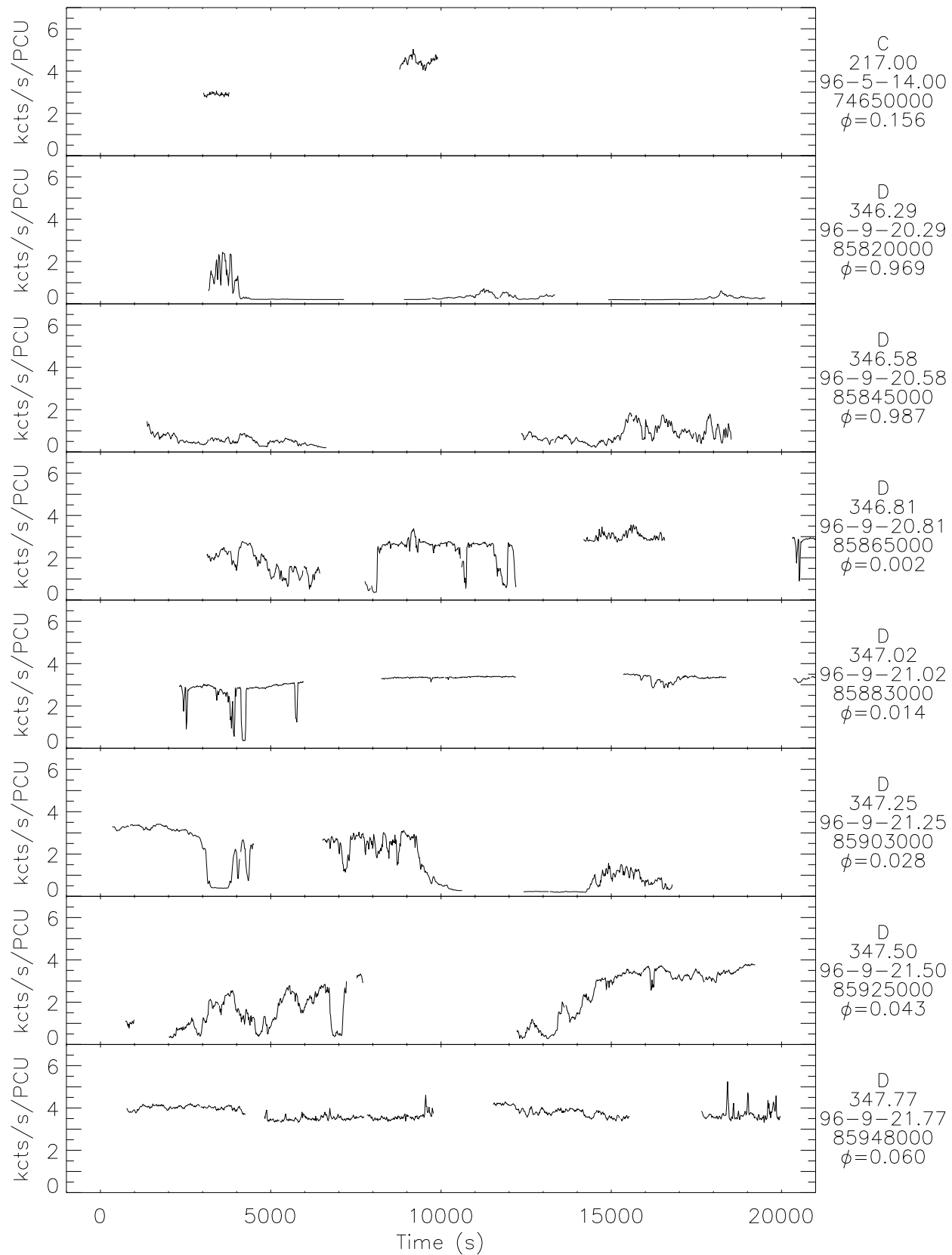
Each 20-ks panel is labelled along the right side with the letter of the study with which it was associated (A–H, see Table 3.1) and several time labels referring to time zero of that panel: the truncated Julian date (JD-2450000.5), the calendar date (YR-MO-DAY), the mission elapsed time (MET = seconds since 1994 Jan. 1.0), and the orbital phase (see equation 1.1).

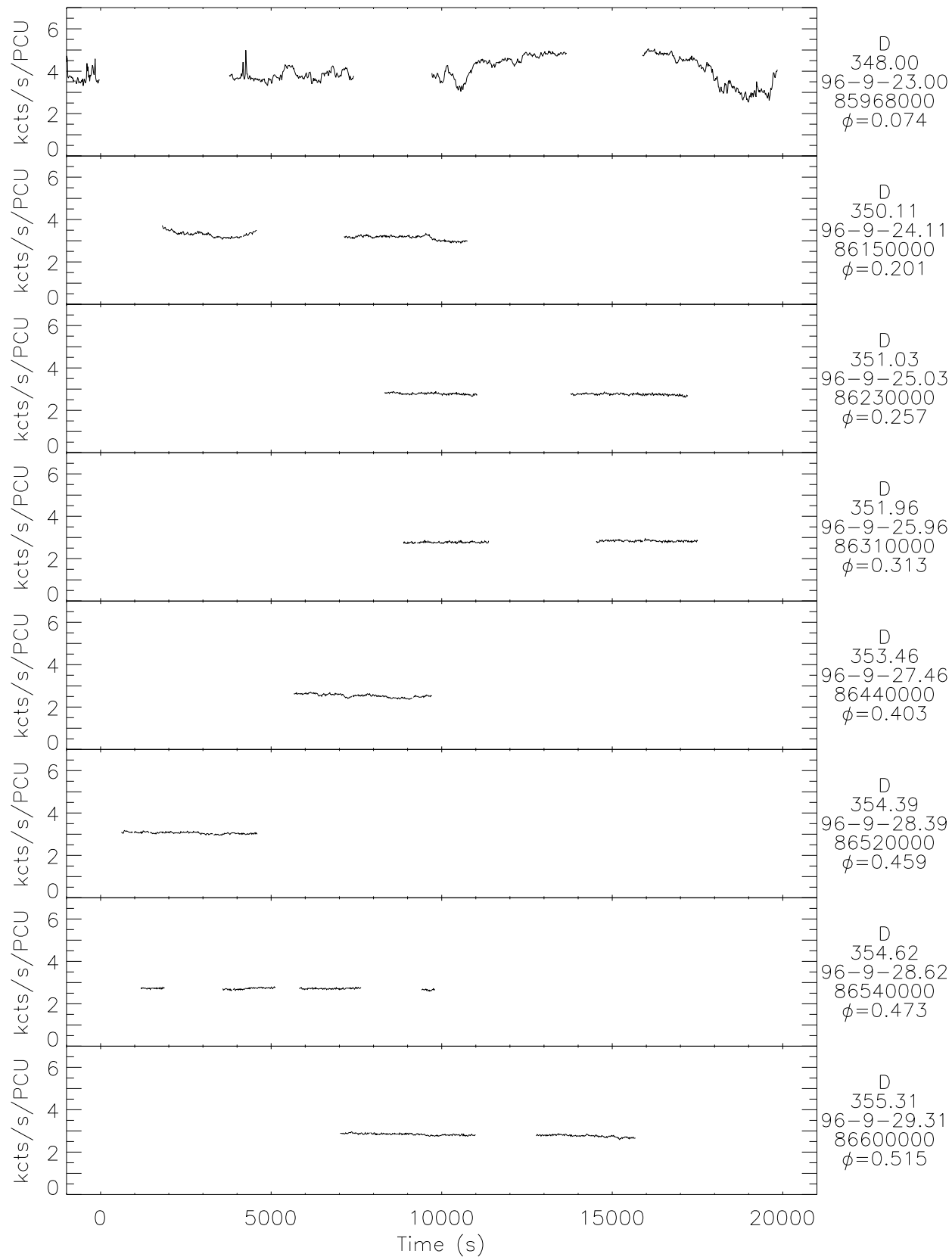
The counting rates are derived from 16 s time bins over the full PCA energy band and are the average rates from PCUs 0, 1, and 2, which were operating during all observations (PCUs 3 and 4 were often switched off). A counting rate of 2.6 kcts/s corresponds to an intensity of ~ 1.0 Crab (1060 μ Jy at 5.2 keV). Background is not subtracted but is negligible. The data have not been corrected for detector deadtime; such corrections would increase the baseline 1 Crab level by about 5% and the peak 2.7 Crab level by about 13%.

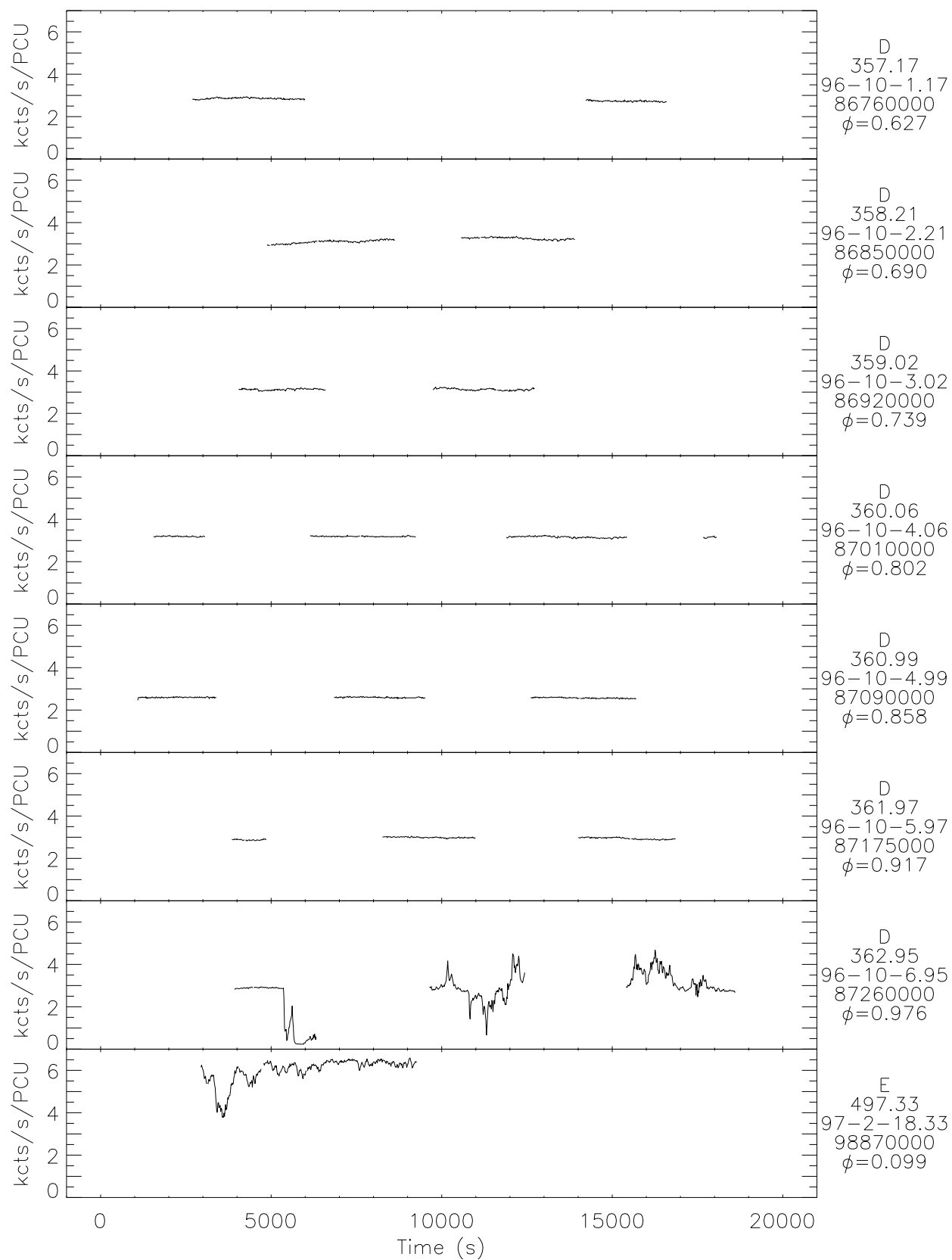


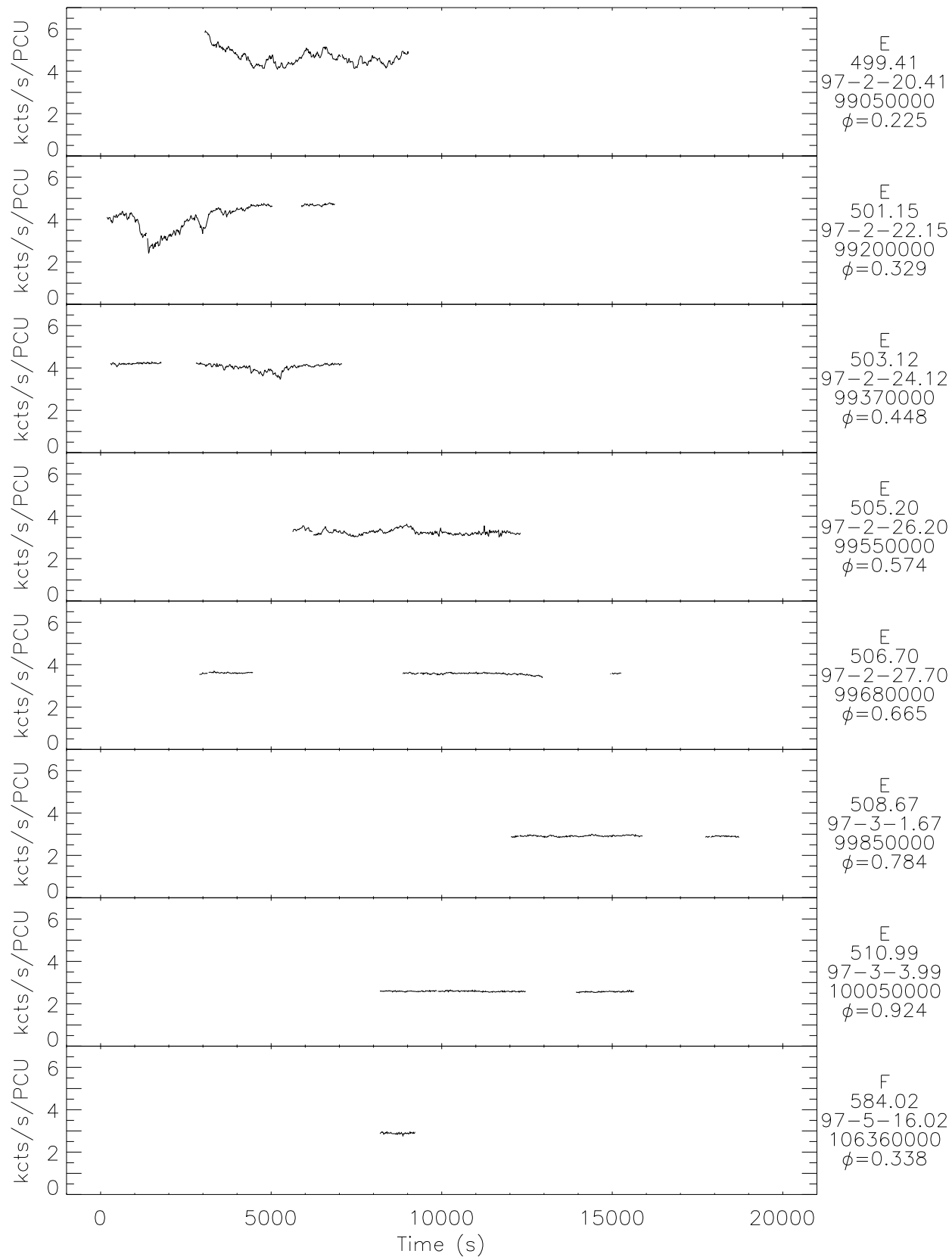


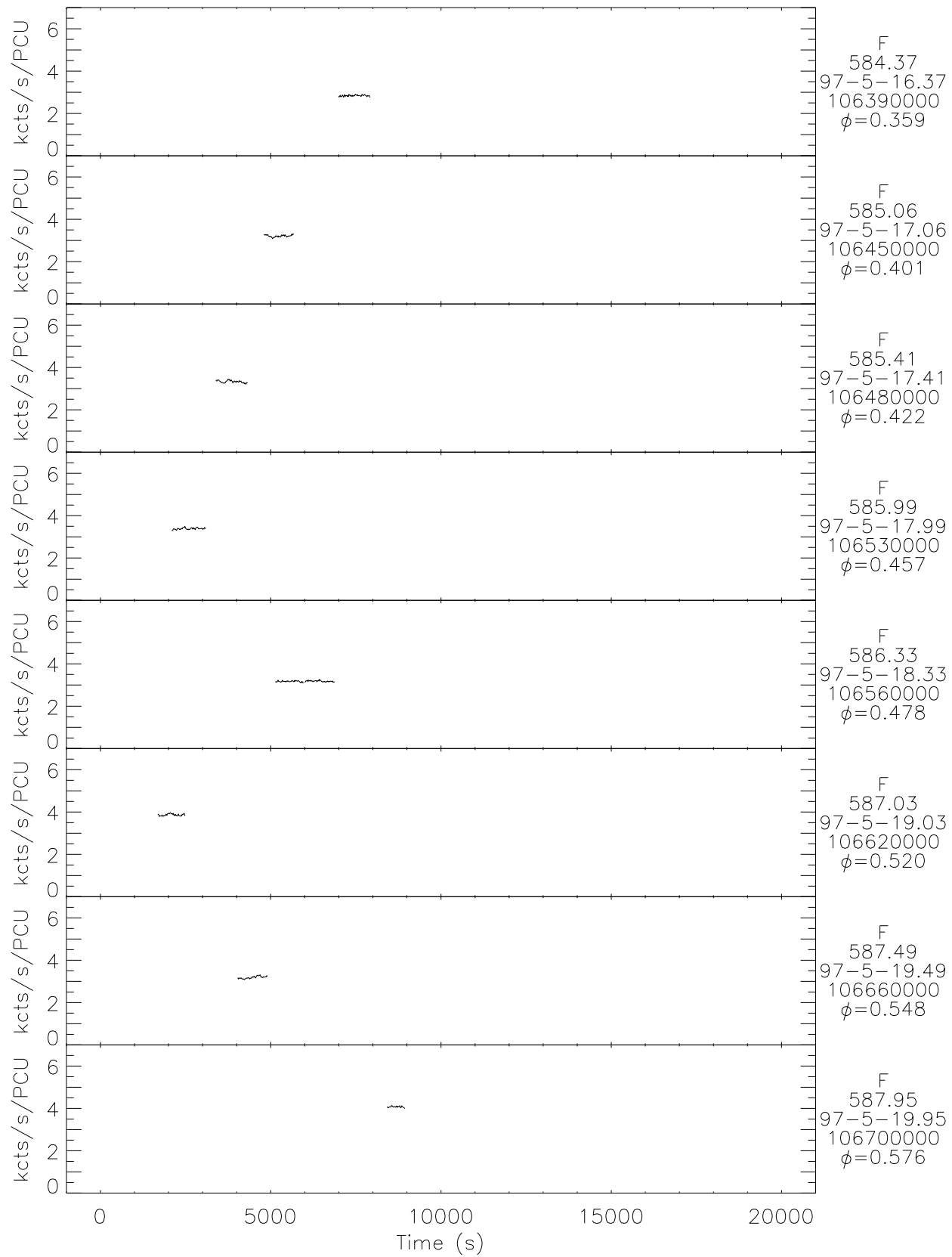


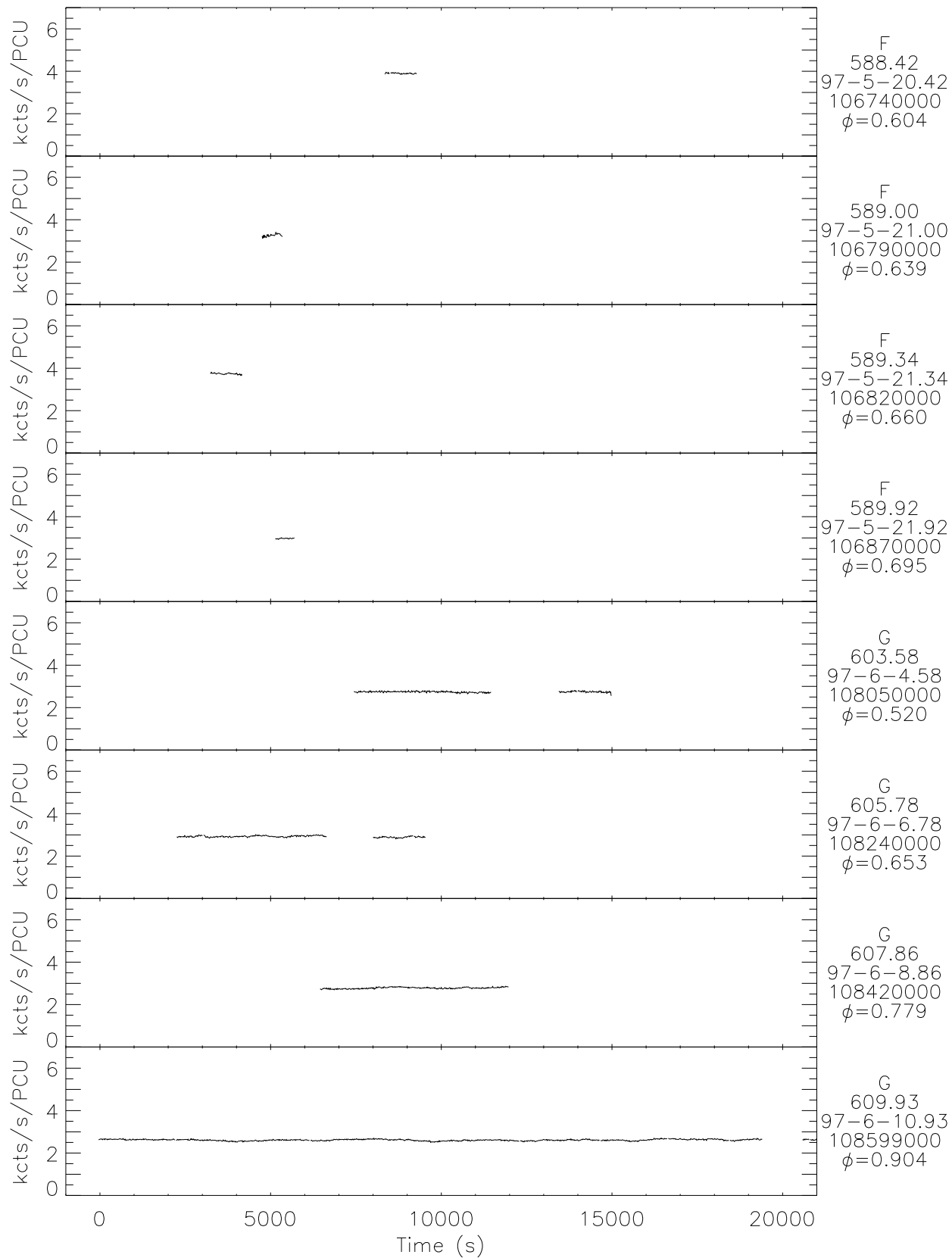


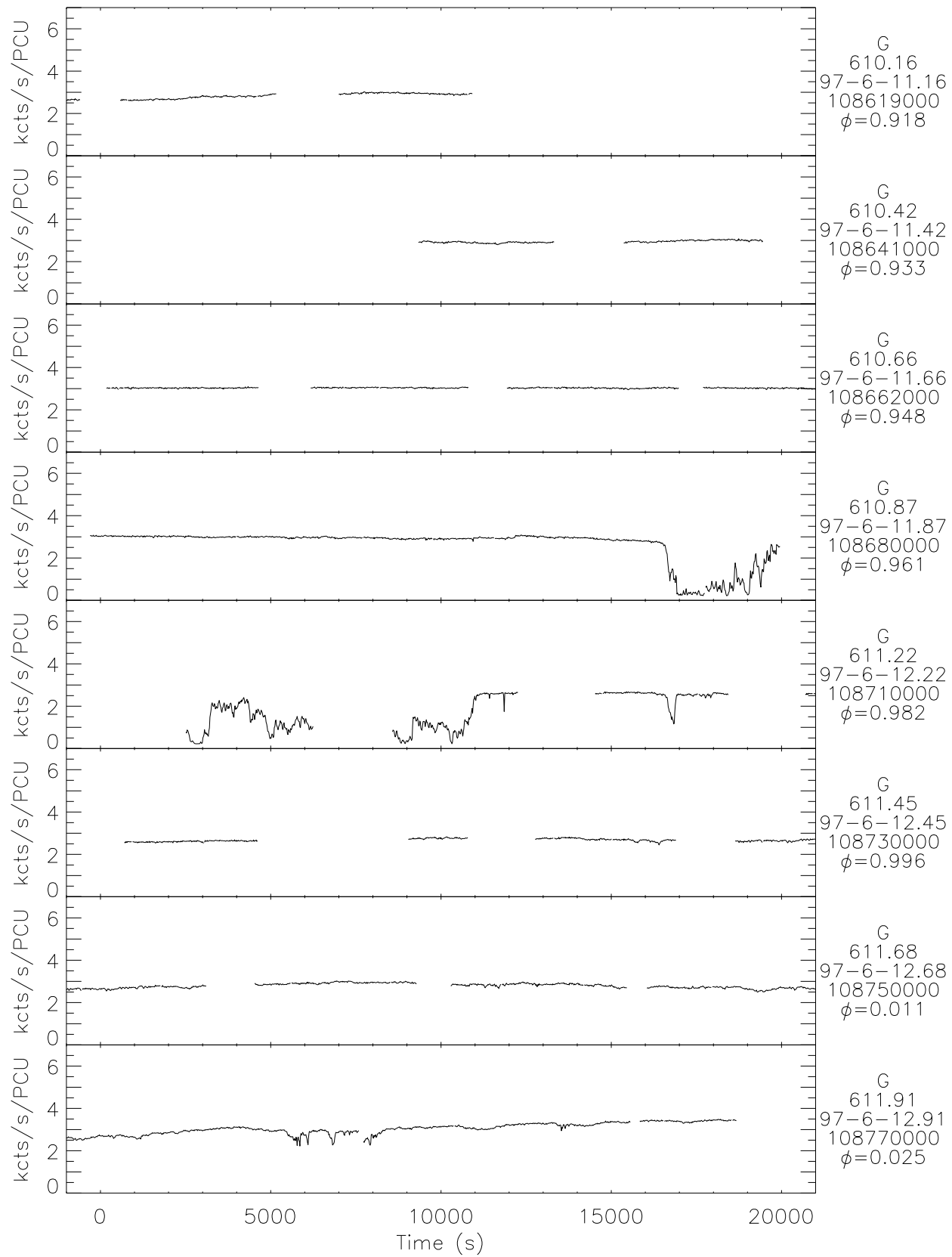


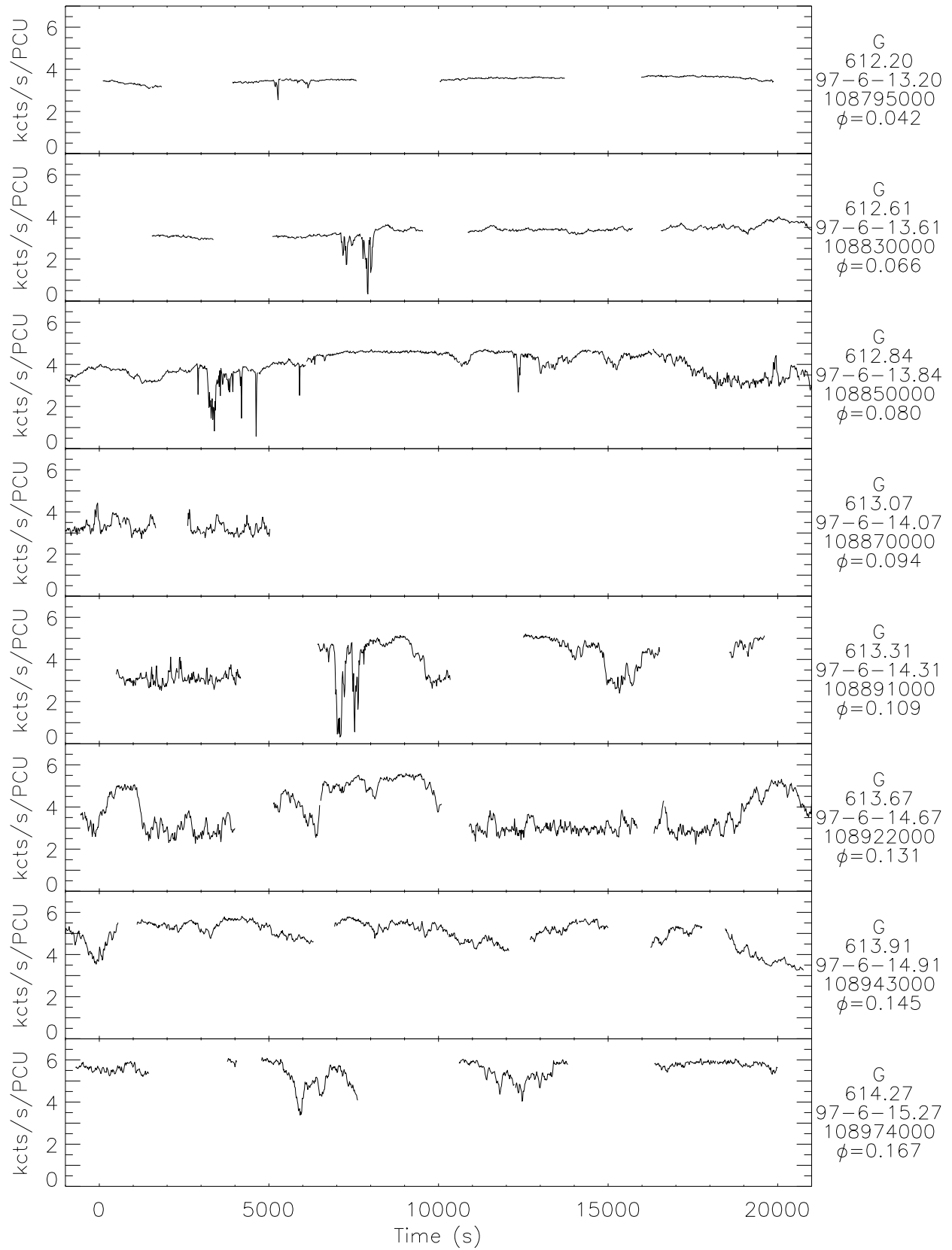


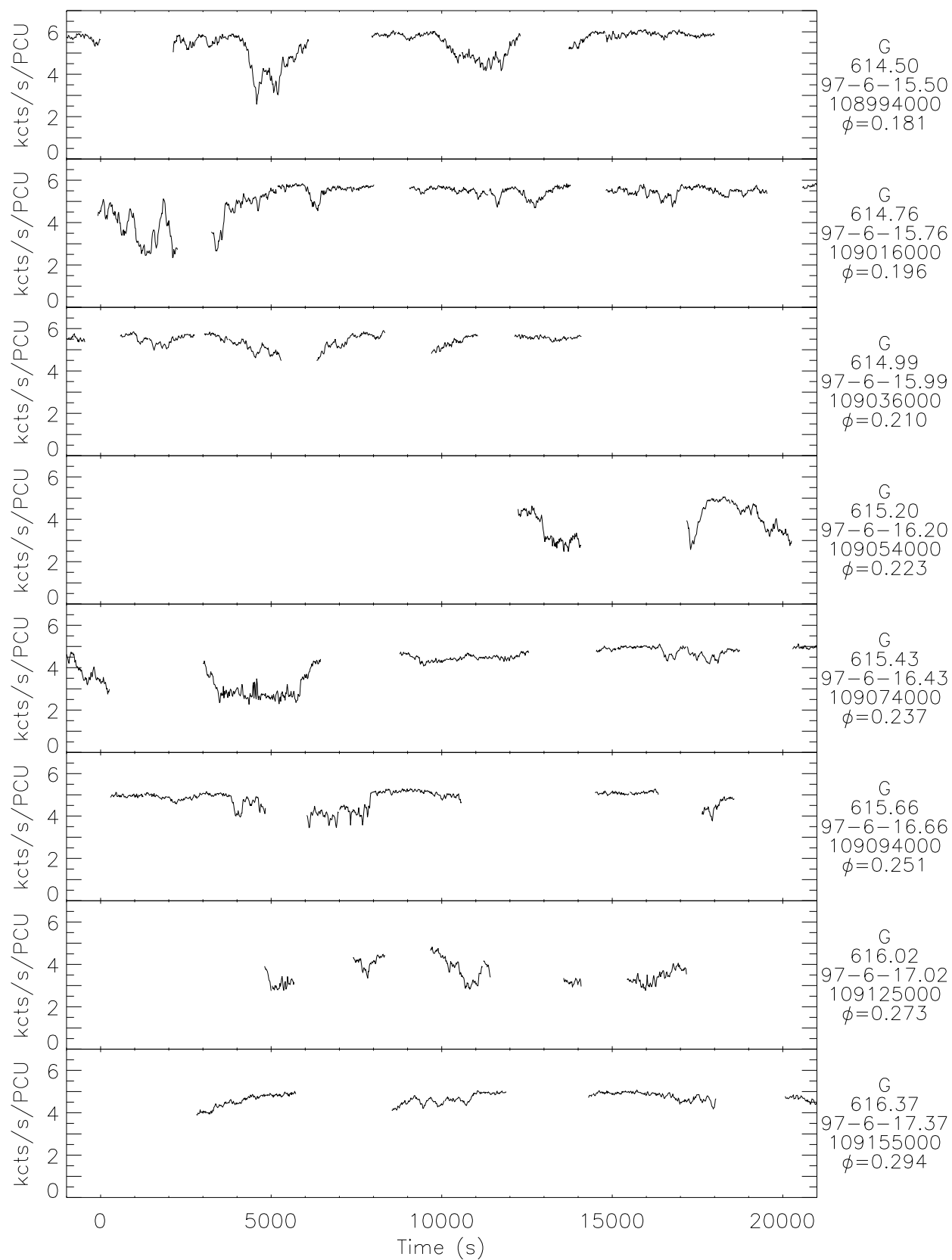


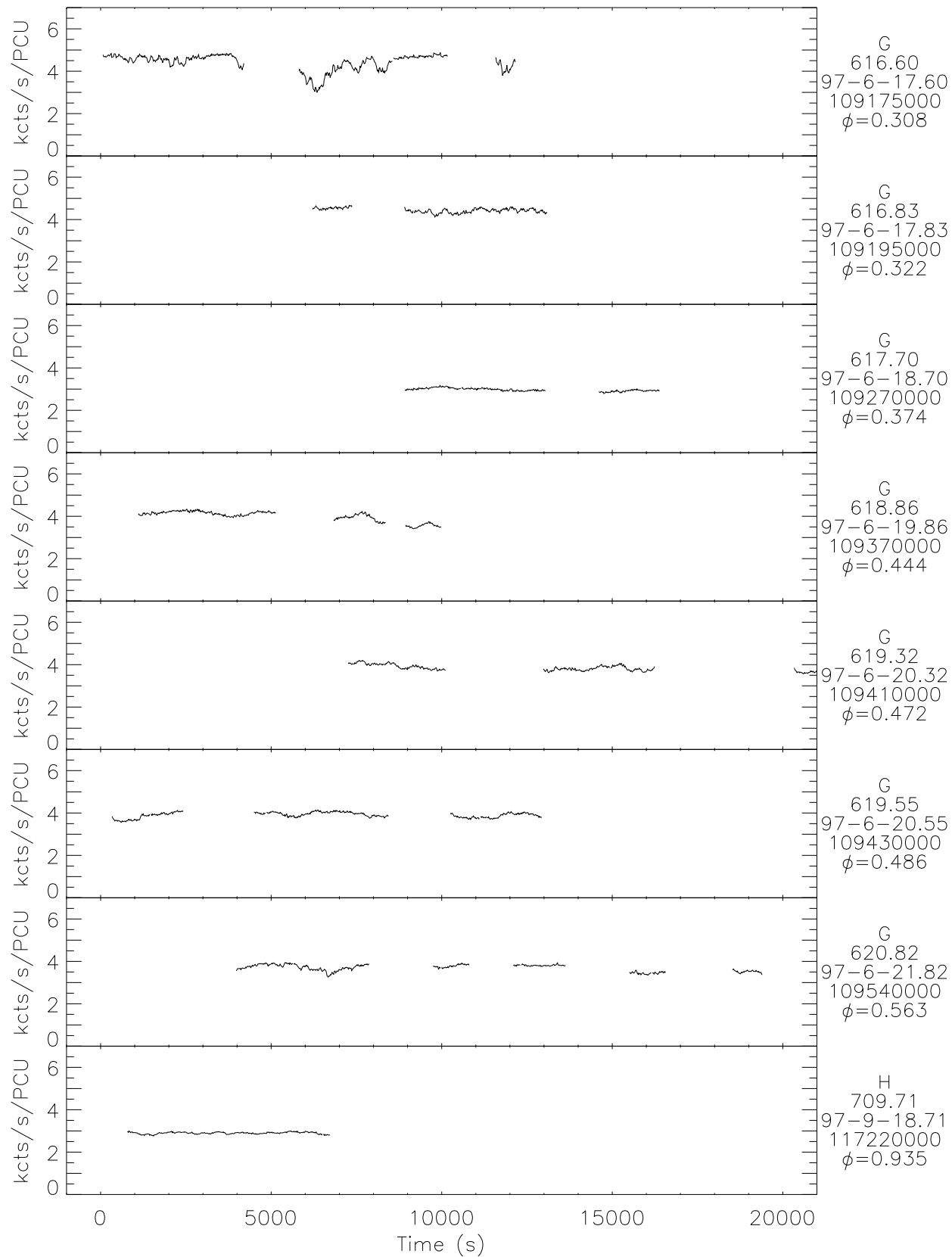


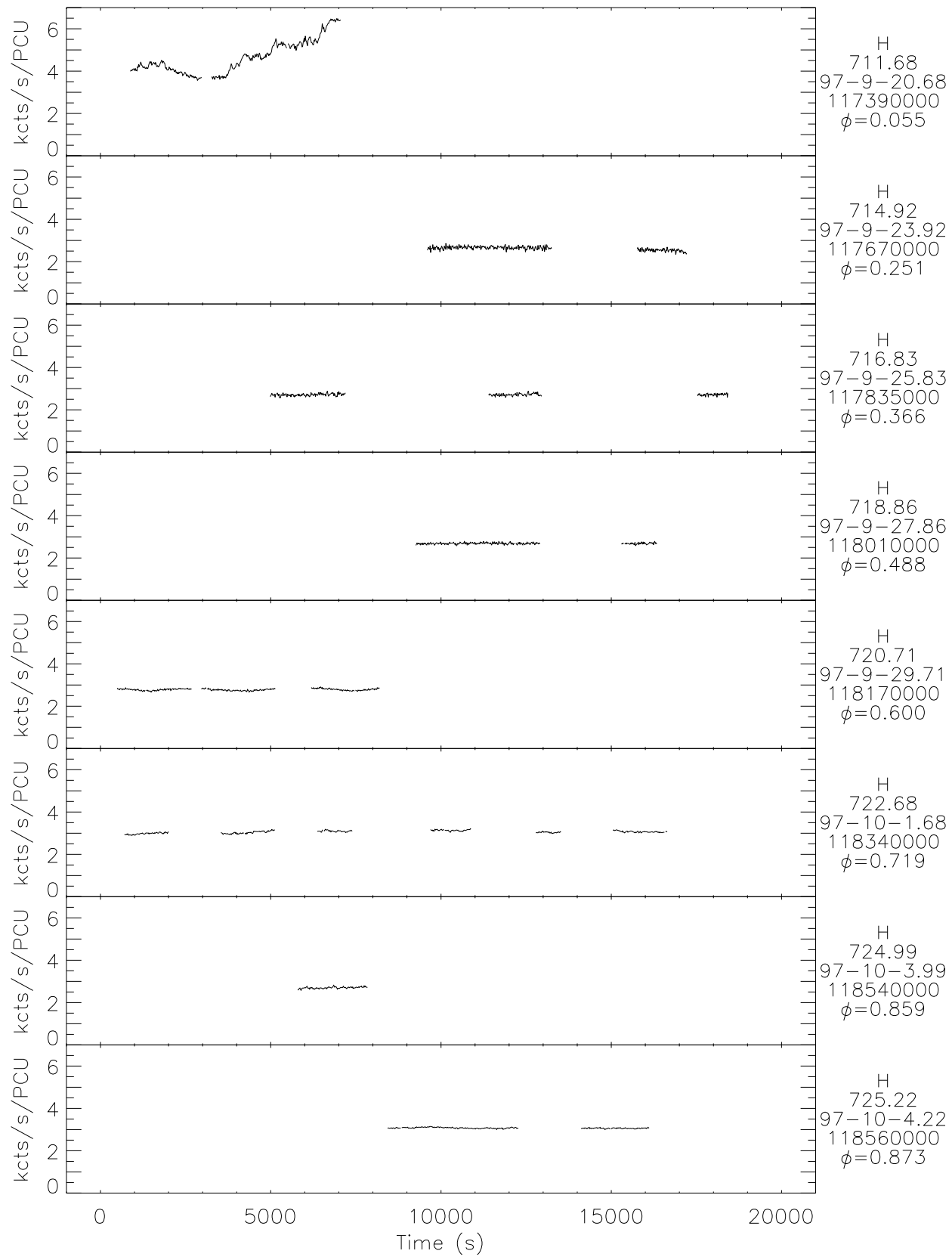












Bibliography

- [1] M. Ali Alpar and Jacob Shaham. Is GX 5-1 a millisecond pulsar? *Nature*, 316:239–241, 1985.
- [2] T. Augusteijn et al. Coordinated X-ray and optical observations of Scorpius X-1. *The Astrophysical Journal*, 265:177–182, 1992.
- [3] Yoram Avni. The eclipse duration of the X-ray pulsar 3U 0900-40. *The Astrophysical Journal*, 209:574–577, 1976.
- [4] Christopher M. Becker. *Studies of Supersoft X-ray Sources in the ROSAT Database of Pointed Observations*. PhD thesis, Massachusetts Institute of Technology, 1997.
- [5] T. Belloni and G. Hasinger. An atlas of aperiodic variability in HMXB. *Astronomy and Astrophysics*, 230:103–119, 1990.
- [6] T. Belloni and G. Hasinger. Variability in the noise properties of Cygnus X-1. *Astronomy and Astrophysics*, 227:L33–L36, 1990.
- [7] Lars Bildsten. Rings of fire: Nuclear burning as the origin of sub-Hertz noise and weak X-ray bursts in accreting neutron stars. *The Astrophysical Journal*, 418:L21–L24, 1993.
- [8] Lars Bildsten. Propagation of nuclear burning fronts on accreting neutron stars: X-ray bursts and sub-Hertz noise. *The Astrophysical Journal*, 438:852–875, 1995.
- [9] H. Bondi and F. Hoyle. *Monthly Notices of the Royal Astronomical Society*, 104:273, 1944.
- [10] H. V. Bradt, R. E. Rothschild, and J. H. Swank. X-ray Timing Explorer mission. *Astronomy and Astrophysics Supplement Series*, 97:355–360, 1993.
- [11] Hale Bradt, Robert Shirey, and Alan Levine. Observations of Circinus X-1 with RXTE. In L. Scarsi, H. Bradt, P. Giommi, and F. Fiore, editors, *Nuclear Physics B Proceedings Supplements, The Active X-ray Sky: Results from Beppo-SAX and Rossi-XTE*. Elsevier Science B. V., 1998.

- [12] W. N. Brandt, A. Fabian, T. Dotani, F. Nagase, H. Inoue, and T. Kotani. ASCA observations of the iron K complex of Circinus X-1 near zero phase: spectral evidence for partial covering. *Monthly Notices of the Royal Astronomical Society*, 283:1071–1082, 1996.
- [13] Deepto Chakrabarty and Edward H. Morgan. The 2 hour orbit of the bursting millisecond X-ray pulsar SAX J1808-3658. Submitted to *Nature*, 1998.
- [14] L. Chiapetti and S. J. Bell Burnell. X-ray observations of Circinus X-1 in its low state. *Monthly Notices of the Royal Astronomical Society*, 200:1025–1031, 1982.
- [15] R. DiStefano, L. A. Nelson, W. Lee, T. Wood, and S. Rappaport. Luminous supersoft X-ray sources as type Ia progenitors. In R. Canal and P. Lapuente-Ruiz, editors, *Thermonuclear Supernovae*, page 147, 1996.
- [16] Richard G. Dower, Hale V. Bradt, and Edward H. Morgan. Circinus X-1: X-ray observations with SAS 3. *The Astrophysical Journal*, 261:228–250, 1982.
- [17] A. R. Duncan, R. T. Stewart, and R. F. Haynes. $H\alpha$ position determination of the binary Circinus X-1. *Monthly Notices of the Royal Astronomical Society*, 265:157–160, 1993.
- [18] P. Eggleton. Approximations to the radii of Roche lobes. *The Astrophysical Journal*, 268:368–369, 1983.
- [19] P. P. Eggleton. *Evolutionary Processes in Binary and Multiple Stars*. Cambridge Press, Cambridge, 1997.
- [20] B. Fortner, F. K. Lamb, and G. S. Miller. Origin of 'normal-branch' quasiperiodic oscillations in low-mass X-ray binary systems. *Nature*, 342:775–777, 1989.
- [21] J. García-Sánchez and J. M. Paredes. Particle injection in the Circinus X-1 radio outbursts. *Astronomy and Astrophysics*, 323:867–880, 1997.
- [22] R. Giacconi. Scorpius x-1. *Monthly Notices of the Royal Astronomical Society*, 9:L439, 1962.
- [23] I. S. Glass. Variations of Circinus X-1 in the infrared. *Monthly Notices of the Royal Astronomical Society*, 183:335–340, 1978.
- [24] I. S. Glass. Long-term infrared behavior of Cir X-1. *Monthly Notices of the Royal Astronomical Society*, 268:742–748, 1994.
- [25] W. M. Goss and U. Mebold. The distance of Cir X-1. *Monthly Notices of the Royal Astronomical Society*, 181:255–258, 1977.

- [26] Amos Harpaz, Saul Rappaport, and Noam Soker. The rings around the Egg Nebula. *The Astrophysical Journal*, 487:809–817, 1997.
- [27] G. Hasinger and M. van der Klis. Two patterns of correlated X-ray timing and spectral behaviour in low-mass X-ray binaries. *Astronomy and Astrophysics*, 225:79–96, 1989.
- [28] G. Hasinger, M. van der Klis, K. Ebisawa, T. Dotani, and K. Mitsuda. Multifrequency observations of Cygnus X-2: X-ray observations with Ginga. *Astronomy and Astrophysics*, 235:131–146, 1990.
- [29] P. Hut. Tidal evolution in close binary systems. *Astronomy and Astrophysics*, 99:126–140, 1981.
- [30] P. C. Joss. Helium-burning flashes on an accreting neutron star — A model for X-ray burst sources. *The Astrophysical Journal*, 225:L123–L127, 1978.
- [31] Paul C. Joss and Saul A. Rappaport. Neutron stars in interacting binary systems. *Annual Review of Astronomy and Astrophysics*, 22:537–592, 1984.
- [32] L. J. Kaluzienski, S. S. Holt, E. A. Boldt, and P. J. Serlemitsos. Evidence for a 16.6 day period from Circinus X-1. *The Astrophysical Journal*, 208:L71–L75, 1976.
- [33] E. Kuulkers and M. van der Klis. GX 340+0 with EXOSAT: Its correlated X-ray spectral and timing behavior. *Astronomy and Astrophysics*, 314:567–575, 1996.
- [34] E. Kuulkers, M. van der Klis, T. Oosterbroek, K. Asai, T. Dotani, J. van Paradijs, and W. G. H. Lewin. Spectral and correlated timing behavior of GX 5-1. *Astronomy and Astrophysics*, 289:795–821, 1994.
- [35] E. Kuulkers, M. van der Klis, and B. A. Vaughan. Secular variations in the Z source Cygnus X-2. *Astronomy and Astrophysics*, 311:197–210, 1996.
- [36] E. Kuulkers, R. Wijnands, T. Belloni, Mario Mendez, M. van der Klis, and J. van Paradijs. Absorption dips in the light curves of GRO J1655-40 and 4U 1630-47 during ourburst. *The Astrophysical Journal*, 494:753–758, 1998.
- [37] F. K. Lamb, N. Shibasaki, M. A. Alpar, and J. Shaham. Quasi-periodic oscillations in the bright galactic-bulge X-ray sources. *Nature*, 317:681–687, 1985.
- [38] P. Lamb and P. W. Sanford. Compton scattering effects observed in Sco X-1 and similar sources. *Monthly Notices of the Royal Astronomical Society*, 188:555–563, 1979.
- [39] L.D. Landau and E.M. Lifshitz. *The Classical Theory of Fields*. Pergamon, Oxford, 1962.

- [40] D. A. Leahy, W. Darbro, R. F. Elsner, M. C. Weisskopf, P. G. Sutherland, S. Kahn, and J. E. Grindlay. On searches for pulsed emission with application to four globular cluster X-ray sources: NGC 1851, 6441, 6624, and 6712. *The Astrophysical Journal*, 266:160–170, 1983.
- [41] Myron Lecar, J. Craig Wheeler, and Christopher F. McKee. Tidal circularization of the binary X-ray sources Hercules X-1 and Centaurus X-1. *The Astrophysical Journal*, 205:556–562, 1976.
- [42] Alan M. Levine, Hale Bradt, Wei Cui, J. G. Jernigan, Edward H. Morgan, Ronald Remillard, Robert E. Shirey, and Donald A. Smith. First results from the All-Sky Monitor on the Rossi X-ray Timing Explorer. *The Astrophysical Journal*, 469:L33–L36, 1996.
- [43] W. G. H. Lewin, J. van Paradijs, and E. P. J. van den Heuvel, editors. *X-ray Binaries*. Number 26 in Cambridge Astrophysics Series. Cambridge University Press, Cambridge, 1995.
- [44] Walter H. G. Lewin, Lori M. Lubin, Jianmin Tan, Michiel van der Klis, Jan van Paradijs, Wim Penninx, Tadayasu Dotani, and Kazuhisa Mitsuda. Quasi-periodic oscillations in the Z source GX 5-1. *Monthly Notices of the Royal Astronomical Society*, 256:545–570, 1992.
- [45] Yukihiro Makino. *Circinus X-1 Observed with Ginga*. PhD thesis, Osaka University, Japan, 1993.
- [46] K. Makishima, Y. Maejima, K. Mitsuda, H. V. Bradt, R. A. Remillard, I. R. Tuohy, and R. Hoshi. Simultaneous X-ray and optical observations of GX 339-4 in an X-ray high state. *The Astrophysical Journal*, 308:635–643, 1986.
- [47] R. Mignani, P. A. Caraveo, and G. F. Bignami. Assymmetric $H\alpha$ disk emission dominates the HST/FOS spectrum of Circinus X-1. *Astronomy and Astrophysics*, 323:797–800, 1997.
- [48] M. Coleman Miller, Frederik K. Lamb, and Dimitrios Psaltis. Sonic-point model of kilohertz quasi-periodic brightness oscillations in low-mass X-ray binaries. *The Astrophysical Journal*, 1998. in press.
- [49] K. Mitsuda et al. Energy spectra of low-mass binary X-ray sources observed from Temna. *Publications of the Astronomical Society of Japan*, 36:741–759, 1984.
- [50] A. Moneti. Optical and infrared observations of Circinus X-1. *Astronomy and Astrophysics*, 260:L7–L10, 1992.
- [51] E. H. Morgan, R. A. Remillard, and J. Greiner. RXTE observations of QPOs in the black hole candidate GRS 1915+105. *The Astrophysical Journal*, 482:993–1010, 1997.

- [52] P. Murdin, D. L. Jauncey, R. F. Haynes, I. Lerche, G. D. Nicolson, S. S. Holt, and L. J. Kluźienski. Binary model of Circinus X-1. *Astronomy and Astrophysics*, 87:292–298, 1980.
- [53] G. D. Nicolson, M. W. Feast, and I. S. Glass. Recent changes in the optical, infrared and radio emission from Circinus X-1. *Monthly Notices of the Royal Astronomical Society*, 191:293–299, 1980.
- [54] T. Oosterbroek, M. van der Klis, E. Kuulkers, J. van Paradijs, and W. G. H. Lewin. Circinus X-1 revisited: Fast-timing properties in relation to spectral state. *Astronomy and Astrophysics*, 297:141–158, 1995.
- [55] W. Penninx, W. G. H. Lewin, J. Tan, K. Mitsuda, M. van der Klis, and J. van Paradijs. Quasi-periodic oscillations in the Z source GX 340+0. *Monthly Notices of the Royal Astronomical Society*, 249:113–121, 1991.
- [56] P. Predehl and J. H. M. M. Schmitt. X-raying the interstellar medium: ROSAT observations of dust scattering halos. *Astronomy and Astrophysics*, 293:889–905, 1995.
- [57] William H. Press, Brian P. Flannery, Saul A. Teukolsky, and William T. Vetterling. *Numerical Recipes in C*. Cambridge University Press, Cambridge, 1988.
- [58] S. Rappaport, P. C. Joss, and F. Verbunt. A new technique for calculations of binary stellar evolution, with application to magnetic braking. *The Astrophysical Journal*, 275:713–731, 1983.
- [59] S. Rappaport, P. C. Joss, and R. F. Webbink. The evolution of highly compact binary stellar systems. *The Astrophysical Journal*, 254:616–640, 1982.
- [60] S. Rappaport, Ph. Podsiadlowski, P. C. Joss, R. DiStefano, and Z. Han. The relation between white dwarf mass and orbital period in wide binary radio pulsars. *Monthly Notices of the Royal Astronomical Society*, 273:731–741, 1995.
- [61] Eric M. Schlegel (editor). *The RXTE Technical Appendix*. NASA / Goddard Space Flight Center, Greenbelt, MD, 1995. Currently available via the world wide web or anonymous ftp at <ftp://legacy.gsfc.nasa.gov/xte/nra/appendix.f/>.
- [62] Robert E. Shirey, Hale V. Bradt, Alan M. Levine, and Edward H. Morgan. X-ray timing and spectral evolution of Circinus X-1 versus orbital phase with the Rossi X-ray Timing Explorer. *The Astrophysical Journal*, 469:L21–L24, 1996.

- [63] Robert E. Shirey, Hale V. Bradt, Alan M. Levine, and Edward H. Morgan. Quasi-periodic oscillations associated with spectral branches in RXTE observations of Circinus X-1. *The Astrophysical Journal*, 506, 1998.
- [64] A. Skumanich. *The Astrophysical Journal*, 171:565, 1972.
- [65] Alan P. Smale. A type i burst with radius expansion observed from Cygnus X-2 with the Rossi X-ray Timing Explorer. *The Astrophysical Journal*, 498:L141–L145, 1998.
- [66] M. A. Smith. Rotational studies of lower main-sequence stars. *Publications of the Astronomical Society of the Pacific*, 91:737–745, 1979.
- [67] R. T. Stewart, J. L. Caswell, R. F. Haynes, and G. J. Nelson. Circinus X-1: A runaway binary with curved radio jets. *Monthly Notices of the Royal Astronomical Society*, 261:593–598, 1993.
- [68] R. T. Stewart, G. J. Nelson, W. Penninx, S. Kitamoto, S. Miyamoto, and G. D. Nicolson. Long-term infrared behavior of Circinus X-1. *Monthly Notices of the Royal Astronomical Society*, 253:212–216, 1991.
- [69] A. F. Tennant. High-frequency oscillations from Cir X-1. *Monthly Notices of the Royal Astronomical Society*, 226:971–978, 1987.
- [70] A. F. Tennant. Observations of 1.4-Hz quasi-periodic oscillations in Cir X-1. *Monthly Notices of the Royal Astronomical Society*, 230:403–414, 1988.
- [71] A. F. Tennant, A. C. Fabian, and R. A. Shafer. The discovery of X-ray bursts from Cir X-1. *Monthly Notices of the Royal Astronomical Society*, 219:871–881, 1986.
- [72] A. F. Tennant, A. C. Fabian, and R. A. Shafer. Observations of type I X-ray bursts from Cir X-1. *Monthly Notices of the Royal Astronomical Society*, 221:27P–31P, 1986.
- [73] James L. Terman, Ronald E. Taam, and Craig O. Savage. A population synthesis study of low-mass X-ray binary systems. *Monthly Notices of the Royal Astronomical Society*, 281:552–564, 1996.
- [74] J. A. Tomsick, I. Lapshov, and P. Kaaret. An X-ray dip in the X-ray transient 4U 1630-47. *The Astrophysical Journal*, 494:747–752, 1998.
- [75] Hiroshi Tsunemi, Shunji Kitamoto, Makoto Manabe, Shigengori Miyamoto, and Koujun Yamashita. All Sky Monitor on board the Ginga satellite and its performance. *Publications of the Astronomical Society of Japan*, 41:391–403, 1989.

- [76] M. van der Klis. Fourier techniques in X-ray timing. In H. Ögelman and E. P. J. van den Heuvel, editors, *Timing Neutron Stars*, pages 27–69. Kluwer Academic Publishers, 1989.
- [77] M. van der Klis. Similarities in neutron star and black hole accretion. *The Astrophysical Journal Supplement Series*, 92:511–519, 1994.
- [78] M. van der Klis. Rapid aperiodic variability in X-ray binaries. In W. G. H. Lewin, J. van Paradijs, and E. P. J. van den Heuvel, editors, *X-ray Binaries*, pages 252–307. Cambridge University Press, 1995.
- [79] M. van der Klis. Kilohertz quasiperiodic oscillations in low-mass X-ray binaries. In R. Buccheri and J. van Paradijs, editors, *The Many Faces of Neutron Stars*, page (in press). Dordrecht: Kluwer, 1998.
- [80] B. A. Vaughan et al. Searches for millisecond pulsations in low-mass X-ray binaries II. *The Astrophysical Journal*, 435:362–371, 1994.
- [81] Brian A. Vaughan and Michael A. Nowak. X-ray variability coherence: How to compute it, what it means, and how it constrains models of GX 339-4 and Cygnus X-1. *The Astrophysical Journal*, 474:L43–L46, 1997.
- [82] F. Verbunt and C. Zwaan. Magnetic braking in low-mass X-ray binaries. *Astronomy and Astrophysics*, 100:L7–L9, 1981.
- [83] J. A. J. Whelan et al. The optical and radio counterpart of Circinus X-1 (3U 1516-56). *Monthly Notices of the Royal Astronomical Society*, 181:259–271, 1977.
- [84] Rudy Wijnands and Michiel van der Klis. KiloHertz quasi-periodic oscillations in the Z sources GX 340+0, Cygnus X-2, GX 17+2, GX 5-1, and Scorpius X-1. In S. S. Holt and T. Kallman, editors, *Proceedings of the 8th Annual Astrophysics Conference in Maryland*, 1997.
- [85] Rudy Wijnands and Michiel van der Klis. Discovery of the first accretion-powered millisecond X-ray pulsar. Submitted to *Nature*, 1998.
- [86] K. S. Wood et al. Searches for millisecond pulsations in low-mass X-ray binaries. *The Astrophysical Journal*, 379:295–309, 1991.
- [87] K. Yoshida, K. Mitsuda, K. Ebisawa, Y. Ueda, R. Fujimoto, and T. Yaqoob. Low state properties of the low-mass X-ray binary X1608-522 observed with Ginga. *Publications of the Astronomical Society of Japan*, 45:605–616, 1993.

- [88] W. Zhang, K. Jahoda, J. H. Swank, E. H. Morgan, and A. B. Giles. Dead-time modifications to fast Fourier transform power spectra. *The Astrophysical Journal*, 449:930–935, 1995.
- [89] W. Zhang, E. H. Morgan, K. Jahoda, J. H. Swank, T. E. Strohmayer, G. Jernigan, and R. I. Klein. Quasi-periodic X-ray brightness oscillations of GRO J1744-28. *The Astrophysical Journal*, 469:L29–L32, 1996.
- [90] W. Zhang, T. E. Strohmayer, and J. H. Swank. Discovery of two simultaneous kilohertz quasi-periodic oscillations in the persistent flux of GX 349+2. *The Astrophysical Journal*, 500:L167–L169, 1998.